UNIVERSITY OF STRATHCLYDE, GLASGOW, UK

FACULTY OF ENGINEERING, DEPARTMENT OF BIOMEDICAL ENGINEERING

Micro-Particle Image Velocimetry for Lymphatic Flow

---

by
Konstantinos MARGARIS

A thesis presented in fulfilment of the requirements for the degree of Ph.D. in Bioengineering, 2014

Copyright Declaration

This thesis is the result of the author's original research. It has been composed by the author and has not been previously submitted for examination which has led to the award of a degree.

The copyright of this thesis belongs to the author under the terms of the United Kingdom Copyright Acts as qualified by University of Strathclyde Regulation 3.50. Due acknowledgement must always be made of the use of any material contained in, or derived from, this thesis.

Signed:

Date: 9/3/2015

Dedicated to the memory of my beloved father, Professor Nikolaos I. Margaris (1949-2013),

Dean of the Engineering Faculty, Aristotle University of Thessaloniki, Greece.

“I often say that when you can measure what you are speaking about, and express it in numbers, you know something about it; but when you cannot measure it, when you cannot express it in numbers, your knowledge is of a meagre and unsatisfactory kind; it may be the beginning of knowledge, but you have scarcely in your thoughts advanced to the state of Science, whatever the matter may be.”

Lord Kelvin, Lecture on ”Electrical Units of Measurement” (3 May 1883), published in Popular Lectures Vol. I, p. 73

Contents

List of Figures

List of Tables

Glossary

μ-PIV micro Particle Image Velocimetry.

A-V Atrio-Venticular.

bpm Beats per minute.

CAMP Contraction Amplitude.

CS Control Surface.

CV Control Volume.

CW Continuous Wave.

DAQ Data Acquisition System.

EDD End Diastolic Diameter.

EF Ejection Fraction.

ESD End Systolic Diameter.

FOV Field of View.

FPF Fractional Pump Flow.

fps Frames per second.

FREQ Contraction Frequency.

IW Interrogation Window.

L-V Left Ventricle.

LED light-emitting diode.

PCA Principal Component Analysis.

PIV Particle Image Velocimetry.

PM Pulsed Mode.

PTV Particle Tracking Velocimetry.

Re Reynolds number.

RMS Root mean square.

WD Window Deformation.

WSS Wall Shear Stresses.

Mathematical symbols

Symbol	**Description**	**Units**
c	Calibration constant	mm/px
ψ	Scaling magnification factor	mm/px
D	Stokes-Einstein diffusion coefficient	m^2/s
Δt	Pulse separation time	μs
ΔP_{axial}	Axial pressure gradient	cmH_2O
d_p	Particle physical diameter	m
d_τ	Particle image size on sensor	px
d_w	Wall thickness	m
d	Vessel internal diameter	m
ϵ_b	Uncertainty due to Brownian motion	mm/s
ϵ_d	Uncertainty due to particle location estimation	mm/s
ϵ_t	Total uncertainty	mm/s
ϵ_u	Uncertainty of velocity due to experimental setup	mm/s
$f_\#$	Objective f-number	-
f	Lens focal length	mm
ϕ'	Particle response time constant	-
ϕ	Particle volume fraction	-
$\bar{V}$	Volume	mm^3
k_B	Boltzmann's constant	$\frac{m^2kg}{s^2K}$
V_{fluid}	Median value of fluid velocity	mm/s
V_w	Median value of wall radial velocity	mm/s
L	Calibration scale distance on sensor	px
λ	Wavelength of light	nm

Symbol	Description	Units
λ_d	Distance of calibration scale to camera lens	mm
l	Calibration length scale	mm
M	Magnification	-
t_{diff}	Particle diffusion time	s
μ	Dynamic viscosity	$Pa \cdot s$
ν	Kinematic viscosity	m^2/s
NA	Objective numerical aperture	-
p, P	Pressure	Pa, cmH_2O
P_{avg}	Transmural pressure	cmH_2O
Q, Q_{th}	Experimental/Theoretical flow rate	$\mu l/hr$
ρ_f	Fluid density	kg/m^3
ρ_p	Particle density	kg/m^3
r_i	Vessel internal radius	m
σ_w	Wall stress	Pa
T	Absolute temperature	K
τ_p	Particle response time	t
t	Time	s
τ	Shear stress	Pa, dyn/cm^2
$u, \mathbf{v}$	Particle velocity (bold letters denote vector quantity)	mm/s
w_{L1}	Uncertainty of distance measurement on image	px
w_{L2}	Uncertainty due to aberrations	px
w_l	Accuracy of calibration scale	μm
w_{t1}	Pulse timing uncertainty	μs
w_{t2}	Delay generator uncertainty	ns
$\mathbf{X}_p, \Delta\mathbf{X}_p$	Particle position/displacement on sensor (bold letters denote vector quantity)	px

Abstract

The lymphatic system constitutes a vital part of the systemic circulation, maintaining tissue fluid homeostasis; its biological significance is not limited to fluid balance, as it is a part of the immune system, facilitating immune cell trafficking and initiating the immune system response to pathogens. However, the hydrodynamics/biomechanics of the lymphatic system have been relatively understudied when compared to the cardiovascular system. In contrast with the latter, where the heart provides the necessary energy for blood flow, the lymphatic system relies on the active contraction of vessels and one-way valves to generate and sustain flow.

The present thesis describes the development of an optical flow diagnostic method for resolving the 2-dimensional flow field at the mid-plane of isolated contracting mesenteric rat lymphatic vessels, *in-vitro*. The aim was to develop an experimental protocol for accurately estimating flow parameters, and in addition, estimate lymphatic functional parameters, with high spatial and temporal resolution. Previous studies *in-situ* have relied on lymphocytes as tracers, but their low density however resulted in a reduced spatial resolution.

The time-resolved micro-Particle Image Velocimetry technique, a well established method has been employed to study this transient flow. To that end, a bespoke light source was developed, utilising high-power light-emitting diodes, as well as associated control and image processing software. Image analysis was performed with PIV cross-correlation algorithms and was facilitated by custom vessel wall detection algorithms. In terms of flow parameters, flow velocity, flow rate and shear stresses were estimated from the raw images. Additionally, the dynamic pressure was estimated allowing for extraction of pressure volume curves and estimation of work performed during contraction by the lymphatic vessels. It was also possible to obtain an estimation of lymphatic wall stress. The results were extended to lymphatic functional parameter estimation, such as contraction amplitude and fractional pump flow. Statistical analysis was undertaken, in order to reveal possible relationships between the experimental parameters and the derived hydrodynamic/biomechanical results. Analysis of the uncertainty of the measurements showed that method employed provides exceptional accuracy.

The results demonstrated the successful application of the micro-PIV technique in lymphatic vessels and yielded interesting observations, either previously unreported in the literature or contradicting previous reports. The wall velocity was shown that it may be comparable to the fluid one; an observations that questions the assumptions of previous attempts to study lymph flow. It was also observed that the flow rate may not increase during contraction depending on the hydrodynamic conditions. Although an incidental finding, vibrations were shown to increase the contraction frequency of lymphatic vessels.

Acknowledgements

This PhD, as I presume many others, was at the beginning a venture into the unknown. For guiding me through these uncharted waters, and for occasionally leaving me to hit the shallows, I have my supervisor, Dr Richard Black, to thank. This work would not have taken the form it has today without his advice and guidance.

In terms of funding, first and foremost, I would like to thank the Scottish Funding Council for giving me a fully funded PhD Studentship. The PIV experiments in lymphatic vessels were carried out in collaboration with Texas A&M University. My two visits were made possible with additional funding. I am grateful to the Royal Society of Edinburgh for the award of a John Moyes Lessels travel scholarship and to Strathclyde University for providing additional funding under the Strathclyde Exchange Programme, an EPSRC funded project.

Although the funding was critical in undertaking my research trip, its successful completion wouldn't have been possible without the host departments in Texas A&M University. I am indebted to Dr J. Moore, Jr. and Dr D. Zawieja for hosting my visit in their labs and making available to me their resources in terms of equipment, funds and time, their own and that of their research assistants. Dr Zhanna Nepiyushchikhich undertook the vessel isolation and cannulation procedure and her efforts were paramount in the PIV experiments in lymphatic vessels.

During the development phase of the light source, a Nikon microscope and two Photron camera (as part of a μ-PIV system) were supplied on loan from the UK Engineering & Physical Sciences Research Council instrument pool. Dr Keith Matthieson and Dr Nial McAllinden from the Institute of Photonics, University of Strathclyde, UK provided laboratory space for the micro-PIV system on loan and gave access to equipment, such as a power meter and a spectrometer.

The technical staff of the Biomedical Engineering department deserve merit for their involvement in my project. John MacLean did an excellent job putting together the electrical/electronic parts of the LED light source and for showing me the basic, yet necessary electronics skills for my work. Stephen Murray modified existing and manufactured custom parts necessary for the light source and experiments. His input in the designs and his manufacturing skills are very much appreciated.

I would also like to thank Dr Paul Murray (Department of Electronic & Electrical Engineering, Strathclyde University, UK) for his input in image edge detection algorithms and Dr. Christos Diou (Department of Electrical and Computer Engineering, Aristotle University of Thessaloniki, Greece) for developing one of the algorithms used for vessel wall detection.

Ms. Maria Latta, the future Mrs, deserves special merit for hand drawing figures 1.1 and 1.2, as the cherry on the top of my dissertation.

Chapter 1

The Lymphatic system[1]

The lymphatic system is a one-way transport system that operates in conjunction with the circulatory system. Its primary function is to transport excess interstitial fluid, from the interstitial space, back to the blood circulation, via the thoracic duct [17]. Along with the excess interstitial fluid, excessive proteins and wastes are transported back to the circulation. The lymphatic system also acts as a conduit for immune cells and facilitates the immune response [137]. Lymph nodes across the network filter the interstitial flow and breakdown bacteria, viruses and waste. The lymphatic system is, therefore, not part of the circulatory system alone; rather it is an integral part of the immune system. It plays an important role in the dissemination of cancer [136, 138]. Its role in transplantation is also significant. Latest findings suggest that early lymphangiogenesis in a transplanted graft may be responsible for early rejection, but it is beneficial later on [29]. Additional latest findings implicate the lymphatic system in cardiovascular disease, obesity, hypertension and other inflammatory disorders [61].

Failure of lymph drainage can be a consequence of infection, trauma, surgery, transplantation, medication, venous disease or it may be congenital [136, 143]. The build up of interstitial fluid results in swelling, pain and increases the risk of infection. This condition is known as lymphoedema and current treatments have limited success. Arm lymphoedema is very common in breast cancer patients and lower limb lymphoedema may lead to incapacity in severe cases.

The environment of the lymphatic system does not contribute to the destruction of cancer cells, contrary to that of the circulatory system [136]. In the cardiovascular system, the serum is toxic to those cells and the high shear stresses developed in the blood stream destroy the majority

---

[1] The contents of this chapter, with changes, except those of section 1.2.3, have been published in the Journal of the Royal Society Interface [82].

of tumour cells. On the other hand, the flow in the lymphatic system is of low Reynolds number and lymph composition is similar to plasma.

Despite the importance of the lymphatic system in health and disease, it remains overlooked in terms of research especially relatively to the circulatory system [37, 121]. While in other areas tissue engineering has made some progress towards therapy, in lymphatics it is still in its infancy [138].

1.1 Anatomy

The lymphatic system is composed of a network of vessels, termed lymphatics, lymph nodes and lymphoid organs. The interstitial fluid enters through the small lymphatic capillaries (also called initial or terminal lymphatics) that gradually combine to form larger diameter vessels, namely the pre-collectors, collectors, trunks and ducts. The interstitial fluid, which is termed lymph when inside the lymphatics, is being pumped slowly by the contraction of the lymphatic vessels, which contain smooth muscle on their walls. Retrograde flow is prevented by series of one-way valves. The segment of a lymphatic vessel between two valves is referred to as a lymphangion.

The lymphatic network is asymmetrical: the right part of the head and thorax and the right arm drains into the right subclavian vein whereas the lymphatic vessels of the rest of the body converge to the thoracic duct which empties at the junction of the jugular and left subclavian veins.

1.1.1 Initial lymphatics

Initial lymphatic capillaries have a diameter of about 10 to 60 μm with a wall thickness ranging from 50 to 100 nm and are blind ended. Electron microscopy revealed that lymphatic capillaries are usually collapsed with irregular walls and do not have a continuous basal lamina. They comprise a monolayer of non-fenestrated endothelial cells [138]. They are supported by anchoring filaments (6 to 10 nm in diameter) that keeps them from completely collapsing when interstitial fluid pressure increases [70]. Their unique structure allows them to function as a one-way valve system that allows fluid to flow into them but close in order to stop back flow as the internal pressure rises. Trzewik et al. [144] demonstrated this function experimentally, although they were not the first to postulate about the existence of primary lymphatic valves.

Leak and Burke [70] investigated the structure of the lymphatic capillaries, and speculated that they could function as valves, although at that time no proof was provided.

1.1.2 Precollecting lymphatics

The precollecting lymphatics connect the capillaries to the collecting vessels. They contain bicuspid one-way valves, but unlike the collecting vessels, where they are located at regular intervals, their distribution becomes more irregular towards the capillary vessels, and may comprise of a single leaflet. [124, 143]. The precollectors contain one or more layers of smooth muscle cells within their walls, and are capable of performing spontaneous contractions. However, portions without muscle exist. In these parts, the endothelial layer in the precollectors is similar to that of initial lymphatics with a discontinuous basal lamina. Thus these structures absorb fluid instead and therefore the precollectors have dual role: absorption and propulsion of lymph [124].

1.1.3 Collecting lymphatics

The larger collecting lymphatics differ from the capillaries and precollectors, as they have a complete basal lamina and therefore the primary lymphatic valves are absent. They contain another type of valve that prevents retrograde flow: the secondary one. The wall structure is similar to that of blood vessels. Three layers can be identified, the intima, media and adventitia [12]. An oblique layer has been reported by Telinius et al. [140] in the human thoracic duct. They are composed of endothelial cells, smooth muscle and collagen fibres, respectively. It has been observed that the muscle bundles are arranged in a hellicoidal manner in both collecting and precollecting vessels [124]. The part of the vessel between two valves is known as a lymphangion (figure 1.1).

Lymphangions are innervated with sympathetic and parasympathetic nerves, and can perform rhythmic contractions. In humans, the lymphangions present within the head and neck have an average diameter of 0.2 mm and a length of 2 mm, yielding a diameter to length ratio of 0.1 [106]. Collecting lymphatics are approximately 1-2 mm in diameter in human lower extremities [105]. The largest (and deeper) lymphatic vessels, also referred to as trunks and ducts, have a diameter of the order of 2 mm, and the diameter to length ratio can be close to unity.

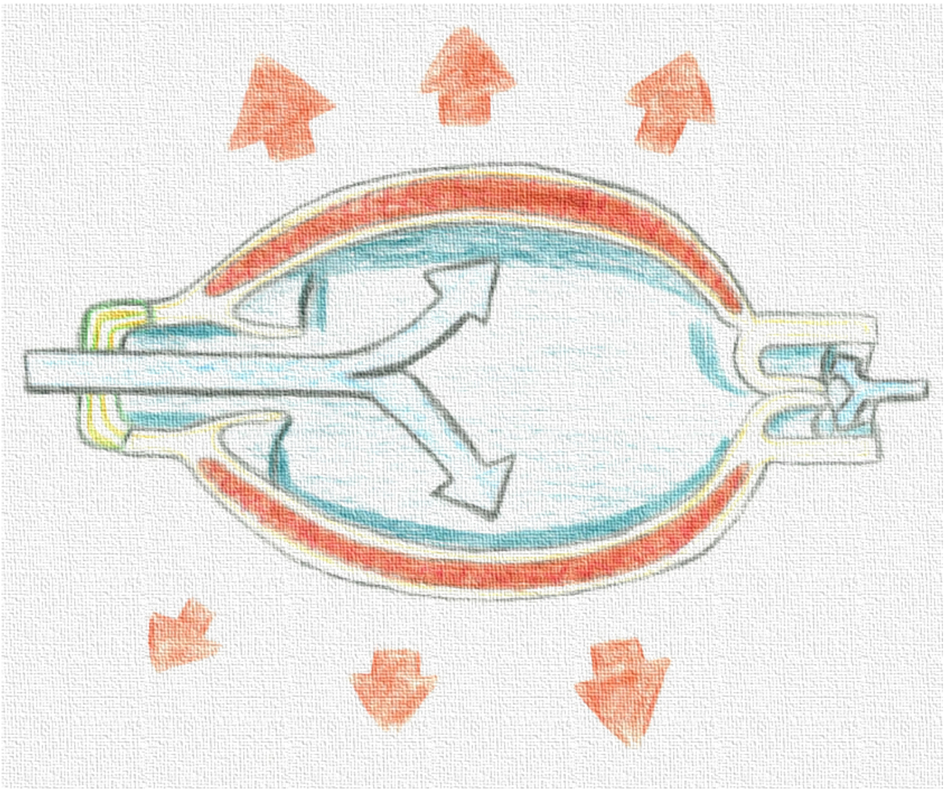

Figure 1.1: Schematic representation of a lymphangion, redrawn from Quere [113]. Lymphangions have been reported to double or triple their diameter during diastole [8, 97]

1.1.4 Secondary Valves

Generally, the lymphatic secondary valves are of the bicuspid type, regardless of species studied [73, 83]. However, up to five leaflet valves have been observed as well as single leaflet ones [43]. Data regarding the size, the geometry and the number of valves is scarce, and, in humans especially, there is a lack of data on the structure and operation of the lymphatic valves [45], although valve size varies with the vessel calibre [106].

Studies of the rat spinotrapezius muscle by Mazzoni et al. [83] have shown that smooth muscle cells are absent from the valve leaflets, indicating that these are passive structures.[2] The valves comprise of a monolayer of endothelial cells on a collagen matrix. Mazzoni et al. [83] suggested that the valve operation is determined by the pressure and viscous forces associated with the lymph flow. Based on the anatomy of valves studied and the presence of a buttress structure,[3] the authors speculated that tension by surrounding tissues may also contribute. Recently, Davis et al. [26] investigated the valve gating in rat mesenteric lymphatics. The authors

---

[2] Although smooth muscle cells are present in bovine valve leaflets, no evidence of an active valve mechanism has been reported in the literature [26]

[3] An explanation of the lymphatic valve anatomy is given in Appendix D

observed that opening and closing of valves was occurring only because of a pressure gradient, however the vessel muscle tone influenced the required pressure gradient. In studies of the thoracic duct of monkeys by Lee et al. [73] have showed the presence of bicuspid valves, but no buttress structure, indicating that there may be differences in the details of valve operation depending on species and anatomical site.

1.1.5 Lymphoid organs

Lymphoid organs are classified as being either primary or secondary organs. The primary organs are the thymus and bone marrow, and are responsible for the production and maturation of lymphocytes. The secondary organs include the spleen, Peyer's patches, appendix, the tonsils and the nodes. They are responsible for further maturation of lymphocytes and initiation of an immune response. Only the structure and function of the lymph nodes will be discussed in the context of this paper, as they are the only lymphoid organs that play a role in the active lymph transport [113].

The structure of the node is highly complex and not easily visualised, owing to the large number of cells that are resident within it [99]. A representation of the lymph node structure is shown in figure 1.2.

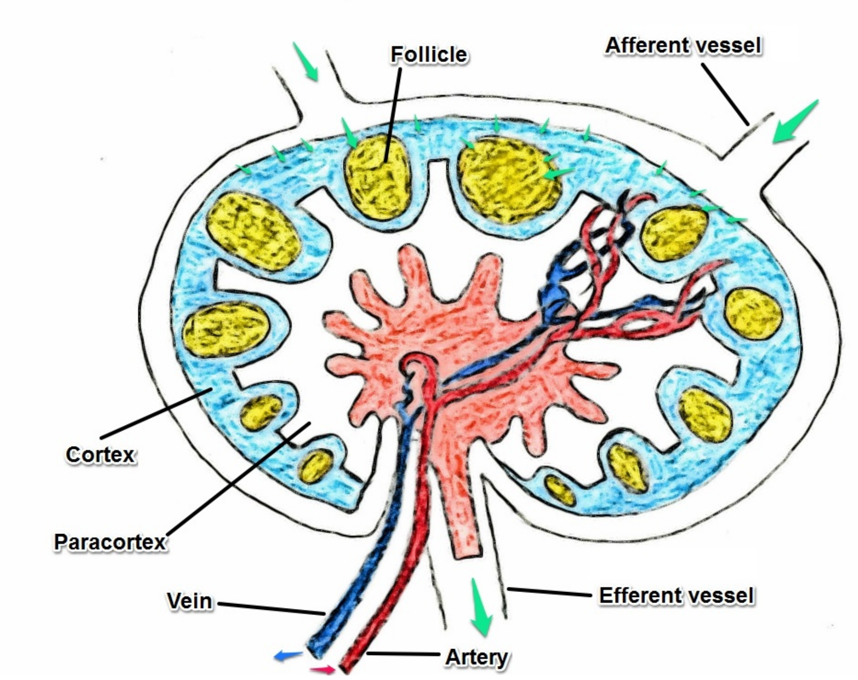

Figure 1.2: Schematic of a lymph node.[4] Lymph flows around the lymphoid compartment and part of it enters in the paracortex and follicles where cells of the immune system remove pathogens and foreign material.

The exterior walls of the node are covered with lymphatic smooth muscle, thus exhibiting contractile behaviour like the lymphatic vessels, although the frequency of contraction is lower. Hughes and Allen [58], McGeown and Gallagher [84] report a frequency of 0.78 beats/min in bovine nodes, while Thornbury et al. [141] observed contractions at a frequency of 0.5-1 beats/min in ovine nodes. Tumer et al. [145] performed a frequency analysis and found the dominant rhythms to lie within the ranges of 0.01-0.04 Hz, 0.05-0.07 Hz and 0.09-0.14 Hz. In contrast, lymphatic collecting vessels contract at a frequency in the range of 0.6-10 beats/min [87, 86, 98, 160], although up to 30 beats/min have been reported in the literature [128]. Limited information exists on human nodal contractility, its presence and its regulating mechanisms [45].

Lymph nodes present a relatively high resistance to flow, which depends on the flow rate of lymph [15, 107]. Papp et al. [107] reported that the resistance of the node in dogs was 100 times larger than that of the thoracic duct, while Browse et al. [15] found that the resistance of the nodes fell by up to six times as the flow rate in the afferent lymphatics increases. They concluded that the reduction in resistance was due to swelling of the node, which created more space for lymph to flow, thereby reducing their resistance. Nevertheless, despite this reduction, the nodes still impose a large resistance to the flow.

It is not surprising that the nodes have a large resistance, if one considers their internal structure. Lymph flows into the subcapsular sinus and is immediately forced to flow around the lymphoid compartment[5] and into the paracortex; where it is filtered by macrophages that reside on the outer surface of the lymphoid compartment. Most of the lymph exits the node from the efferent lymphatics without entering the lymphoid compartment. While in figure 1.2 multiple afferents and one efferent vessel are shown, any possible combination of the number of these vessels has been observed in humans [106] as well as mice [67]. Kowala and Schoefl [67] also observed that there is no constant relationship of the number of afferent vessels and the number of nodal compartments. Whether this variation in numbers of vessels is for overall node resistance reduction, increased lymph filtering efficiency or both is uncertain.

The outer surface of the lymphoid compartment is covered by sinus-lining cells that create an almost impermeable membrane [122]. Large molecules cannot penetrate this layer, thus creating an effective barrier that prevents pathogens from reaching the bloodstream. Lymphocytes,

---

[4] Redrawn from the US National Institute of Health, National Institute of Allergy and Infectious Diseases, `http://www.niaid.nih.gov/topics/immuneSystem/Pages/structureImages.aspx`

[5] Also called lymphoid lobule [155]

lymph and smaller molecules can enter through specialized channels [99, 122]. The exclusion of large molecules from the lymphoid compartment explains the well established fact that the protein composition of efferent lymph is higher than the afferent one, although the exact mechanisms of mass exchange are not fully understood.

The amount of lymph entering is low and therefore the inside of the lymphoid compartment is relatively fluid free, although a controversy in the literature does exist as according with Tretbar et al. [143], up to 50% of the lymph is lost inside this compartment. Lymph flows within specialized channels, refered to as the conduit system [49, 122] that start from the sinus lining cells and end on the lumen of venules that penetrate inside the lymphoid compartment. The cells lining these venules have a special adaptation that allows lymphocytes to freely enter the node from the blood and are named High Endothelial Venules (HEV). The HEV also allow lymph to return to the bloodstream.

1.2 Physiology

The interstitial fluid is taken up by the small lymphatic capillaries in a process known as lymph formation. Lymph is then pumped against a pressure gradient towards the jugular vein, by rhythmic contractions of the lymphangions and by external motion of skeletal muscle, arteries and veins. This process is referred to as lymph propulsion. Lymph formation depends on external (or extrinsic), but local, effects such as interstitial fluid pressure and extracellular matrix strain and is thus a local process [136]. Lymph propulsion on the other hand is a systemic process regulated by a large number of factors; streamwise pressure gradients, transmural pressure, nerves and hormones.

1.2.1 Lymph formation

Several mechanisms have been proposed for the formation of lymph in initial lymphatics. Of those, only the interstitial pressure and volume theory has been widely accepted [6]. Yet, the exact regulatory mechanisms are unclear [46].

Lymph enters through openings in the endothelial layer of the capillaries, which act as one-way valves. They open when interstitial pressure increases and permit interstitial fluid flow inside the initial lymphatics. As the pressure inside the vessel rises, the valve closes. Flow inside the initial lymphatics is thought to be facilitated by fluctuations of interstitial fluid pressure and due to the suction of the collecting lymphatics downstream [119]. Studies in a number of mammalian species (rodents, canine, ovine, bovine, humans) have shown no evidence of smooth muscle cells in the initial lymphatics. It follows that the driving force of lymph formation must be due to extrinsic factors. The sole exception to this is the bat [6, 128]

Lymph formation is organ dependent because of the differences in the structure and mechanical properties between tissues [127].

1.2.2 Lymph propulsion

After the filling of the initial lymphatics, lymph has to be pumped against a pressure gradient. Lymph propulsion is performed by the rhythmic contractions of the smooth muscles of lymphangions and facilitated by the presence of the one-way valves that prevent retrograde flow. The contractions propagate from one lymphangion to the next like a wave that causes both radial contraction and axial shortening of the vessels [36, 160]. It has been reported that lymphangions rotate as well *in vitro* [80], most likely owing to the helical disposition of these cells within the vessel wall [124]. Although there is evidence to support that the contraction wave is transmitted between lymphangions through endothelial gap junction [160], it has been observed that the propagation of the wave may become discontinuous. This suggest that lymphangions have a self regulating mechanism mediated by pacemaker cells that are thought to reside downstream of the valves [86]. The contraction wave can travel in an orthograde or retrograde direction. Evidence shows that either propagation direction is equally likely to take place [160] and that the volume of fluid pumped is not significantly affect by it [86].

There is some controversy regarding the nature of individual lymphangion contraction however. The accepted view is that lymphangions contract in a peristaltic manner, that is, the contraction is a radial constriction of the vessel travelling along its length, similar to the oesophagus or the ureter [43, 136]. Evidence supporting this view exist in the literature [98] with 84% of the contractions observed propagating along the entire length of the lymphangion [160]. Peristalsis in guinea pig mesenteric lymphatics has also been reported [36]. The peristaltic character of contraction is disputed by others[6] and videos captured with high-speed camera by Davis et al. [26] show the entire wall contracting at roughly the same time. It should be noted that these studies were conducted in different species; bovine in Ohhashi et al. [98] and rats in Davis et al.

---

[6] Dr. J. E. Moore, Texas A&M University. personal communication

[26].

Lymph propulsion in collecting vessels is affected by preload, afterload, transmural pressure, shear stresses in addition to nerve and humoral mediators. These are termed intrinsic mechanisms. The details of these mechanisms and especially the molecular regulation are not fully understood [92]. Extrinsic mechanisms such as skeletal muscle contraction, motion of adjacent organs and arterial pulsations also influence lymph flow. External forces such as massaging, a common treatment modality for lymphoedema, were once thought to affect lymph flow but the evidence show that their effect is on the filling of initial lymphatics rather than on the pumping of the larger collecting vessels [5].

It is not clear whether extrinsic mechanism can have a significant or even dominant role in the pumping of lymph. Olszewski [102], Olszewski and Engeset [103] consider extrinsic mechanisms secondary to the intrinsic pumping based on their results on humans. On the other hand, Negrini et al. [94] found that, in rabbits, pleural lymph flow is due to respiratory movements up to 40% of the total volume, although it cannot be excluded that at other sites the intrinsic mechanism is not the dominant one.

Passive flow due to a positive pressure gradient may also occur in oedema, during which, lymph formation is increased [5]. In fact, Gashev et al. [44] report that for low levels of lymph formation the intrinsic mechanism is dominant but as these levels rise the active lymph pump is inhibited and the vessels become conduits. However, according to the authors, this does not prove that the flow related inhibition decreases total flow *in vivo*, since at higher levels of lymph formation, passive flow may be dominant.

1.2.3 Lymphatic muscle contractility

Lymphatic smooth muscle contraction is influenced by mechanical, fluidic, neuronal and hormonal factors [14]. Lymphatic smooth muscle has been shown to have a combination of striated and smooth muscle contractile apparatus [92], but have also differences in contractile characteristics that materialise in functional differences between lymphatic and vascular muscle [150]. It is thought that the phasic contractions are regulated by the striated components of the lymphatic muscle, whereas the smooth muscle governs the tonic contractions.

Contraction is pressure/stretch sensitive; that is, as pressure builds up within a vessel, it reaches a threshold value at which the vessel contracts to propel lymph [56], but phasic contractions can occur even at zero transmural pressure [46] indicating pacemaking capacity of lymphatic vessels. The pacemaking in lymphatic vessels is established in the literature and studies have been undertaken to locate the pacemaking cells location, still it is uncertain whether there exists a specialized pacemaker cell [3].

The contractile function of lymphatic vessels has been linked with the wall shear stresses (WSS) imposed by the flow [44, 46]. WSS is hydrodynamic factor known to influence the function of blood vessels and it is not surprising that research has shown the link of WSS and lymphatic muscle contractility. Although, the evidence of the effect of WSS on lymphatic muscle function exist, little work has been done to accurately measure and quantify WSS at controlled laboratory conditions in terms of the hydrodynamic factors involved. It is yet unclear how sensitive lymphatic vessels are to WSS [42].

1.3 Related Work & Objectives

1.3.1 Measurements of lymph flow

Experimental attempts to quantify lymph flow have been very limited in number. The most recent one, with which the experimental methodology employed in the present thesis is most closely related to, is the work by Dixon and co-workers [30, 31, 32]. By employing a microscope with continuous wave illumination and a high speed camera, lymphocytes inside contracting lymphatic vessels were imaged in the exteriorised rat mesenteric area *in-situ*. An image correlation algorithm was used to estimate the velocity of the lymphocytes [32]. At the same time the vessel diameter was measured. The flow rate was then estimated assuming circular cross-section and fully developed parabolic velocity profile. The need for Poiseuille flow assumption was necessary, because the lymphocyte density is low and very few cells were present in each frame. Therefore it was not possible to resolve the 2-dimensional flow field at the microscope focal plane. Even if the lymphocyte density had been higher, their relatively large size in comparison to the vessel lumen diameter (approximately 10 μm cells inside 100 μm vessels) would yield a low spatial resolution. It was also observed, in these studies, that the contrast of lymphocytes is poor, which decreases the success of the correlation algorithm. In engineering terminology, the method employed is a Particle Tracking Velocimetry (PTV); an image correlation algorithm was employed for particle matching between frames. Measuring lymph flow *in-situ* also made the method susceptible to motion artefacts from animal movement and, in addition, it was not possible to control, or quantify, fluidic and biological factors, such as inflow/outflow pressure and neuronal/hormonal stimulation.

Another fundamental assumption to the aforementioned method was that during contraction, at least for most of it, the wall radial velocity was much smaller than the fluid velocity. This assumption allowed the radial fluid velocity to be neglected, simplifying the mathematical problem of flow rate estimation.

The method by Dixon et al. [32] was used by Akl et al. [2] to measure and compare lymph flow in rat mesenteric lymphatic vessels *in-situ* and in isolated vessels *in-vitro*. This study demonstrated that a carefully executed preparation of an isolated vessel has no significant impact in its contractile behaviour and thus can be used to study the contractile characteristics *in-vitro* without the complexities of undertaking an *in-vivo* study.

Despite these drawbacks, these studies have been the most recent and only attempts in estimating fluid velocity and its temporal variations inside collecting lymphatic vessels. Several other attempts have been made to measure lymphatic flow rate in a variety of species, which will be reviewed in the following paragraphs, however they are restricted to average flow rate measurements or tracking volumes of fluorescently tagged particles; whilst very useful from a physiological or clinical perspective these methods cannot give an estimation of the local fluidic environment and especially wall shear stresses which is an important parameter that affect lymphatic function.

Onizuka et al. [104] and Naito et al. [93] implanted an ultrasound flow probe in sheep to measure the flow rate of the thoracic duct. The flow rates measured were three to six times greater than the ones measured in cannulated vessels and this fact was attributed to the invasive cannulation procedure. However, the authors did not clarify any effects the presence of the ultrasound probe had on the contraction of the thoracic duct. With this method there is no way to a priori exclude the possibility of the vessel coming into contact with the probe as it contracts. The authors did not report measurements of lymph velocity or WSS.

McGeown et al. [85] used a method that utilizes a transducer to measure lymph flow rate in conscious sheep by means of vessel cannulation. Lymph was let to accumulate on the transducer arm and the weight of the fluid caused a tension reading on the transducer. The reading of tension was correlated with lymph volume leaving the cannulated vessel. This method, however, does not yield detailed flow field information.

Fedosov et al. [34] developed an invasive method using a focused laser beam. The velocity and direction of lymphocytes was determined by cross-correlation of intensity fluctations of the speckle field between two points. The method was applied *in vivo* in the rat mesenteric area, however very limited results on measurements from different vessels were presented. Whether the method is able to measure a 2-dimesional flow field is unclear from the work published. According to Fedosov et al. [34] the velocity measured is in relative units and therefore calibration was necessary with video microscopy. Using a focused laser beam also raises concern of potential damage of the lymphatic vessels.

Non invasive *in vivo* methods have also been utilised in lymph flow measurements. Due to the lack of optical access of the vessels the visible wavelengths are not suitable and near-infrared (NIR) imaging is necessary. Although vessels and nodes up to 3cm below the surface can be visualised [130] the use of longer wavelengths has an adverse impact on the intensity of light emitted which necessitates the use of more sensitive sensors and reduces the spatial resolution. The studies in swine by Sharma et al. [130] and in mice by Kwon and Sevick-Muraca [68] displayed the capability of the method to measure average velocity of tagged 'packets' of indocyanine green (ICG) and contraction frequency, no spatially resolved information can be obtained rendering the method unsuitable for accurately resolving the flow field in lymphatic vessels. On the other hand, the importance of these studies, and of others as reviewed in Lucarelli et al. [77] and Zhang et al. [161], in clinical lymphatic imaging, is undebatable.

The aforementioned studies target the flow in larger collecting lymphatic vessels. Swartz et al. [135] and Berk et al. [10] utilised fluorescent photo-bleaching to measure the flow in the lymphatic capillaries of the mouse tail. The method uses a fluorescent dye, instead of cells or particle tracers. Although it is possible to measure velocity, the lack of individual tracers reduces the spatial resolution and no spatially resolved flow fields were reported by the authors. Additionally, diffusion of the fluorescent dye induces experimental errors in determination of the fluid velocity [1].

1.3.2 Diameter measurements

Measuring the diameter of lymphatic vessels is necessary in order to calculate the flow rate by integration of a velocity field at a given cross-section. Diameter tracing from image or video files can be a challenging procedure, as image based algorithms will be affected by noise from surrounding structures and vessel orientation. It can be computationally very expensive as well. Measuring micro-vessel wall motion is a more active area in the systemic circulation, but some work has been carried out in lymphatic vasomotion measurement. A brief summary of previous work is given below, although development of automated diameter tracing algorithms is not an objective of the present thesis, it is necessary to trace the inner vessel wall to obtain flow rate and other parameters.

Beresford-Smith et al. [9] used radar tracking techniques, Kalman filtering and Probabilistic Data Association Filter (PDAF), to track the diameter of isolated guinea-pig lymphatic vessels at a number of different vessel locations simultaneously. While the algorithm was considered computationally robust, accurate and immune to vessel orientation, it was assumed that no vessel motion perpendicular to the initial cross-section occurred. In other words, the algorithm would be challenged from longitudinal, rotational or orthogonal to the measurement plane motion of the vessel during contraction, which may occur owing to the muscle fibre orientation in the vessel wall as discussed in section 1.1.

Davis [25] used a combination of contrast thresh-holding and iterative regression to measure the outer diameter (OD) of micro-vessels, including lymphatics. An initial manual measurement by the user is needed for the internal diameter (ID), which is then computed automatically from the OD by assuming an incompressible wall. This method can track the diameter at a single point of the vessel wall, pre-defined by the user.

Dielenberg et al. [28] further improved the algorithm by Beresford-Smith et al. [9], by employing noise filtering and using the centre of mass of pixel brightness of the vessel wall to measure its motion. The method was able to measure wall motion in real time at different sites along the vessel simultaneously. Longitudinal or rotational vessel motion would again challenge this algorithm.

In order to alleviate some of the issues faced by the previously mentioned methods, Sheng and Xiu [131] implemented an automated method using feature matching to recognise and track the vessel wall and eliminate the influence of surrounding structures and image drift. The authors claim that this approach is more accurate and robust in *in vivo* measurements and can work with any vessel orientation and track diameter at multiple location.

1.3.3 Key Objectives

Flow velocity measurements in collecting lymphatic vessels are but a few. Quantitative flow measurements of 2d or 3d velocity fields have not been published thus far. The body of evidence that fluid flow, either through a pressure/stretch or via a shear mechanism, affects lymphatic contractility, is growing. Still there are few reports on the influence of flow parameters on lymphatic pumping [14] and the details of the regulation mechanisms are not fully understood [92]. Out of the previous studies discussed in section 1.3.1 only a few were performed under controlled environment, (see Akl et al. [2]) and other studies *in-vivo* such as the work be McGeown et al. [85] controlled the pressure invasively by means of cannulation of lymphatic vessels. The lymph flow measurement approach employed in the latter study would be incapable of producing detailed information of the flow field. Therefore, there is need for such experimental efforts, that will provide further insight in lymph propulsion mechanisms and regulation.

The key objective of the work presented in this thesis was to develop a system for measuring flow inside micro-lymphatic vessels *in-vitro*, under a controlled hydrodynamic environment. The aim was to develop such system with increased spatial and temporal resolution with respect to the systems already published in the literature, allowing for a more detailed view of the flow field in lymphatic vessels and valves. At the same time the goal was to interrogate the flow field non-invasively. Following the development of such system, the first major objective was to measure the flow under different hydrodynamic conditions and derive the flow quantities of interest: flow rate, wall shear stresses and pressure. The next logical step was to estimate lymphatic functional parameters, such as ejection fraction, fractional pump flow and contraction work, defined similarly to ventricular functional parameters. The latter parameter, contraction work has not been report in the literature thus far. These parameters would be estimated non-invasively. Once these objectives are met, the system can be extended to *in-situ* measurements or used to infer the flow field by tracking the movement of tracer particles in lymphatic vessels at constant hydrodynamic conditions but with chemical, electrical, or other stimuli.

In summary, the objectives on which this thesis is based are:

1. Develop a flow measurement apparatus for *in-vitro* lymph flow measurements

2. Estimate flow parameters

3. Estimate lymphatic parameters

4. Extend the application of the system beyond the *in-vitro* context

1.4 Thesis structure

The thesis is organized in the following chapters. The Materials & Methods, chapter 2, starts by giving an introduction to the Particle Image Velocimetry (PIV) method (Section 2.1) and continues with the development of the bespoke light source (Section 2.2), the experimental protocol (Section 2.3) and the methods used to estimate the fluidic and lymphatic functional parameters (Section 2.4). Chapter 3 presents the results of the research. Qualitative and quantitative measurements in isolated lymphatic vessels are given in sections 3.1 and 3.2, respectively. The sections that follow discuss the vessel wall radial velocity (Section 3.3), pressure estimation (Section 3.4) and the flow pattern in rat mesenteric valves (Section 3.5). The results chapter concludes with section 3.6, where, an attempt is been made to link and establish relationships between the fluidic and lymphatic functional parameters with the experimental parameters, using statistical analysis. A discussion of the results follows in chapter 4. Concluding remarks are given in chapter 5 and future work is suggested in chapter 6.

Chapter 2

Materials & Methods

2.1 Particle image velocimetry (PIV)

2.1.1 General

PIV is a well established optical method of quantitative flow characterisation. The underline principles of PIV are well understood [1, 116]. PIV can resolve 2D and 3D flow fields in the macro and micro scales depending on hardware implementation. It may also provide high temporal resolution to capture the instantaneous velocity of the interrogated flow.

The physical principle is simple. A flow with optical access is seeded with particles that scatter light. A light source is used to illuminate the particles in the flow using either continuous or pulsed illumination. The particles scatter light which is captured into frames by a digital camera at a frame rate large enough to capture the desired details of the flow. The frames are analysed with statistical correlation techniques to calculate the most probable position of particles in a frame. The difference of the position of individual particles in each frame along with the known time interval between frames is used to calculate the velocity of the particles. The velocity field can then be used to derive other flow characteristics such as pressure, vorticity, turbulence and shear stresses.

The spatial and temporal resolution (or dynamic range) of the PIV method depend mainly on the equipment used and the light source but are also influenced by the choice of particles. These factors will be discussed in the next sections.

The major disadvantage of the PIV method is the need for optical accessibility of the flow. This can be alleviated to a certain extent by using infrared or near-infrared illumination, however due to the longer wavelength the spatial resolution is reduced and more heat is generated at these wavelengths which can potentially damage soft tissue.

2.1.2 Light sources

The illumination source for PIV can be either continuous wave (CW) or pulsed wave (PW). It needs to have sufficient energy so that the frames recorded are of high signal to noise illumination. Each frame should be exposed to illumination for only a short amount of time in order to freeze the image on the sensor and avoid streaking of particles (motion blur). Thus the exposure time is a function of the velocity of the particles. A wide variety of light sources have been used in PIV; halogen lamps, lasers, laser diodes, light-emitting diodes (LED), with wavelengths ranging from ultra-violet (UV) to infrared (IR).

The most common source of illumination of modern PIV systems is a laser source, either CW or PW. Lasers provide high energy light and very short high repetition rate pulses of the order of nanoseconds when needed. On the downside they are very expensive, require safety measures to avoid eye exposure. Due to the coherent nature of their light, surfaces (eg. walls) produce speckle that degrades the measurement accuracy of near wall velocities.

Recently, LED sources have become widely available at a very low cost in comparison with lasers and have been successfully used in PIV and micro-PIV [21, 47, 53, 156]. LEDs can be pulsed at high repetition rates with short pulses of microsecond order using higher than their nominal current to achieve higher energy pulses. Due to the less coherent nature of their light they are speckle free, but the generation of a light sheet is more problematic and a considerable amount of light may be lost. However, in micro-PIV, volume illumination is used, as will be discussed in section 2.1.5, therefore the non-coherent light is an advantage. LEDs have drawbacks as well, using high currents has its own safety issues and may degrade the lifetime of the LED. Depending on the LED construction materials, the wavelength of the emitted light may shift depending on the current supply, pulse duty cycle and repetition rate which can have implications especially in micro-PIV with fluorescent particles [156]. LED light characteristics, wavelength and intensity, also vary between production batches.

Moreover, the power of a laser beam is close to the evaporation point of common particle materials [1]. This raises concerns on the potential damage that a laser may cause to living tissues; a light-emitting diode is advantageous in this respect, as well.

2.1.3 Tracer particles

Particles used in PIV must satisfy two requirements. They should have a low response time to fluid flow changes (ie. follow flow faithfully) and scatter sufficient light to be captured by the recording device [112]. To minimize gravity effects tracer particles should also have density equal to the flow medium. This is more easily achieved for liquids than gases. Scattering of the light is influenced by the wavelength of the light, particle diameter and particle refractive index. The wavelength selection depends on application, typically visible wavelengths are used and infrared when optical accessibility is limited. Particle diameter is dictated by the size of the conduits and should be at least two to three order of magnitude lower than the smallest conduit dimension. When small diameter particles cannot be avoided one can compensate for the loss of scattering efficiency by increasing light intensity, coating the particles or using hollow glass spheres. The latter are especially suitable for water flows as they are inexpensive, neutrally buoyant and the mismatch of refractive indices between the hollow core and the glass shell provides strong scattering.

The particle response time in a flow [1, 88] is given by

$$\tau_p = \frac{(\rho_p - \rho_f) \cdot d_p^2}{18 \mu_f \phi'} \tag{2.1}$$

where ρ_p,ρ_f are the particle and fluid density respectively, d_p is the particle diameter, μ_f is the fluid dynamic viscosity and ϕ' is a constant that depends on the particle Reynolds number. For low Reynolds numbers $\phi' = 1$. Hence, particles with density closed to their surrounding fluid have lower response time.

In addition to the characteristics of tracer particles for PIV measurements outlined above, particles used in the study of biological flows within living tissues must be biocompatible, so they do not disrupt the natural function of cells. This may be achieved by appropriate coating of the particles with a biocompatible substance; in the present work the working medium was an albumin-enriched physiological solution. The layer of albumin that coated the particles after mixing them in the solution ensured that no adverse reaction of the vessels took place.

Light scattering from particles depends on the relative ratio of particle size to wavelength of incident light. When the particle size is larger than λ scattering is governed by Mie's theory. When the wavelength is larger than the particle size then Rayleigh scattering theory applies. In the present thesis, particles of $1\,\mu m$ up to $3\,\mu m$, were used, hence the particle size is larger than the wavelength of light in the visible spectrum and Mie's theory applies.

2.1.4 Image Recording

Historically, the first PIV recordings were made using photographic films. The films then had to be digitised in order for velocity calculations to be performed. With the advent of digital cameras the photographic film has been largely displaced. CCD and CMOS sensors have advanced considerably and now offer similar resolution as the photographic film. Moreover, the frames are directly stored into digital format thus simplifying the recording process considerably.

The choice of camera depends on the nature of the flow, desired resolution and illumination conditions. Hain et al. [54] compared commercial CCD, CMOS and intensified cameras for the purposes of PIV recording. CCD cameras outperform CMOS in image quality and should be chosen when high spatial resolution is sought. CMOS cameras on the other hand are the preferred choice when high velocity gradients are expected as their frame rate is generally higher. The use of an intensifier to amplify the light signal in low levels of illumination reduces the spatial resolution of the system but it is usually cheaper then investing in a stronger light source [54].

2.1.5 μ-PIV

Micro-PIV (μ-PIV) was introduced by Santiago et al. [125] in 1998 and considerable advancements have been made since then [75, 152]. While the underline principle of micro-PIV is the same as its macro scale counterpart, the implementation of the method requires different or additional equipment and special consideration is necessary in the selection of the various components in order to increase the signal to noise ratio. A schematic of a typical PIV experimental setup for micro-flows, or micro-PIV (μ-PIV) is shown in figure 2.1. Micro-PIV is based on traditional PIV but uses a microscope objective for magnification and fluorescence particles that emit at different wavelengths than the excitation source for an increase in the signal to noise ratio. Volume illumination is used in micro-PIV, in contrast to the light sheet illumination used in macro scale PIV, as it is difficult to create a very thin sheet and align it with the microflow [89]. Therefore all the particles in the flow contribute to the light intensity of the recorded frame and eventually to the cross-correlation function. The purpose of the objective is to provide the necessary magnification but also creates a focal plane that can be thought of as being the equivalent of a light sheet. The particles that are further away from the focal plane are out of focus and contribute less to the correlation function.

The second significant difference of micro-PIV is the use of fluorescent particles that when excited by light emit at a different wavelength. Using a filter or a dichroic mirror only the emitted light is allowed to pass through to the sensor in an effort to increase signal to noise ratio. Even this measure is sometimes not enough and an intensifier is necessary despite the adverse effect in spatial resolution. Due to the high magnification and numerical aperture the image formed by the particles on the sensor is dominated by geometric optics rather than diffraction [75].

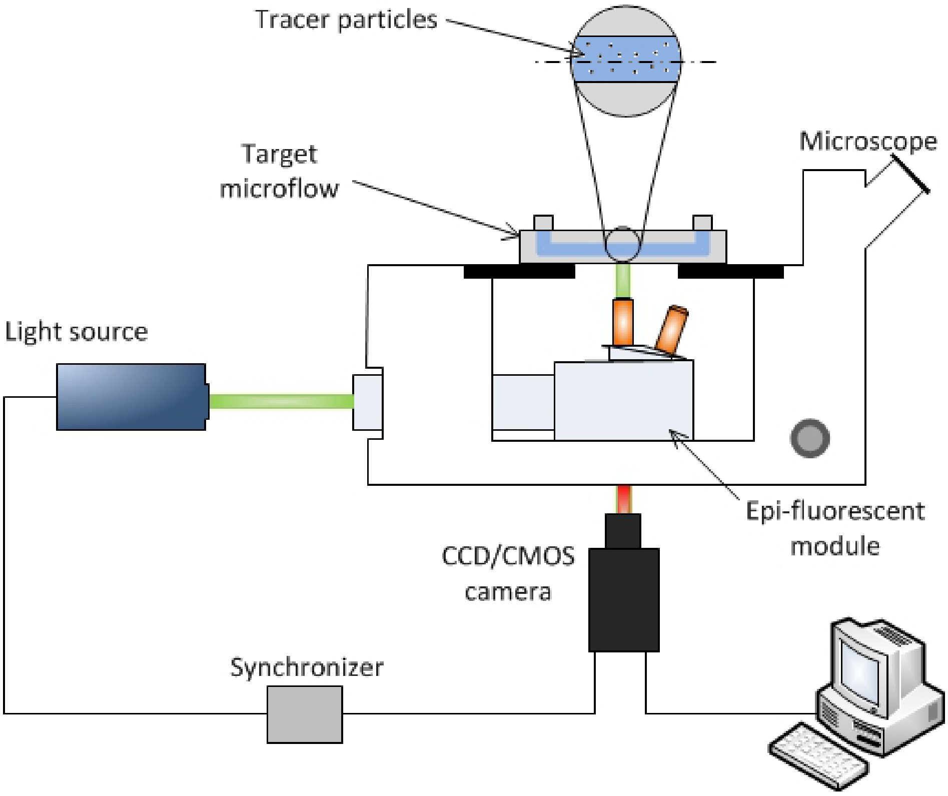

Figure 2.1: Schematic of a typical μ-PIV setup. A light source, usually a class IV laser, illuminates the flow via an epifluorescent microscope module. The micro-flow is seeded with fluorescent micro-particles that emit light at higher wavelength than that of the light source. The particle emission is recorded on a camera. A synchronization device is used to control the timing of the light source and camera exposure. The images are analysed in a computer. This typical μ-PIV setup has been modified for the purposes of the current work, see figure 2.9.

2.1.6 PIV image analysis and pre/post-processing

Image analysis

PIV analysis algorithms are well documented in the literature [1, 116]. The image acquisition sequence generates a large number of image pairs. Since the frame rate and pulse separation time are known, each pair of images may be spatially cross-correlated in order to calculate the velocity vectors of individual particles within the field of view (FOV). Briefly, a pair of frames is analysed in each step (figure 2.2). The images are divided into smaller Interrogation Windows (IWs).[7] The interrogation windows from the two frames are cross-correlated. The result of the cross-correlation is the displacement of the sum of all particles inside an interrogation window [64] and divided by the known pulse separation time the velocity vector is obtained. Other flow parameters may be derived from the resulting velocity field.

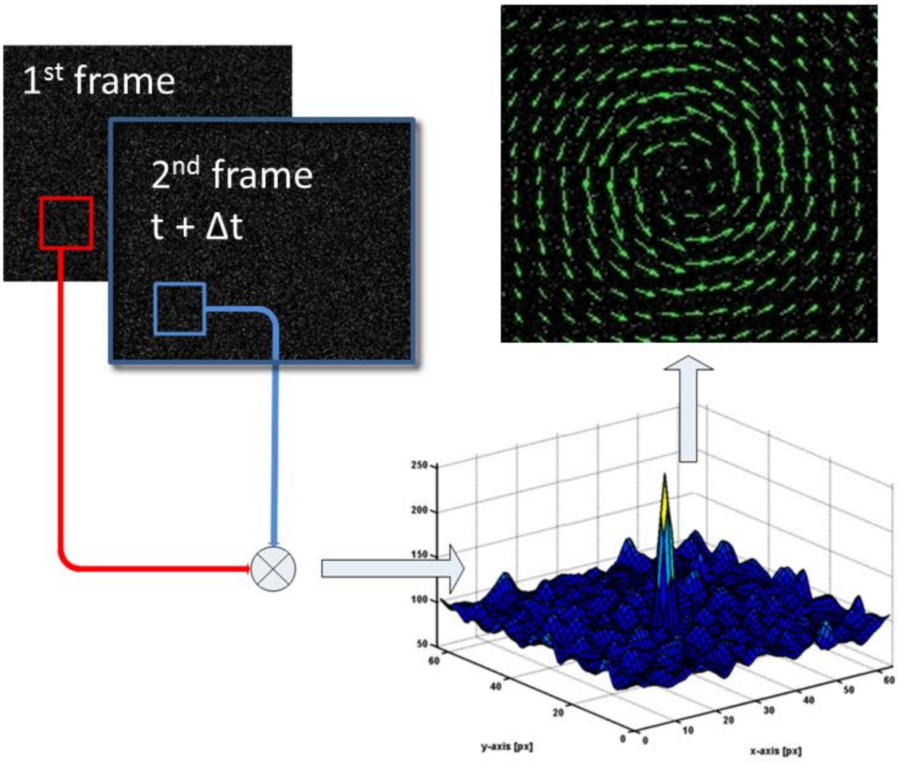

Figure 2.2: PIV image analysis. Two frames separated by a know time Δt are divided in IWs. The cross-correlation of the IWs yields a correlation peak that corresponds to the particle displacement. The result for a computer generated image of a Rankine Vortex is shown on the top right.

---

[7] Unless otherwise stated, 64x64 px interrogation window with 75% overlap was used. With the current setup, the velocity vector spacing obtained is approximately 9.2 μm.

Here the analysis was performed with the open-source Matlab toolbox PIVlab.[8] The software was supplemented with vessel wall detection algorithms for masking the wall from the PIV analysis and image filters for pre-processing the images in order to increase the signal to noise ratio in the correllation plane. Moreover, the post processing of the resulting vector fields was performed with a novel and robust method developed by Garcia [41].

Pre-processing

Image filtering may improve the signal to noise ratio in the cross correlation plane in PIV image analysis. The filter used for pre-processing the lymphatic PIV images was developed by Gui et al. [50].[9] This filter is a combination of a 3x3 rectangular smooth filter and an unsharp mask filter. The former removes single pixel random noise, while the latter removes low frequency background noise. The filter coefficients are determined by equation 2.2 and further details on the filter implementation are found in the original publication.

$$C(i,j) = \begin{cases} \frac{1}{9} - \frac{1}{(2r+1)^2}, & \text{if} -1 \leq i \leq 1 \, and -1 \leq j \leq 1 \\ -\frac{1}{(2r+1)^2}, & \text{otherwise} \end{cases} \tag{2.2}$$

An example of the cross-correlation result in the correlation plane, without any pre-processing is shown in Figure 2.3a. Using the filter by Gui et al. [50] results in an increase in the signal to noise ratio from approximately 1 (Fig. 2.3a) to 2.5 (Fig. 2.3b). A result of the application of this filter in an image of particles within a lymphatic vessel is shown in figure 2.4b.

---

[8] http://pivlab.blogspot.co.uk

[9] Other filters were implemented in Matlab, based on the work of Deen et al. [27] and Honkanen and Nobach [57]. The PIVlab filters were also tested. After sampling several frames, they didn't show any benefit over the filter by Gui et al. [50]. However, a rigorous analysis was not performed.

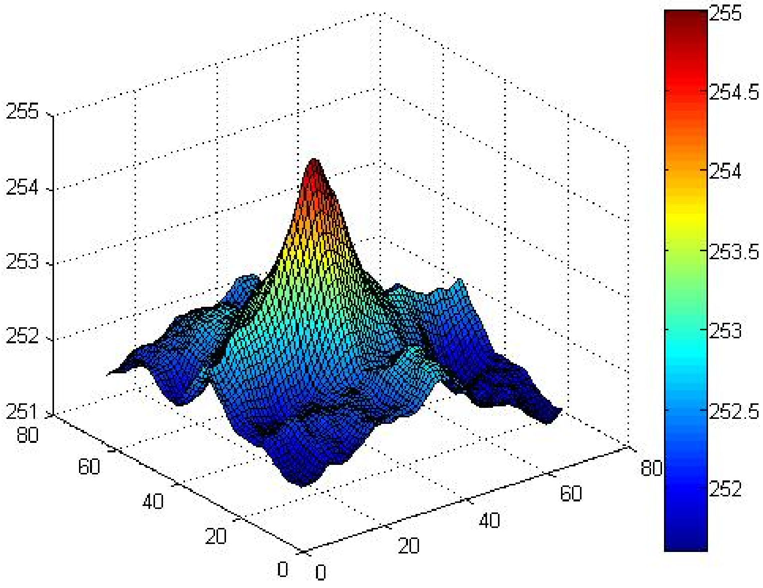

(a) Correlation peak without filtering

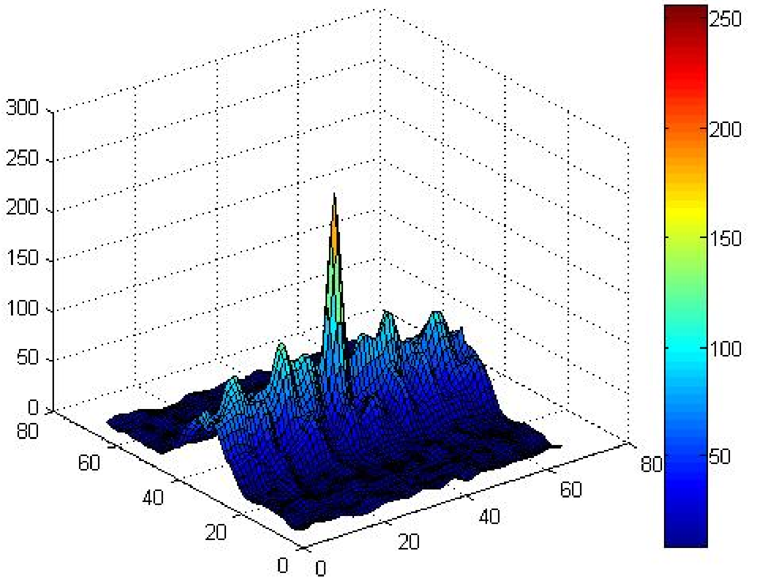

(b) Correllation peak with using the image filter proposed by Gui et al. [50]

Figure 2.3: The use of filtering greatly improved the signal-to-noise ratio in the correlation plane, from slightly larger than 1 (a) to 2.5 (b).

Post-processing

In PIV, post-processing of the resulting vector field is neccessary, in order to remove outliers from the results. PIVlab implements a number of post-processing options that are common in PIV analysis such as the Standard Deviation Filter and the Local Median Filter [1, 116]. In addition, the user can manually reject a vector and allow the software to automatically interpolate the missing data. However, the newly introduced filter by Garcia [41], provides the means for automatically detecting and removing outliers from the velocity vector fields. This method, a least square penalized method, was used in the post processing of all the image analysis performed, as it requires no user input and greatly facilitates the post-processing of large data sets.

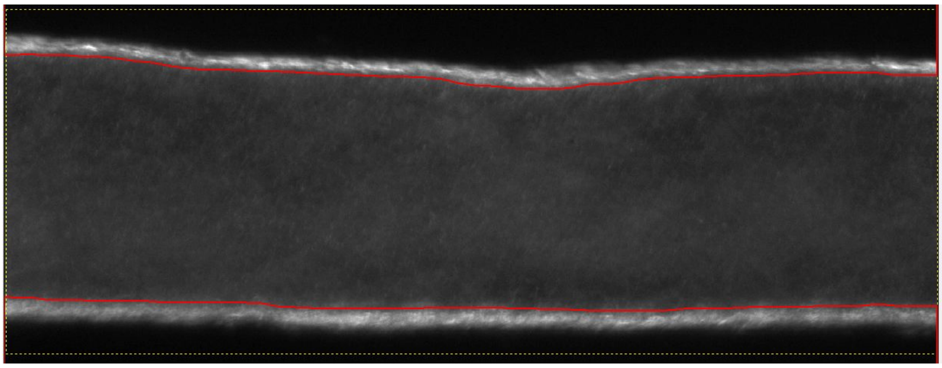

(a) Raw PIV image of lymphatic vessel. The flow is seeded with 1 μm particles. Red line denotes the detected vessel inner wall. Due to the volume illumination of the flow, light scattered from out of focus particles blurs the image.

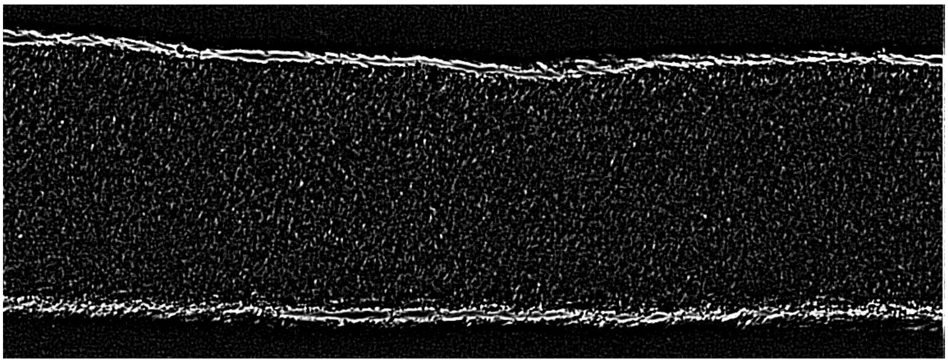

(b) The above image after been processed with a combination of unsharp and smoothing filters prior to PIV analysis [50]. Noise from out of focus particles is substantially reduced.

Figure 2.4: Raw PIV image in a lymphatic vessel with vessel wall detected (a) Image after filtering (b)

2.2 LED light source

The developed light-emitting diode (LED) light source utilises high-power white and monochromatic LEDs (CBT-90 white/green, CBT-140 white and PT-120 green) by Luminus Devices, USA (www.luminus.com). The driving electronics are from the same manufacturer (DK-136M development kit) and are capable of driving the LEDs with current pulses of up to 36A with virtually any desired value of pulse duty cycle from 0 to 100%. Power is provided by a 650W power supply (XP Power, Singapore). Control and synchronization of the source was implemented with LABView and a National Instruments DAQ device (National Instruments, USA). A 5 axes kinematic mount (EKSMA Optics, Lithuania) provides alignment of the LED with a fibre optic cable which delivers the light to an inverted microscope (Zeiss). In order to increase the light collection efficiency of the LED-Fiber optic combination, several lens combination were tried and the best was found to be an aspheric condenser lens with numerical aperture (NA) of 0.9, taken from an old microscope (Leitz Ortholux). Light was delivered either through the microscope optical path, above the specimen or by placing the fibre optic at an angle with respect of the specimen. The two former will be referred to as bright-field modes, while the latter as scattering mode. Light power measurements were performed with a power meter (Thorlabs PM100A/S120VC). A spectrometer (AVS-MC2000, Avantes BV, The Netherlands) was used to measure the LED spectrum. A photo-diode (SM05PD1A, Thorlabs) was used to verify the time response of the LED to the driving current pulses. In order to have increased frequency response a 12V bias circuit was implemented based on supplier's guidelines.

The LED light source was characterised in terms of LED power output and emission spectrum during Continuous Wave (CW) or Pulsed Mode (PM) illumination at different levels of input current, pulse frequency and duty cycles. Figure 2.5 compares the energy per pulse of different LEDs of the same manufacturer that were tested, while figures 2.6 to 2.8 show the effects of LED current, pulse frequency and duty cycle on the emitting wavelength.

The LED can operate in frequencies up to 3 kHz, with up to 36 A current pulses. The time separation between two successive pulses can be as low as 5-10 μs. With this order of pulse separation magnitude, and taking into account the one-quarter rule in PIV [153], in theory velocities in excess of 100 mm/s can be measured at 20x magnification [22]. In practice, the maximum velocity that can be measured also depends on the pulse high time duration, which in turn depends on whether there is sufficient light intensity to provide enough contrast at a short

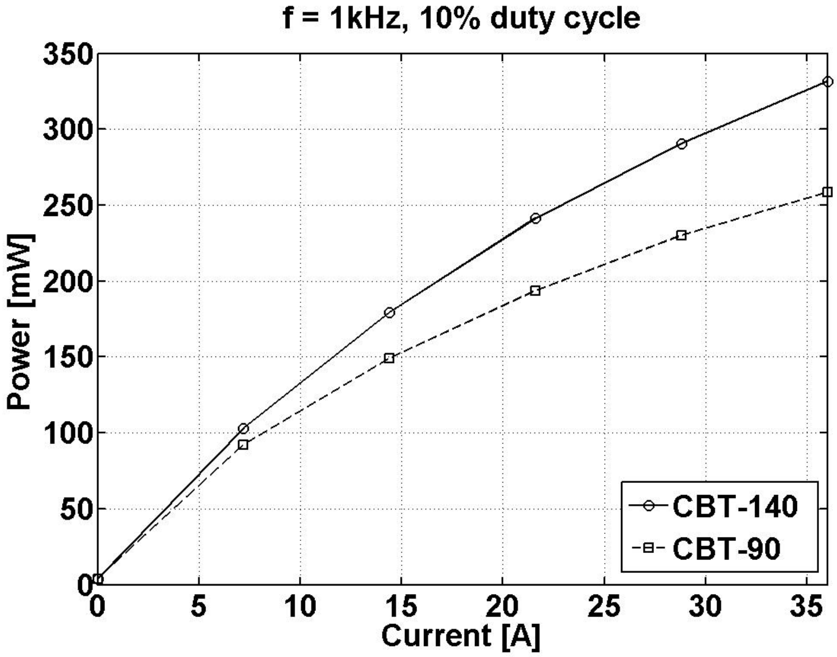

Figure 2.5: Comparison of power output from two wihte LEDs. Measurement was performed at the exit of a 6-foot long (1.8 m) fibre optic cable. A condenser lens (NA = 0.9) was located at the LED-Cable interface.

time interval in order to eliminate particle streaking. In most cases the system could yield good contrast with up to 50 μs pulse duration which is sufficient for many flows of biological interest besides lymph flow.

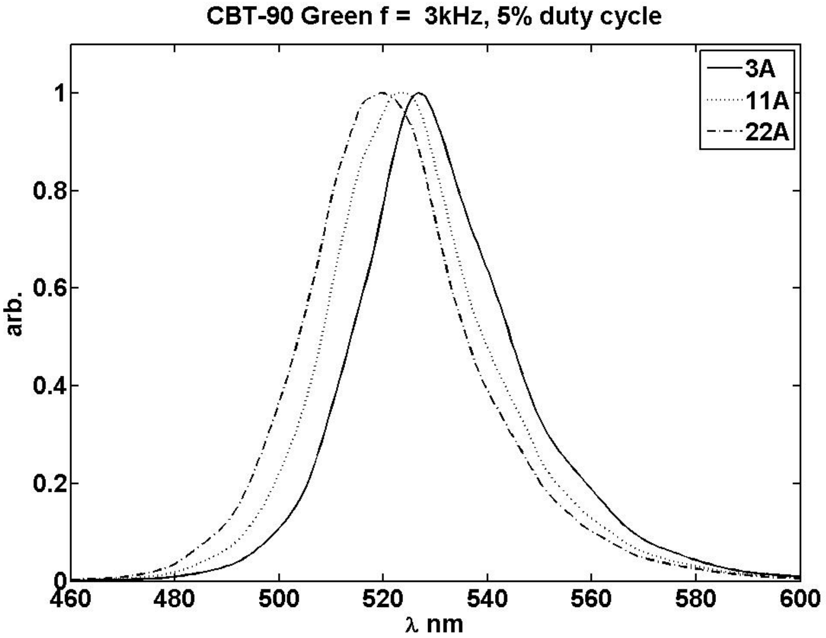

Figure 2.6: Wavelength shift due to increased current

The optical power output increased in a slightly non-linear manner as the control voltage

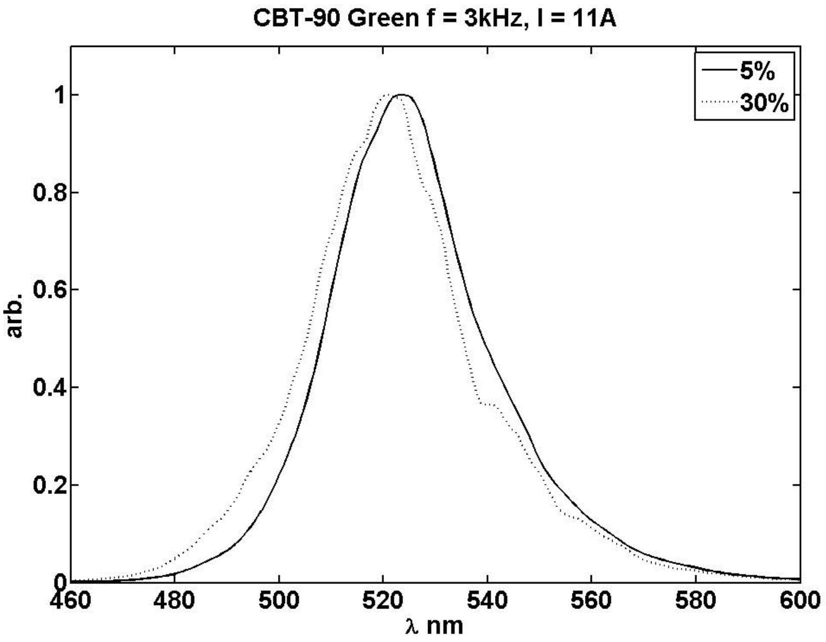

Figure 2.7: Wavelength shift due to duty cycle increase

of the LED was increased. Figure 2.5 compare the different LEDs (white and green) from the same manufacturer. As expected [156], due to their construction and materials, the LEDs central emitting wavelength shifts to a lower wavelength as the LED current increases (Fig. 2.6). This is most likely a thermal effect due to the increase in junction temperature, as Figures 2.7 and 2.8 show that the effect is less pronounced when the high time is altered at constant frequency and current level, or when the frequency is modified at constant current level and duty cycle. Wavelength shift is of importance in PIV measurements with fluorescent particles. The LED emitted wavelength should be as close as possible to the absorption wavelength of the particles to maximize the intensity of light emitted from the particles.

2.3 Experimental protocol

2.3.1 Vessel isolation

Experiments in lymphatic vessels were carried out in Texas A&M Health Science Center at Temple, Texas. Messenteric lymphatic vessels were isolated from anaesthetized Sprague-Dawley rats, following an established experimental protocol [26, 31]. The mesentery was exteriorized following a midline abdominal incision and placed inside a bath of physiological solution. Lymphatic vessels were identified, running along side the mesenteric arteries and were

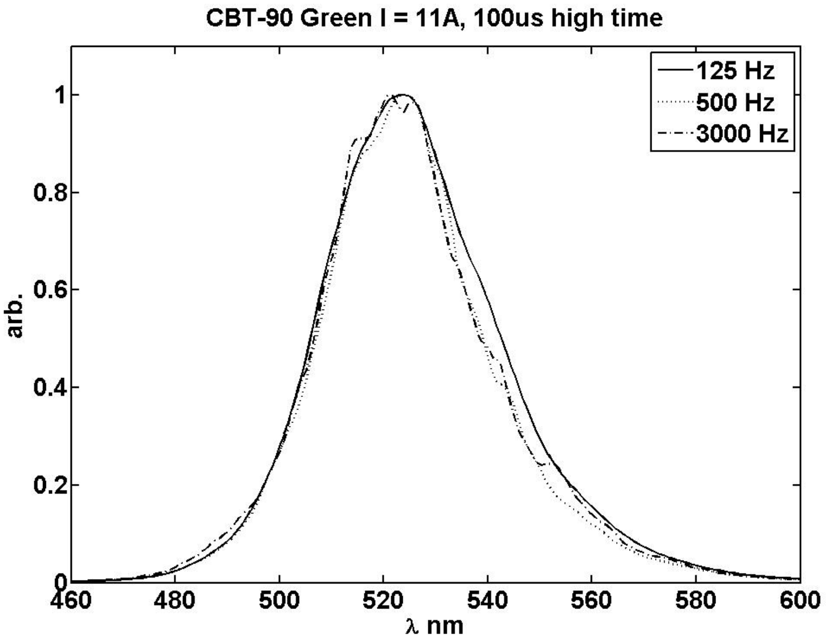

Figure 2.8: Effect of frequency on central wavelength shift

cleared of the surrounding connective and adipose tissue. The vessels were then carefully removed and placed in a petri dish containing an albumin enriched physiological solution (APSS). The chemical composition is given in Davis et al. [26] and the references therein. A suitable vessel was then transferred to a specialized vessel chamber (CH-1, Living Systems Instrumentation, USA, http://www.livingsys.com/) and was cannulated with resistance matched micro-pipettes. The pressure was increased to 3 cmH_2O and the vessel was observed for contractions. The vessel chamber is shown in Figure 2.12.

2.3.2 Particle administration

Following the successful isolation of vessels, polystyrene micro-particles of 1 μm diameter (Polysciences Europe GmbH, Germany) were either introduced into the upstream pipette with the vessel uncannulated to avoid damage, or via an injection port (Figure 2.9b). In the latter case the vessel was cannulated and was isolated by a 3-way valve to avoid damage during particle injection. Approximately 0.5 ml of particle solution was required; after initial trials 0.5% weight-to-volume particle concentration was used in order to have 7-10 particles per interrogation window, which is an optimum value in PIV [1]. Data on the refractive index of lymphatic tissue are difficult to find in the literature, however Galanzha et al. [40] report a value of 1.38 for rat mesenteric tissue, which is close to the refractive index of water (RI = 1.33). The vessel bath solution has the same refractive index as the working solution and serves to compensate for the distortion caused by the curved vessel wall [162]. Therefore the major source of refractive index mismatch errors are likely to originate from the aperture on the vessel chamber bottom (RI = 1.58) and the air objective used (RI = 1). Temperature was regulated at physiological levels $36 - 38^o C$ and pressure was adjusted by changing the height of the input and output reservoirs.

2.3.3 Micro-PIV setup

A μ-PIV setup was constructed around a Zeiss inverted microscope, following the guidelines available in the literature [1, 75, 116]. The setup used is shown in figure 2.9a. The most significant difference with respect to a typical system, shown in figure 2.1, was the light delivery method. The vessel wall creates background noise and, as the vessel contracts, the wall comes into focus at the 20x magnification used in bright-field illumination (Figure 2.11a). To overcome this issue, instead of delivering the light via the epi-fluorescent module or from above the specimen, it was delivered with a fibre-optic cable from above and at an angle of about 45 degrees with respect to the microscope stage. By means of this approach a greater amount of light scattered from objects in the microscope focal plane, giving rise to greater contrast image as shown in figure 2.11b. The low numerical aperture of the objective used (M = 20x, NA = 0.5) ensured that stray light from the bottom wall was not significant.

The flow was seeded with micro-particles and the LED light source was used to provide suitable short burst pulses to freeze the particle motion and avoid streaking. Images were taken by a CMOS (or CCD) camera and transfered to a computer for analysis. Although, fluorescent particles are commonly used in μ-PIV, in the present setup non-fluorescent 1 μm particles (density $\rho = 1.05 g/cm^3$) were used. The particle response time to acceleration, assuming water properties at 37^o for the solvent, is aproximatelly 0.08 μs and is considered to be low enough for the flows under investigation in this study [116]. The particle frequency response is close to unity, making them excellent tracers [1]. Their settling time is also long; it takes approximately 30 minutes for particles of 1 μm diameter to settle 50 μm, which is approximately the radius of rat mesenteric lymphatic vessels [Polysciences]. This time is long enough compared to the time scales of the flow and therefore gravity is considered to have insignificant influence in the results.

Frame straddling is a method for increasing the temporal resolution of a PIV system and

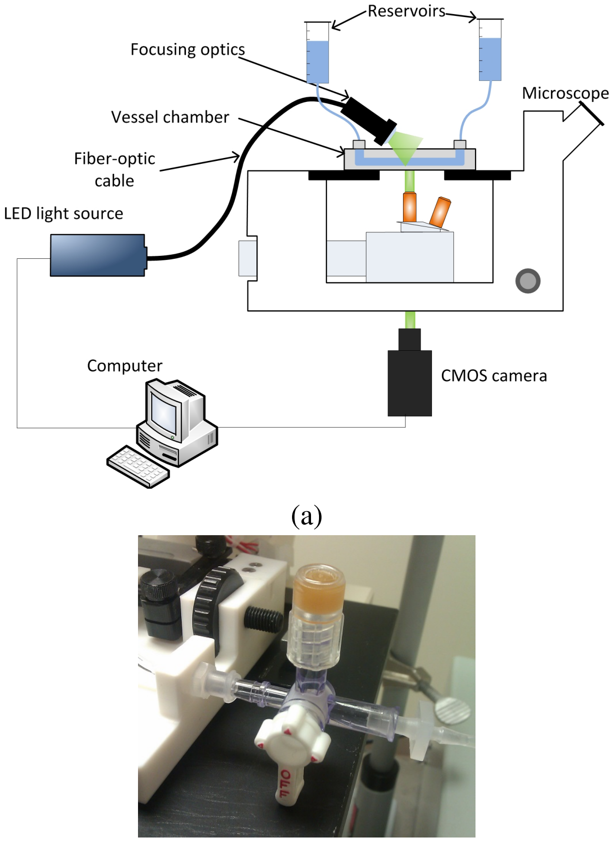

(a)

(b)

Figure 2.9: Experimental setup & Camera-Light synchronization.: (a) Typical μ-PIV setup. A light source illuminates particles seeded in the flow, with high frequency pulses, through a microscope objective. A camera captures images in synchrony with the light source which are transfered to a computer for spatial cross-correlation analysis. (b) Injection port that was used to deliver particles. A 3-way valve was used to isolate the vessel during particle injection for protection against pressure.

is illustrated in figure 2.10. The light pulses are placed in such manner as to 'straddle' the interframe time, thus this becomes the limit of the temporal resolution. In modern high-speed cameras this time is below 2 μs. The PIV pair of frames are acquired at half the camera frame rate, but modern cameras usually have high enough frame rate to compensate for the loss in acquisition rate.

2.3.4 Flow measurements

The vessel chamber was placed on top of an inverted microscope (Zeiss) and a Plan-Achromat 20x magnification objective was used (NA = 0.5). Light was delivered from on top of the specimen and at an angle using a fibre optic cable (figure 2.12). The LED light source and camera

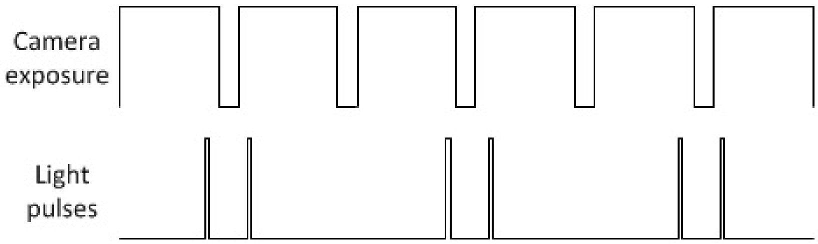

(a) Example of frame straddling.

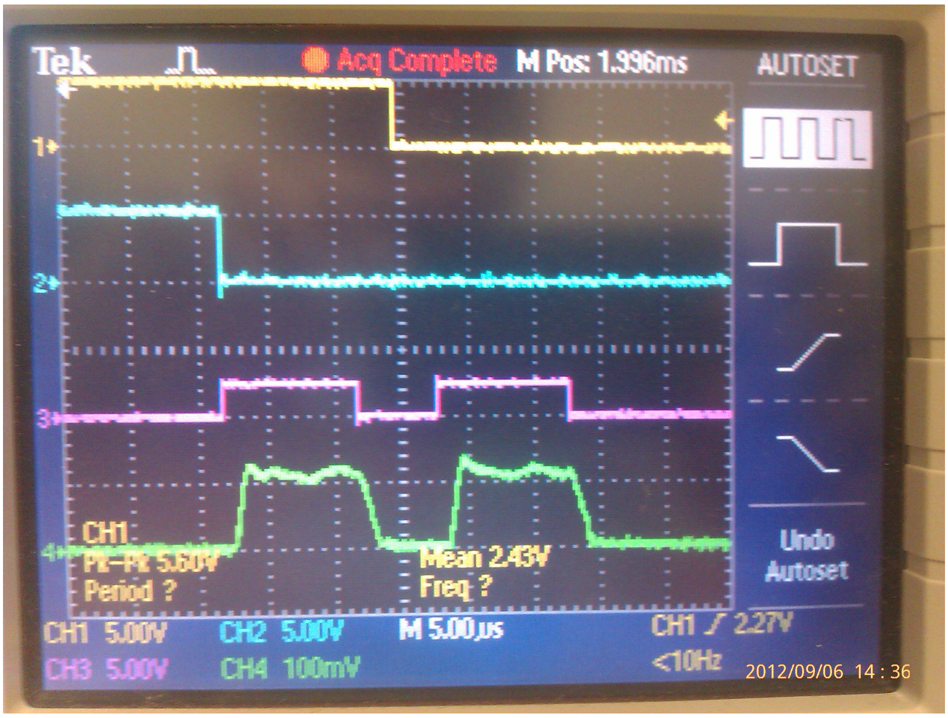

(b) Colour of signal from top to bottom: Yellow: Camera exposure signal; Cyan: Delay signal; Magenta: Pulse trigger signal; Green: Photodiode response to LED pulses.

Figure 2.10: Frame straddling principle (a)
Frame straddling with a LED, demonstrated by an oscilloscope (b)

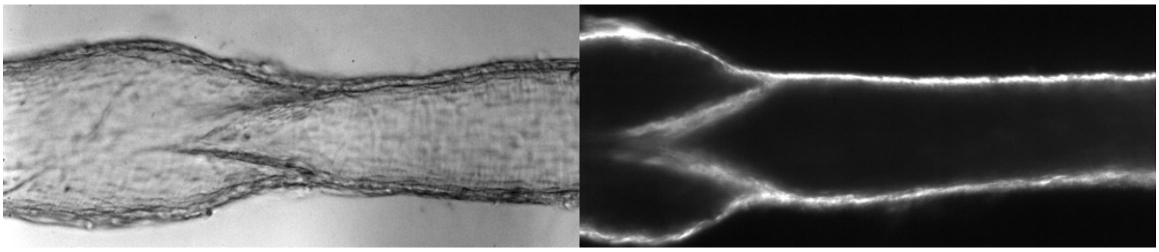

(a) (b)

Figure 2.11: Image of a lymphatic vessel and valve at 20x magnification: (a) brightfield and (b) side-scattering illumination mode.

were synchronized with a National Instruments DAQ device and LabView Software. A Phantom V5.2 high-speed CMOS camera was used for image acquisition. Images were transferred to a computer for analysis with PIV Software in Matlab (see section 2.1.1). The microscope was placed on an air table for vibration isolation. To reduce vibrations and facilitate the table top levelling, the light source was placed on the floor next to the table. On top of the table, besides the microscope/camera and the vessel chamber, the standing reservoirs and the temperature controller were also placed. Therefore the only source of vibration on the table was the camera cooling fan, but this was unavoidable.[10]

Pressure was controlled by changing the height of the inflow and outflow standing reservoirs. The height of the reservoirs was adjusted in such manner as to maintain constant transmural pressure of 3cmH_2O, unless stated otherwise. The axial pressure gradient was set to values of -5, -3, -1 cmH_2O, were lymphangions had to pump against pressure, 0 cmH_2O and +1, +3 and +5 cmH_2O; in the latter case the contraction is not required to create or sustain the flow as it is pressure driven.

Pressure gradient definition

The definition and sign of the axial pressure gradient adopted in this thesis, differs than the standard terminology used in fluid mechanics. Axial pressure gradient in this context is defined as $\Delta P_{axial} = P_{in} - P_{out}$. Therefore, when the inflow reservoir is raised higher than the outflow one, the pressure gradient is positive (favourable) and drives the flow. In contrast, when the outflow reservoir is raised higher than the inflow one, ΔP_{axial} becomes negative (adverse); forward flow, that is, flow along the direction of the vessel as allowed by the orientation of the one-way valves, cannot be maintained by the axial pressure gradient.

In fluid dynamics, the axial pressure gradient is defined as $dP/dx = P_{out} - P_{in}$ and has a negative sign in the Navier-Stokes equations [59]; the Navier-Stokes equations for one dimensional viscous flow with no external body forces is given below:

$$\rho \frac{du}{dt} + u\frac{du}{dx} = -\frac{dP}{dx} + \mu \frac{d^2u}{dx^2} \tag{2.3}$$

---

[10] Some initial flow measurements were performed with the table not activated and with the light source placed on the table. The light source enclosure contained 3 cooling fans that caused vibrations. Some interesting implications of this are demonstrated in section 3.6.1

Therefore, according to the sign convention in the Navier-Stokes equations, positive forward flow occurs with a negative axial pressure gradient, as a fluid flows from a high towards a low pressure ; backflow occurs at positive axial pressure gradient. Table 2.1 compares the terminology adopted in this thesis with the fluid mechanic one.

Table 2.1: Comparison of terminology for the axial pressure gradient

	Present terminology	Fluid Mechanics Terminology	Flow direction
Definition of ΔP_{axial}	$\Delta P_{axial} = P_{in} - P_{out}$	$dP/dx = P_{out} - P_{in}$	-
Sign when P_{in} is higher than P_{out}	+ (favourable)	-	Forward
Sign when P_{in} is lower than P_{out}	- (adverse)	+	Backflow

Most vessels were pre-conditioned prior to flow measurements, by cycling through different transmural pressures 0-1, 0-3 and 0-5 cmH_2O for 5 minutes. In some preparations a peristaltic pump was used to circulate the bath solution, and this will be noted in the results chapter. The pH after the experiments, which lasted at least 1-2 hours per vessel was measured in some cases and it was found to be in the range of 7.4-7.6, that is, close to the physiological range.

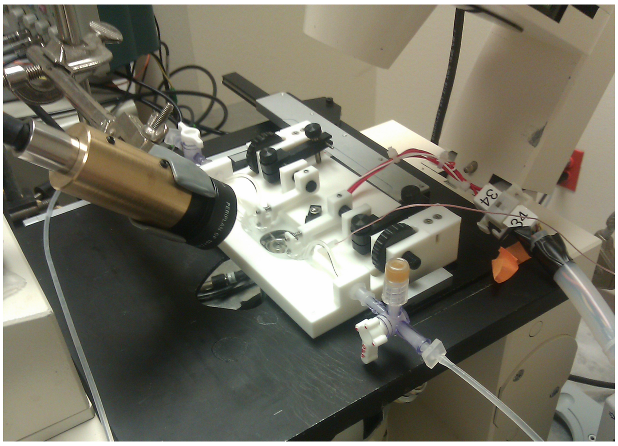

Figure 2.12: Vessel chamber on microscope and light delivery

For each vessel, measurements were performed at different axial pressure gradients with values -3, -1, -5, 0, +1, +3, and +5. Flow was measured for up to one minute at each value of ΔP_{axial}. In all cases images were taken 5 minutes after each pressure adjustment.

The camera was set at a specific frame rate, initially 250 fps, but later on this was dropped down to 10-70 fps, as the high frame rate did not give additional information. The light pulse duration was 50 μs and the pulse separation time was varied, so that the pixel displacement of particles between two successive frames was about 5-10 pixels. In practice this was translated in pulse separation times of 50 μs up to several ms for slow flows.

Figure 2.13 gives a schematic of a cannulated vessel. Most measurements were taken from the first lymphangion of the vessel; this part was termed ”A”. In one vessel, measurements were taken from the second lymphangion in the series ”B”, as well. The distance of the pipette tip to the first valve was 3 to 5 times the vessel End Diastolic Diameter (EDD) at least, in order to minimize entrance effects. Arguably the second complete lymphangion of a cannulated vessel is more representative of *in vivo* conditions. The micro-pipettes cause entrance effects that dissipate along the vessel length and therefore it is preferable to perform flow measurements away from the pipette tip. However, as shown in Section 4.2.7, Figure 4.5, due to the low Reynolds number of the flow the entrance length was always less than half the vessel EDD diameter. Given the fact that the distance of the first valve from the pipette tip was at least 3 times the vessel EDD it can be considered that the entrance effects have dissipated and do not affect the measurements in the first lymphangion. The short entrance length of the flow guarantees that measurements may be taken from a vessel containing only two valves, ie a single complete lymphangion, provided that the distance of the first valve from the pipette tip is sufficiently long.

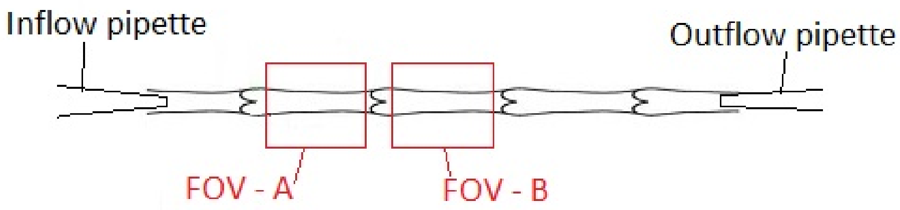

Figure 2.13: Vessels containing 2, 3 or 4 valves (1,2 or 3 complete lymphangions) were cannulated with glass micro pipettes and secured with sutures. The distance of the pipette tip to the first valve was 3 to 5 times the vessel diameter at least, to allow for suturing and to minimize entrance effects. The microscope objective was focused on the first lymphangion (FOV - A). In one vessel PIV measurements were also taken in the second lymphangion (FOV - B).

Table 2.2 provides a comprehensive list of the successful experiments with lymphatic vessels and contains the experimental parameters and conditions. Each experiment has a number indicated in the first column and the vessel number for each experiment is indicated in the second column. The third column lists the average, or transmural pressure, of each experiment. In all but one experiment the average pressure was maintained at 3 cmH_2O. Measurements were taken at different axial pressure gradient ΔP_{axial}. Negative value indicates that the outflow reservoir was set higher than the inflow, forcing the vessel to pump against a pressure gradient. Positive values indicate a favourable pressure gradient. Each measurement has a unique identification (id) number; a total of 78 successful measurements were performed. The number of valves of each vessel is also shown in the table. The vessels that were not pre-conditioned are also depicted. Table 2.2 also depicts the activation of the air table and the perfusion system, the animal gender and weight in grams. In all experiments, temperature was maintained at physiological levels.

2.4 Estimation of lymphatic functional and fluidic parameters

2.4.1 Definitions of parameters

PIVlab, been a toolbox for flow measurements already provided the basic flow quantities that can be derived from a typical PIV experiment such as velocity, vorticity, divergence, shear/strain rate. Since these are only basic quantities, PIV lab was extended to provide more quantities of interest in terms of fluid flow (Flow rate, WSS, pressure) and lymphatic function parameters such as internal diameter, Ejection Fraction (EF), Contraction Amplitude (CAMP), Contraction Frequency (FREQ) and Fractional Pump Flow (FPF). These quantities are defined as (see also figure 2.14):

1. Ejection fraction[11] $EF = (EDD^2 - ESD^2)/EDD^2$
2. Contraction amplitude $CAMP = EDD - ESD$
3. Frequency of contractions $FREQ$
4. Fractional pump flow $FPF = EFxFREQ$[12]

---

[11] EDD = end diastolic diameter, ESD = end systolic diameter

[12] FPF gives the fractional change in lymphatic volume per minute[44]

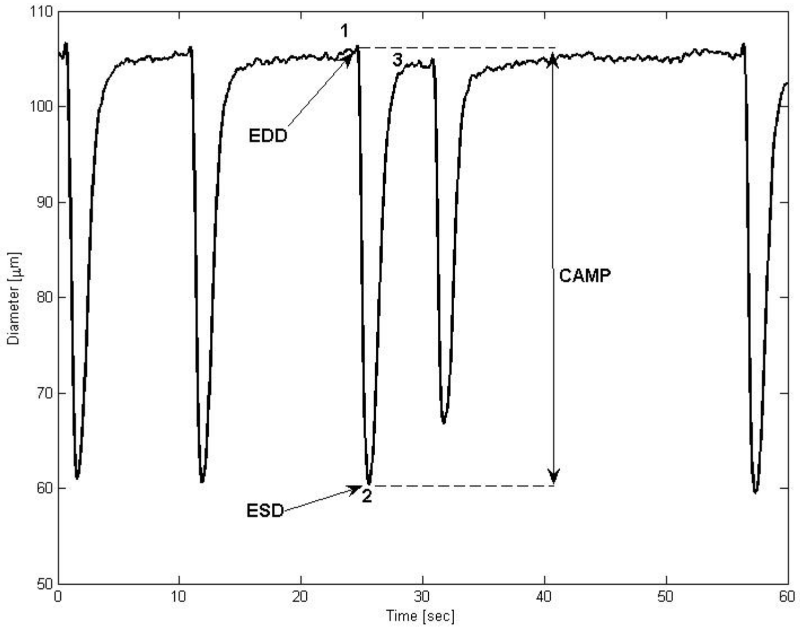

Figure 2.14: A typical lymphatic diameter tracing featuring 5 contractions cycles. One contraction cycle is denoted, starting at the EDD (point 1) with the vessel contracting until its ESD (point 2) and then passively distending back to the EDD (point 3). Contraction amplitude is defined as the difference of EDD and ESD.

Table 2.2: List of flow measurement experiments in lymphatic vessels

Experiment number	**Vessel number**	$\mathbf{P_{avg}[cmH_2O]}$	$\mathbf{\Delta P_{axial}[cmH_2O]}$ [13]						**Number of valves**	**Pre-conditioned**	**Air table**	**Perfusion**	**Weight**	**Gender**
			-3	**-1**	**0**	**1**	**3**	**5**						
1	1	3	1	2		3	4	5	3	NO	NO	NO	340	M
2	2		6	7	8	9		10					330	
	3			11	12	13	14	15					230	
3	4					16		17	2		YES			
	5					18								
4	6		19	20		21	22	23	3				360	F
	7		24	25	26	27	28	29				YES	220	M
5	11			30	31	32	33	34	2	YES			300	
	11	5	35	36	37	38	39	40						
	13	3		41	42	43	44	45	3					
6	16		46	47	48	49	50	51				NO [14]	290	
	17			52	53	54	55	56						
7	20-Part A		57	58	59	60	61	62	4			YES	250	
	20-Part B		63	64	65	66	67	68						
	22			69	70	71	72	73	3					
	23			74	75	76	77	78				NO [14]		

---

[13] The number contained in these cells is the measurement id number. The reader can refer to this table when reading the results of Sections 3.2, 3.3 and 3.4

[14] Due to problems in the temperature regulation of the bath medium, perfusion was stopped in order for the temperature to rise at 36-38 degrees. pH after experiment was about 7.6-7.7 at 19°C.

2.4.2 Vessel wall detection algorithms

The contractions of the lymphatic collecting vessels, necessitate the use of a vessel wall detection algorithm, so that the wall may be identified and removed from the analysis of PIV images. Three different approaches were used and each has its advantages and disadvantages. In all of the different wall detection implementations, Canny edge detection was used; a well known and widely used algorithm. The differences of the methods lie in the way the images were pre-processed prior to the application of the Canny edge detection in Matlab.

Thresholding and erosion

The simplest way of detecting the image is via image contrast thresholding. By appropriately selecting the thresholding limit the internal contents in the vessel and the vessel wall appear as a white area in the black&white images. The image is then eroded with an erosion tool size approximately equal to the vessel wall thickness. The result of the erosion is that only the contents of the vessel appear as a white area in the image. The application of the Canny edge detection will result into two edges that are the vessel inner walls. Figure 2.17 shows an example of the steps of the algorithm.

This approach is simple and very easily implemented in Matlab. It also has the lowest computational time of the three different approaches. It has disadvantages however. Using erosion with a fixed size erosion tool implies that the vessel wall is of constant thickness, which is not always the case. Furthermore, the quality of the thresholding[15] depends on the selection of contrast thresholding value and it was found during the application in lymphatic vessel images that one single selected value may not work well for an entire data set from a single acquisition. Despite these drawbacks the success was high enough to allow for automatic vessel wall detection and manual correction when necessary.

The first step, using contrast thresholding is shown in figure 2.17a. This step resulted in the vessel wall and contents having equal grayscale value. The erosion step that followed reduced the width of the white region in figure 2.17a by the width of the vessel wall. Finally the result of the Canny edge detection is shown in figure 2.17b and overlayed on the corresponding PIV image in figure 2.17c.

---

[15] Quality is defined as the ability of the thresholding to provide a uniform area of the vessel wall and contents without gaps inside the vessel. When such gaps are present, they will be detected as edges and need to be removed.

1	1	1
1	1	1
1	1	1

Figure 2.15: Erosion 3x3 square structuring element

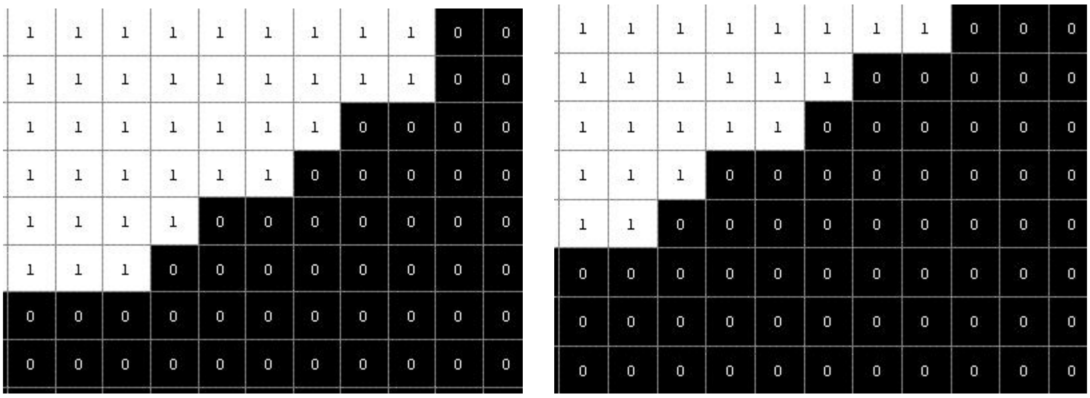

1	1	1	1	1	1	1	1	1	0	0
1	1	1	1	1	1	1	1	1	0	0
1	1	1	1	1	1	1	0	0	0	0
1	1	1	1	1	1	0	0	0	0	0
1	1	1	1	0	0	0	0	0	0	0
1	1	1	0	0	0	0	0	0	0	0
0	0	0	0	0	0	0	0	0	0	0
0	0	0	0	0	0	0	0	0	0	0

(a)

1	1	1	1	1	1	1	1	0	0	0
1	1	1	1	1	1	0	0	0	0	0
1	1	1	1	1	0	0	0	0	0	0
1	1	1	0	0	0	0	0	0	0	0
1	1	0	0	0	0	0	0	0	0	0
0	0	0	0	0	0	0	0	0	0	0
0	0	0	0	0	0	0	0	0	0	0
0	0	0	0	0	0	0	0	0	0	0

(b)

Figure 2.16: Erosion with a 3x3 square structuring element (a) Initial image and (b) Final image.

Morphological operations - Erosion

Erosion is a morphological operation applied mainly to binary images [81]. Mathematically erosion is an operator which when applied to a binary image, it erodes away the boundaries of regions of foreground pixels. Foreground areas then shrink in size, while holes become larger. Erosion is applied to an image by means of a structuring element; a typical 3x3 square element is shown in Figure 2.15. An example of the application of this element in a binary image is shown in Figure 2.16. The original image is shown in 2.16a. The structuring element is applied in each pixel of the image. The effect of the structuring element is that any pixel that is not completely surrounded by foreground pixels is replaced by 0, that is, it is made a background pixel. The result to this operation is the erosion of the image boundaries and the final image is shown in Figure 2.16b.

(a) First step: Contrast thresholding

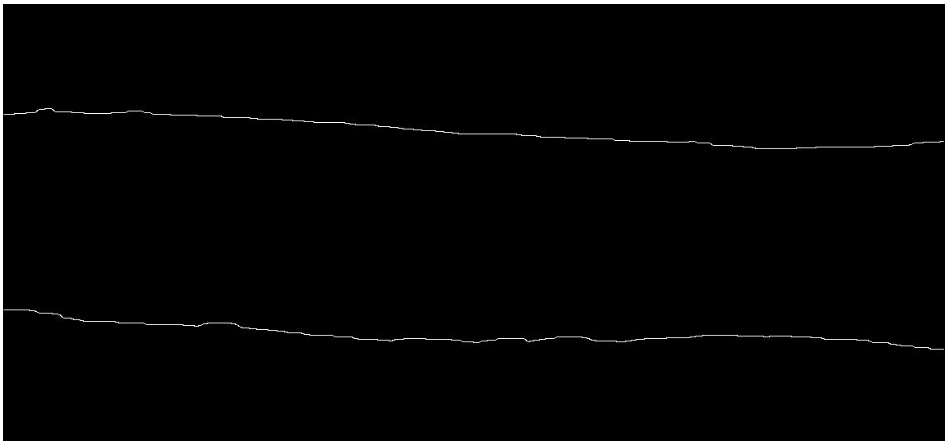

(b) Second step: Erosion and Canny edge detection

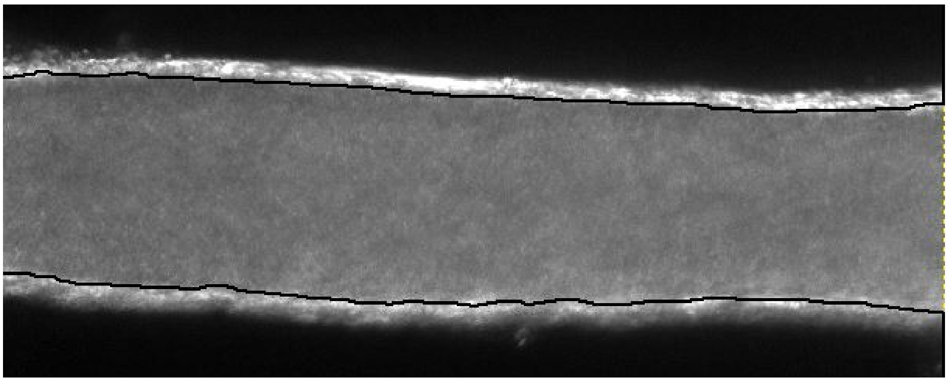

(c) Detection result overlayed on PIV image

Figure 2.17: Thresholding/Erosion Algorithm steps

Mask filtering

A variation of the thresholding algorithm was developed to increase the robustness of the vessel wall detection. Instead of directly thresholding the image, a mask filter was used to create a uniform, in terms of contrast, image of the vessel wall and its contents [71]. The filter size was the parameter of this algorithm. Afterwards the erosion step and Canny edge detection were carried out as above. Figure 2.18 shows the intermediate steps.

Again this algorithm depends on the vessel wall thickness being constant, but proved to be the more robust algorithm of those used in the present work. In most cases it was able to automatically detect the vessel wall with reasonable accuracy without erroneous detection, but at the expense of increased computation time; in fact this was the slowest algorithm requiring 1.5 sec on average, while the simple thresholding needed approximately 0.5 seconds. The third approach, explained in the following section, required 1 sec on average to complete the calculation. The computation time is based on a Windows 7 x64 based PC with Intel Core 2 Duo T9500 CPU and 4 GB RAM.[16]

(a) First step: Mask filtering and thresholding

---

[16] Windows 7 is a trademark of Microsoft Corporation. Core 2 Duo is a trademark of Intel Corporation.

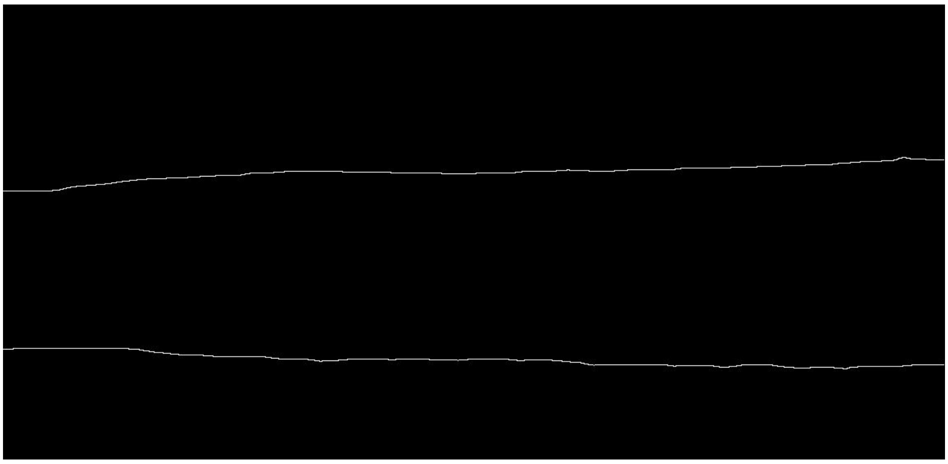

(b) Second step: Erosion and Canny edge detection

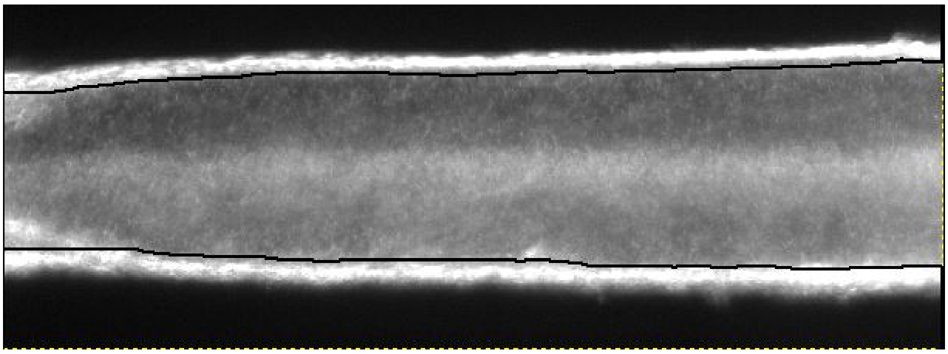

(c) Detection result overlayed on PIV image

Figure 2.18: Mask filtering steps

Principal component analysis

This approach, while still using the Canny edge detection as a first step, did not make use of contrast thresholding. The algorithm was developed by Dr. Cristos Diou, Department of Electrical and Computer Engineering, Aristotle University of Thessaloniki, Greece. The details shall be the subject of a future publication. Briefly the algorithm steps are the following steps:

1. Application of a Canny edge detector to identify candidate boundary regions
2. Application of Principal Component Analysis (PCA) [74] to identify the principal direction of the vessel
3. Rotation of the image so that the vessel is in the horizontal axis
4. Selection of the inner boundary regions above and below the centroid
5. Rotation back to the original image and display

The major difference of this algorithm is the use of PCA to determine the orientation of the detected edges. In PCA a scatter matrix is formed for each edge using the pixel coordinates [74]. If an edge is composed by n number of pixels with coordinates (x_i, y_i) then the scatter matrix is computed by the following equations:

$$S = \begin{pmatrix} s_{11} & s_{12} \\ s_{21} & s_{22} \end{pmatrix} \tag{2.4}$$

where

$$\begin{aligned}
s_{11} &= \frac{1}{n} \sum_{i=1,\ldots,n} (x_i - x_m)^2, \\
s_{12} = s_{21} &= \frac{1}{n} \sum_{i=1,\ldots,n} (x_i - x_m)(y_i - y_m), \\
s_{22} &= \frac{1}{n} \sum_{i=1,\ldots,n} (y_i - y_m)^2, \\
x_m &= \frac{1}{n} \sum_{i=1,\ldots,n} x_i, \\
y_m &= \frac{1}{n} \sum_{i=1,\ldots,n} y_i
\end{aligned}$$

The angle θ of each line is then from the first eigenvalue λ_1 (larger) of the scatter matrix, while the second eigenvalue λ_2 is a measure for the straightness of the edge and is zero for an ideal straight line. The equations for the angle and eigenvalues are given below:

$$\theta = \arctan \frac{(\lambda_1 - s_{11})}{s_{12}} \tag{2.5}$$

where

$$\lambda_{1,2} = \frac{1}{2} \left\{ s_{11} + s_{12} \pm \sqrt{(s_{11} - s_{12})^2 + 4s_{12}^2} \right\} \tag{2.6}$$

After determining the edge orientation, the image is rotated so that the vessel longitudinal axis is horizontal and the inner wall edges are determined by their distance from the image centroid.

This approach in wall detection is independent of the vessel wall thickness and offers a robust approach in case the vessel longitudinal axis deviates significantly from the horizontal. The computational cost was between the previous two approaches based on contrast thresholding.

Figure 2.19 shows the algorithm intermediate steps. The first step of detecting all the edges in the image, both internal/external vessel wall and edges due to the presence of particles is shown in Figure 2.19a. After carrying out steps 2 and 3, the fourth step detects and removes the external and internal (due to particles) edges, leaving only the internal wall edge in the image which is rotated back to the original orientation (figure 2.19b). The resulting edge overlayed on the PIV image is shown in figure 2.19c.

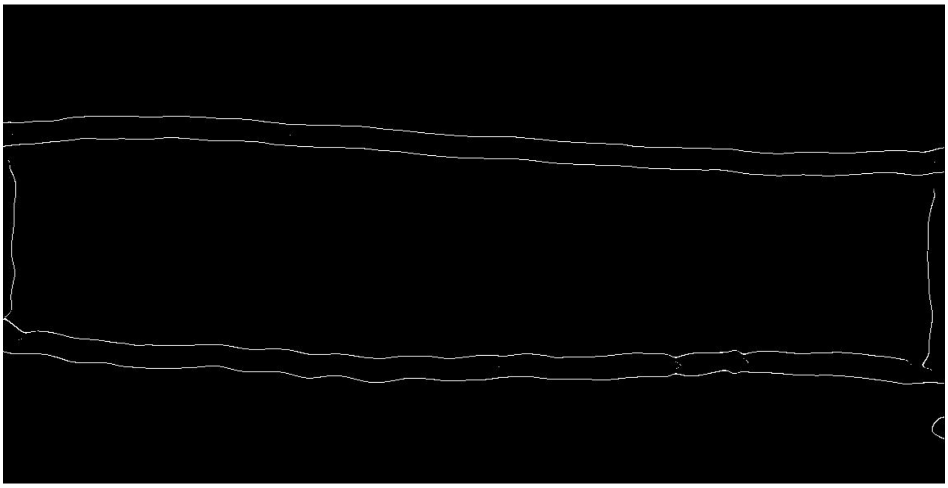

(a) First step: detection of all edges

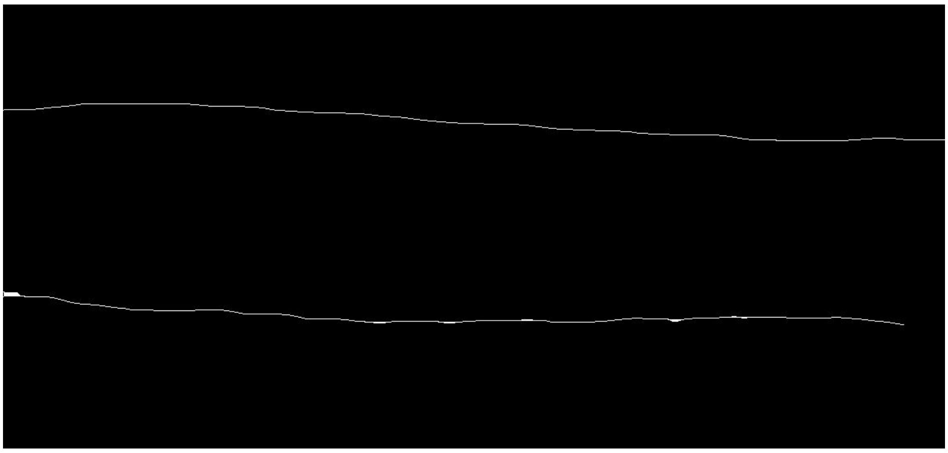

(b) Final internal edges detected

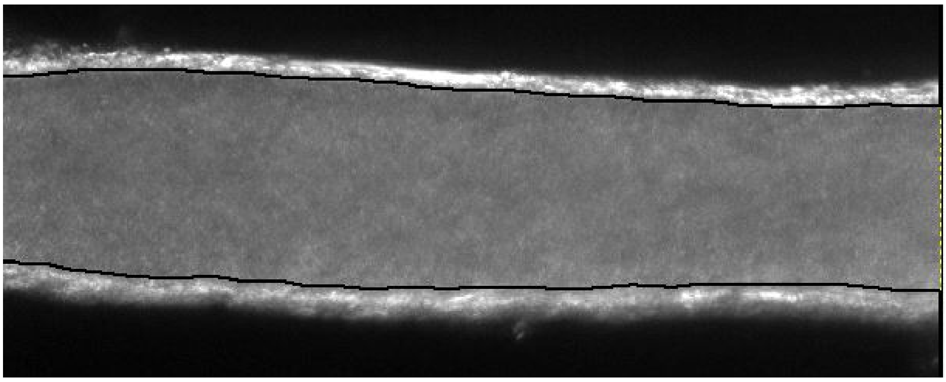

(c) Detection result overlayed on PIV image

Figure 2.19: Principal component analysis algorithm steps

2.4.3 Contraction frequency

Estimation the frequency of contractions of the lymphatic vessels (FREQ) was performed using open source Matlab code[17] for detecting the maxima and minima of data series. With this approach it was possible to get an automatic estimate of the frequency and greatly facilitate the processing of large data sets.

The frequency of lymphatic contractions may change, even when the experimental conditions remain constant, as figure 2.20 indicates, where the duration between two successive contractions changes. The pattern is not always the same between vessels and it may also change in reaction to the experimental conditions. This is evident in figure 2.20a and 2.20b, which shows the contraction pattern of the same lymphangion at different axial pressure gradients. In figure 2.20a at favourable pressure gradient a plateau is present at maximum diameter. On the other hand, at the negative pressure gradient in figure 2.20d the plateau is not present and the contraction pattern resembles a shark tooth.

Due to these variations, the algorithm used to detect the peaks and valleys faced difficulties in accurately detecting the peaks just prior to each contraction. Figure 2.20 shows examples of such problematic cases. Detecting the valleys showed no accuracy issues (figure 2.20d) as the slope of the diameter curve changes abruptly in all cases. Therefore, it was considered to be more accurate to measure the frequency by detecting only the valleys of each data series. The frequency estimation algorithm was as follows:

1. All the valleys in a diameter trace were detected
2. If the number was less than two the frequency was given a value of NaN
3. If the valley number was two or three then the frequency would be equal to the reciprocal of the time difference between the values (An average value was used when three valleys were detected)
4. When more than four valeys were present, the first and last valley were discarded to avoid the degenerate case shown in figure 2.20d, where the last contraction was not fully recorded. The frequencies computed by each pair of successive peaks were averaged.

---

[17] (http://www.mathworks.co.uk/matlabcentral/fileexchange/25500-peakfinder)

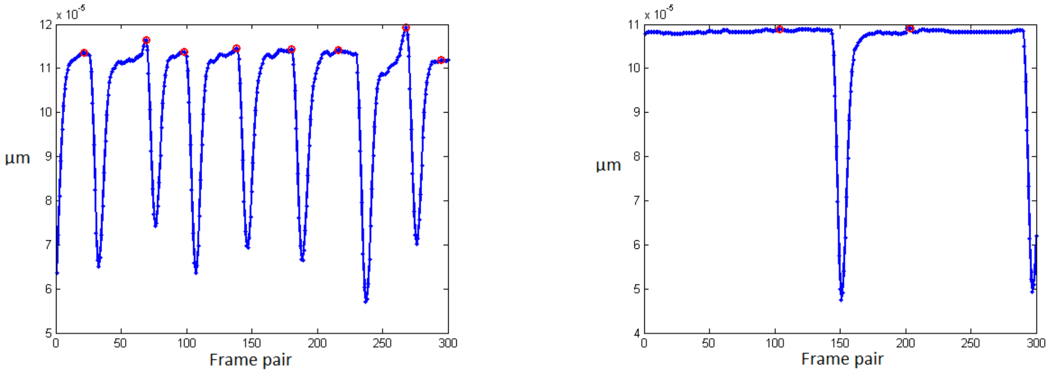

(a) Numerous contraction of almost constant frequency. Peaks are correctly determined. However the last contraction has not been recorded completely and needs to be discarded.

(b) Only one complete contraction recorded. Peaks are incorrectly identified.

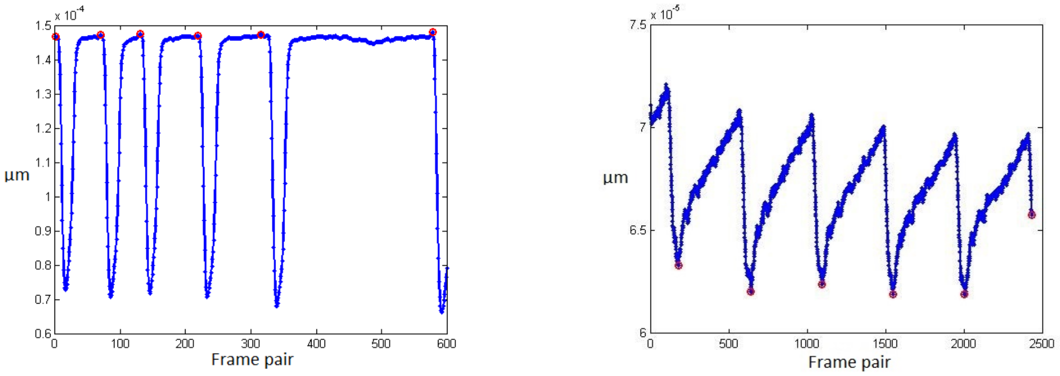

(c) Numerous contractions recorded but with varying frequency. The end of contraction during the second to last plateau is incorrectly identified.

(d) Contraction pattern at negative pressure gradient. This pattern has a more shark-tooth shape and the plateau at the EDD is not present

Figure 2.20: Detection of maximum diameter for frequency calculation. The abscissa in the graphs shows the number of pair of frames, not time.

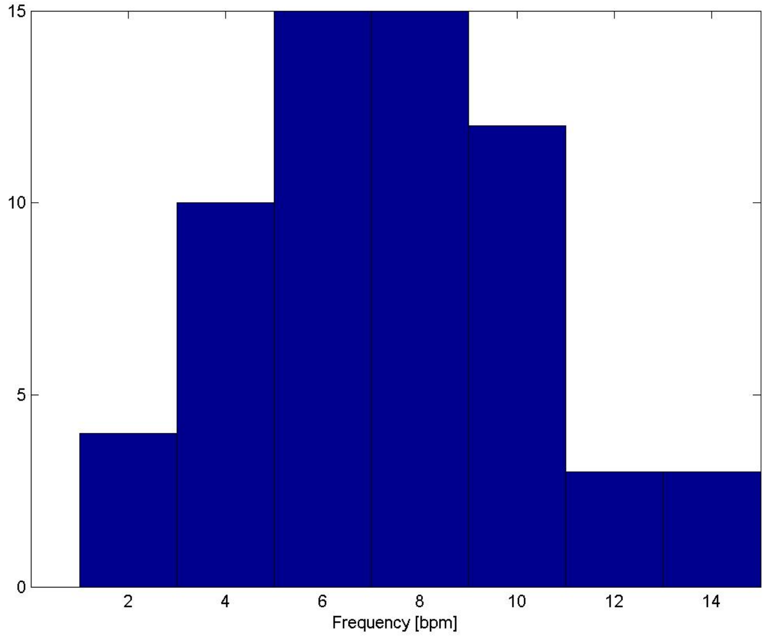

(a) Contraction frequency histogram. The most frequent occurring value of 6-8 bpm is within physiological expected values

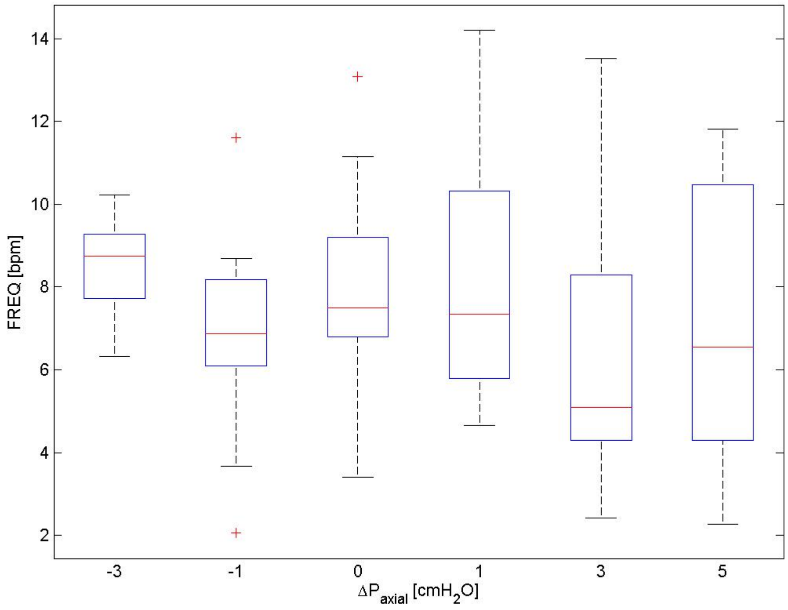

(b) Contraction frequency vs. axial pressure gradient

Figure 2.21: Contraction frequency statistics. Result is from automatic frequency calculation using minima detection.

Figure 2.21a shows the histogram of frequency and figure 2.21b shows the contraction frequency grouped by axial pressure gradient, as calculated with the automatic frequency estimation. For reasons explained later on, in section 3.6.1 the figures of this section show data of frequency for measurements that had the air table activated.

Accuracy of automatic frequency estimation

The algorithm for frequency estimation greatly facilitates the processing of results, but it is necessary to assess its accuracy. Unfortunately, the only way to determine the accuracy of such an algorithm, is by inspecting all diameter tracings, manually extracting the contraction frequency and comparing it with the value calculated by the algorithm. Manual extraction is in itself, besides time consuming, subject to human errors.

After manual extraction for the contraction frequency, the values were compared with the automatically calculated values. Figure 2.22 shows the same information as figure 2.21 but for manual frequency extraction. The degree of accuracy of the algorithm is shown in figure 2.23, where the relative error is plotted as a percentage. It is obvious that there are cases where the automatic algorithm has a large error of 100%. This situation occurs when there are very few contractions within a measurement (1-2) or when the lymphangion contraction frequency varies considerably between cycles. The mean error however is 12.6% and the median value is 7.5% and therefore the automatic algorithm is quite accurate most of the time.

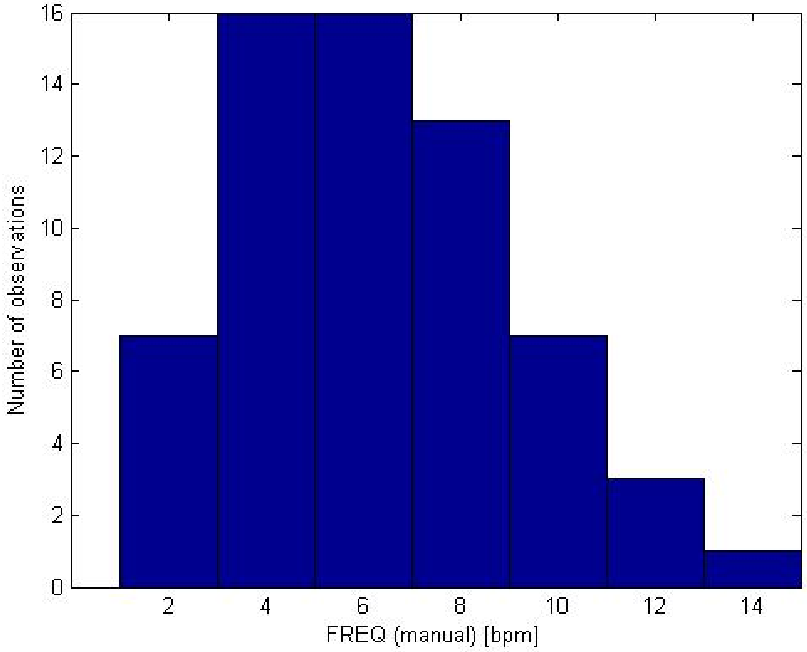

(a) Contraction frequency histogram from manual extraction. The results from the manual extraction of FREQ are quite similar with those from the automatic estimation in figure 2.21a.

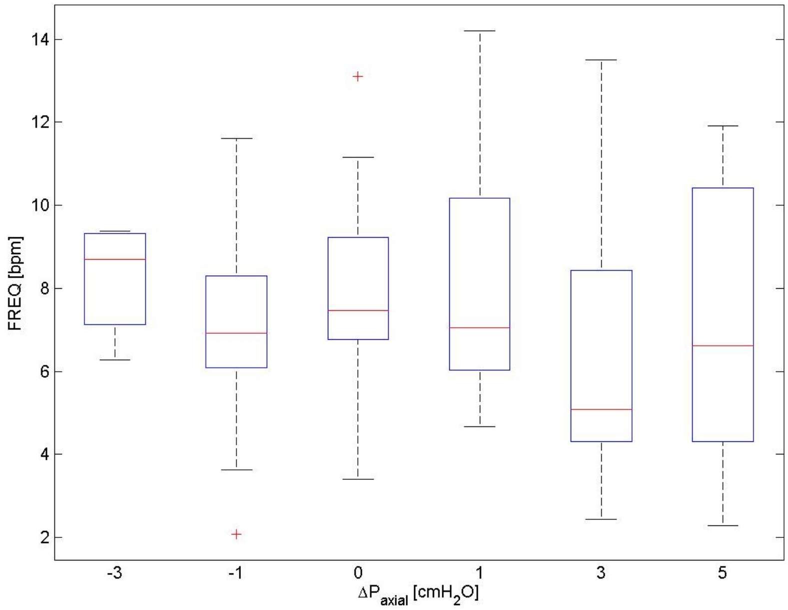

(b) Contraction frequency (manual calculation) vs axial pressure gradient

Figure 2.22: Contraction frequency grouped by the axial pressure gradient. Manual frequency calculation using minima detection.

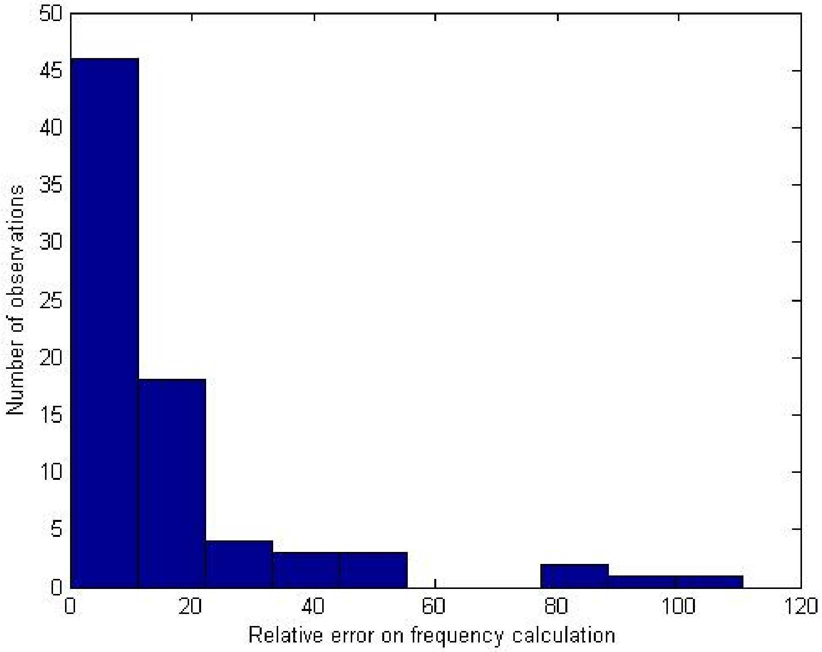

Figure 2.23: Relative error of automatic frequency calculation, using minima detection.

A second attempt to automatically estimate the contraction frequency was attempted, using Fast Fourier Transform (FFT), with an aim of improving the accuracy of estimation. The FFT of the diameter vector tracing was calculated in Matlab. The DC term was dropped and the contraction frequency was assumed to be equal to the first harmonic frequency. However, this approach proved to be more inaccurate than the minima detection explained earlier. Figure 2.24 shows the relative error of the FFT approach with respect the manual frequency extraction. The mean and median relative error are 45.9% and 20% respectively, values that are higher than those obtained with the peak detection approach. The cause of this is shown in figure 2.25. A diameter tracing, which constitutes the original signal, is shown on top, the frequency spectrum in the middle and the reconstructed signal on the bottom; 257 harmonics are required to reconstruct the original signal. Due to the change of duration of lymphatic contractions, the first harmonic frequency is not representative of the average contraction frequency during the measurement time frame. The signal in the figure has 5 full contraction cycles per minute, but the first FFT harmonic is at 16 bpm. Such changes in the time interval between contractions are frequent in lymphatic vessels thus making the use of FFT for frequency calculation unreliable.

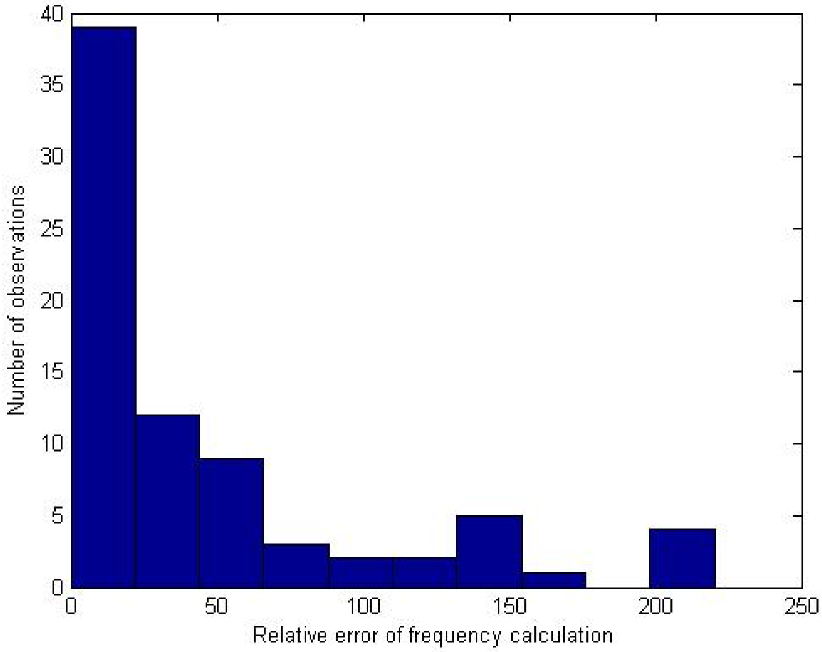

Figure 2.24: Relative error of frequency calculation with FFT.

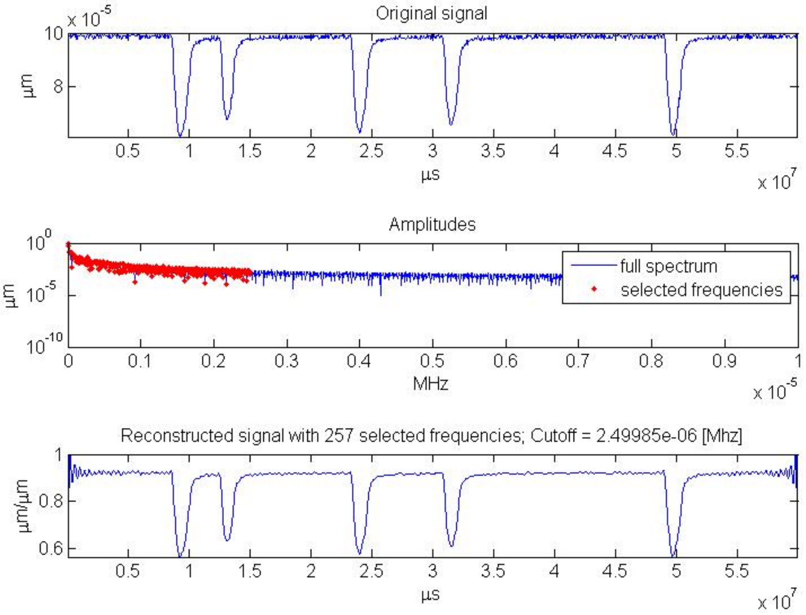

Figure 2.25: FFT spectrum and signal reconstruction. From top to bottom: Original signal of diameter tracing in meters. FFT harmonics of diameter tracing. Reconstruction using 257 harmonics.

2.4.4 Flow rate

Volumetric flow rate is not available in PIVlab. Hence, the toolbox was supplemented with custom code for calculating the volumetric flow rate from the PIV results. The calculation was performed with numerical intergration of the velocity profile at a selected cross section. It was assumed that the vessel has a circular cross section with a diameter determined by the vessel wall detection algorithm. Unless otherwise stated, a cross section in the middle of the FOV was selected.

A theoretical flow rate was also calculated, by using the average PIV velocity at a given cross-section and using the well known formula for laminar flow inside a circular conduit.

$$Q_{th} = \frac{\pi \cdot r_i^2}{2} \cdot v_{avg} \tag{2.7}$$

2.4.5 Wall Shear Stresses

Wall shear stress (WSS) are a notoriously difficult parameter to estimate experimentally [120, 148]. The accuracy of the estimation dependes on the spatial resolution of the PIV experiment, the accuracy of the velocity estimation, and the WSS calculation algorithm. In this particular application accuracy in WSS estimation will depend heavily on the accuracy of the detection of the vessel wall position.

PIVlab computes the shear rate with the simple Matlab function 'gradient', without using a particular fitting between velocity values. Multiplying the shear rate by the dynamic viscosity will yield the shear stresses. However, this is a somewhat inaccurate method of estimating WSS values. To overcome this software limitation, a more accurate method of estimating WSS was implemented. From the velocity profile at the middle vessel cross section, four velocity vectors were extracted from each vessel wall. A third degree polynomial was fitted at each wall and WSS were calculated for each wall by calculating the slope of the polynomial at the wall. The values of each wall were averaged to yield the WSS at the middle cross section.

In this implementation, the actual velocity from the PIV analysis at the wall was used; this is generally non-zero and although this deviates from the no-slip velocity condition at the wall[18]

---

[18] Assuming no-slip boundary condition at the wall generally seems as a reasonable assumption. However, the presence and magnitude of a slip velocity will depend on the wetting properties and micro-structure of the lymphatic endothelial cells lining the vessel wall. To the author's knowledge conclusive evidence on this do not exist in the

it has been shown to yield better results than replacing the velocity value at the wall with zero [66].

A drawback of the present WSS estimation is that it assumes that the normal to the vessel wall is orthogonal to the main flow direction. This is not always the case with lymphatic vessels due to the contraction and the fact that the vessel wall may not be straight. An improved approach would need to determine the normal vector at the wall location were WSS are to be computed and derive the velocity gradient with respect to this normal direction. This approach was used by Poelma et al. [109], but was not implemented here and is left as future work.

Since the experiments were carried out at physiological temperatures of $36 - 38^oC$ and APSS is an aqueous solution it was assumed that APSS has the same properties as pure water at the same temperatures. Density was assumed to be $\rho = 993\ kg/m^3$ and dynamic viscosity was $\mu = 6.78 \times 10^{-4}\ Pa \cdot s$

The theoretical WSS, assuming fully developed laminar flow, where also derived from the velocity measurement. The following equation was used from Dixon et al. [31]

$$\tau = \frac{2\mu \cdot v_{avg}}{d} \tag{2.8}$$

2.4.6 Pressure calculation

It is possible to calculate the pressure in a flow field from PIV measurement data [1, 18, 116, 147]. Estimating pressure from PIV data is an ongoing research topic. The methods available to date can be divided in two categories; on one hand pressure may be estimated by solving the pressure Poisson differential equation [39, 76] with appropriate boundary conditions [48]. On the other hand, taking advantage of the scalar nature of pressure, one can integrate velocity data along different paths[19] within the flow field [24, 51].

In the present work the method of integrating along paths was selected, mainly due to the lower computational cost and because of the recent availability of open source Matlab tools.[20] This method was developed by Dabiri et al. [24].

---

literature.

[19] These integration paths should not be confused with the term pathlines used in fluid dynamics (trajectories of individual particles). Perhaps a better term is integration direction, however the term integration path is used in the literature and has been adopted here [18].

[20] Queen 2.0 Pressure field calculation, http://dabiri.caltech.edu/software.html, accessed 20/05/2014.

The direct integration methods for pressure estimation are based on direct integration of the pressure gradient term in the Navier-Stokes equation which, for incompressible flow, is:

$$\nabla p = -\rho \left(\frac{\partial \mathbf{u}}{\partial t} + (\mathbf{u} \cdot \nabla)\mathbf{u} - \nu \nabla^2 \mathbf{u} \right) \tag{2.9}$$

Following equation 2.9, the pressure difference between two points $\mathbf{x}_1$ and $\mathbf{x}_2$ is given by:

$$p_2 - p_1 = \int_{\mathbf{x}_1}^{\mathbf{x}_2} \nabla p d\mathbf{x} \tag{2.10}$$

The method by Dabiri et al. [24] is an improvement of the standard path integration and includes paths along the diagonal directions originating from points within the flow field (Figure 2.26). Hence, eight values of pressure are computed for each point and the median, instead of the mean, is selected as the estimated pressure value. The software is also capable of handling masked regions by assigning a NaN value to those points. The median calculation in Matlab ignores NaN values, effectively removing the effect from the result. It is noted that a limitation of the method used is that the pressure estimation is relative to a zero reference pressure.

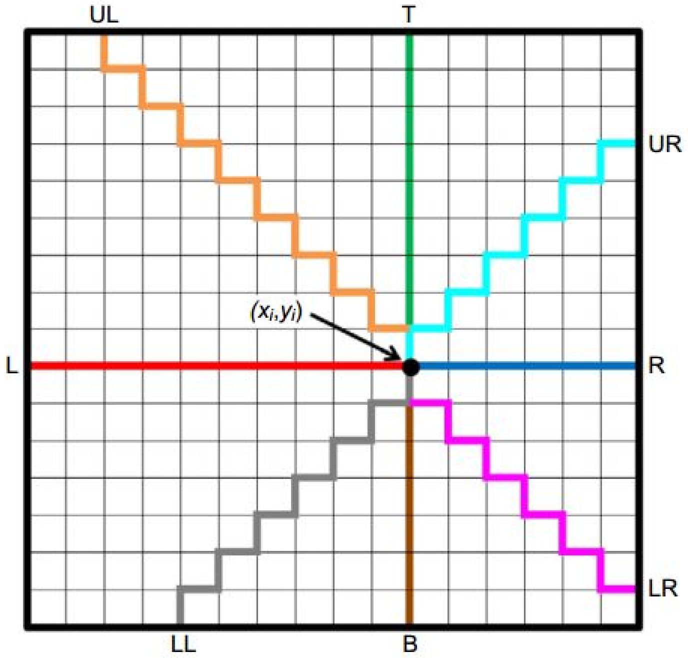

Figure 2.26: Integration paths. The method by Dabiri et al. [24] uses eight integration paths that originate from the domain boundaries. Each path propagates towards the integration point (x_i, y_i). Direction are from left (L), upper left (UL), top (T), upper right (UR), right (R), lower right (LR), bottom (B) and lower left (LL). Image used with permission [24].

Using a Matlab script, text files with the lymphatic μ-PIV results were written for input to queen 2.0 which output was again written in text files. The results from the pressure field calculation was read again with a Matlab script and pressure vs time and P-V plots could be generated. In the present work, the temporal filter in queen 2.0 was activated; a few test cases with temporal filter off, showed negligible differences and although temporal filtering increases calculation time it provides smoother results.

Using the same Matlab code for finding the minimum diameter (section 2.4.3), each diameter tracing was split into contraction cycles. A simple approach was used, where the ESD diameter was detected and data ± 2 s around each ESD were kept and considered to form the contraction cycle. This approach was selected because the diameter tracing curves usually have the distinctive plateau discussed in section 2.4.3. This feature makes it more complicated to find the exact time of contraction start and finish. The time/diameter data of each cycle were used to split the P-t curves in cycles and calculate the volume vs time. Thus it was straightforward to plot the Pressure-Volume (P-V) curves of each contraction cycle.

The available P-V data made it possible to estimate the work done during the contraction cycle. Work can be calculated by calculating the area inside the P-V loop with numerical integration. However, this proved to be a non-trivial mathematical problem, due to the shape of the P-t curves, in certain cases, that made the P-V loop self-crossing, that is, the P-V loop is a non-manifold geometry (see figures in section 3.4). Standard algorithms to compute the area of a polygon in Matlab fail in the presence of self-intersections. The solution to the problem was given by an open-source Matlab function by A. Owaid[21] [7] that computes the area of any loop, manifold or non-manifold, by converting the numerical data to pixel representation. This algorithm was developed to calculate the area of hysteris loops that may self-cross and correctly calculates the area enclosed by the P-V curves.

2.4.7 Wall radial velocity

The radial velocity of the vessel wall may also be computed using the diameter tracings, by numerical differentiation. Differentiating experimental data suffers from noise amplification due to the inherent noise of the input data. A method employing wavelet transformations for performing a more accurate numerical differentiation has been employed. The method was

---

[21] http://www.mathworks.com/matlabcentral/fileexchange/33570-area-under-a-curve-calculation, accessed 05/07/2014

developed by Jianwen et al. [60]. An implementation of the method in Matlab can be found on-line.[22]

The ratio of the wall radial velocity to the fluid velocity can thus be calculated. In the work by Dixon et al. [31] the fluid velocity was assumed to be greater than the wall velocity for most of the duration of the contraction cycle. The results from the μ-PIV method described herein can provide quantitative evidence that may, or may not validate, this hypothesis.

2.4.8 Filtering of time series

The resulting time series of data required filtering for removing high frequency noise. Frequency was performed with a low-pass filter in Matlab, namely the Savitzky-Golay (S-G) filter [126]. Unless otherwise stated, a polynomial order of 3 and a window size of 11 was used.

The S-G filter was preferred over a Butterworth low-pass filter as the latter exhibited edge effects. The S-G filter proved to be more tolerant in that respect. Figure 2.27 shows a comparison of the two filters.

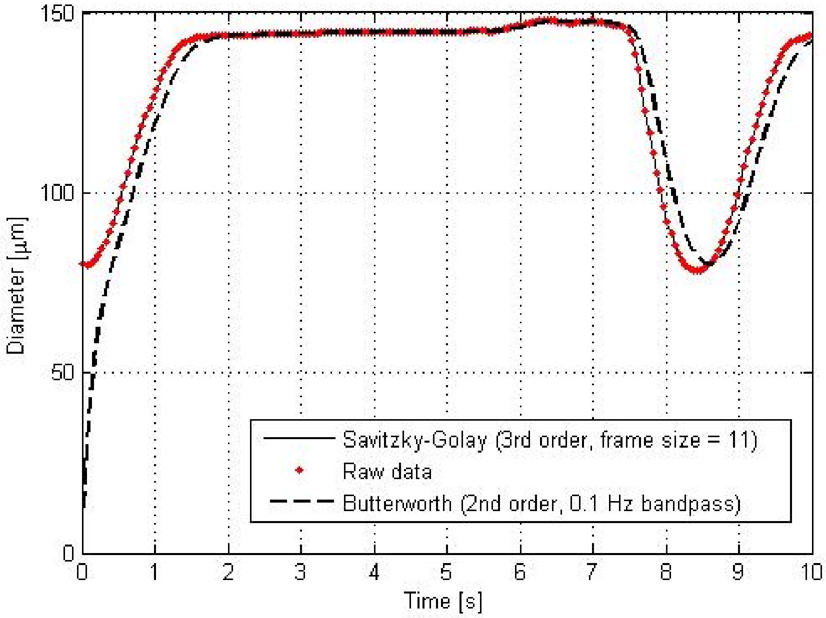

Figure 2.27: Comparison of low-pass filters for time varying quantities. The S-G filter performs better than the Butterworth filter and does not exhibit the edge effect of the Butterworth filter.

---

[22] `http://www.mathworks.co.uk/matlabcentral/fileexchange/13948-numerical-differentiation-based-on-wavelet-transforms`

Chapter 3

Results

3.1 μ-PIV measurements in lymphatic vessels - Qualitative observations

Contraction mode

The contraction mode of lymphangions is a matter of debate. Only limited evidence of peristaltic contraction similar to the oesophagus exist in isolated bovine lymphatic vessels [98]. The term peristalsis, although clearly stated in numerous studies in isolated rat mesenteric vessels, is usually used to describe the propagation of contraction from one lymphangion to the next and not a true peristalsis.[23]

Experiments were focused almost exclusively in mesenteric vessels; in this case no evidence of peristaltic contraction was found by visual observation of the recorded images. Rat mesenteric lymphangions appear to contract suddenly with the entire wall moving at same time, at least within the limits of the temporal resolution at 500-1000 fps. However, one thoracic duct preparation, clearly exhibited peristalsis, which is shown in video S1 of the supplementary material. This video was acquired using CW illumination with the camera set at 500 frames per second (fps), without imposing a pressure driven flow.

Valve Eddies

Eddies around the leaflets of a thoracic duct valve were recorded with the μ-PIV system. Video S2 of the supplementary material shows such an eddy, recorded with CW illumination at

---

[23] Peristalsis is defined as a radial constriction that propagates in the axial direction

1000 fps. The average pressure was set at $4\ cmH_2O$ and the flow was driven by an axial pressure gradient of $1\ cmH_2O$ These eddies were first reported by Florey [36] in 1927 in guinea-pig lymphatic vessels. Eddies around valve leaflets were also observed in mesenteric lymphatic vessels. Video S4 and video S5 show recirculation at slight negative ($-0.5\ cmH_2O$) and positive ($+0.5\ cmH_2O$) pressure gradient, respectively, at $4\ cmH_2O$ average pressure, recorded at 500 fps in illumination. Quantitative observations of eddies in mesenteric vessels are given in section 3.5.

Contraction effect on flow

Drawing from the knowledge of the function of the left ventricle (L-V), flow occurs during contraction; pressure builds up inside the L-V, until the aortic valve opens (see figure 4.7). In contrast, in lymphatic vessels contractions does not seem to promote flow directly. Evidence already exists that during imposed flow the vessel active contraction inhibits flow [115]. An example is demonstrated in video S3, of a mesenteric lymphatic at $+0.5\ cmH_2O$ axial pressure gradient and average pressure of $4\ cmH_2O$. The vessel diameter reduces considerably and the increased flow resistance stops flow completely, to resume as the vessel expands. The same effect of contraction in flow is shown in video S5 of a valve at similar hydrodynamic conditions.

When the vessel is subjected to a negative pressure gradient, forward flow cannot occur when the vessel is fully distended, since the upstream valve is closed. During contraction, forward flow is again not observed (see video S5). It is only during the vessel distension towards the EDD that net positive flow is seen. Once the EDD is reached flow again stops. Results that quantify the effects of contraction in flow are given in the next section.

3.2 μ-PIV measurements in lymphatic vessels - Quantitative observations

Using the developed μ-PIV system the temporal changes of flow velocity and flow rate during contraction were determined for different values of input and output pressures gradient. The figures in the following sections depict the diameter,[24] flow rate, maximum velocity, and WSS (experimental and theoretical) for different values of axial pressure gradient. These quantities were derived at a location approximately equidistant from the valves of the lymhpangion within the FOV at either end. Section 3.2.1 contains the results for positive pressure gradient, whereas the results for zero and negative pressure gradient are shown in sections 3.2.2 and 3.2.3, respectively.

Each sub-figure has a title on top of the graph which contains measurement information. This information is, in order of appearence in the title: 1) Measurement id, 2) Vessel number and number of valves in round brackets, 3) axial pressure gradient (ΔP_{axial}) and 4) transmural pressure (P_{avg}). Hence the hydrodynamic environment is depicted at the top of each graph, but the reader may refer to Table 2.2 in Section 2.4.1 for the complete conditions of each measurement present in the following sections. The flow rate plots also include the net volume of fluid propelled by the vessel over the duration shown in each graph, calculated by integrating the flow rate vs time curve.

3.2.1 Flow under favourable axial pressure gradient

Flow in lymphatic vessels where the pressure gradient is positive is thought to occur during digestion.[25] Evidence also shows that contraction is inhibited via a shear stress mechanism, as it is no longer necessary to promote flow [44].

The results depicted in figures 3.1 through 3.8 show the effect of contraction on flow rate, velocity and WSS calculated according to method presented in Section 2.4.5. There was no evidence to suggest that, in the current hydrodynamic environment, contraction provided an additional force assisting the net volumetric flow in the axial direction in any way. In fact, in most cases contraction reduced flow rate substantially and even stopped flow completely (figure 3.2a).

---

[24] The diameter is always plotted using a dashed line; all other parameters are shown with a continuous line

[25] Dr D. C. Zawieja, personal communication

Out of phase contractions of adjacent lymphangion are the most likely cause of the observed reduction in flow rate (or velocity) during the end diastolic phase of the contraction cycle. Such flow rate drops are show in figures 3.3a and 3.5a.

Contraction is associated by an increase in velocity in certain cases as shown in figures 3.6b and 3.8b. However, this is not a general case and is not necessarily associated with an increase in flow rate due to the increased resistance caused by the diameter reduction (figures 3.6a and 3.8a). Wall shear stress values derived from the PIV data are systematically lower than the estimated theoretical value based on fully developed laminar flow (see Section 2.4.5 for method of estimation). Several factors may contribute towards the degradation in accuracy of the WSS estimation, such as the lower seeding density close to the wall that affects velocity estimation and the fact that the PIV algorithm uses square IW despite the non straight vessel wall. The degree of discrepancy is highlighted in figure 3.33.

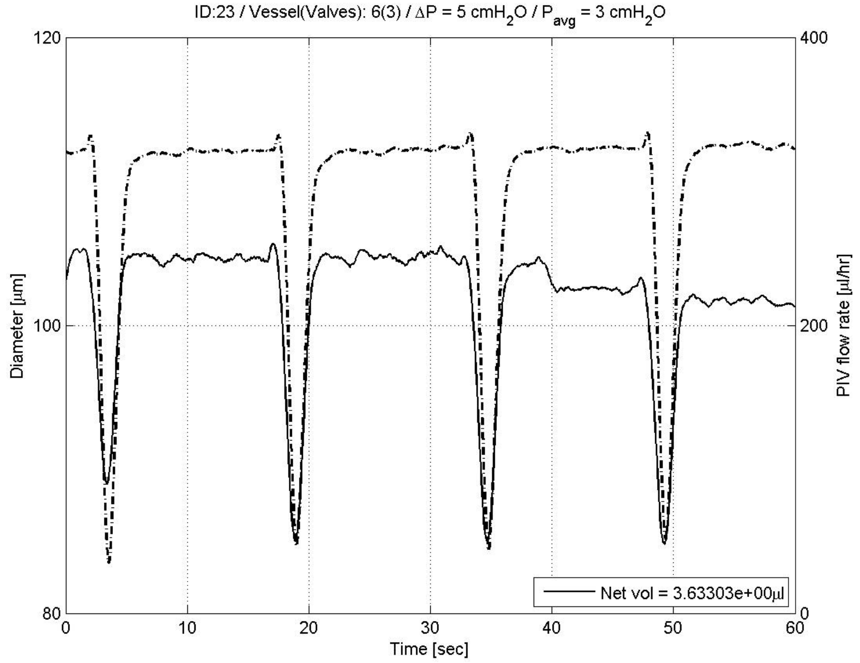

(a) Flow rate vs time and diameter vs time

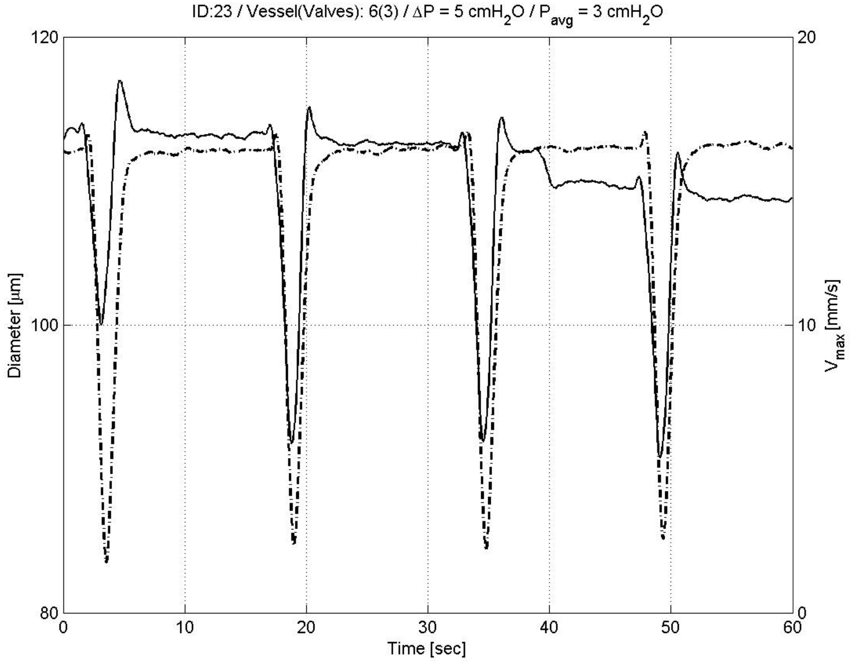

(b) Maximum velocity vs time and diameter vs time

Figure 3.1: Time plots of fluid parameters Flow rate (a), Maximum velocity (b) vs diameter (cont'd)

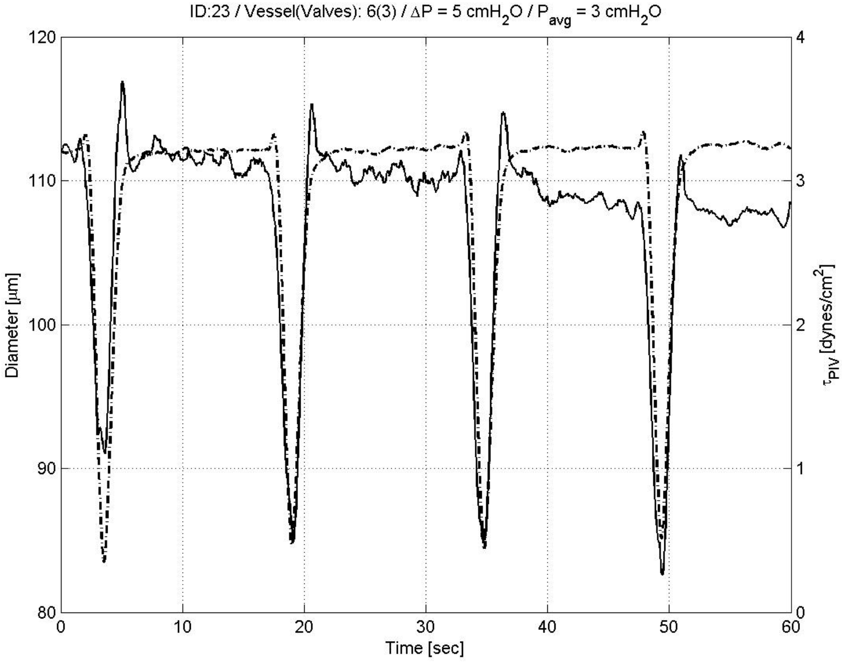

(c) PIV derived WSS vs time and diameter vs time

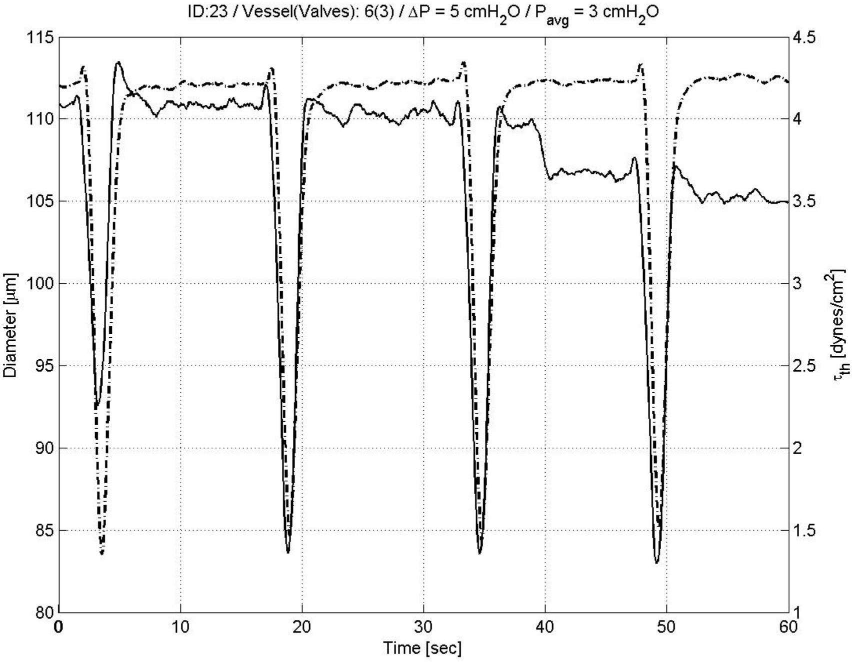

(d) Theoretical WSS vs time and diameter vs time

Figure 3.1: Time plots of fluid parameters PIV WSS (c), Theoretical WSS (d) vs diameter

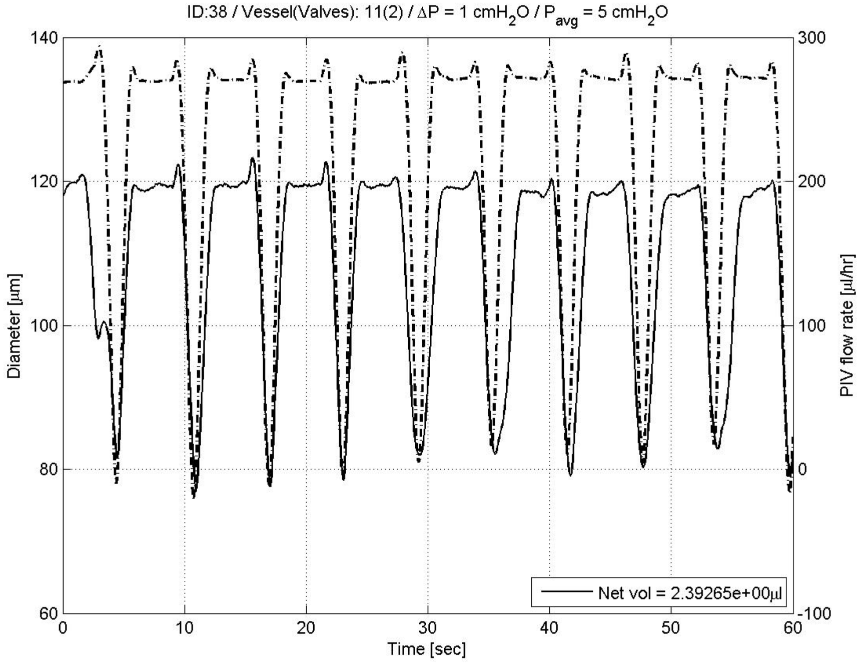

(a) Flow rate vs time and diameter vs time

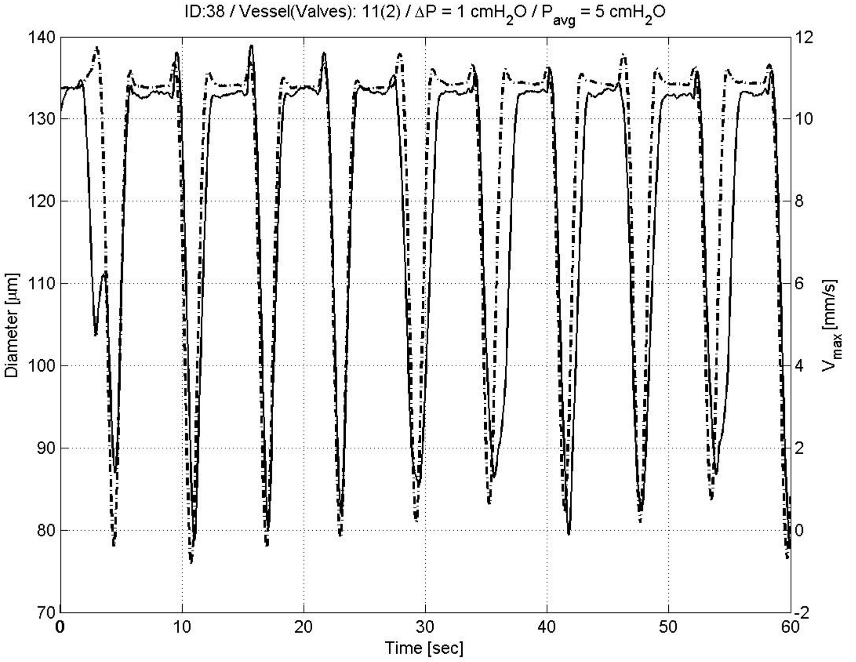

(b) Maximum velocity vs time and diameter vs time

Figure 3.2: Time plots of fluid parameters Flow rate (a), Maximum velocity (b) vs diameter (cont'd)

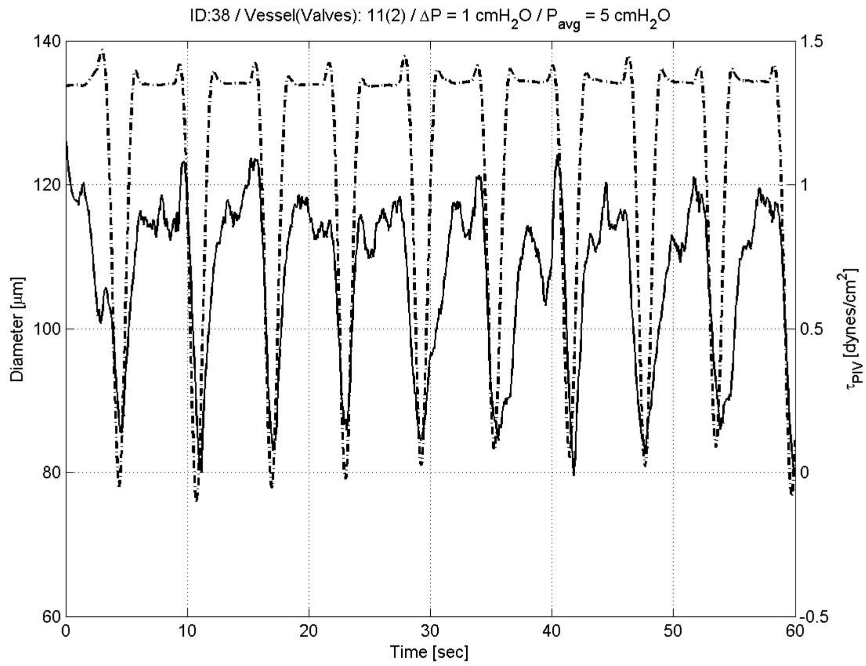

(c) PIV derived WSS vs time and diameter vs time

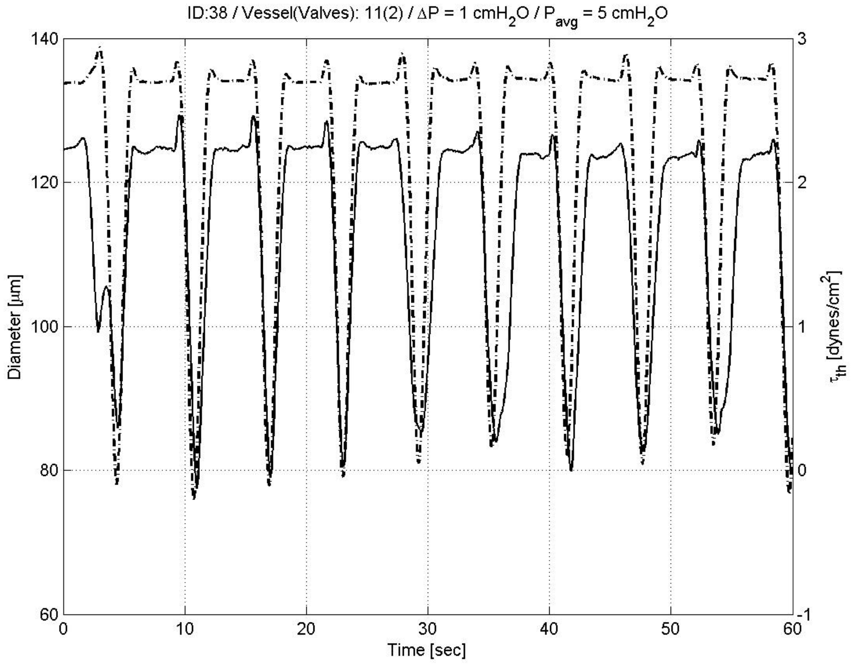

(d) Theoretical WSS vs time and diameter vs time

Figure 3.2: Time plots of fluid parameters PIV WSS (c), Theoretical WSS (d) vs diameter

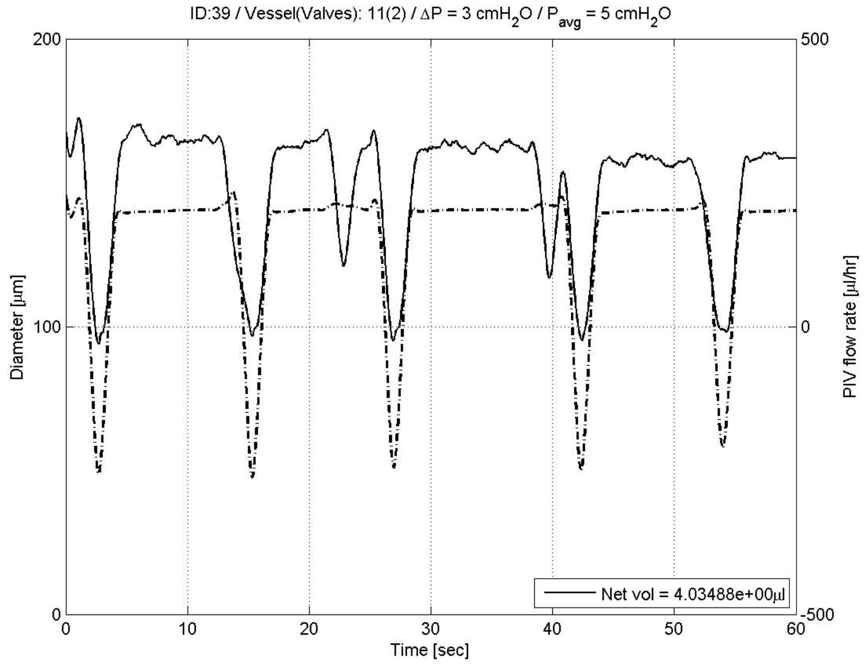

(a) Flow rate vs time and diameter vs time

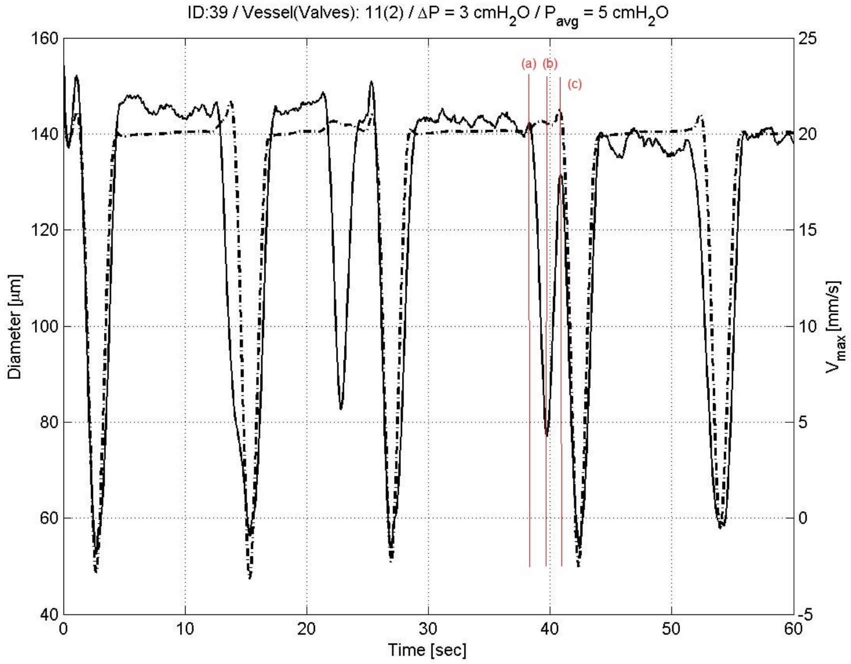

(b) Maximum velocity vs time and diameter vs time

Figure 3.3: Time plots of fluid parameters Flow rate (a), Maximum velocity (b) vs diameter (cont'd)

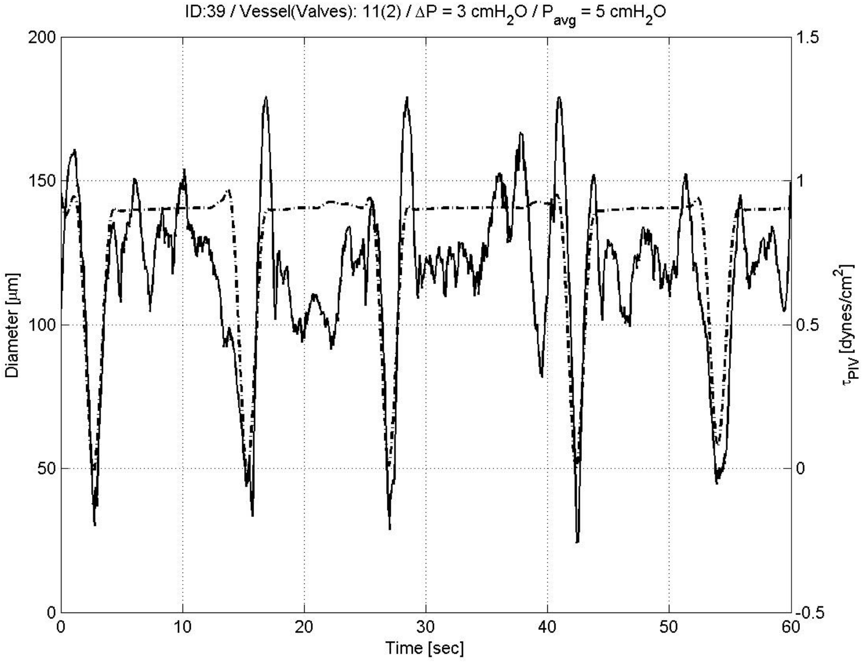

(c) PIV derived WSS vs time and diameter vs time

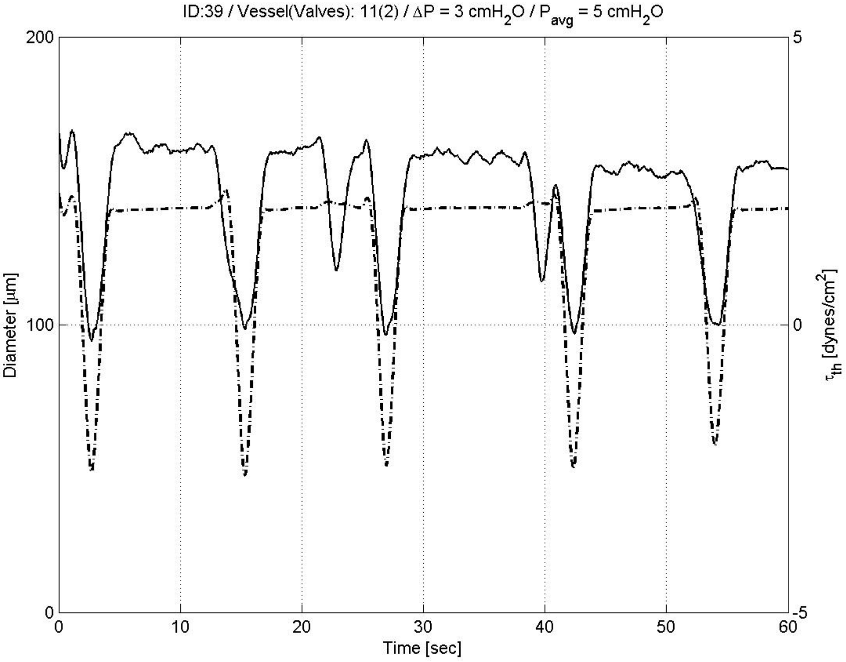

(d) Theoretical WSS vs time and diameter vs time

Figure 3.3: Time plots of fluid parameters PIV WSS (c), Theoretical WSS (d) vs diameter

Figure 3.4 shows the flow field for three different time steps for the lymphangion of Figure 3.3. In all time steps shown the vessel remains at the EDD. The axial pressure gradient remains constant and therefore it should be expected that the flow field remains unchanged through these time steps. At the first time step (Figure 3.4a) the maximum velocity is approximately 21 mm/s. At the second time step (Figure 3.4b), the velocity drops to about $4\ mm/s$ despite the fact that the vessel remains at the EDD. The most likely explanation is that a lymphangion upstream/downstream and outside the FOV contracts, thus increasing the resistance to flow. Then at the final time step (Figure 3.4c) the lymphangion that contracted out of phase has distended, perhaps reaching its EDD,[26] thus reducing the flow resistance and allowing the flow velocity to increase again.

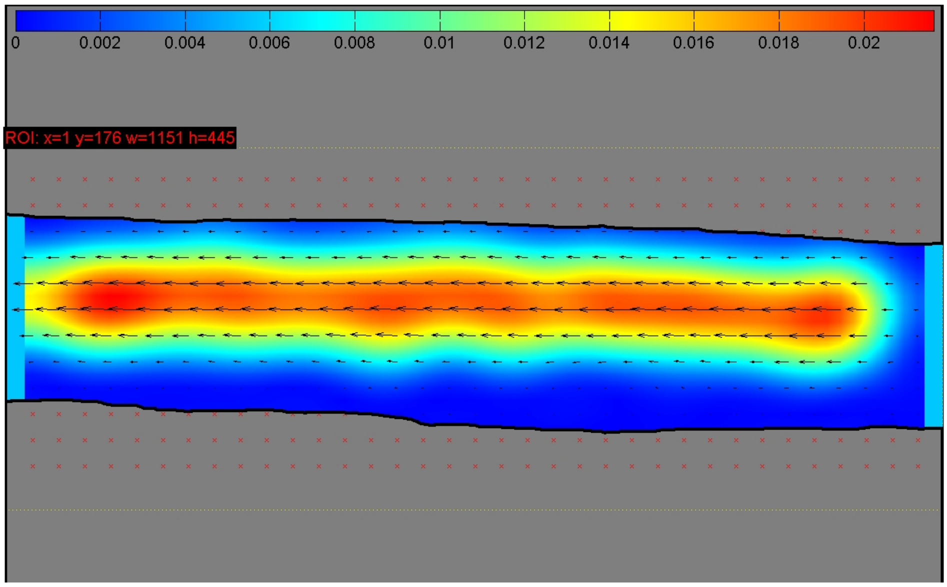

(a) Frame 437, time 38.7 s. The velocity is attains the maximum value (21 mm/s). The vessel is at the EDD.

Figure 3.4: The out of phase contraction of a lymphangion outside the FOV is the most likely source of the change in velocity field demonstrated in this figure. The colour scale is in m/s. Half the computed vectors are shown for clarity. Frames are also marked with a red line in Figure 3.3 (cont'd)

---

[26] Although this is not certain

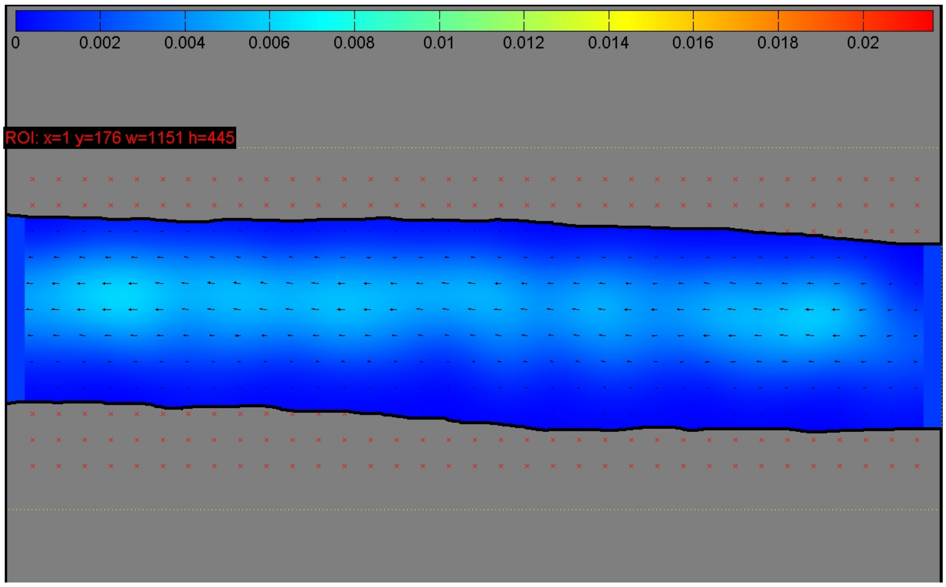

(b) Frame 456, time 39.7 s. The velocity drops to approximately $4\ mm/s$, however the vessel remains at the EDD. This is most likely due to out of phase contraction of an upstream or downstream lymphangion.

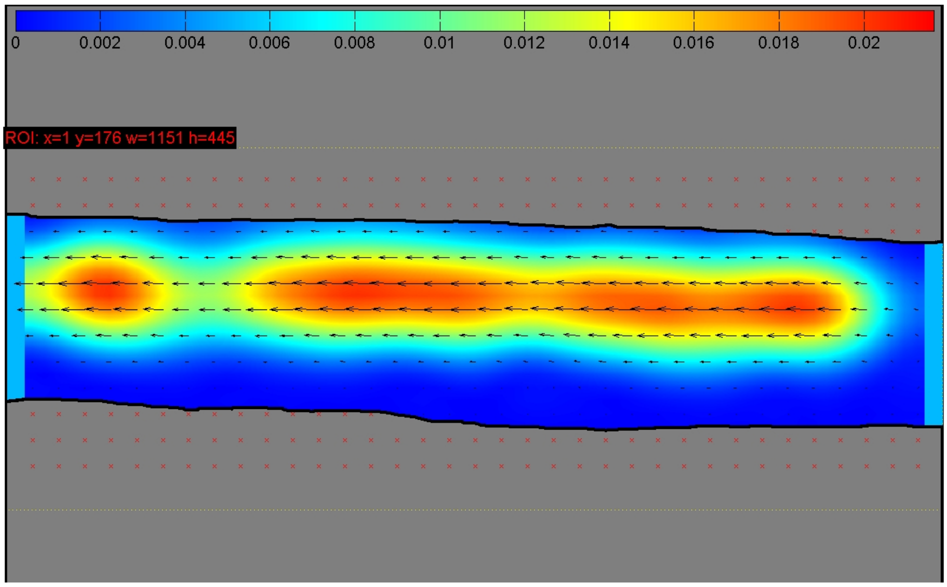

(c) Frame 484, time 40.6 s. At this time step the lymphangion that contracted out of phase has most likely distended. Velocity increases again to $17\ mm/s$. The vessel in the FOV remains at the EDD.

Figure 3.4: The out of phase contraction of a lymphangion outside the FOV is the most likely source of the change in velocity field demonstrated in this figure. The colour scale is in m/s. Half the computed vectors are shown for clarity. Frames are also marked with a red line in Figure 3.3

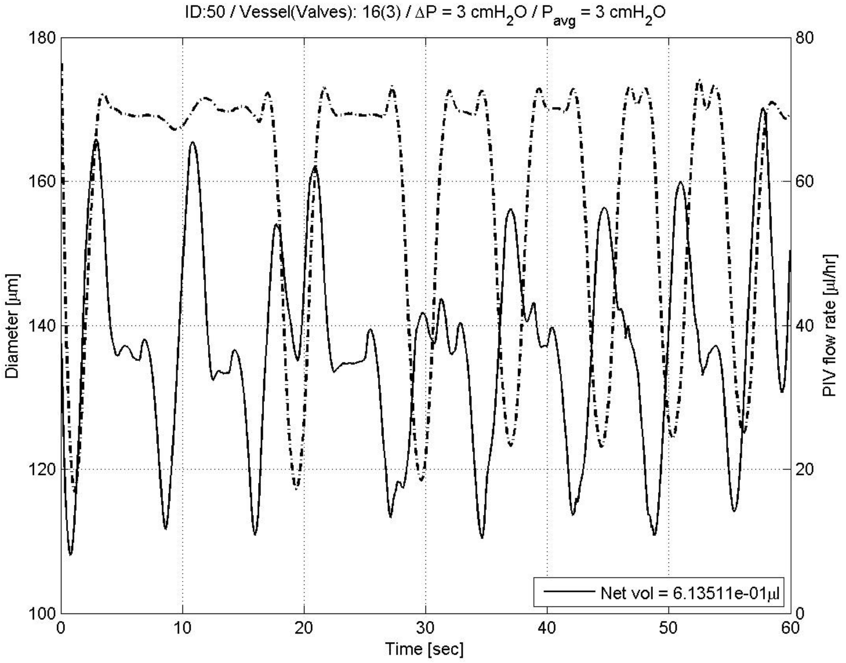

(a) Flow rate vs time and diameter vs time

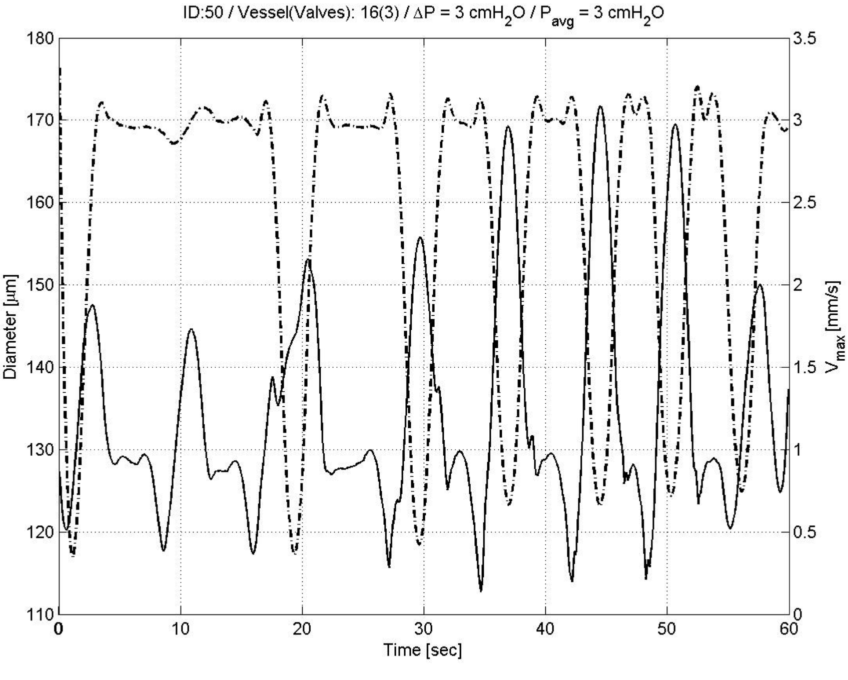

(b) Maximum velocity vs time and diameter vs time

Figure 3.5: Time plots of fluid parameters Flow rate (a), Maximum velocity (b) vs diameter (cont'd)

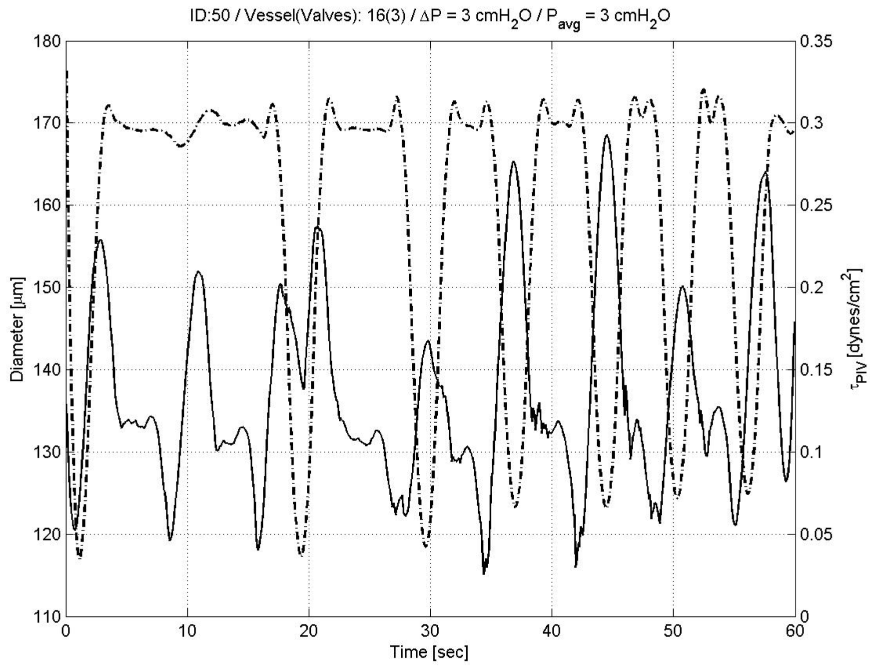

(c) PIV derived WSS vs time and diameter vs time

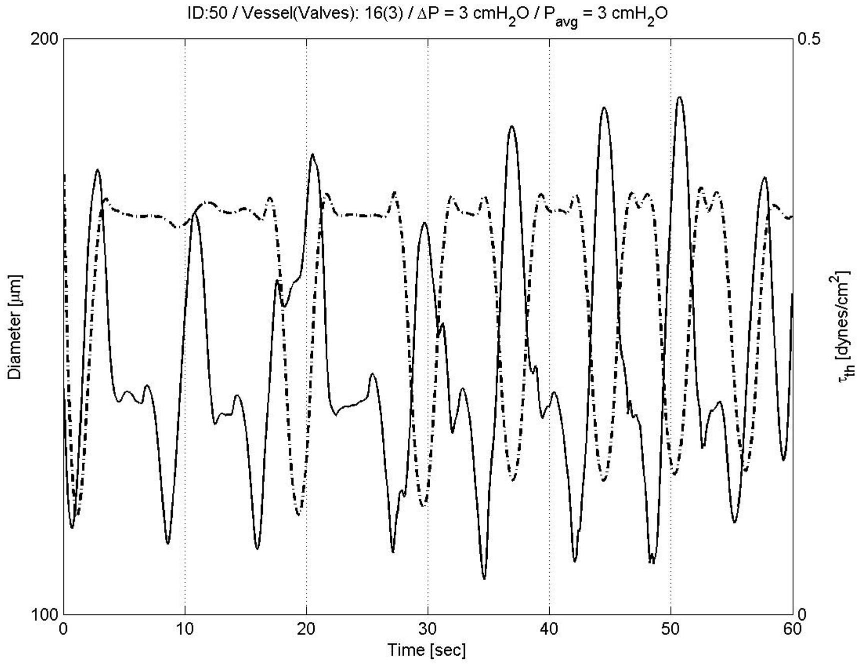

(d) Theoretical WSS vs time and diameter vs time

Figure 3.5: Time plots of fluid parameters PIV WSS (c), Theoretical WSS (d) vs diameter

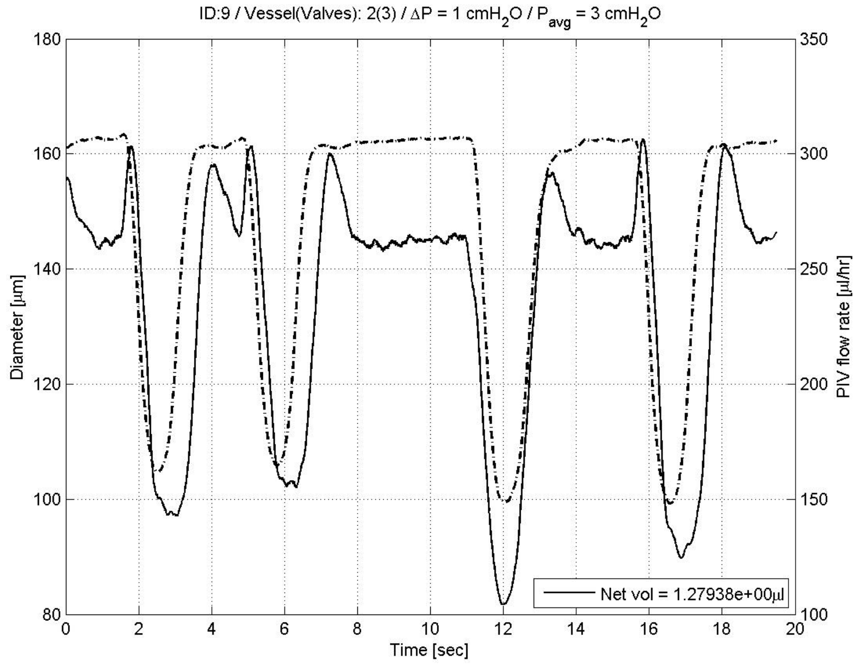

(a) Flow rate vs time and diameter vs time

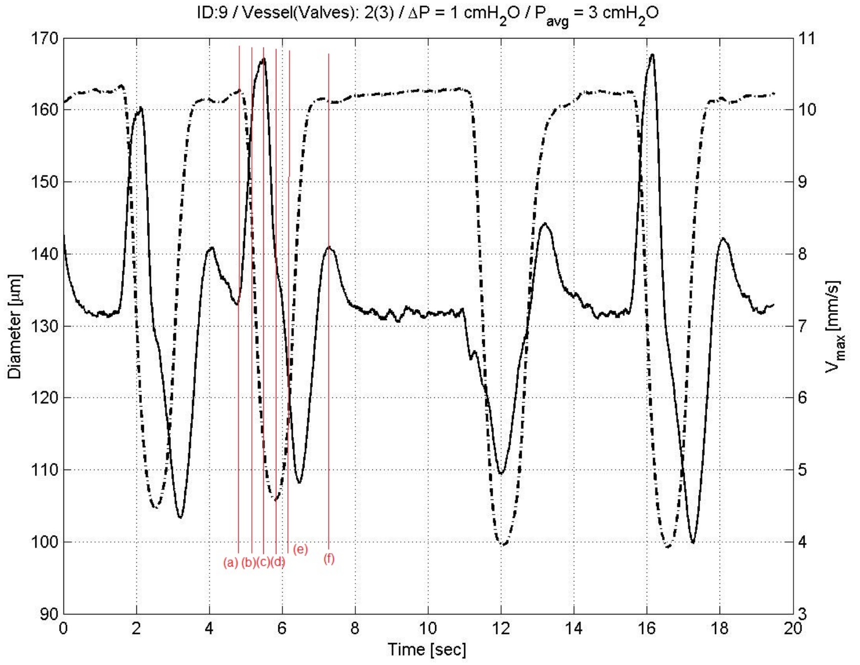

(b) Maximum velocity vs time and diameter vs time

Figure 3.6: Time plots of fluid parameters Flow rate (a), Maximum velocity (b) vs diameter (cont'd)

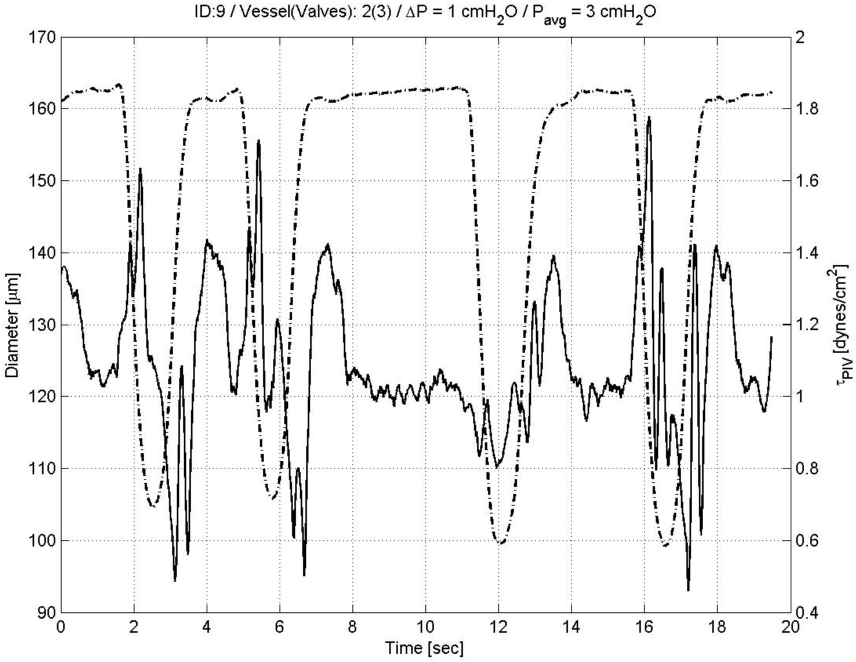

(c) PIV derived WSS vs time and diameter vs time

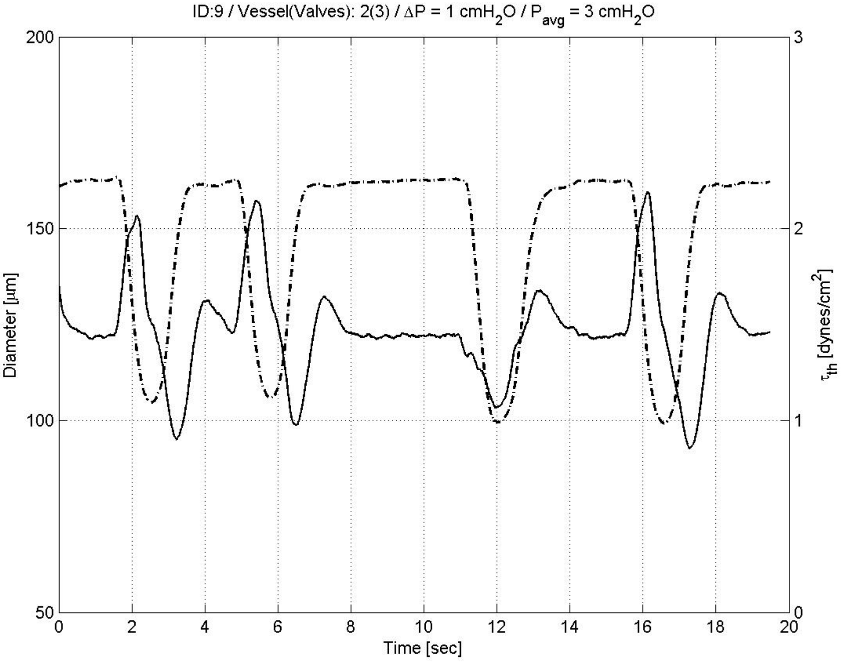

(d) Theoretical WSS vs time and diameter vs time

Figure 3.6: Time plots of fluid parameters PIV WSS (c), Theoretical WSS (d) vs diameter

Figure 3.7 shows the magnitude of the velocity within the same lymphangion as Figure 3.6, during a contraction cycle. In Figure 3.7a the vessel is at the EDD and the maximum velocity is approximately 7 mm/s. As the contraction starts, velocity increases (Figure 3.7b). Contraction continues and the velocity continues to increase (Figure 3.7c). Velocity magnitude then drops as contraction continues towards the ESD (Figure 3.7d). During distension flow velocity increases again (Figure 3.7e) towards the vessel EDD (Figure 3.7f).

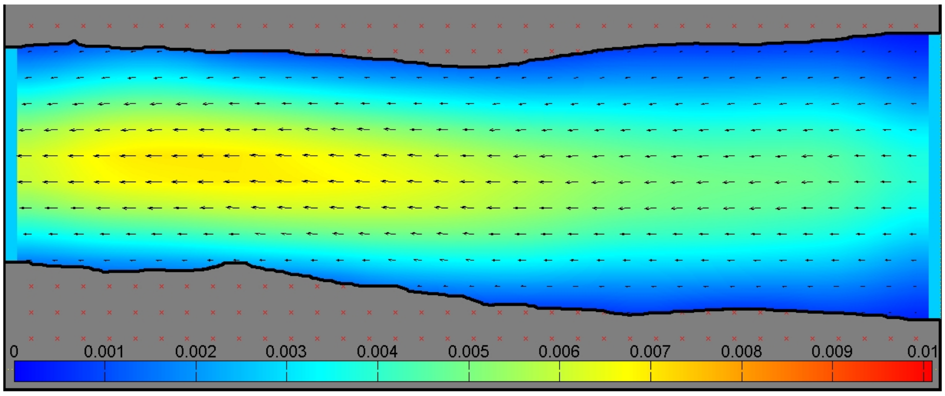

(a) Frame 605, time 4.8 s.

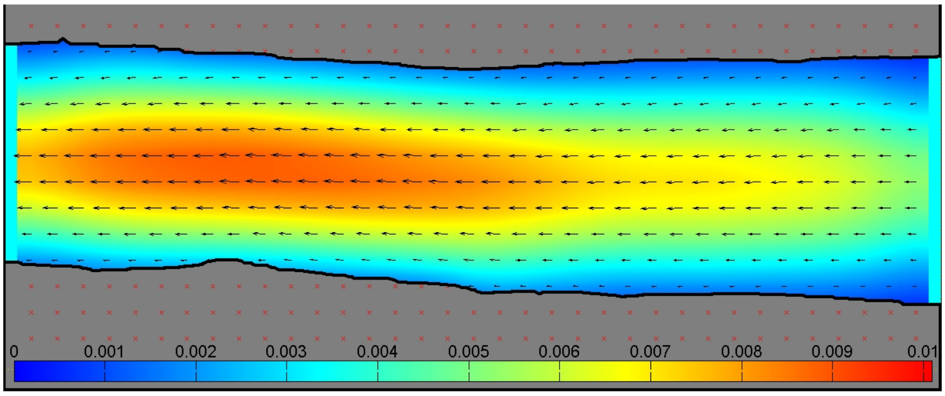

(b) Frame 633, time 5.1 s.

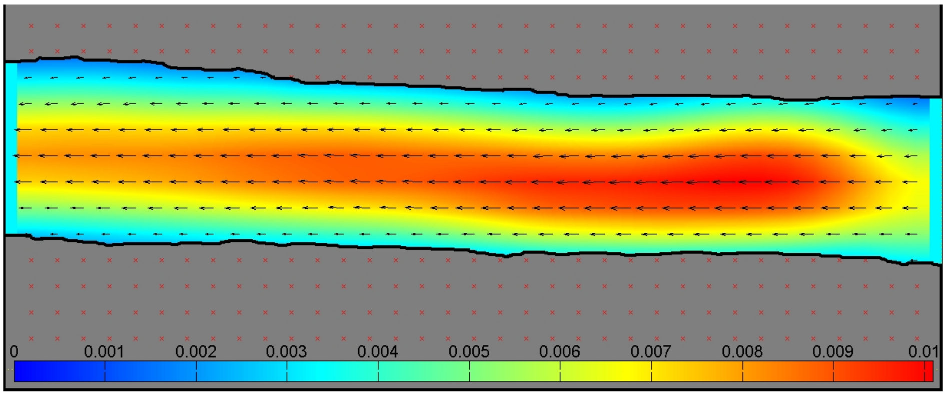

(c) Frame 685, time 5.5 s.

Figure 3.7: Velocity field during contraction at $\Delta P_{axial} = 1\, cmH_2O$. Scale in mm/s. Half the vectors are shown for clarity. Frames are also marked with a red line in Figure 3.6 (cont'd)

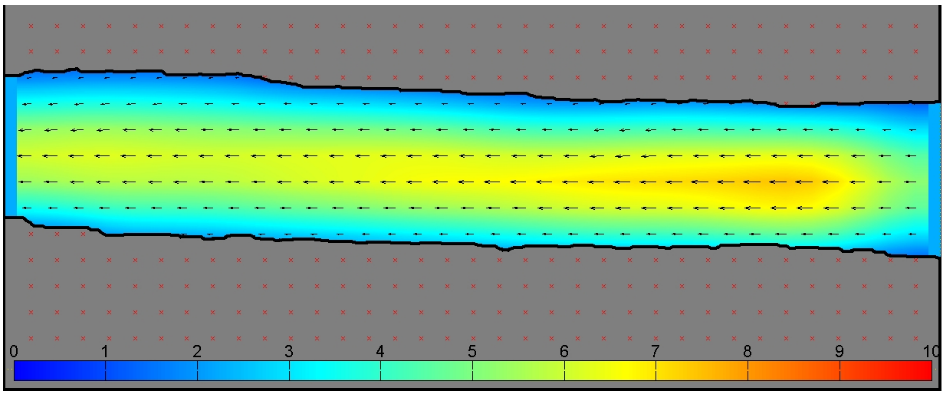

(d) Frame 721, time 5.8 s.

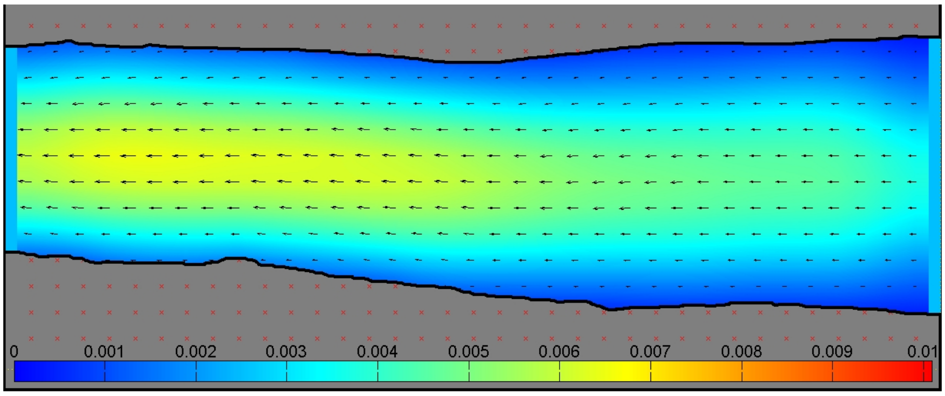

(e) Frame 857, time 6.2 s.

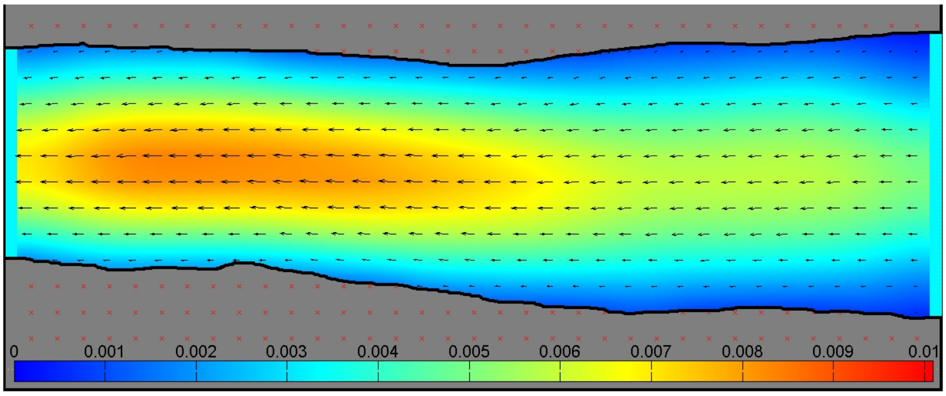

(f) Frame 910, time 7.3 s.

Figure 3.7: Velocity field during contraction at $\Delta P_{axial} = 1\ cmH_2O$. Scale in m/s. Half the vectors are shown for clarity. Frames are also marked with a red line in Figure 3.6

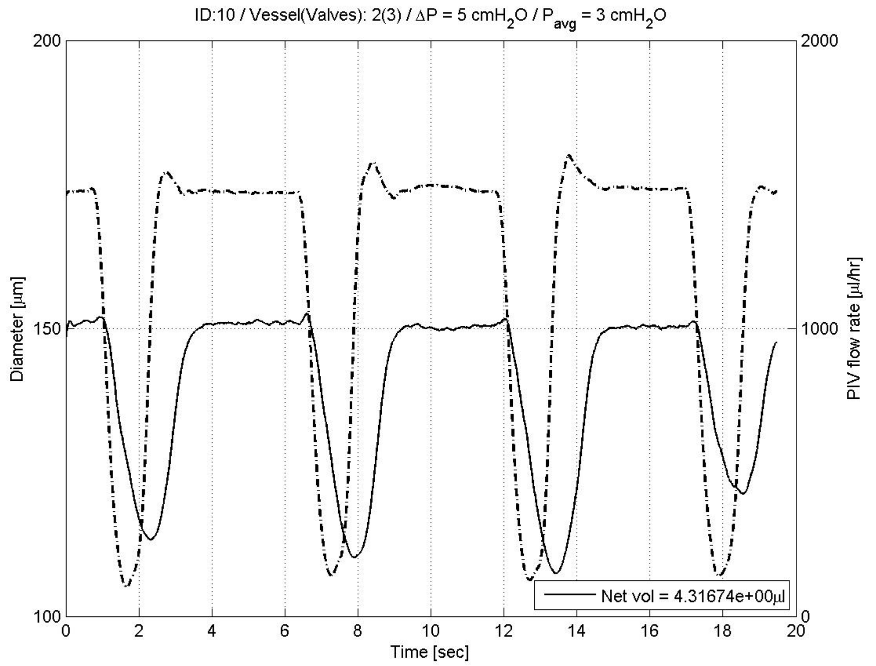

(a) Flow rate vs time and diameter vs time

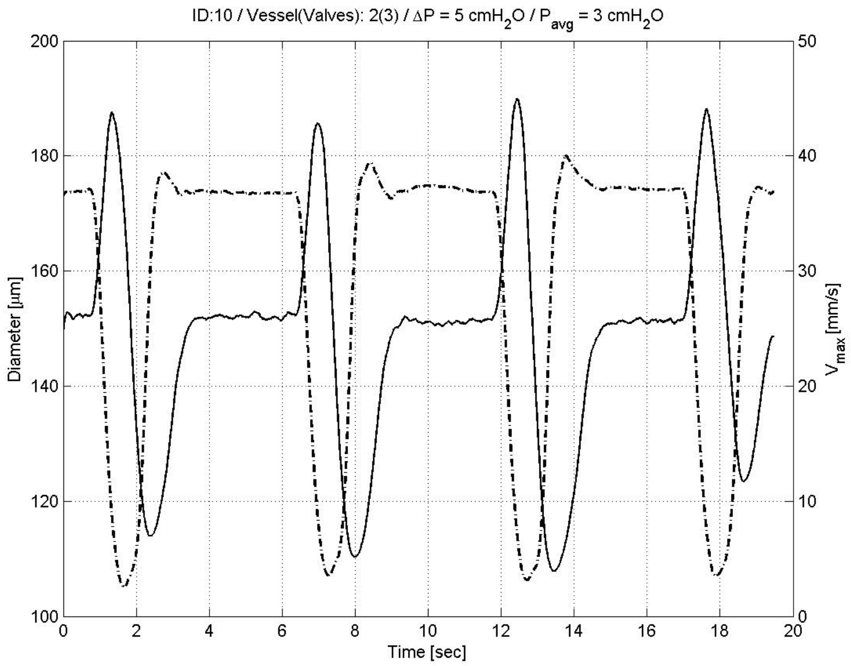

(b) Maximum velocity vs time and diameter vs time

Figure 3.8: Time plots of fluid parameters Flow rate (a), Maximum velocity (b) vs diameter (cont'd)

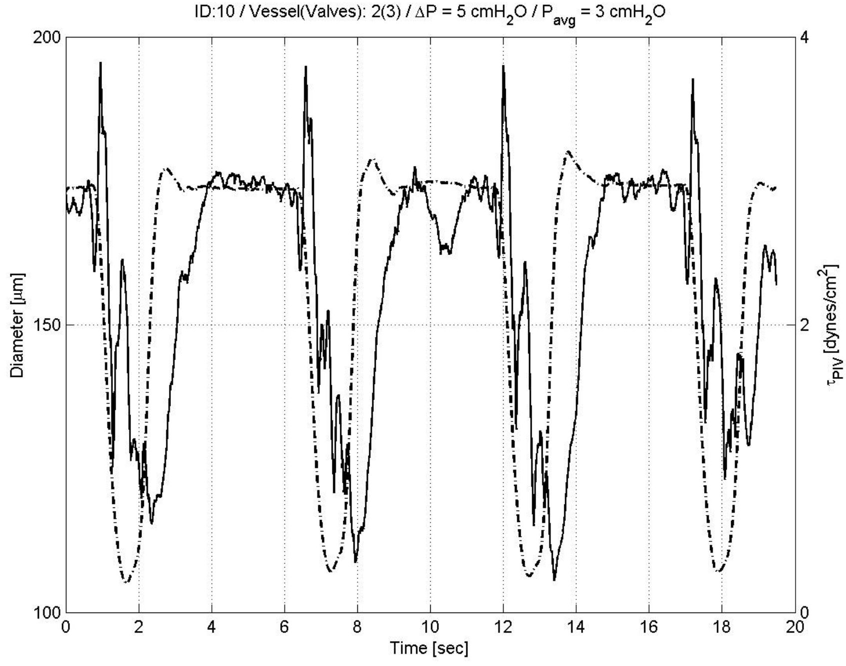

(c) PIV derived WSS vs time and diameter vs time

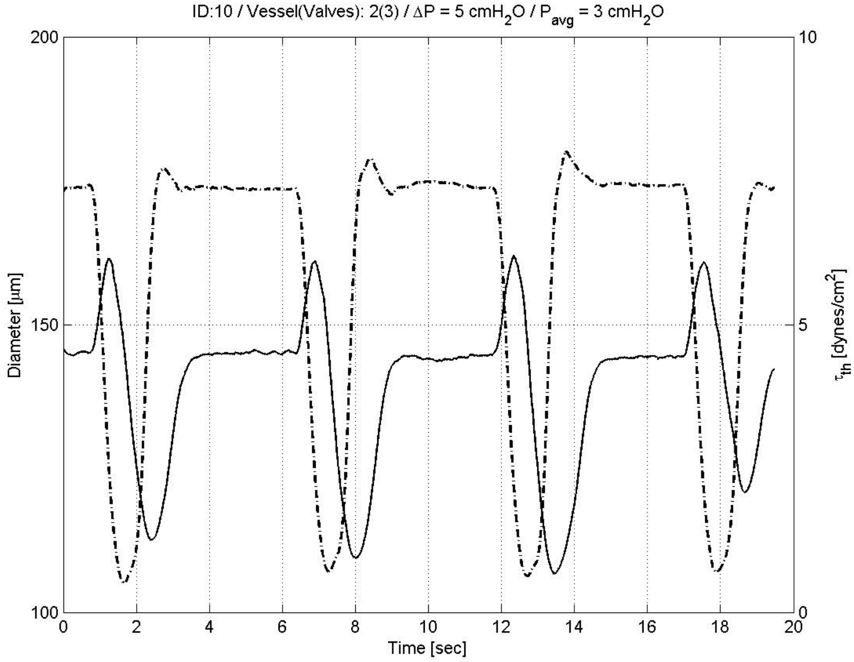

(d) Theoretical WSS vs time and diameter vs time

Figure 3.8: Time plots of fluid parameters PIV WSS (c), Theoretical WSS (d) vs diameter

3.2.2 Flow with no axial pressure gradient

Figures 3.9 to 3.11 show the flow rate, velocity and WSS when input and output pressures are set equal. The temporal variation of these flow quantities in this case change in comparison with the results of the previous section. The fluid is stationary for most of the contraction cycle and positive flow rate occurs for a short period of time and in certain cases positive flow occurs only during the vessel passive distention (figure 3.9a). This is not a general case, however, as is displayed in figures 3.10a and 3.11a. Inspection of the latter figure reveals that, in this case, that largest amount of fluid volume is propelled during the distention phase, with the positive flow rate during contraction been slightly smaller.

As in the previous section, contraction is associated with velocity increase. Whether the flow rate increases during contraction depends on the increase of vessel resistance due to the diameter reduction. PIV WSS appear again to be consistently lower than the theoretical ones.

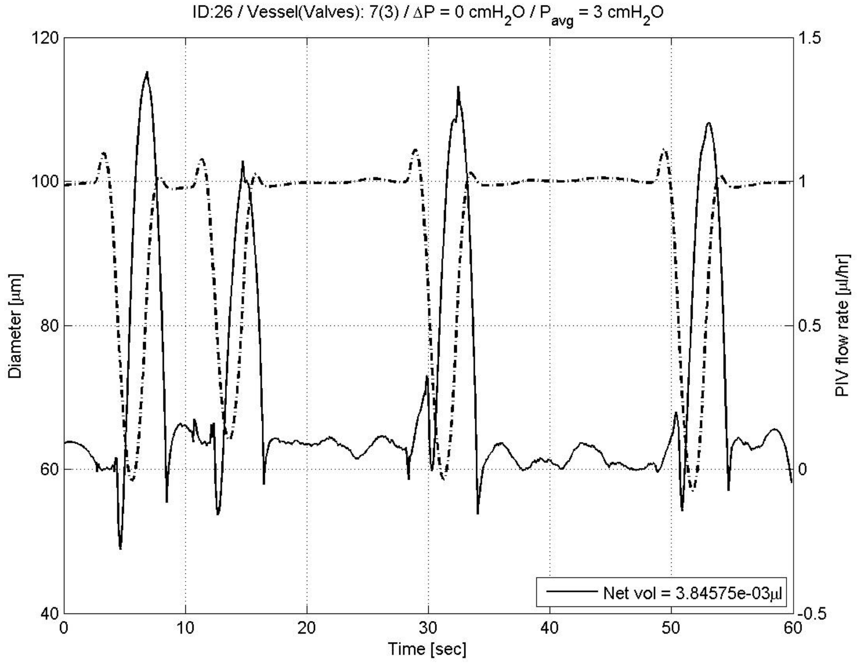

(a) Flow rate vs time and diameter vs time

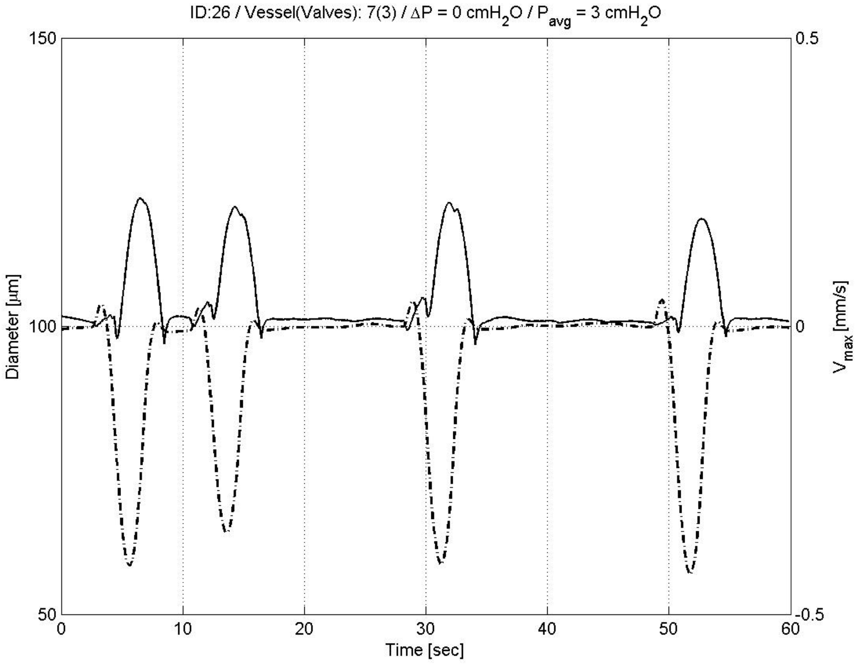

(b) Maximum velocity vs time and diameter vs time

Figure 3.9: Time plots of fluid parameters Flow rate (a), Maximum velocity (b) vs diameter (cont'd)

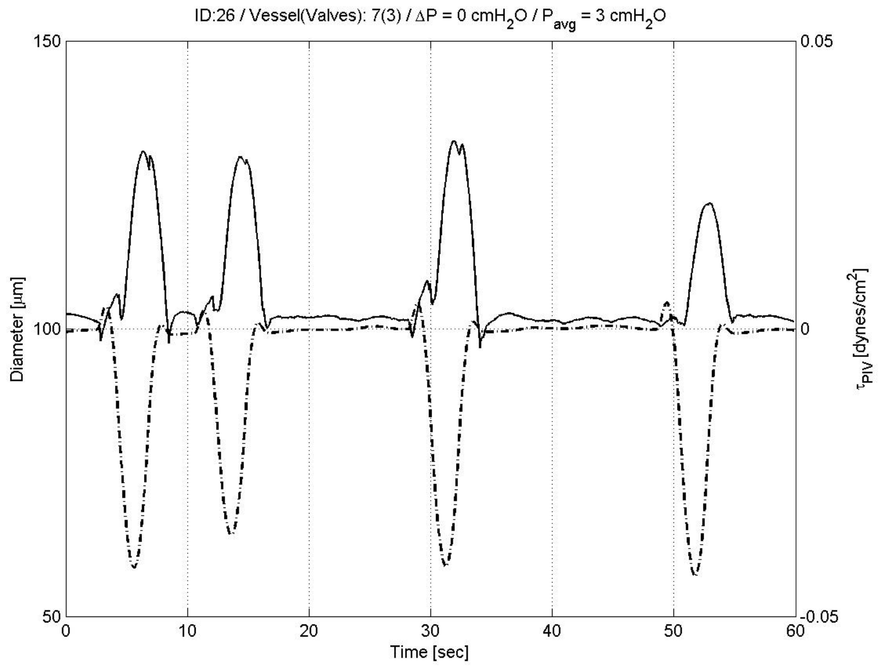

(c) PIV derived WSS vs time and diameter vs time

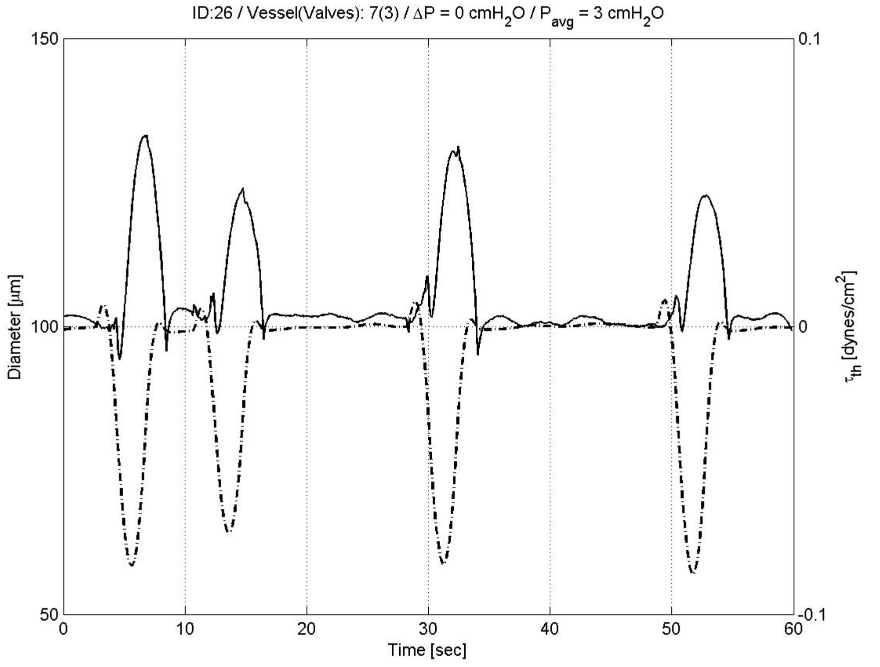

(d) Theoretical WSS and diameter vs time

Figure 3.9: Time plots of fluid parameters PIV WSS (c), Theoretical WSS (d) vs diameter

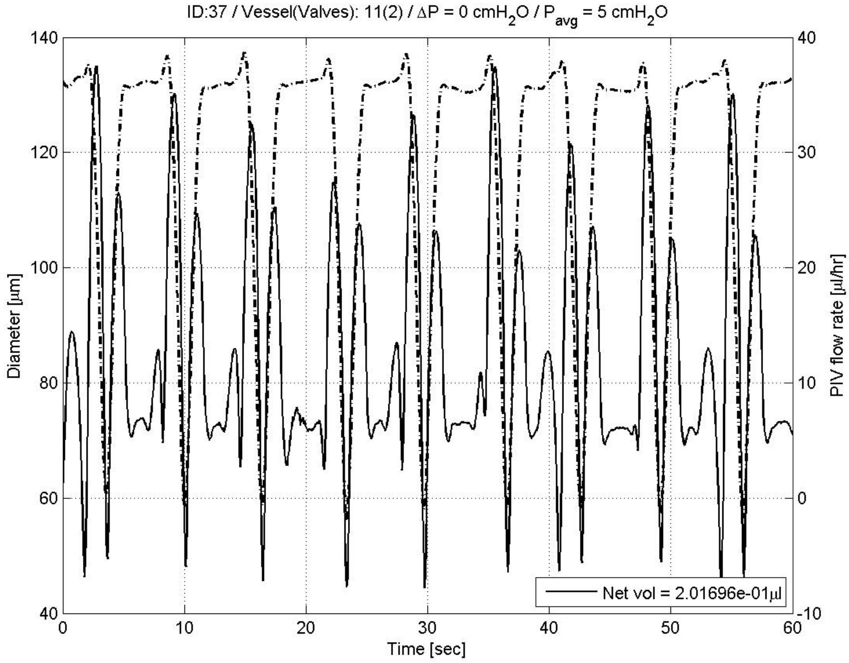

(a) Flow rate vs time and diameter vs time

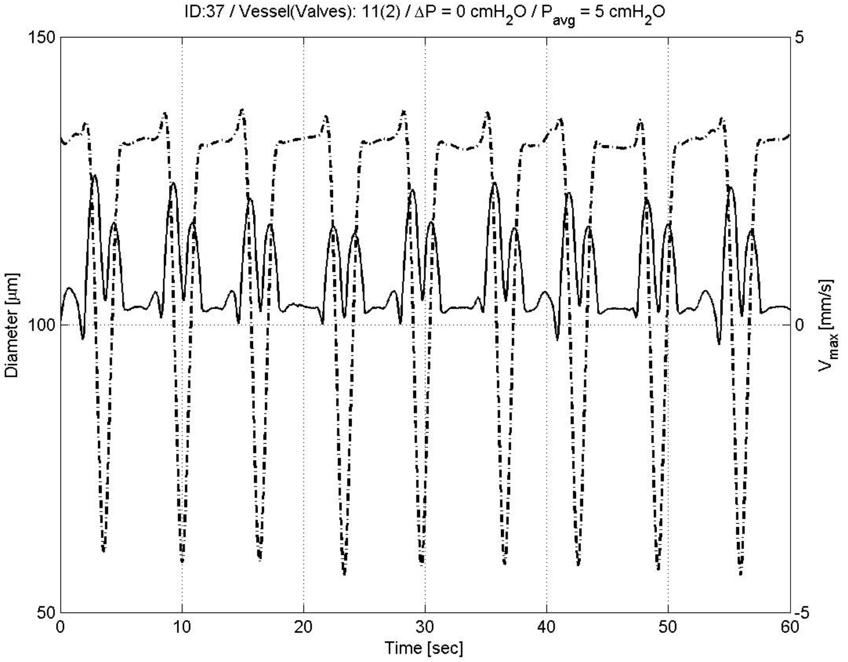

(b) Maximum velocity vs time and diameter vs time

Figure 3.10: Time plots of fluid parameters Flow rate (a), Maximum velocity (b) vs diameter (cont'd)

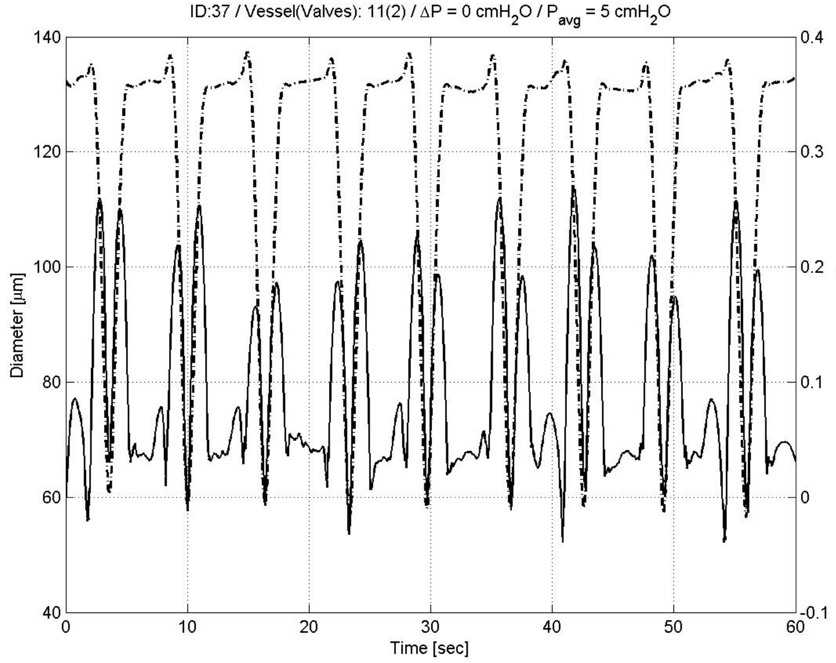

(c) PIV derived WSS vs time and diameter vs time

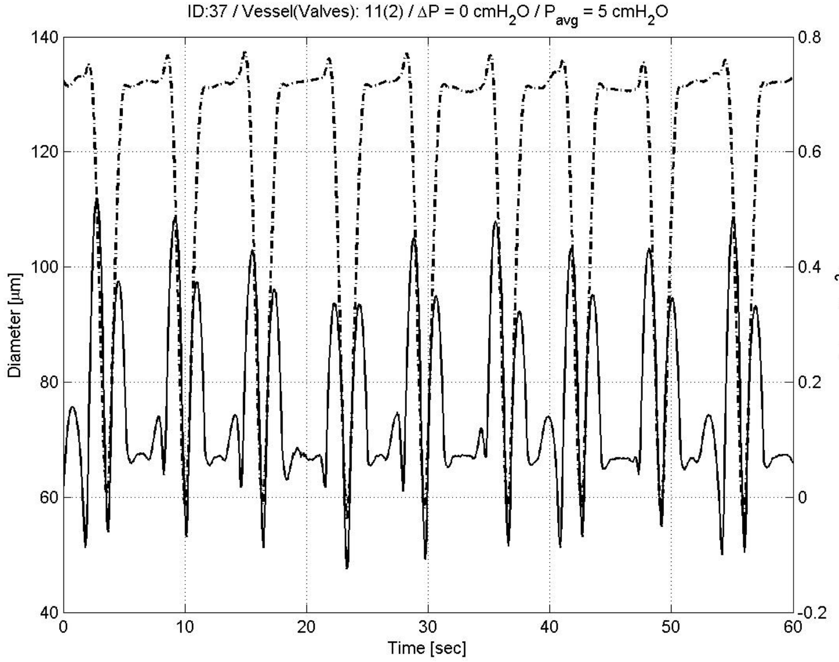

(d) Theoretical WSS vs time and diameter vs time

Figure 3.10: Time plots of fluid parameters PIV WSS (c), Theoretical WSS (d) vs diameter

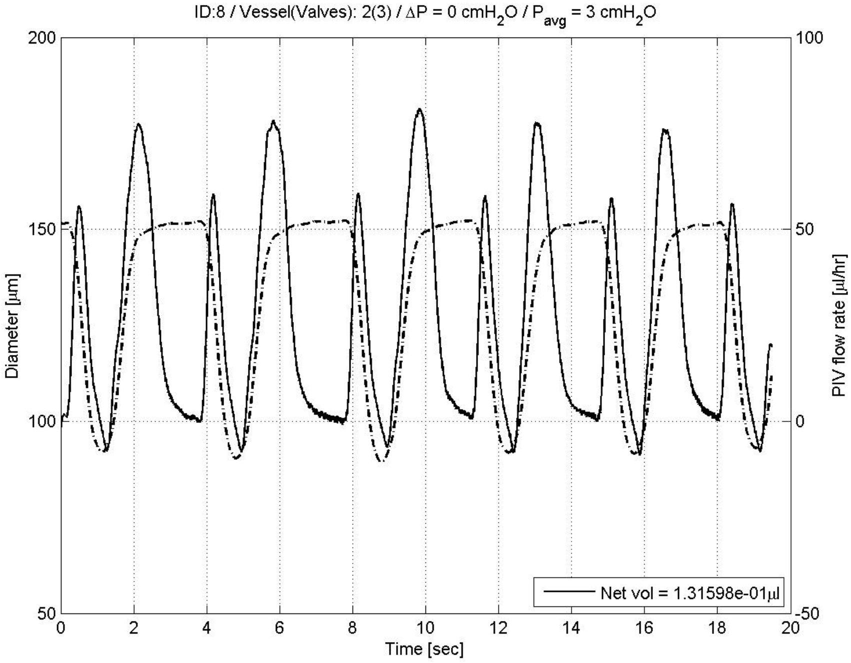

(a) Flow rate vs time and diameter vs time

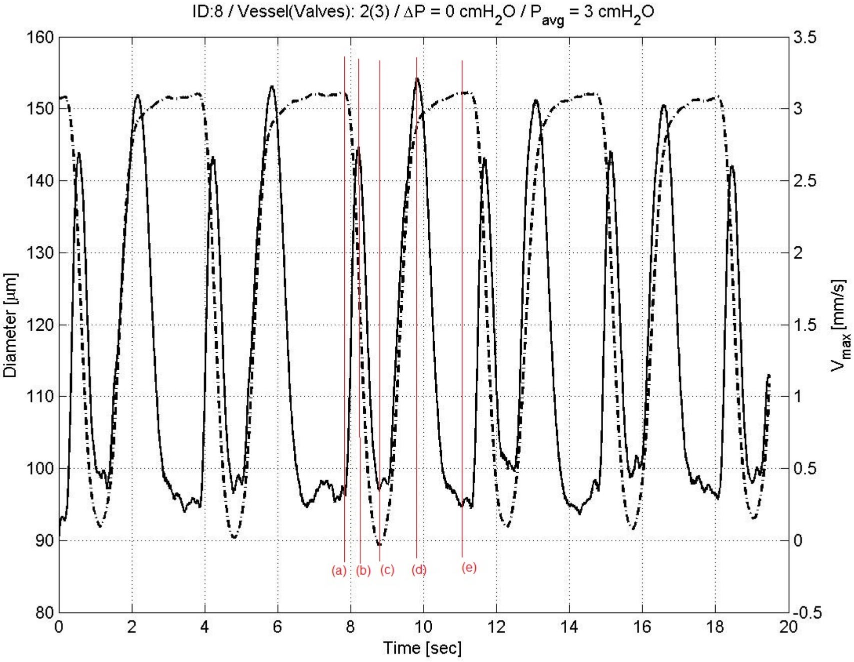

(b) Maximum velocity vs time and diameter vs time

Figure 3.11: Time plots of fluid parameters Flow rate (a), Maximum velocity (b) vs diameter (cont'd)

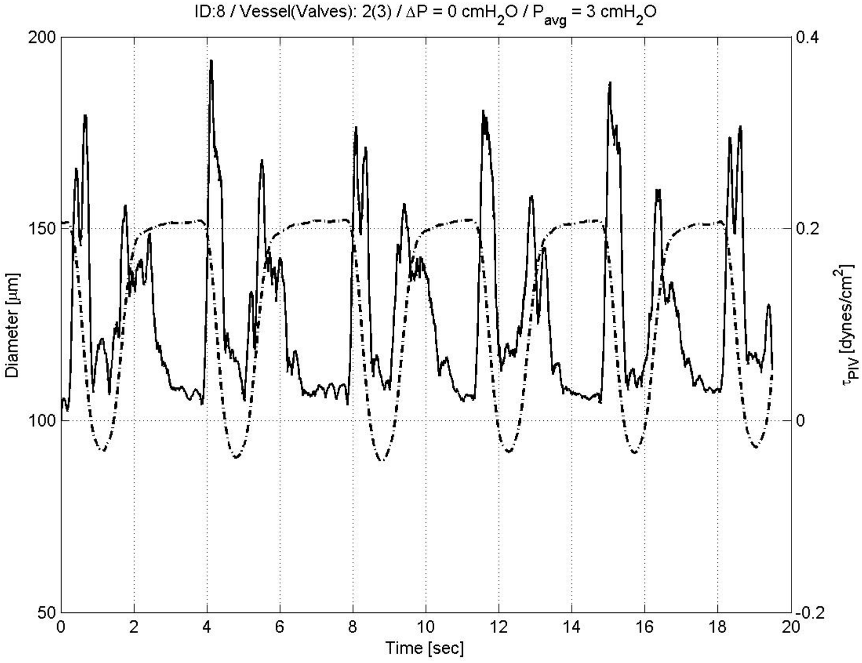

(c) PIV derived WSS vs time and diameter vs time

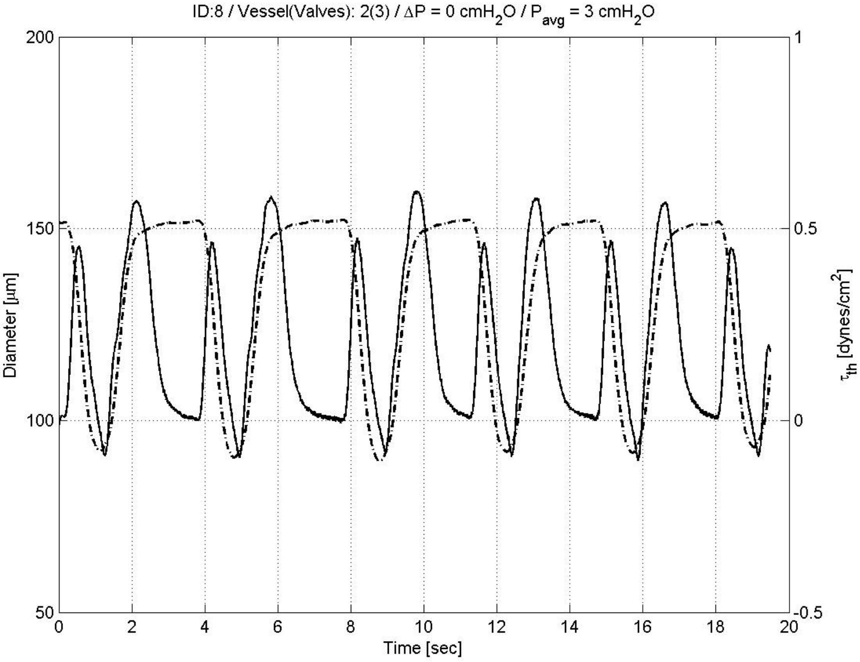

(d) Theoretical WSS vs time and diameter vs time

Figure 3.11: Time plots of fluid parameters PIV WSS (c), Theoretical WSS (d) vs diameter

Figure 3.12 shows the magnitude of the velocity within the same lymphangion as Figure 3.11, during a contraction cycle. In Figure 3.12a the vessel is at the EDD and velocity is zero since the axial pressure gradient is zero, as well. As the contraction starts, velocity attains the maximum value, shown in Figure 3.12b. Contraction continues but the velocity drops to zero as the vessel reaches the ESD, due to the increase in flow resistance (Figure 3.12c). During distension flow velocity increases again briefly (Figure 3.12d) but starts to drop again and as the vessel reaches the EDD, velocity becomes zero (Figure 3.12e).

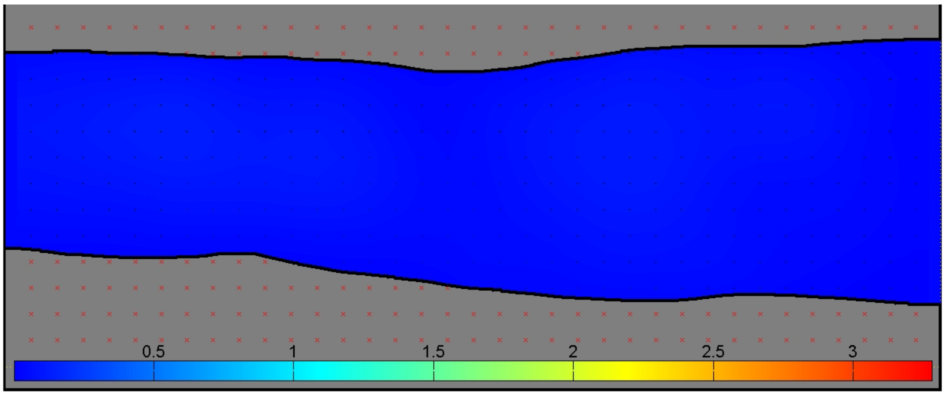

(a) Frame 966, time 7.8 s.

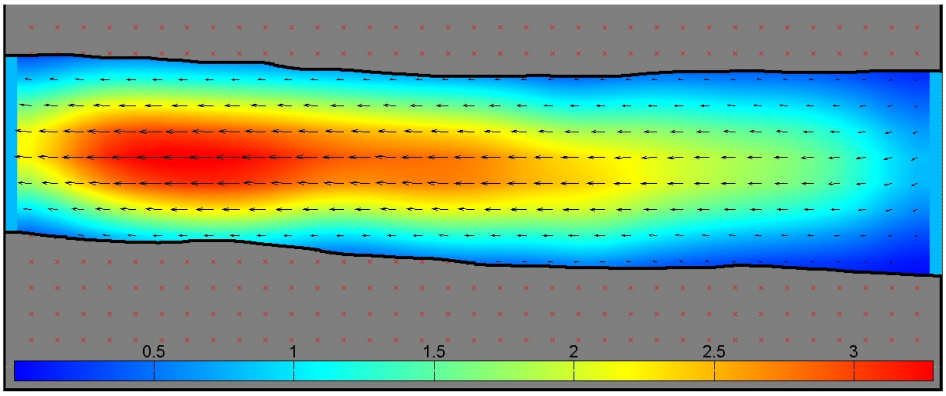

(b) Frame 1022, time 8.2 s.

Figure 3.12: Velocity field during contraction at $\Delta P_{axial} = 0$. Scale in mm/s. Half the vectors are shown for clarity. Frames are also marked with a red line in Figure 3.11 (cont'd)

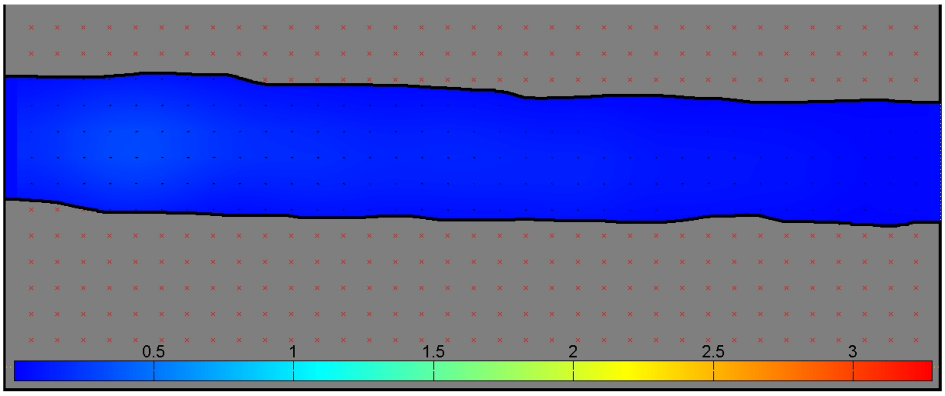

(c) Frame 1120, time 8.8 s.

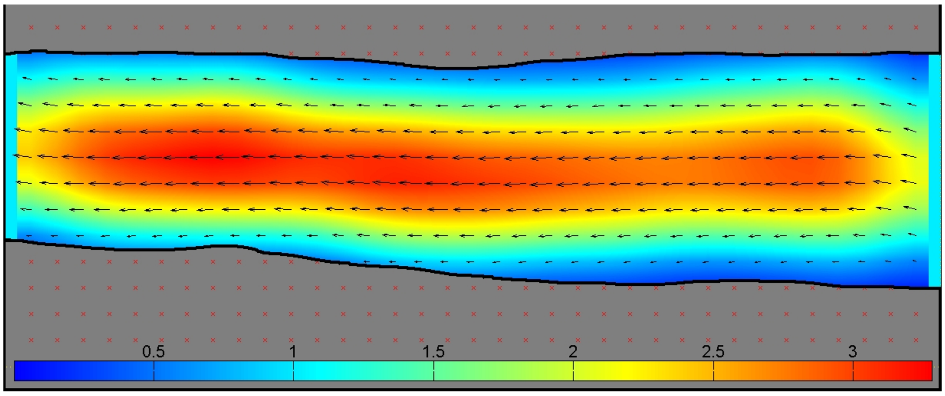

(d) Frame 1218, time 9.9 s.

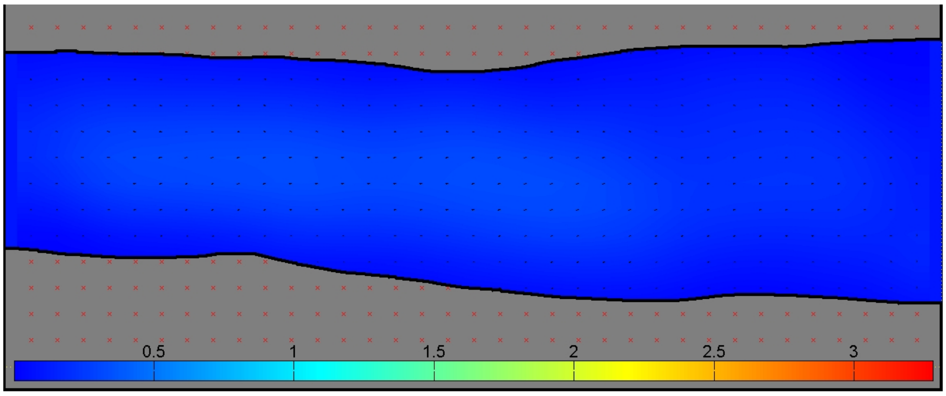

(e) Frame 1390, time 11 s.

Figure 3.12: Velocity field during contraction at $\Delta P_{axial} = 0$. Scale in mm/s. Half the vectors are shown for clarity. Frames are also marked with a red line in Figure 3.11.

3.2.3 Flow under adverse pressure gradient

Figures 3.13 to 3.16, show the flow rate, maximum velocity and WSS during lymphatic contraction at adverse pressure gradient. This hydrodynamic condition is thought to be the most frequently occurring in lymphatic vessels during physiological conditions and in the majority of different anatomical sites. An example is the lower limbs in humans [102, 103].

The flow rate waveform is similar to the one observed when no axial pressure gradient exists (section 3.2.2). Net flow occurs during vessel distension and during contraction (figure 3.13a). However, in figure 3.14a there is no positive net flow during contraction, but small negative back flow, with positive flow occurring during vessel distension only.

In Figure 3.16a a different temporal variations of flow rate is depicted. The distinctive plateau in the diameter is absent with positive flow rate occurring during contraction; during distension reverse flow occurs due to the negative pressure gradient, however, midway to the EDD the flow rate becomes positive. Prior to the vessel contraction sudden changes in flow rate are observed. Unfortunately, due to the FOV restrictions it is not possible to see the contractile state of adjacent lymphangions, or the open/close status of the valves, in order to find the underlying sources for these observations. PIV WSS are again lower than the theoretical value.

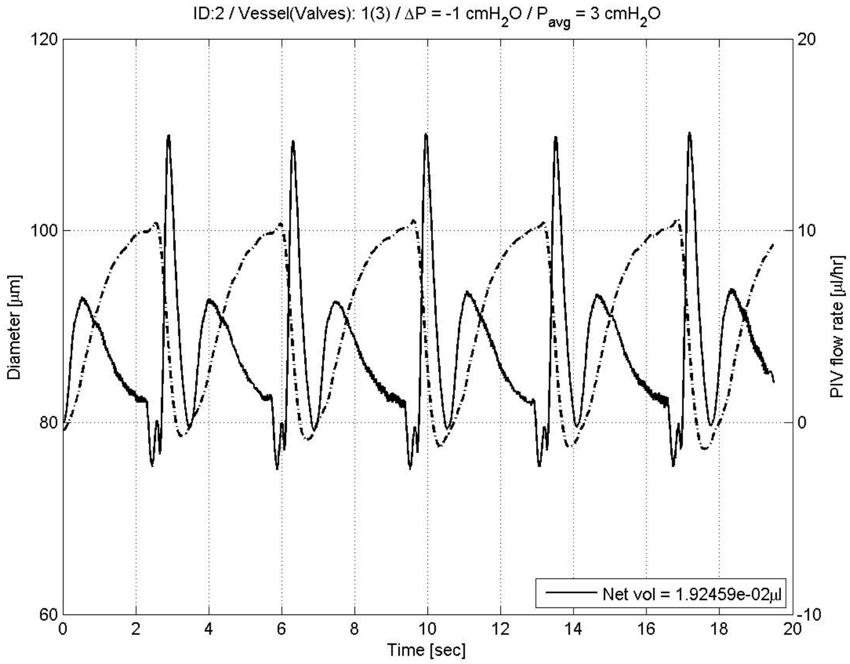

(a) Flow rate vs time and diameter vs time

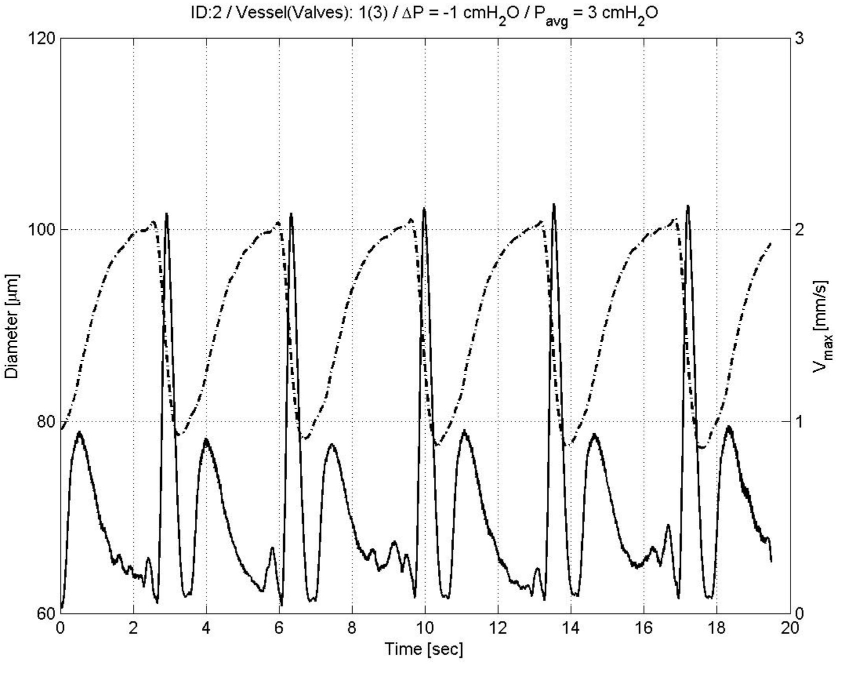

(b) Maximum velocity vs time and diameter vs time

Figure 3.13: Time plots of fluid parameters Flow rate (a), Maximum velocity (b) vs diameter (cont'd)

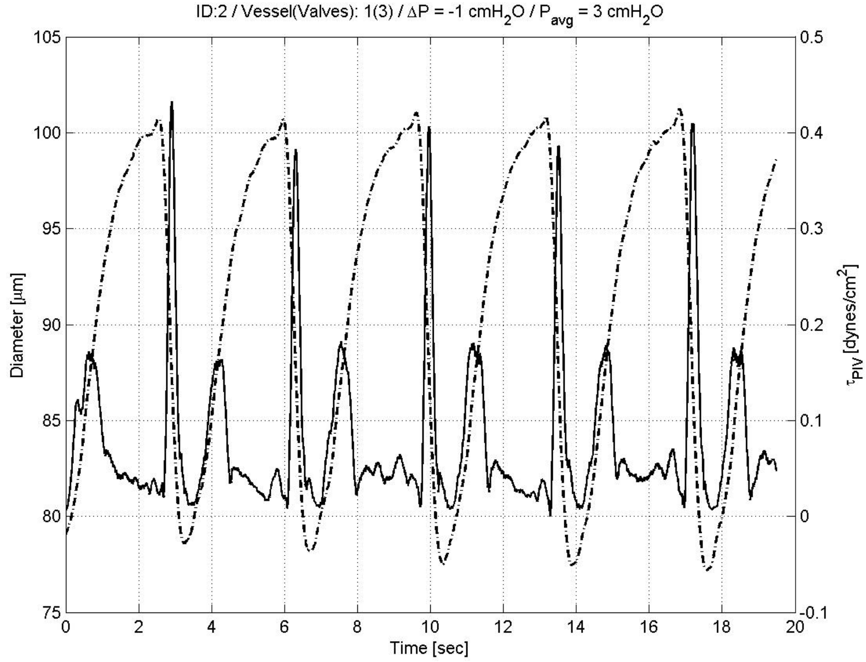

(c) PIV derived WSS vs time and diameter vs time

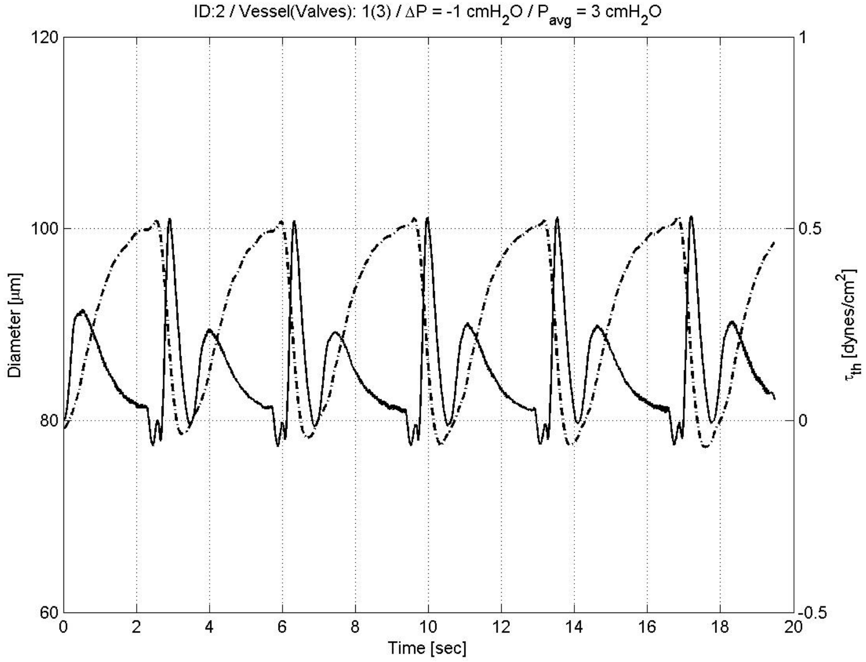

(d) Theoretical WSS vs time and diameter vs time

Figure 3.13: Time plots of fluid parameters PIV WSS (c), Theoretical WSS (d) vs diameter

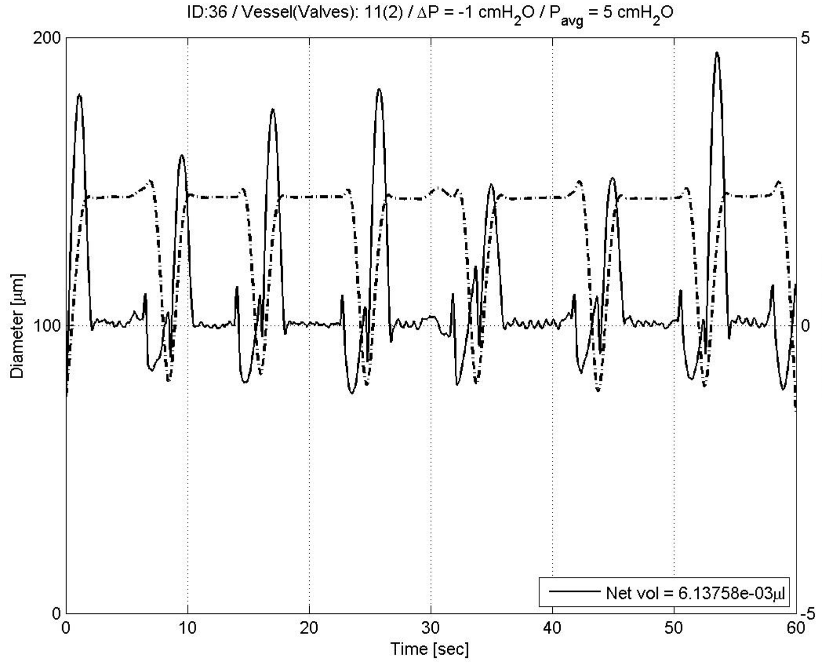

(a) Flow rate vs time and diameter vs time

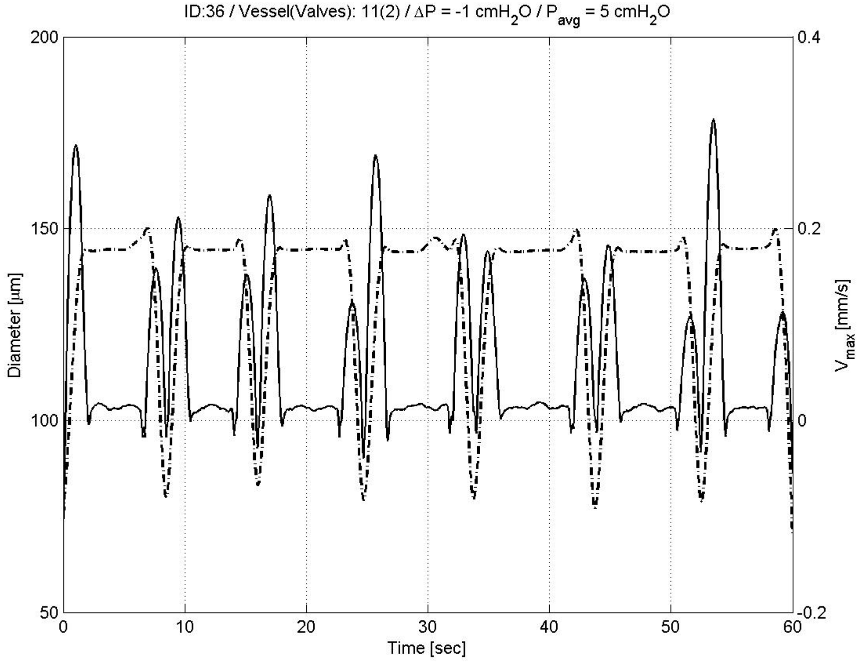

(b) Maximum velocity vs time and diameter vs time

Figure 3.14: Time plots of fluid parameters Flow rate (a), Maximum velocity (b) vs diameter (cont'd)

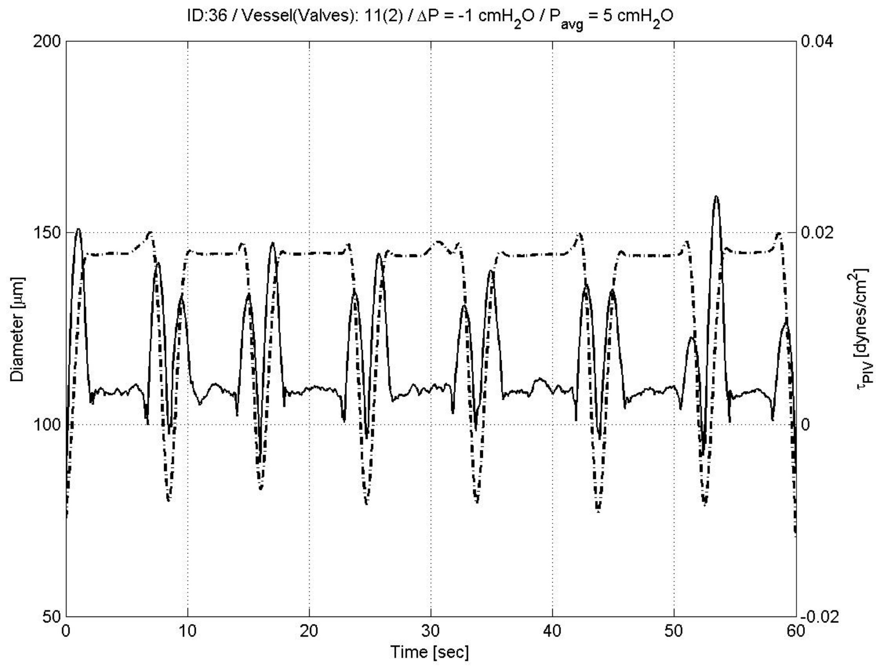

(c) PIV derived WSS vs time and diameter vs time

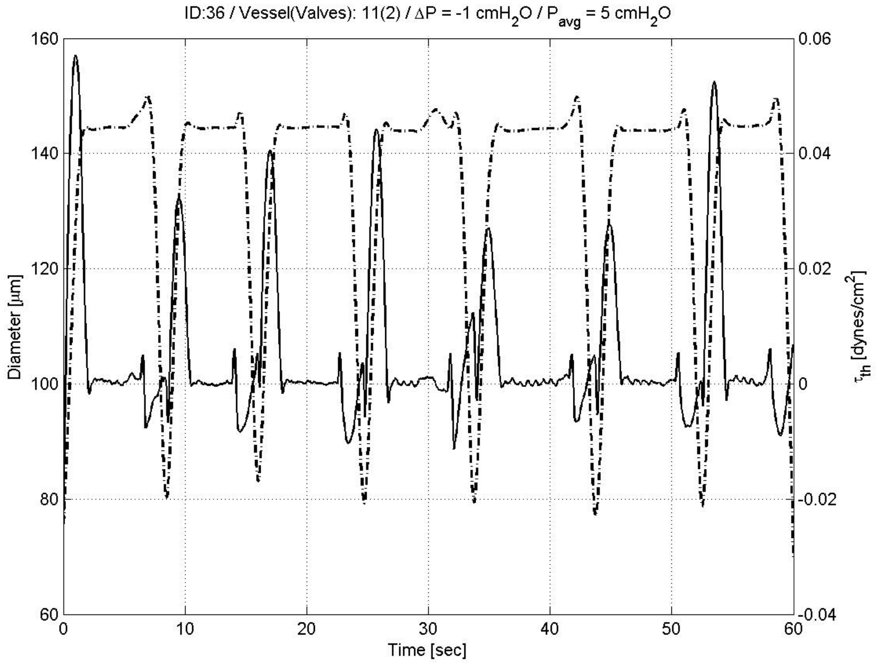

(d) Theoretical WSS vs time and diameter vs time

Figure 3.14: Time plots of fluid parameters PIV WSS (c), Theoretical WSS (d) vs diameter

Figure 3.15 shows the magnitude of the velocity within the lymphangion of Figure 3.14, during a contraction cycle. In Figure 3.15a the vessel is at the EDD and the velocity is zero, as there is the negative axial pressure gradient forces the upstream valve to close. As the contraction starts, velocity increases (Figure 3.15b). Contraction continues and the velocity becomes zero again due to the increase in flow resistance, as shown in Figure 3.15c) where the vessel is at the ESD. Velocity magnitude then rises as the vessel distends towards the EDD (Figure 3.15d). The increase in flow velocity during distenstion is only brief and rapidly drops to zero as the vessel reaches the EDD (Figure 3.15e).

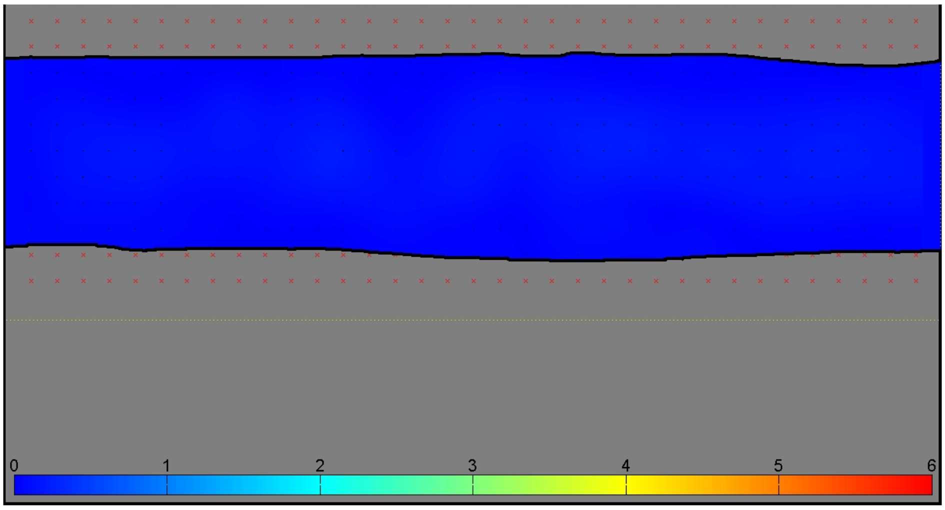

(a) Frame 469, time 23.2 s.

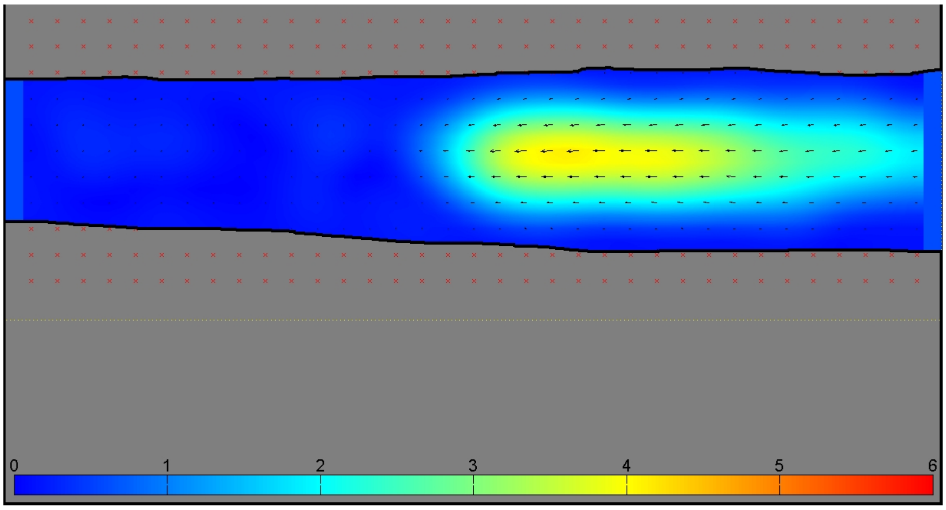

(b) Frame 480, time 23.9 s.

Figure 3.15: Velocity field during contraction at $\Delta P_{axial} = -1\, cmH_2O$. Scale in mm/s. Half the vectors are shown for clarity (cont'd)

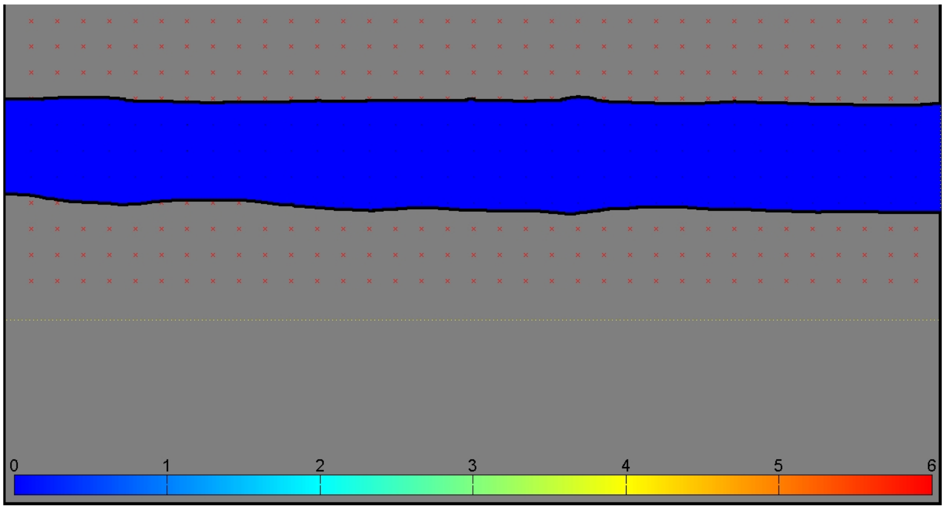

(c) Frame 492, time 24.7 s.

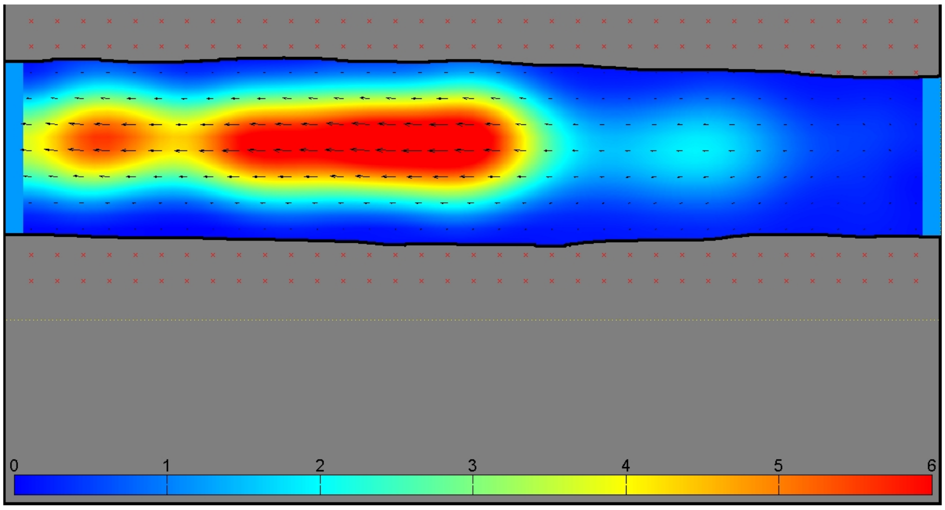

(d) Frame 515, time 25.7 s.

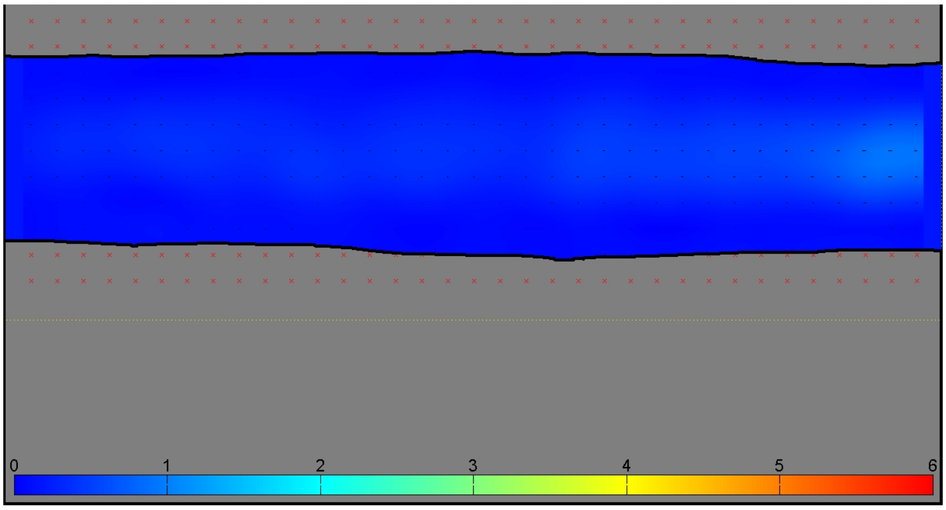

(e) Frame 528, time 26.5 s.

Figure 3.15: Velocity field during contraction at $\Delta P_{axial} = -1\ cmH_2O$. Scale in mm/s. Half the vectors are shown for clarity.

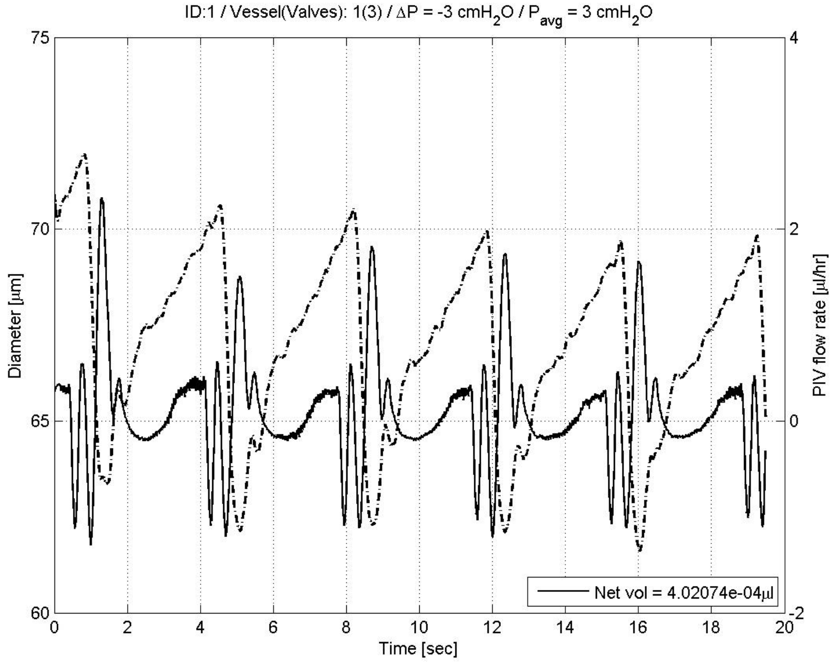

(a) Flow rate vs time and diameter vs time

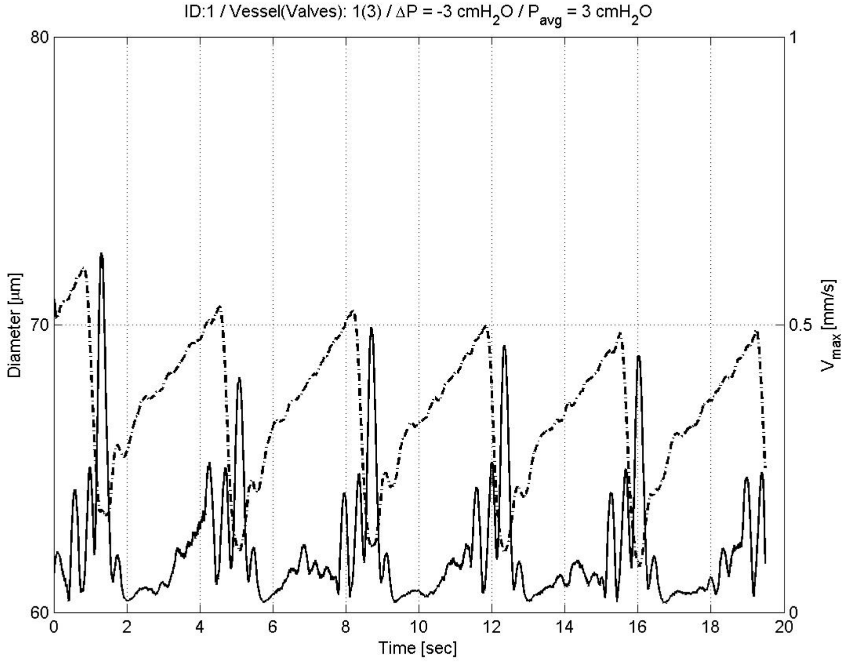

(b) Maximum velocity vs time and diameter vs time

Figure 3.16: Time plots of fluid parameters Flow rate (a), Maximum velocity (b) vs diameter (cont'd)

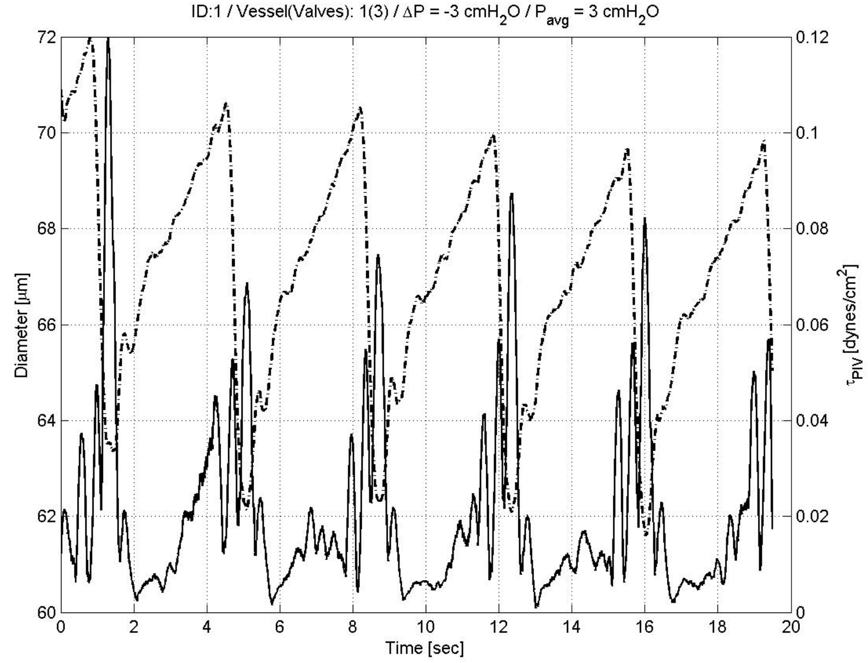

(c) PIV derived WSS vs time and diameter vs time

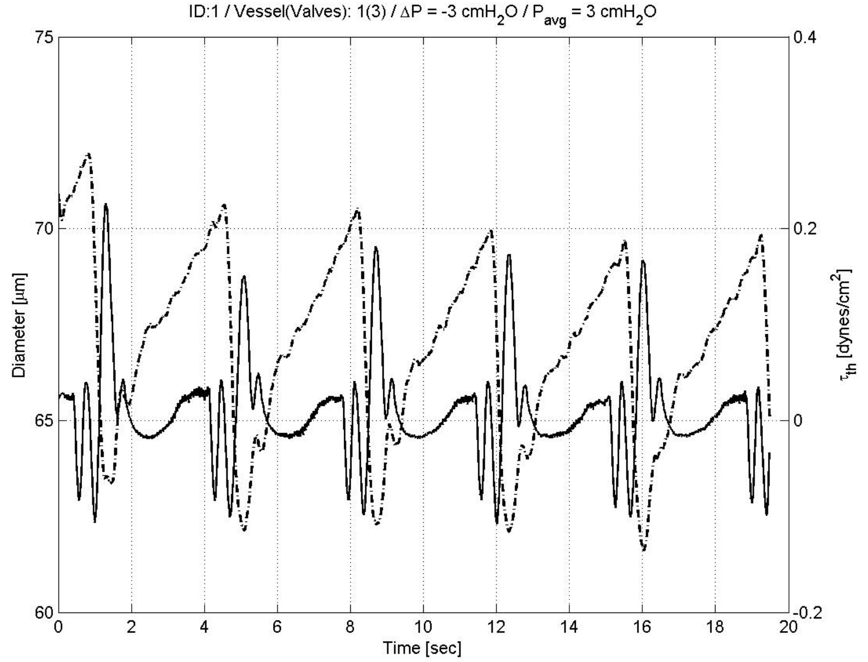

(d) Theoretical WSS vs time and diameter vs time

Figure 3.16: Time plots of fluid parameters PIV WSS (c), Theoretical WSS (d) vs diameter

3.3 Wall radial velocity

Figure 3.17 shows the diameter tracing and the ratio of wall radial to fluid velocity V_w/V_{fluid} for four different vessels at different hydrodynamic conditions. The wall radial velocity may exceed the fluid velocity during contraction.

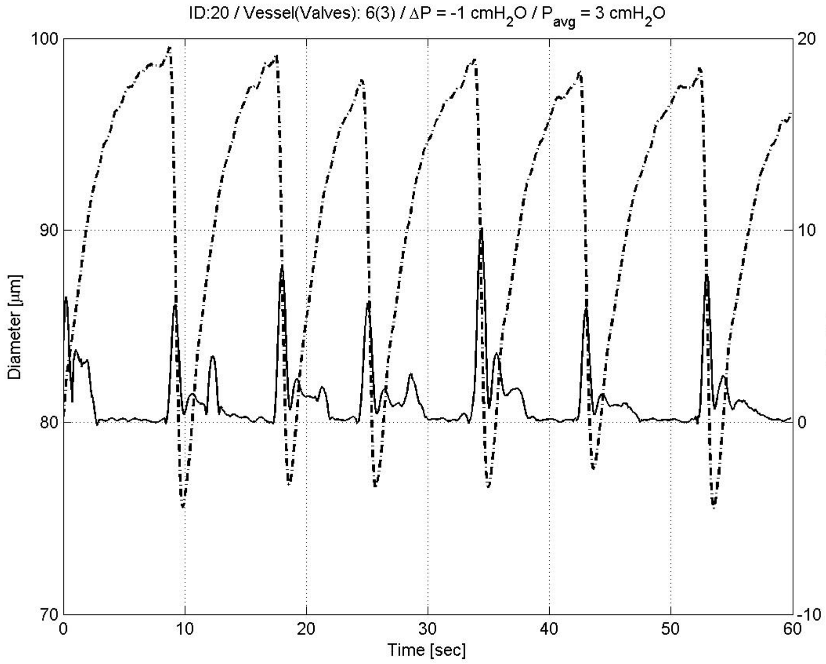

(a) Vessel at negative pressure gradient, where the wall velocity is greater than the fluid during contraction

Figure 3.17: Diameter tracing and wall-fluid velocity ratio for different hydrodynamic conditions. (cont'd)

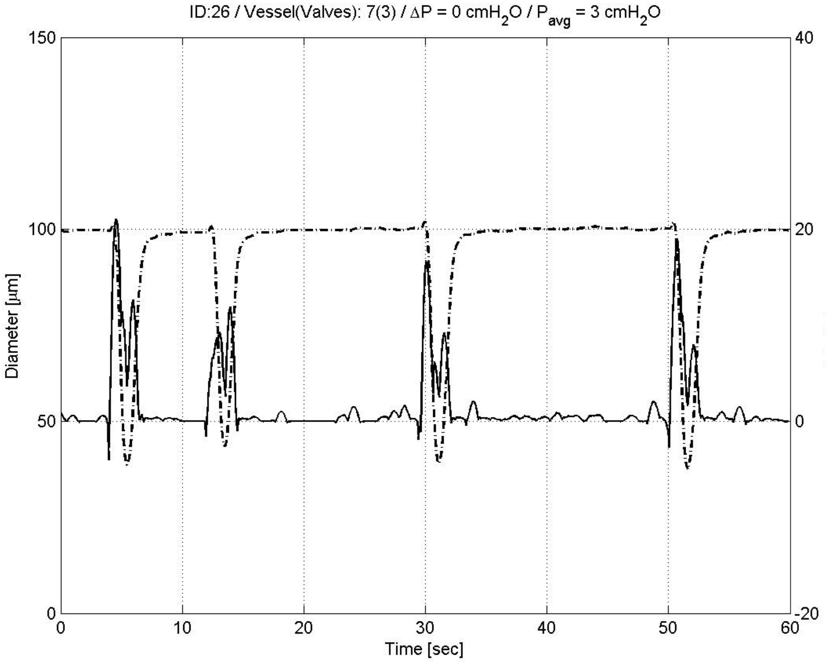

(b) At zero axial pressure gradient the wall velocity is again not negligible

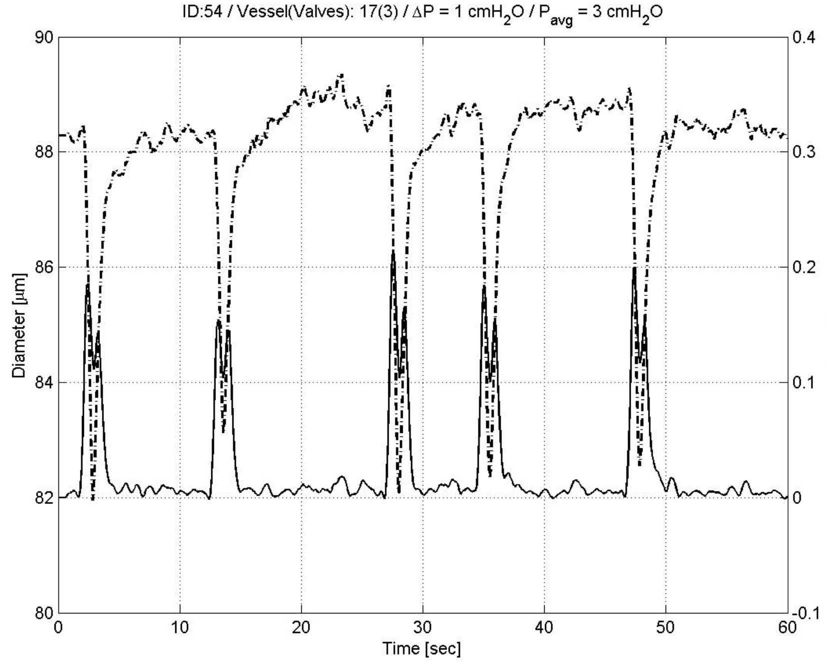

(c) The results of the previous subfigures cannot be generalised

Figure 3.17: Diameter tracing and wall-fluid velocity ratio for different hydrodynamic conditions.

3.4 Pressure estimation

This section presents Pressure-Time and Pressure-Volume curves during lymphatic contraction. The P-V figures show the positive work performed during lymphatic contraction, seen as the area contained within the P-V curves.[27] The shape, however, of the P-V curves does not appear to have a consistent shape.

The pressure vs time and P-V curve for flow driven by a favourable pressure gradient is shown in figure 3.18. The pressure curve exhibits two peaks, one during the vessel active contraction and a second during the passive distension. The dual peaks affect the shape of the P-V loop curve and cause the loop to intersect itself (figure 3.18b). This is in contrast with the P-V loops of the left ventricle of the heart found in physiology textbooks. However, it was found that the dual pressure peaks are not always present during the lymphangion contraction cycle.

Figures 3.19 and 3.20 are two representative P-t and P-V results for zero axial pressure gradient. Again the dual pressure peaks are observed in figure 3.19b, but are absent from figure 3.20b.

Finally, figures 3.20 and 3.22 show two representative cases for negative axial pressure gradient. Dual peaks may or may not be presented, and figure 3.21b also demonstrates that the P-V loop may not be self-intersecting, even in the presence of dual pressure peaks, depending on the relative height of each peak.

---

[27] The contraction cycle number is denoted on the header of the P-V figures. The cycle EF is also denoted in the header, while the work during the contraction cycle is denoted above the P-V curves

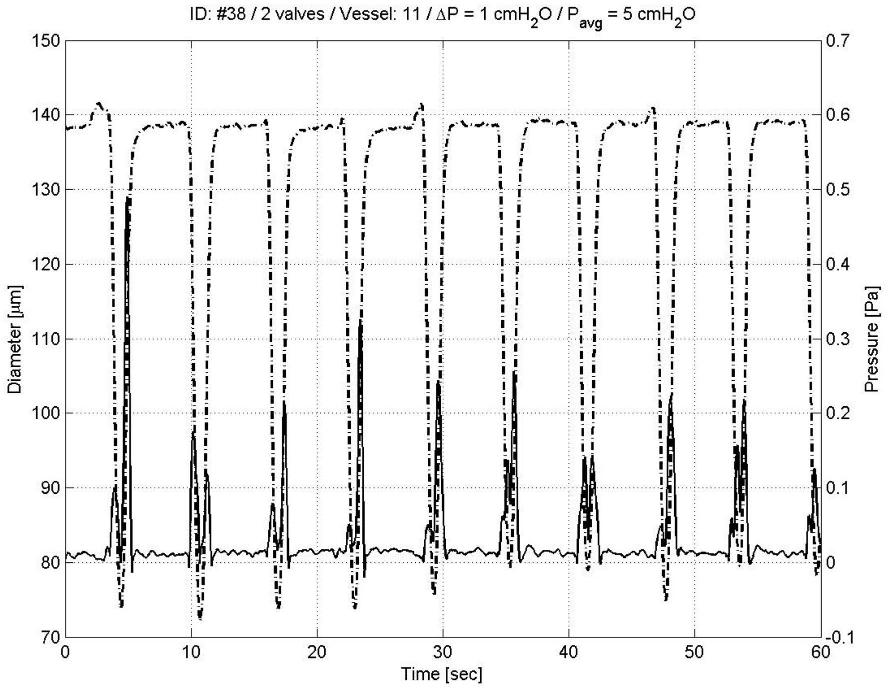

(a) Pressure and diameter vs time.

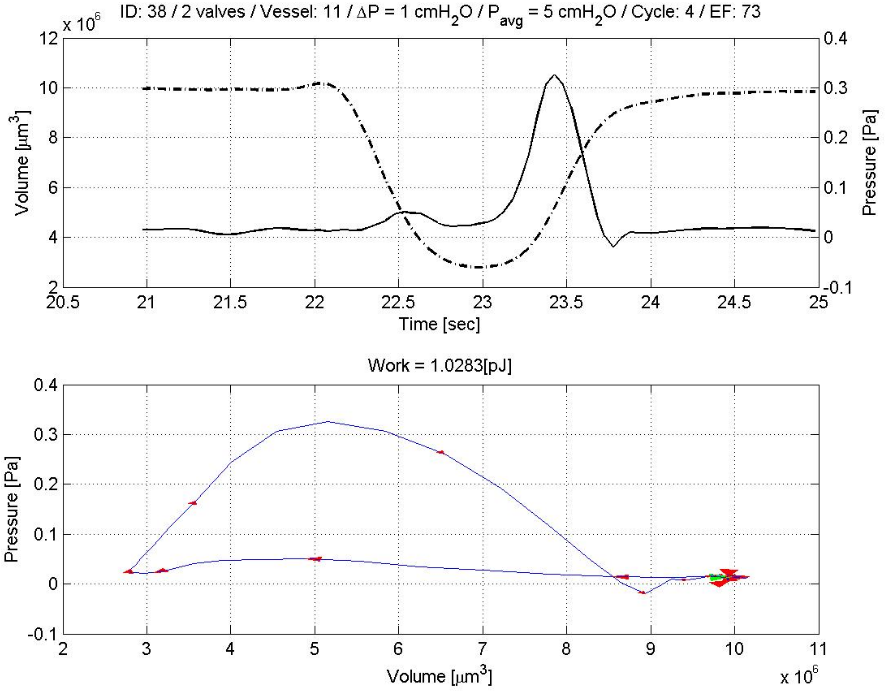

(b) P-V cycle. The two pressure peaks are the cause of the P-V loop self intersection.

Figure 3.18: Pressure-Time & Pressure-Volume relationships at positive ΔP_{axial}. Note that during the contraction cycle, two pressure peaks exist, one during contraction and one during distention.

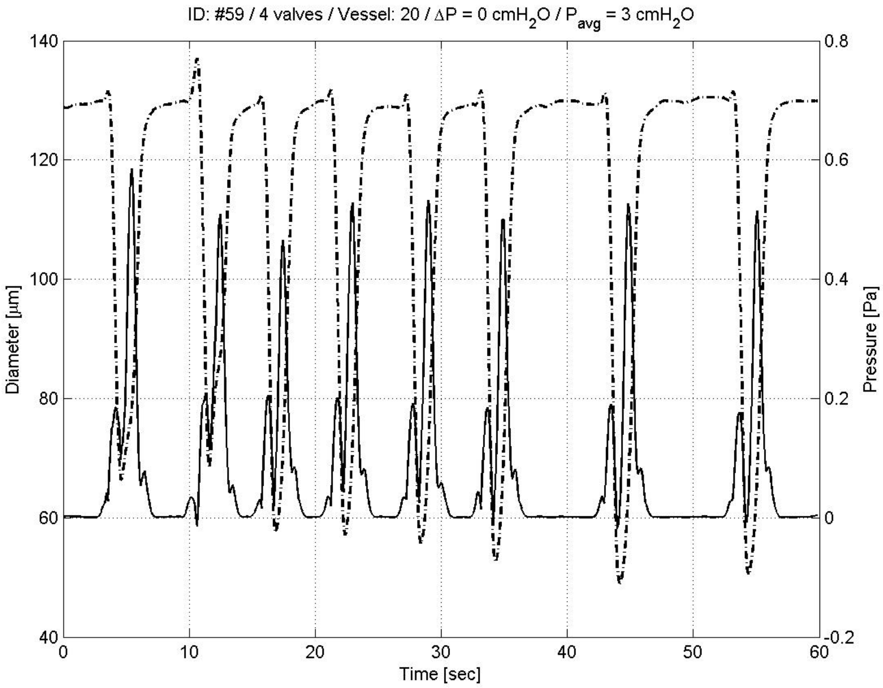

(a) Pressure and diameter vs time.

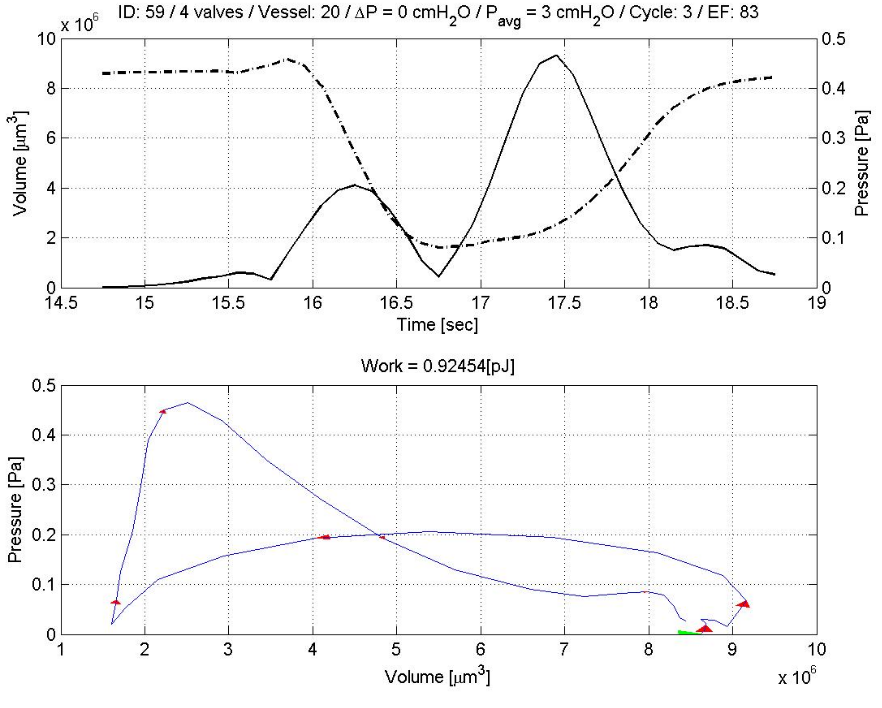

(b) P-V cycle. The P-V loop is again self-intersecting.

Figure 3.19: Pressure-Time & Pressure-Volume relationships at zero ΔP_{axial}. The dual pressure peaks are present in this case, as well.

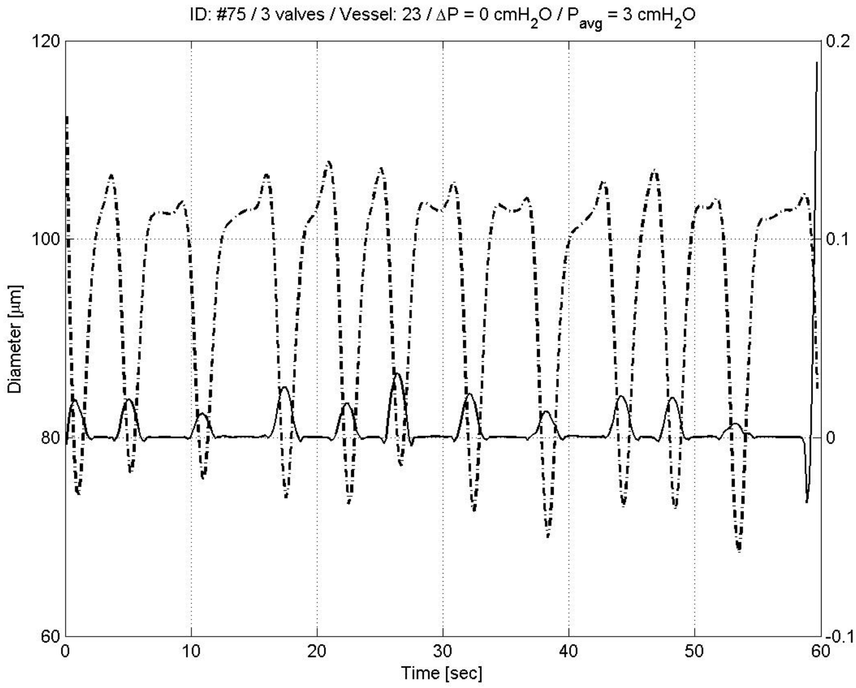

(a) Pressure and diameter vs time.

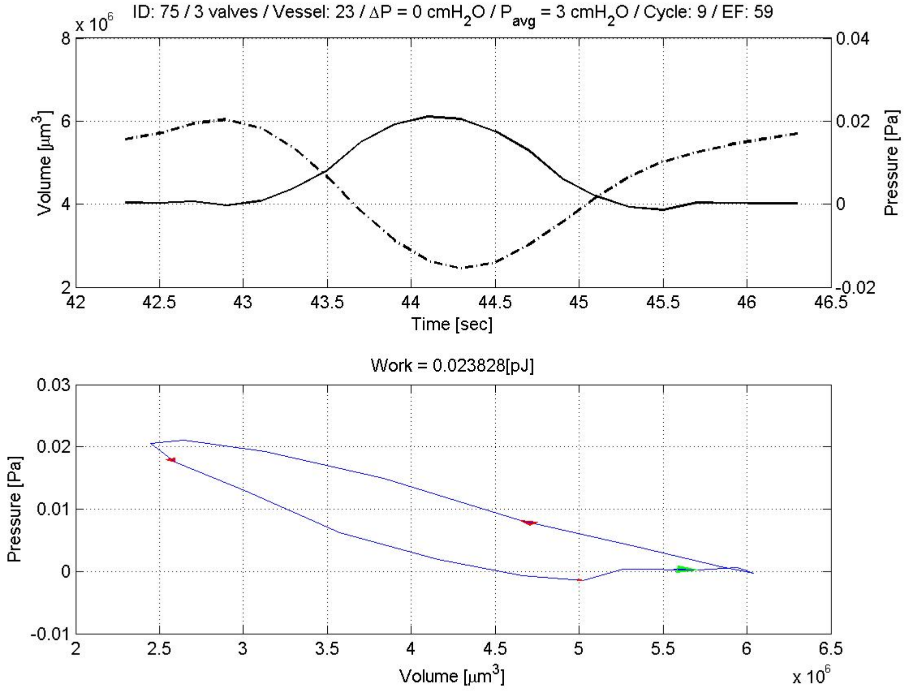

(b) P-V cycle, without self-intersection due to the absence of dual pressure peaks

Figure 3.20: Pressure-Time & Pressure-Volume relationships at zero ΔP_{axial}. The dual pressure peaks are absent.

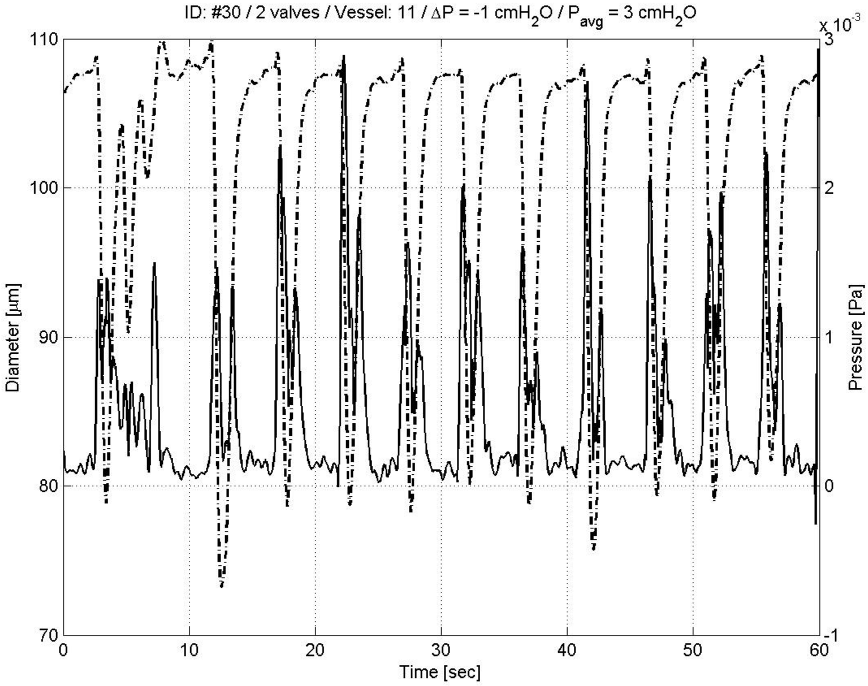

(a) Pressure and diameter vs time.

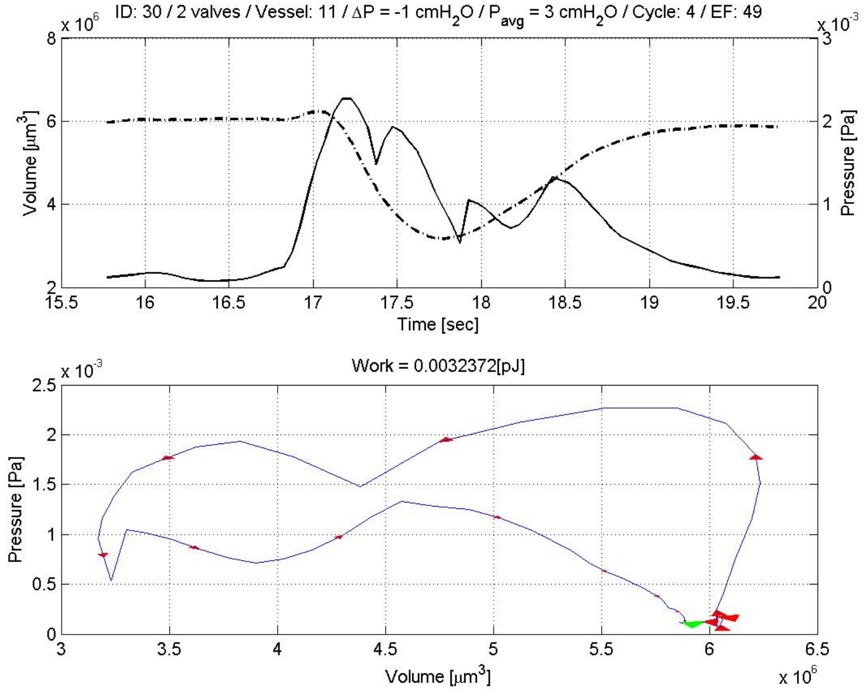

(b) P-V loop for the fourth contraction cycle

Figure 3.21: Pressure-Time & Pressure-Volume relationships at negative ΔP_{axial}. Dual pressure peaks are present, but the P-V loop is not self-intersecting.

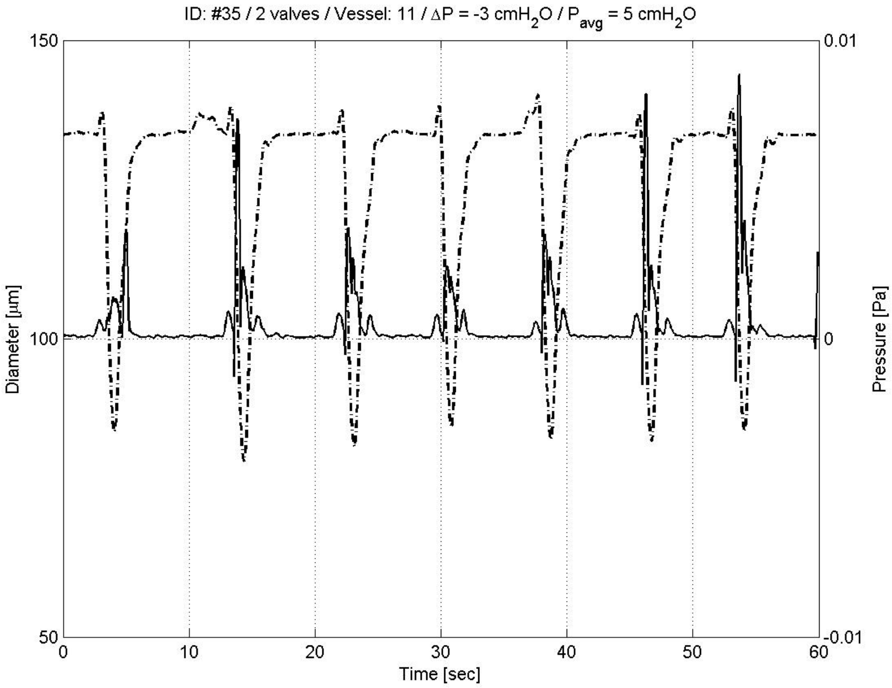

(a) Pressure and diameter vs time.

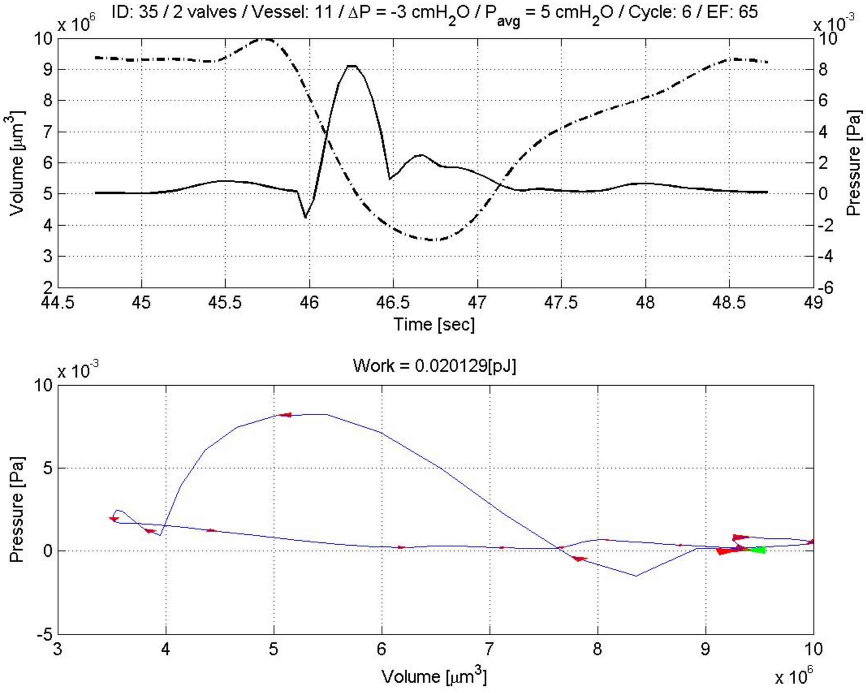

(b) P-V cycle

Figure 3.22: Pressure-Time & Pressure-Volume relationships at negative ΔP_{axial}. Again dual pressure peaks were found in this case; the results showed that self-crossing of P-V loop can occur at any ΔP_{axial}.

3.5 Flow pattern in lymphatic valves

The PIV system was able to resolve secondary flows in the regions behind valve leaflets in rat mesenteric vessels (figure 3.23). Although vortex generation at low Reynolds number in micro-flows may be unexpected from classical fluid mechanics theory, they do occur and have been observed in micro-channel experiments as well [132].

The spatial resolution of PIV provides means of visualising and quantifying these flow structures with much greater detail than other flow diagnostic techniques. On closer inspection of figure 3.23b, however, the velocity inside the valve appears to be zero; clearly this cannot be the case. Arguably, this result may be due to geometrical asymmetries in the valve region. The microscope optics were focused so that the image plane coincided with the mid-plane of the straight vessel segment close to the valve; the plane of maximum velocity between the valve leaflets may not necessarily coincide with the latter. Out-of-plane particle motion and noise from the valve leaflets may also be additional factors affecting the measurement in this region,

Another example of recirculation around a valve leaflet is shown in figures 3.24a and 3.24b. The vessel was placed in a Ca solution but was passive, most likely due to damage during isolation, and it was subjected to positive pressure gradient of $2cmH_2O$ at $4cmH_2O$ transmural pressure. The analysis was performed with 16x16 IW over the lower half of the vessel, to reduce computational time. Only half the vectors are plotted for clarity. The visualization of the flow field was done using the linear integral convolution (LIC) method [16]. LIC essentially transforms a vector field in a texture map in order to reveal flow structures.

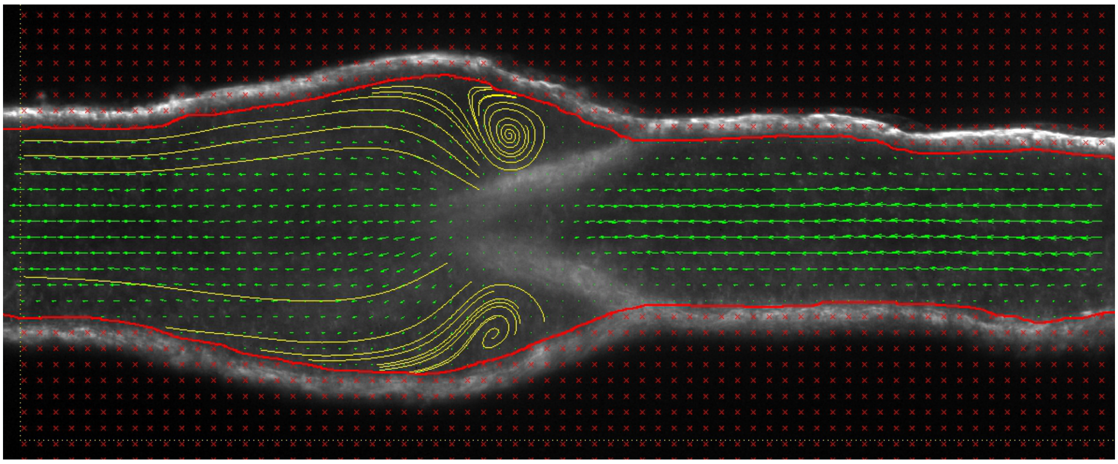

(a) Streamlines identifying recirculation around the lymphatic valve. The vessel diameter upstream the valve is approximately 102 μm

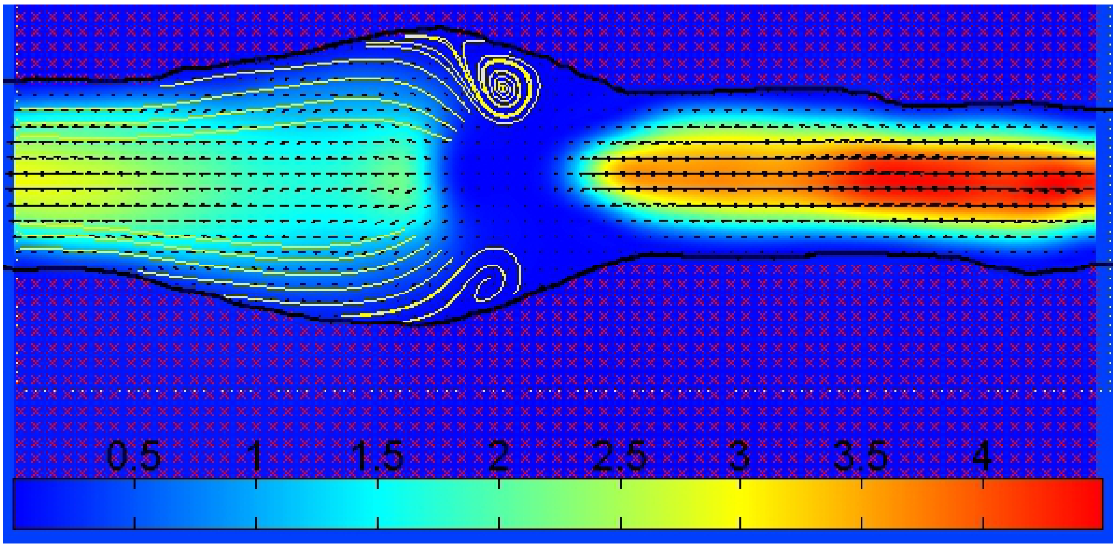

(b) Colormap of the velocity magnitude. The scale is in mm/s. The Reynolds number calculated upstream the valve is approximately 0.5

Figure 3.23: Eddies forming around valve leaflets at an axial pressure gradient of 1 cmH_2O at a transmural pressure of 3 cmH_2O. This measurement was performed in a non contracting vessel and therefore the flow was at steady state. Approximately 100 pair of frames were acquired and the analysis results were averaged. Only one half of the velocity vectors is plotted for clarity.

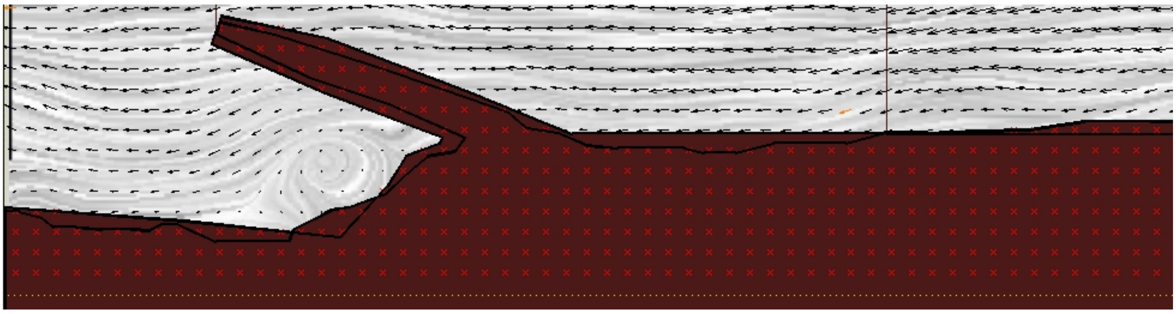

(a) Frame 1

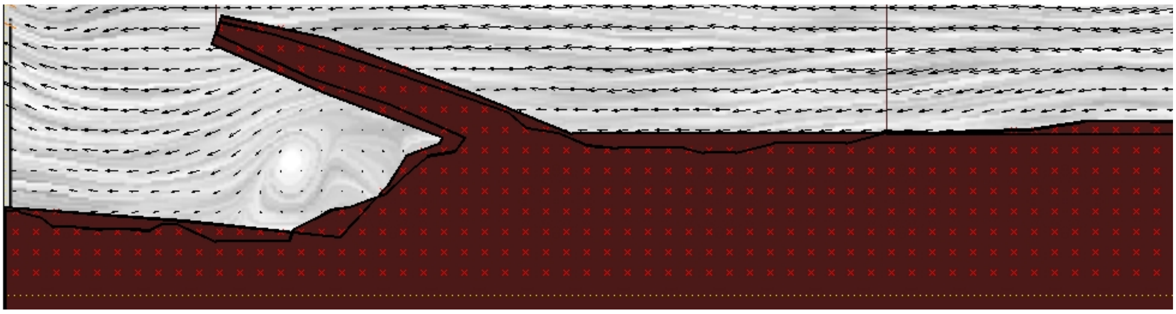

(b) Frame 2

Figure 3.24: Another example of recirculation around valves at $P_{avg} = 4\,cmH_2O$ and $P_{axial} = 2\,cmH_2O$. Flow visualization with LIC. Half the image was analysed to reduce computation time. Only one half of the velocity vectors is plotted for clarity.

3.6 Statistical analysis

This section reports the statistical analysis of the results. Several parameters, fluidic and lymphatic, are reported in histograms and box-plots. The parameters are grouped by axial pressure gradient and transmural pressure, as well as air table activation and preconditioning. In order to analyze differences in the median values of different groups the Wilcoxon rank sum test has been used. The significance level is 5%.

3.6.1 Contraction frequency

Figure 3.25a shows the histogram of lymphatic contraction frequency for the complete data set. In initial trial experiments the light source was positioned on the same air table as the microscope, with the table not activated. The light source enclosure contained 3 fans which were a source of vibration and had an effect on the contraction frequency of lymphangions, as figure 3.25b demonstrates. The effect of the air table activation on FREQ can also be seen by comparing figures 3.25a, which shows the results of the entire dataset, and 2.21a which shows only the the results with the air table active. The maximum contraction frequency drops from 22 bpm to 14 bpm when the table is activated. It is interesting that there is such a profound difference between these groups.

This difference in contraction frequency was further investigated.[28] The distribution shape was investigated with an Anderson-Darling normality test. The test yielded a p-value of 0.875 and 0.603 for the two populations with table 'ON' (n = 63) and 'OFF' (n = 15), respectively, therefore there are not enough evidence to support the hypothesis that the data are not normally distributed. Moreover, a Wilcoxon rank sum test on the two-samples, with table 'ON' or 'OFF',[29] rejected the null hypothesis of equal medians.

Thus the difference in contraction frequency is statistically significant. Due to this result, and unless otherwise stated, all other plots will contain only measurements with the air-table active. After the table activation the light source was also removed from the table.

---

[28] The statistical tests were conducted on both the data sets with the automatic and manual frequency estimation. The results and conlcusions were the same

[29] these samples can be assumed to be independent, since they were conducted with different vessels

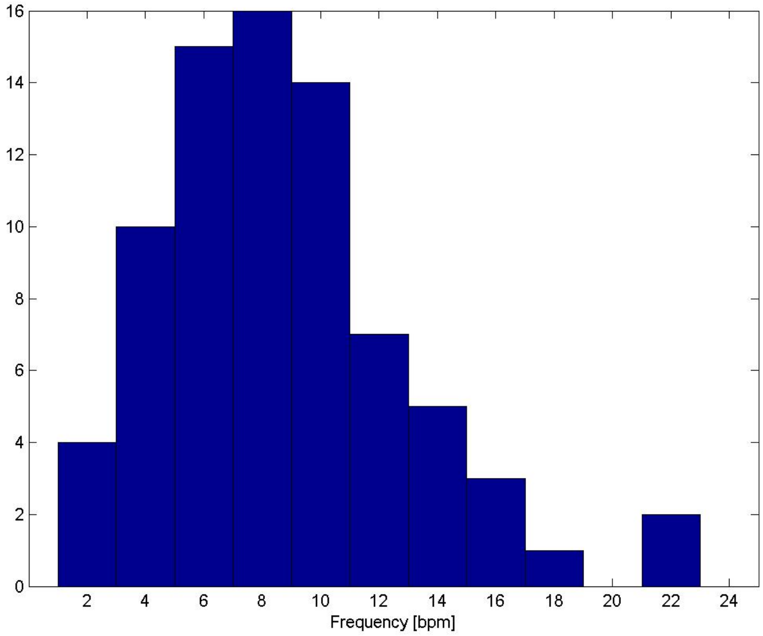

(a) Histogram of contraction frequency. Complete data set.

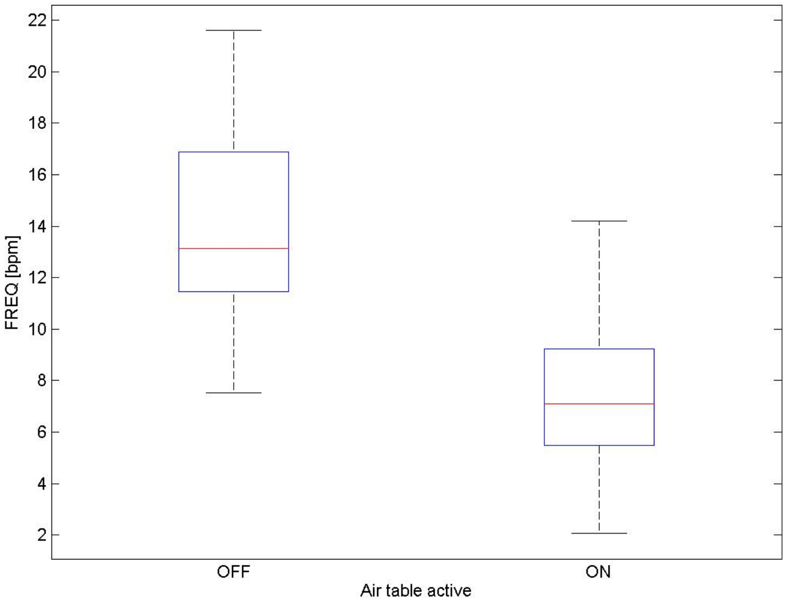

(b) Contraction frequency grouped by Air table activation. The effect of external vibrations is evident

Figure 3.25: Contraction frequency statistics of complete data set.

The dependence of contraction frequency on the axial pressure gradient for different vessels is plotted in figure 3.26. The frequency of contractions of messenteric lymphatic vessels has been shown to decrease with increasing positive axial pressure gradient [44]. Observing figure 3.26 is can be seen that in some vessels the contraction frequency drops as ΔP_{axial} is increased from zero; however the opposite behaviour can be observed as well. Contraction frequency at negative axial pressure gradient appears to be lower or equal than the value at zero ΔP_{axial}, in all but one vessel.

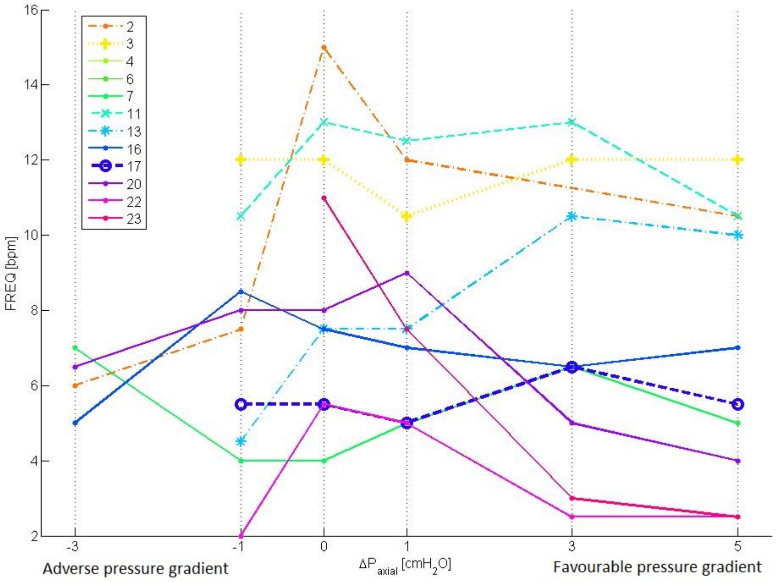

Figure 3.26: Contraction frequency dependence on axial pressure gradient for 10 vessels. The number in the figure legend is the measurement id number of table 2.2.

3.6.2 Reynolds number

The Reynolds number of lymphatic flow is seldomly reported in the literature. Figure 3.27 shows the Reynolds number for different values of ΔP_{axial}. The maximum Reynolds number observed was 10. In the study by Dixon et al. [32] the maximum Reynolds number reported was 5.

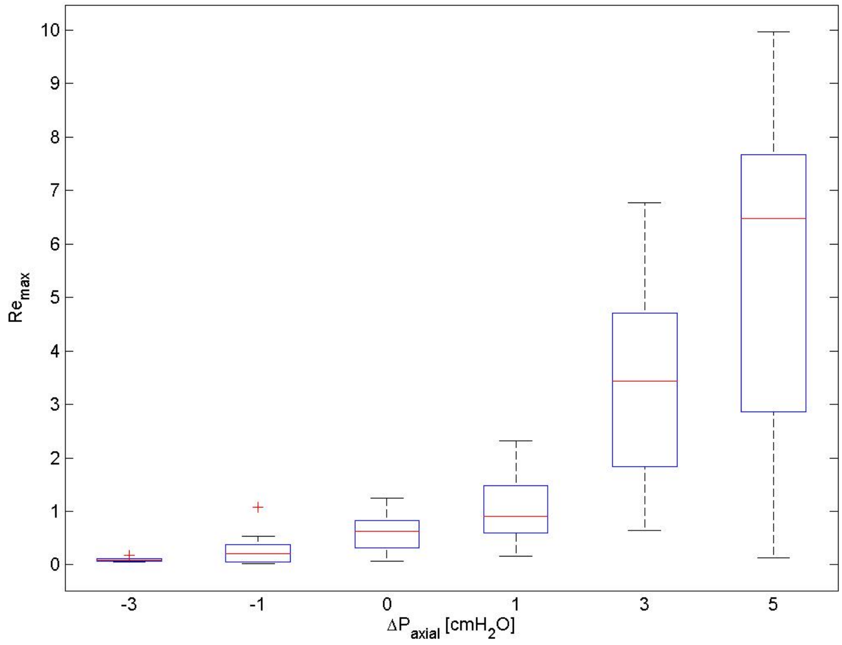

Figure 3.27: Reynolds number vs axial pressure gradient. The Reynolds number corresponding to the maximum velocity is shown.

3.6.3 Velocity magnitude

Maximum velocity is plotted in figure 3.28. It is observed that velocities of up to 54 mm/s were recorded. At 20x magnification the temporal resolution necessary to measure such flow is of the order of 100 μs [22]. Consequently, the development of a high-speed light source and the use of frame-straddling are justified.

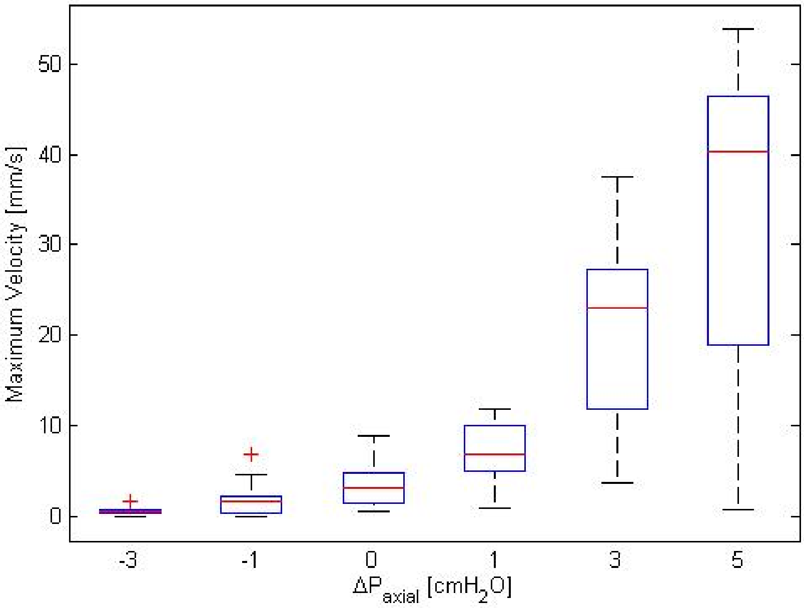

Figure 3.28: Maximum velocity vs ΔP_{axial}

3.6.4 Velocity profile

Figure 3.29 shows the histogram of the ratio of the maximum to average velocity at a cross-section in the middle of the FOV. It is interesting that in most cases this ratio is different than 2, or fully developed laminar flow. Since this is a low Reynolds number flow it is expected theoretically that this ratio is equal to 2. However, this is not the case for all measurements; deviation from the theoretical value may be due to experimental errors in velocity estimation close to the wall and due to the irregular vessel internal geometry.

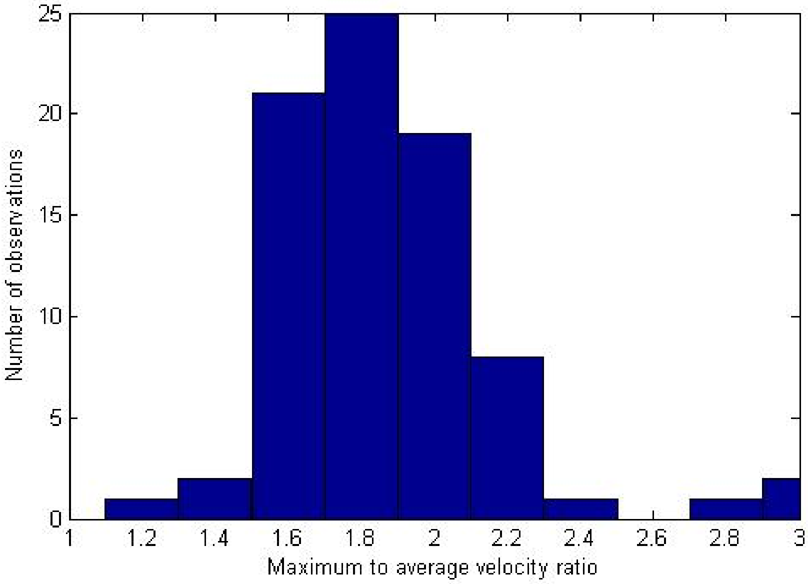

Figure 3.29: Maximum to average velocity ratio

3.6.5 Flow rate

The relationship of axial pressure gradient and volumetric flow rate is plotted in figure 3.30a. Flow rate increases with increasing ΔP_{axial} and the relationship of the median value and the pressure gradient appears to be non-linear, indicating that the flow resistance varies non-linearly. Increasing the transmural pressure appears to have little effect on the flow rate, however the sample size for $P_{avg} = 5\ cmH_2O$ is small. A Wilcoxon rank sum test fails to reject the null hypothesis at the 5% level ($p = 0.8097$), hence the medians should be considered equal.

Figure 3.31 shows the theoretical flow rate, calculated using the average measured velocity at a cross-section and assuming a parabolic velocity profile, as detailed in Section 2.4.4. Theoretical flow rate magnitude is predicted higher than the direct integration of PIV data. Again transmural pressure appears not to affect the flow rate ($p = 0.7653$)

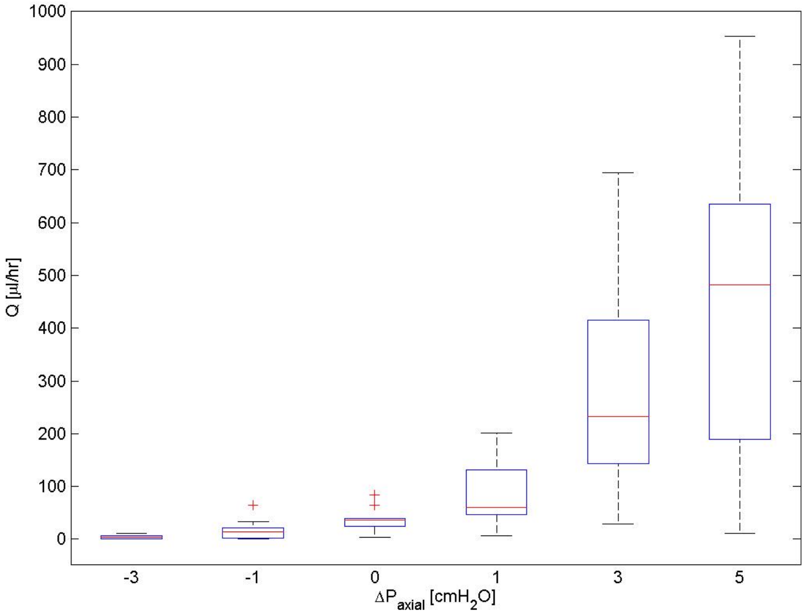

(a) Flow rate vs axial pressure gradient

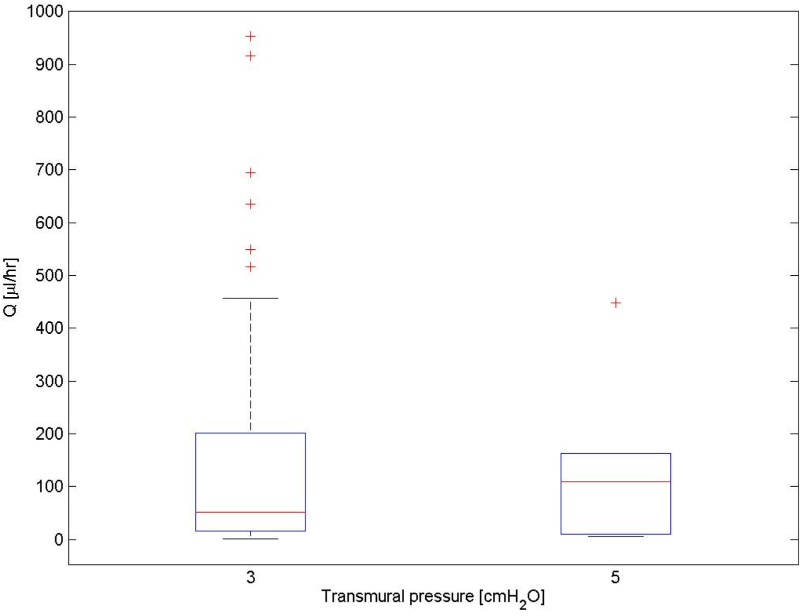

(b) Flow rate vs transmural pressure

Figure 3.30: Flow rate estimated from the PIV data with numerical integration of the velocity profile at a cross section at the middle of the FOV

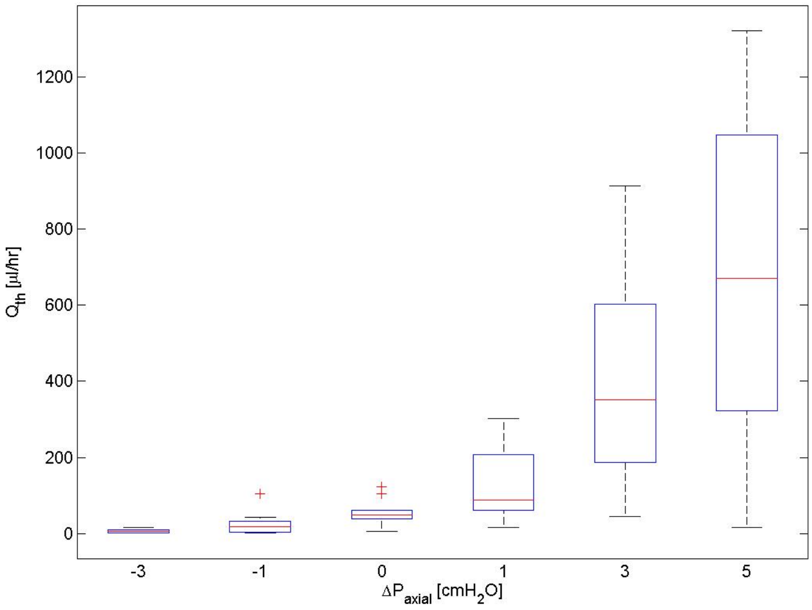

(a) Flow rate vs axial pressure gradient

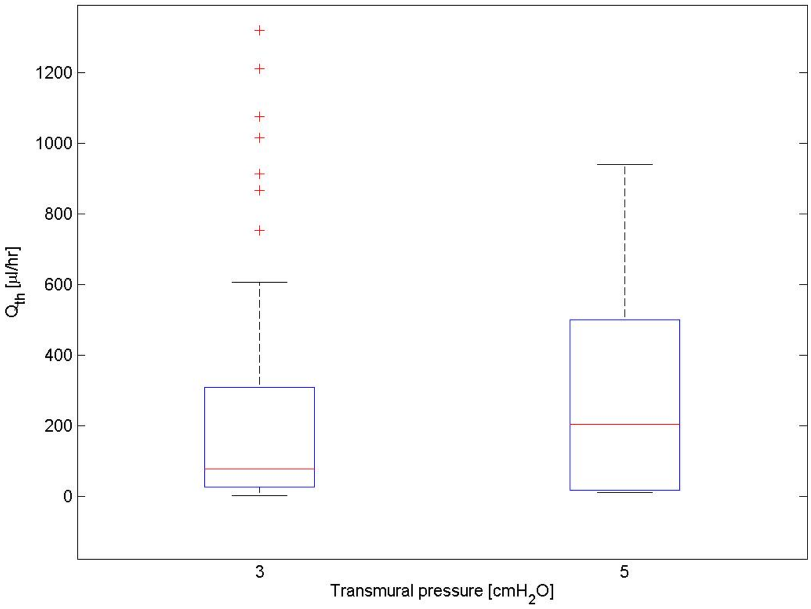

(b) Flow rate vs transmural pressure

Figure 3.31: Theoretical flow rate (Sec. 2.4.4) vs axial pressure gradient and transmural pressure. The average PIV velocity obtained from a cross section at the middle of the FOV was used to estimate the theoretical flow rate which appears to be larger than the one estimated by direct velocity profile integration

3.6.6 Wall radial velocity

Figure 3.32 shows the median value of the ratio of wall radial velocity to fluid velocity, grouped by the axial pressure gradient, for the entire experimental dataset. It is evident that even the median values of this ratio can be close to unity at zero and negative axial pressure gradient. It appears that the assumption of negligible wall radial velocity is not valid at these axial pressure gradients, but is valid at positive axial pressure gradients.

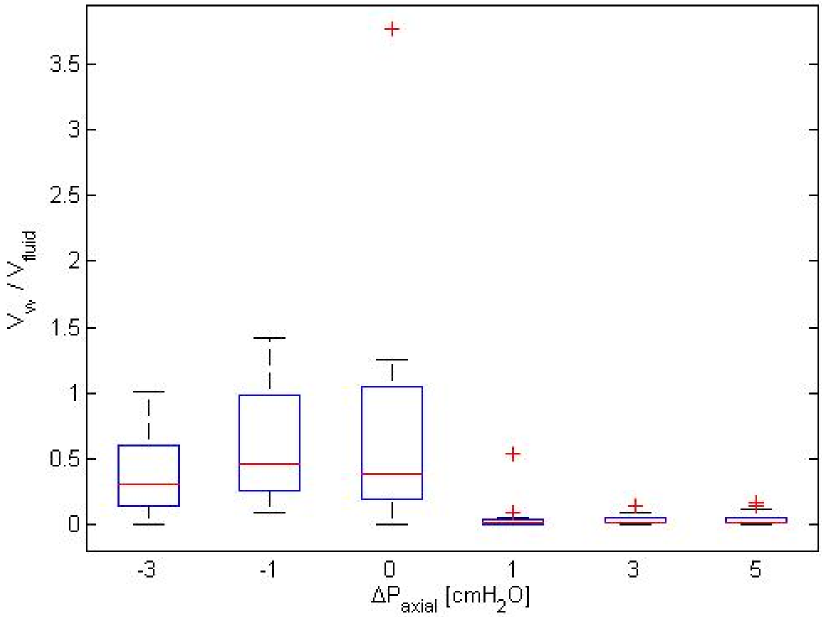

Figure 3.32: Median value of wall radial to fluid velocity ratio, grouped by the axial pressure gradient.

3.6.7 Wall shear stresses

Figure 3.33 shows the relationship between the WSS (maximum value) and axial pressure gradient, as it is calculated from PIV results (figure 3.33a) and laminar flow assumption (figure 3.33b). Table 3.1 presents the maximum, minimum and median values of WSS in tabular format. PIV derived WSS values are up to 58% lower than the calculated (theoretical) values.

Table 3.1: Min, Max and Median values of WSS for different values of ΔP_{axial}

(a) PIV WSS values in dyn/cm^2

ΔP_{axial} $[cmH_2O]$	Median	Max	Min
-3	0.12	0.13	0.06
-1	0.15	1.42	0.02
0	0.59	1.76	0.08
1	1.39	1.79	0.18
3	3.13	5.56	0.44
5	3.92	10.02	0.13

(b) Theoretical WSS values in dyn/cm^2

ΔP_{axial} $[cmH_2O]$	Median	Max	Min
-3	0.14	0.18	0.05
-1	0.46	2.84	0.02
0	0.98	2.97	0.18
1	2.24	2.59	0.29
3	6.21	8.8	1.159
5	7.64	13.77	0.23

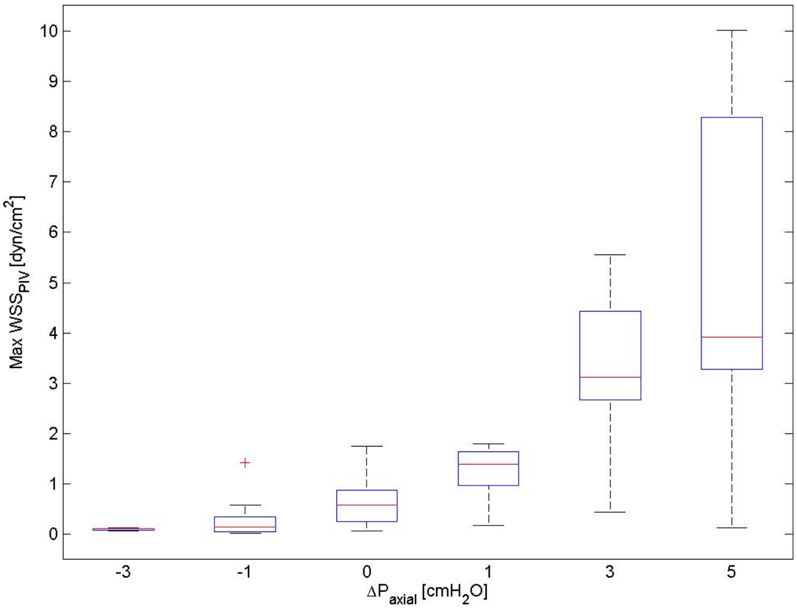

(a) PIV WSS

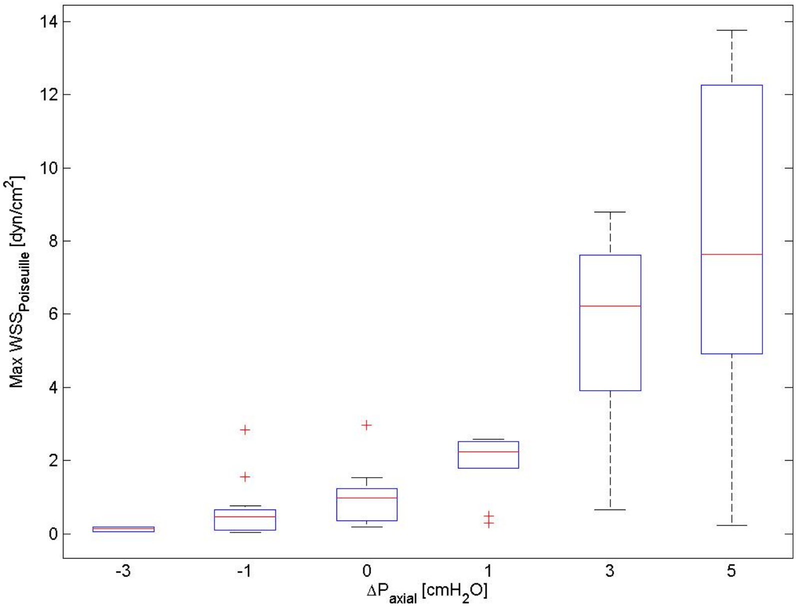

(b) Theoretical WSS

Figure 3.33: Comparison of WSS computed with Poiseuille assumption and the PIV data

3.6.8 Ejection fraction

Ejection fraction is a lymphatic function parameter of interest and figure 3.34a and 3.34b show its relationship with axial pressure gradient and transmural pressure, respectively.

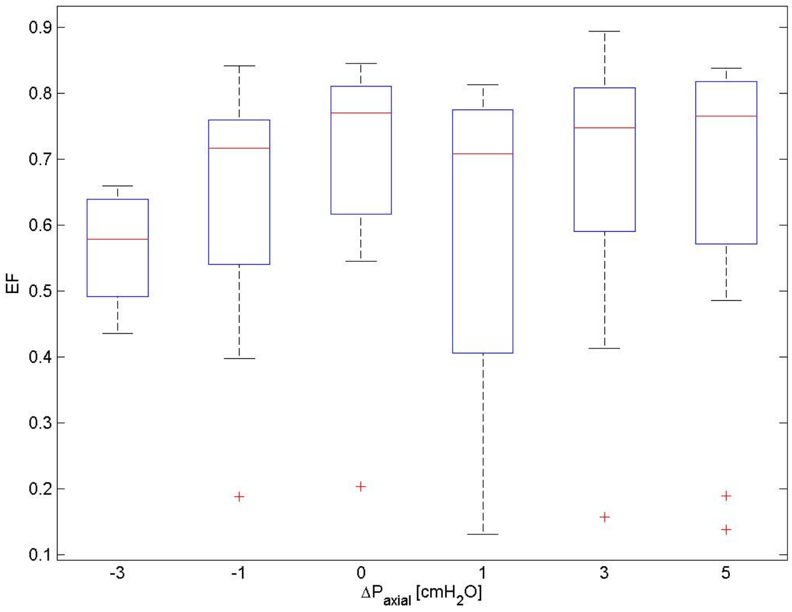

(a) Ejection fraction vs ΔP_{axial}

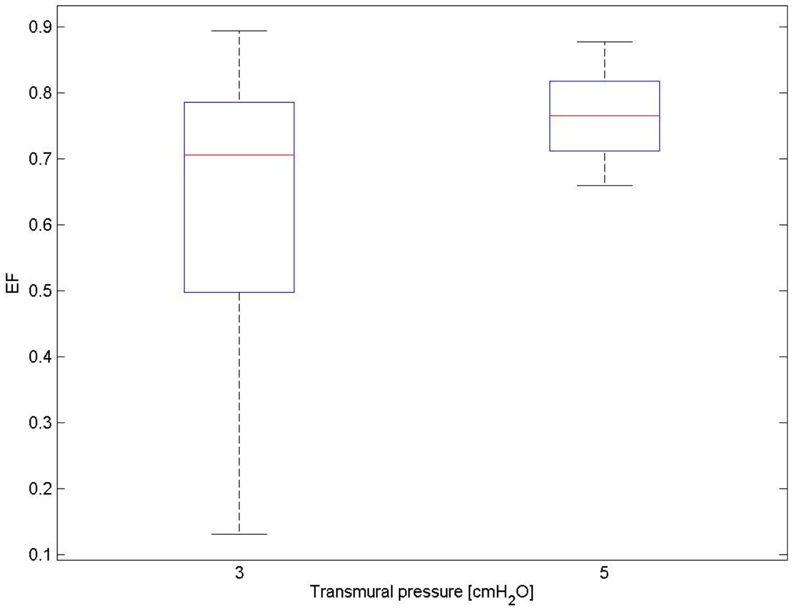

(b) Influence of transmural pressure on EF. The medians of the two groups are considered equal at the 5% significance level ($p = 0.0813$).

Figure 3.34: Ejection fraction (EF)

Figure 3.35 shows the maximum (a) and minimum (b) diameter of the vessels grouped with the transmural pressure. Maximum and minimum diameter vs ΔP_{axial} are shown in figures 3.36a and 3.36b, respectively. Maximum diameter is influenced by the transmural pressure, but the minimum appears unaffected.

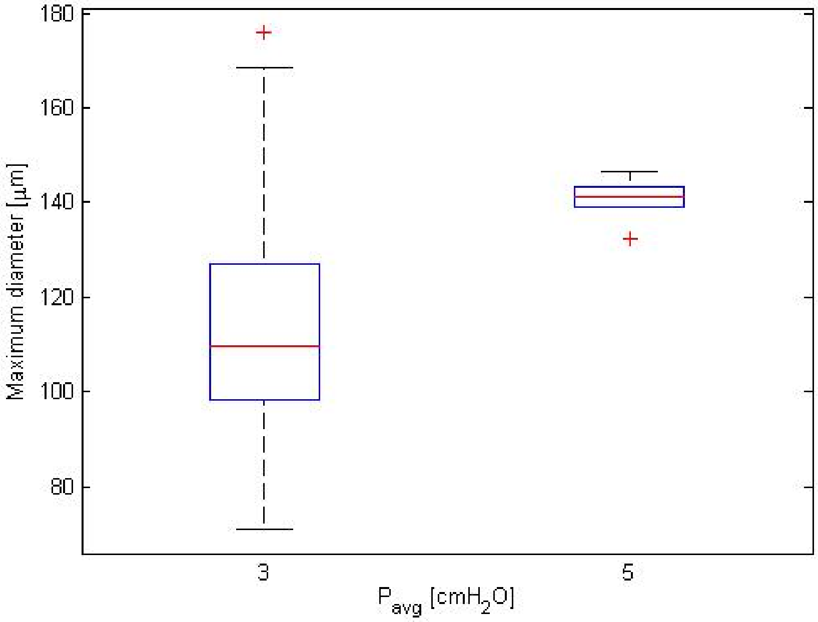

(a) Maximum diameter vs transmural pressure. The medians are shown to be unequal with a rank sum test ($p = 0.0193$).

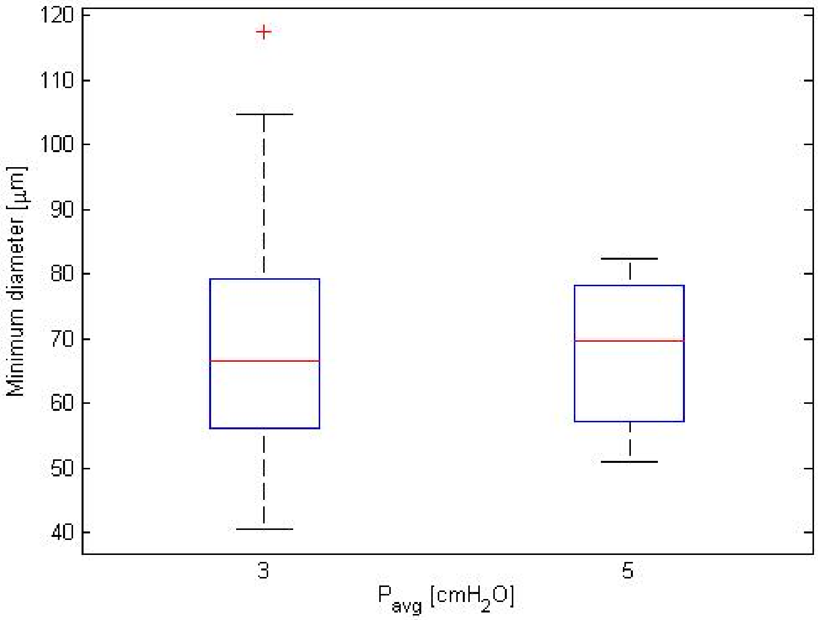

(b) Minimum diameter vs transmural pressure. Not enough evidence are found that the medians are not equal with a rank sum test ($p = 0.736$)

Figure 3.35: Effect of transmural pressure on maximum and minimum diameter

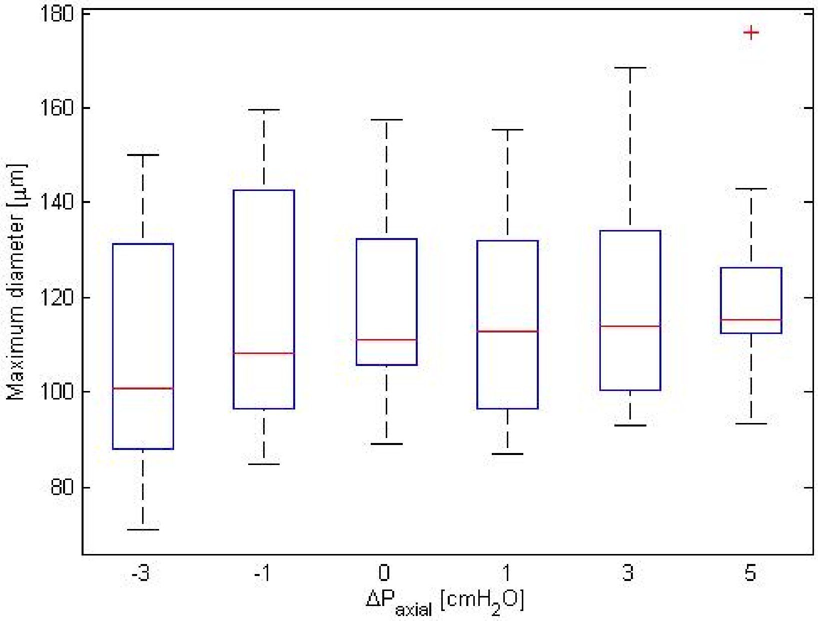

(a) Maximum diameter vs transmural pressure

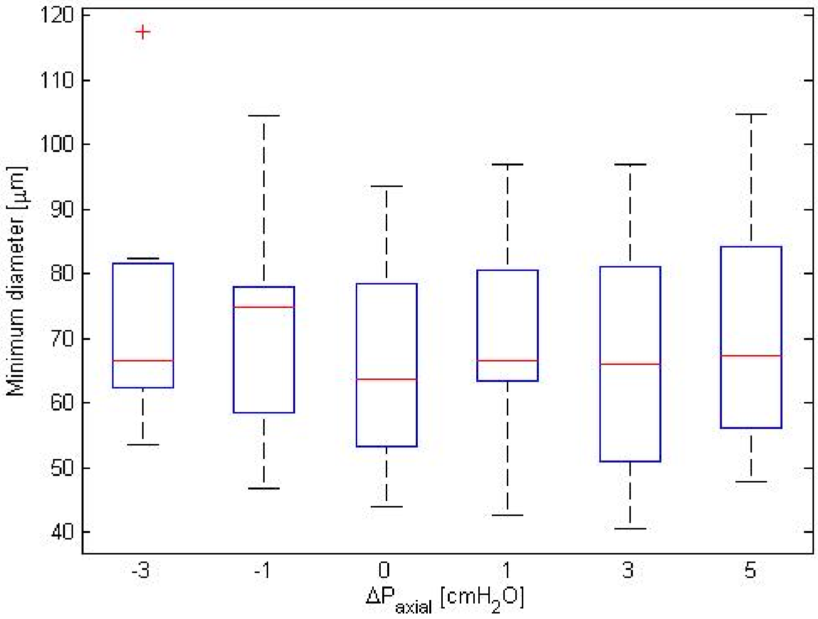

(b) Minimum diameter vs transmural pressure

Figure 3.36: Effect of axial pressure gradient on maximum and minimum diameter

3.6.9 Contraction Amplitude

The contraction amplitude of the lymphatic vessel as defined in section 2.4.1 is a parameter related with the pumping output of a vessel. Figures 3.37a and 3.37b show the variation of CAMP with ΔP_{axial} and P_{avg}, respectively. Figure 3.38 demonstrates the relationship between CAMP and EF for transmural pressure of 3 and 5 cmH_2O.

CAMP is affected by axial pressure gradient and transmural pressure (figures 3.37a and b). The effect of transmural pressure on CAMP is through an increase in maximum EDD of vessels, as shown in figure 3.35a while the ESD remains relatively unchanged (figure 3.35b).

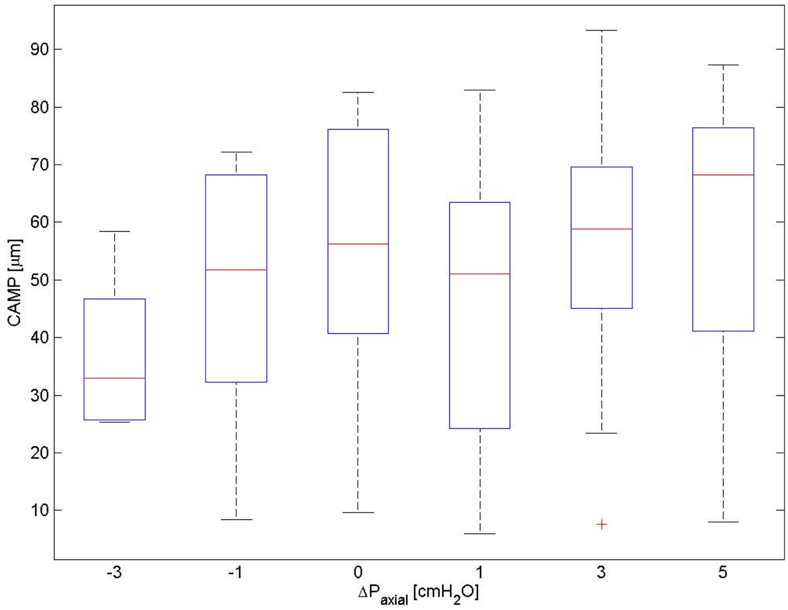

(a) CAMP vs ΔP_{axial}

Figure 3.37: Contraction Amplitude (Cont'd)

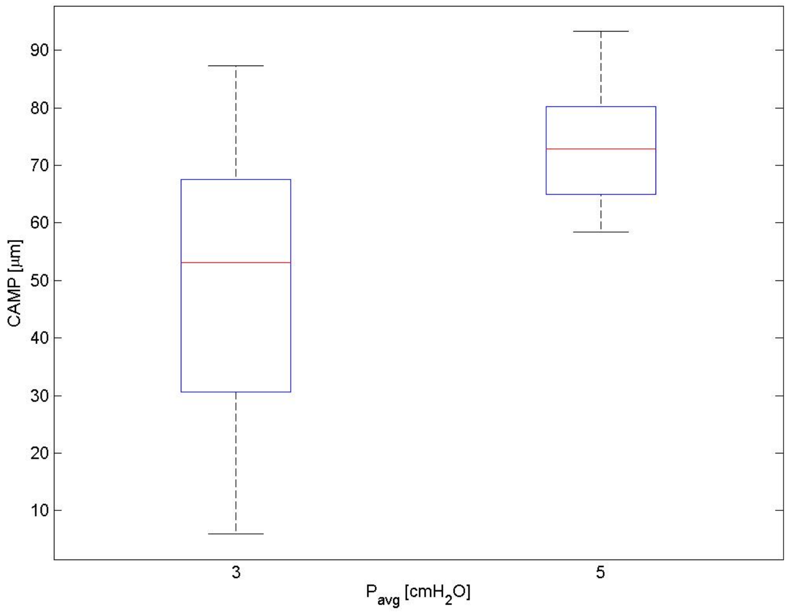

(b) Effect of transmural pressure on CAMP. The medians of the groups are not equal ($p = 0.0165$).

Figure 3.37: Contraction Amplitude (CAMP)

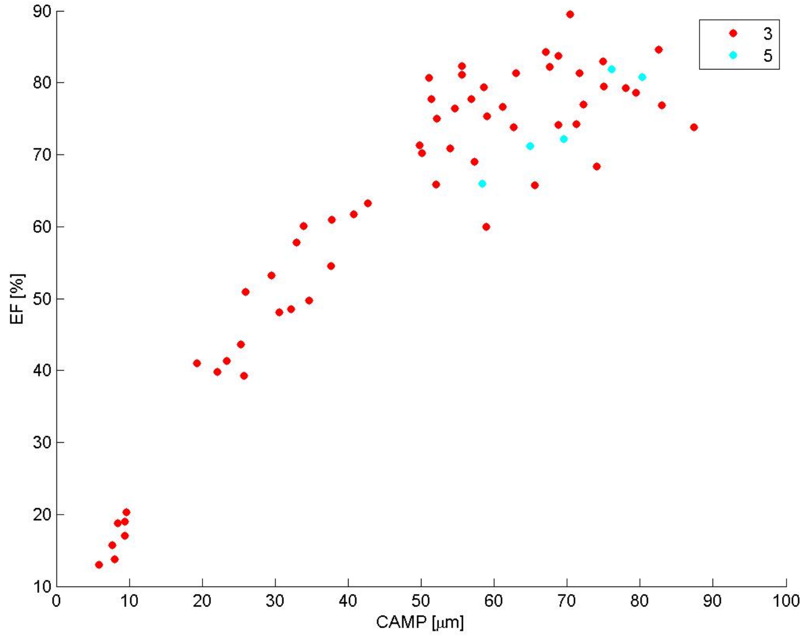

Figure 3.38: Relationship of CAMP and EF. Data for transmural pressures for 3 and 5 cmH_2O (red and cyan dots respectively).

3.6.10 Fractional Pump Flow

FPF is an index of lymphatic vessel capacity; it combines the ejection fraction and frequency of contraction [44]. FPF appears to be affected by both axial and transmural pressure, as shown in figure 3.39, where the FPF is plotted against ΔP_{axial} and P_{avg}. The frequency from the manual estimation[30] has been used to calculate the FPF (see Section 2.4.3 on frequency estimation). In terms of median FPF values, the maximum pumping efficiency appears to occur at zero axial pressure gradient. Although the CAMP (figure 3.37) is higher at higher ΔP_{axial} the reduction in contraction frequency (figure 2.22) compensates and reduces the FPF as ΔP_{axial} increases. However, rank sum tests for the data of figure 3.39b do not provide statistical evidence that the medians of the groups are not equal. Therefore, the medians of these groups should be considered equal. On the other hand, air table activation had an effect on FPF (figure 3.40) which was confirmed by a rank sum test (p =5.3×10^{-5}).

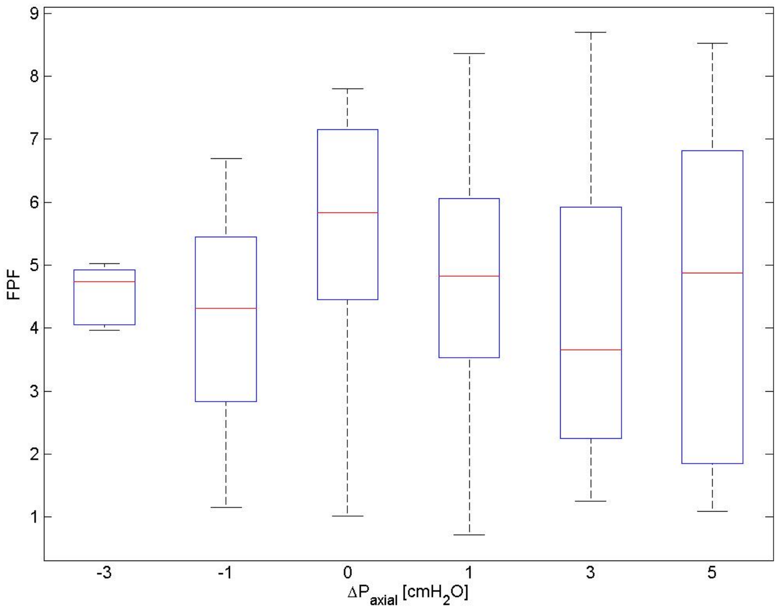

(a) FPF vs ΔP_{axial}

Figure 3.39: Fractional pump flow index. Manual frequency calculation (Cont'd).

---

[30] Manual estimation denotes that the frequency of contraction was estimated by visual observation of the diameter tracings

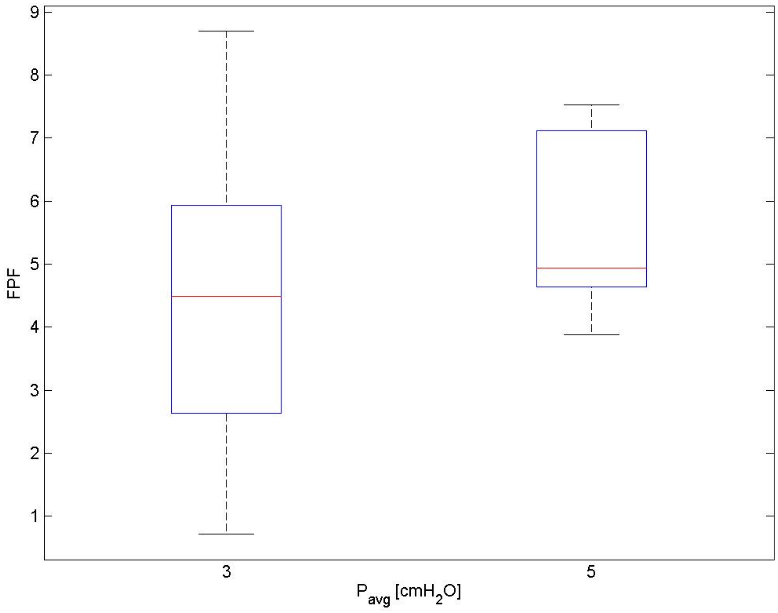

(b) Effect of transmural pressure on FPF

Figure 3.39: Fractional pump flow index. Manual frequency calculation.

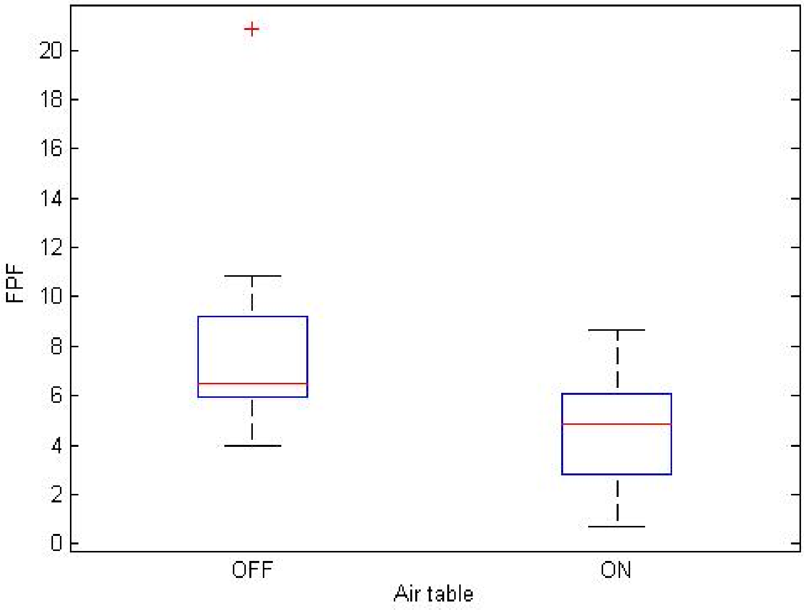

Figure 3.40: Effect of air table activation on FPF. The two samples do not have equal medians.

3.6.11 Pressure and Work Done

Figure 3.41 shows the dynamic pressure relationship with the axial pressure gradient and average pressure. As the pressure calculated is derived from the velocity is it expected to increase with increasing axial pressure gradient. No statistical significant difference can be inferred from the data of figure 3.41b at the 5% significance level.

The relationship between contraction work and the hydrodynamic environment is shown in figure 3.42. Figure 3.43 plots the contraction work grouped by air table activation. A ranksum test fails to reject the null hypothesis, therefore the samples are considered to have equal medians. Although the air table activation had a statistically significant effect on the median and maximum value of contraction frequency, there are no evidence to show that this increase materialized in an increase of contraction work.

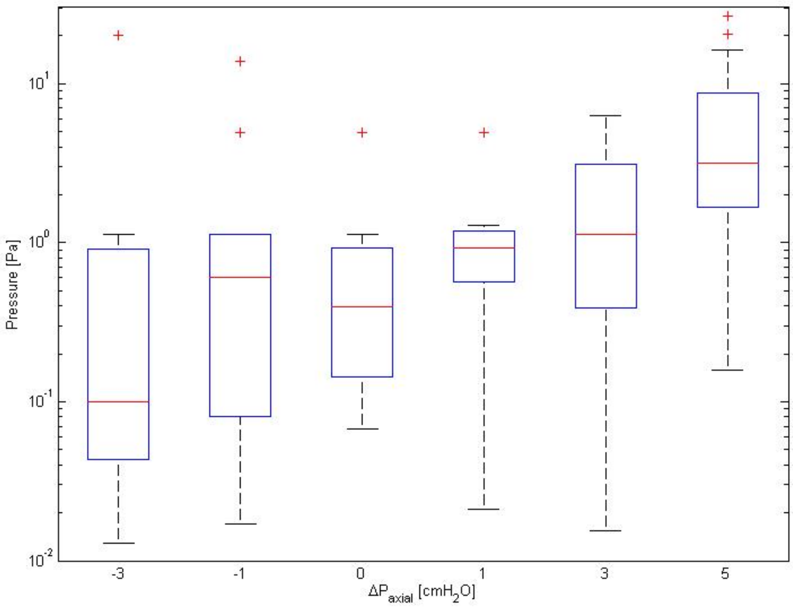

(a) Maximum Dynamic Pressure vs ΔP_{axial}. Pressure is given in logarithmic scale.

Figure 3.41: Effect of pressure conditions on maximum dynamic pressure inside lymphangions (Cont'd).

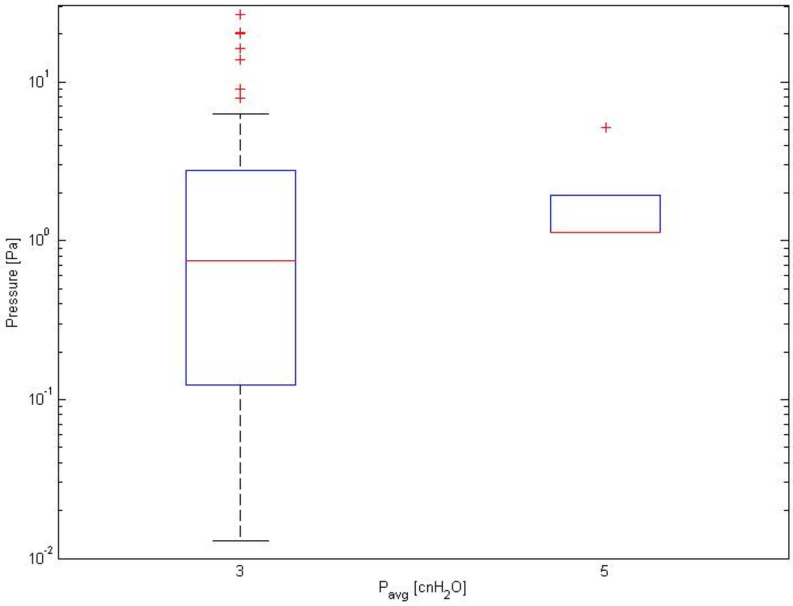

(b) Maximum Dynamic pressure vs P_{avg}. Pressure is given in logarithmic scale.

Figure 3.41: Effect of pressure conditions on maximum dynamic pressure inside lymphangions.

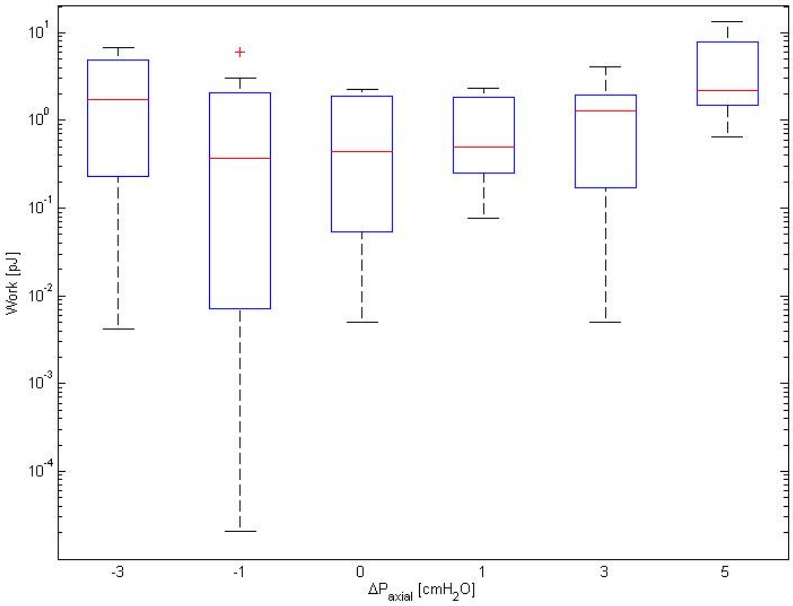

(a) Contraction work vs ΔP_{axial}.

Figure 3.42: Work during contraction cycle (Cont'd).

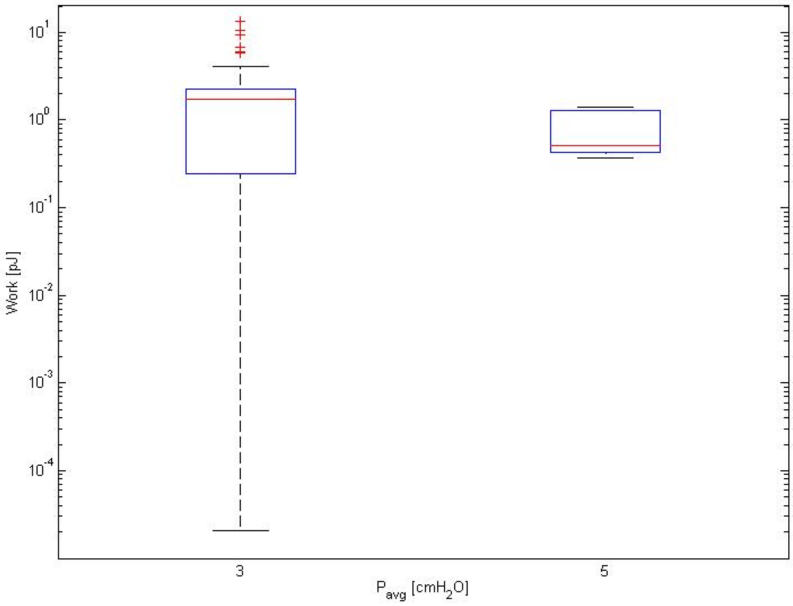

(b) Contraction work vs P_{avg}.

Figure 3.42: Work during contraction cycle.

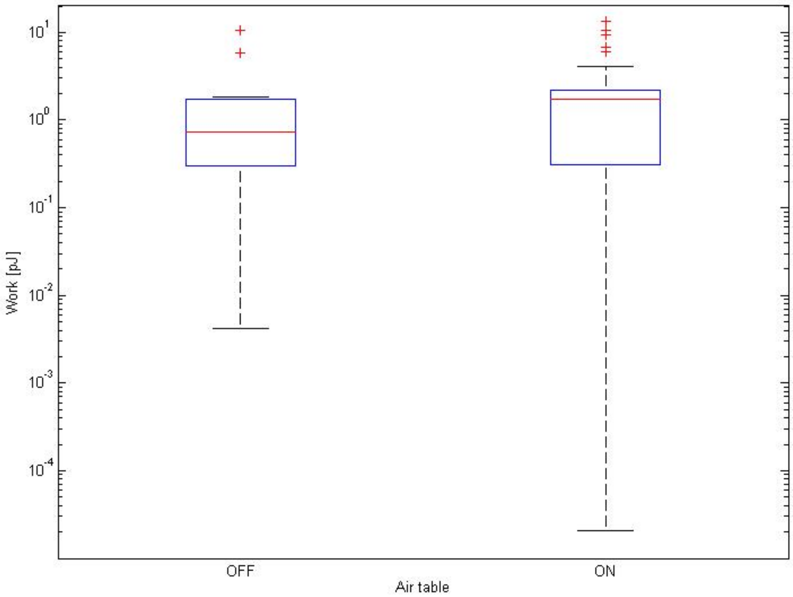

Figure 3.43: Effect of air table activation on contraction work.

3.6.12 Vessel preconditioning

Preconditioning has an effect on the mechanical properties of living tissues [20]. Hence the estimated lymphatic functional parameters may show a dependence on the preconditioning. Figure 3.44 shows statistical box-plots of pre-conditioning on CAMP, FPF, EF and FREQ. In terms of significant statistical difference between the groups shown in the sub-figures of figure 3.44, a Wilcoxon rank sum test for CAMP and EF rejects the null hypothesis at 5% significance level (p-value of 0.0195, 0.043 for CAMP and EF, respectively) and therefore the difference observed is statistically significant. The rank sum test for FREQ and FPF, shows that the null hypothesis cannot be rejected at the 5% significance level (p-values of 0.0639 and 0.7234 for FREQ and FPF, respectively). On the other hand, contraction work appears to be affected by pre-conditioning, with a p-value of 0.0018.

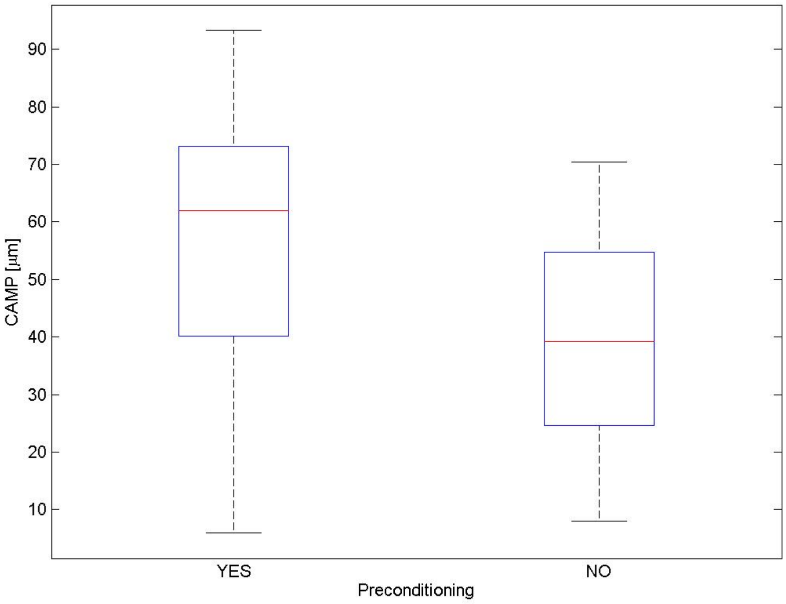

(a) Effect of preconditioning on CAMP

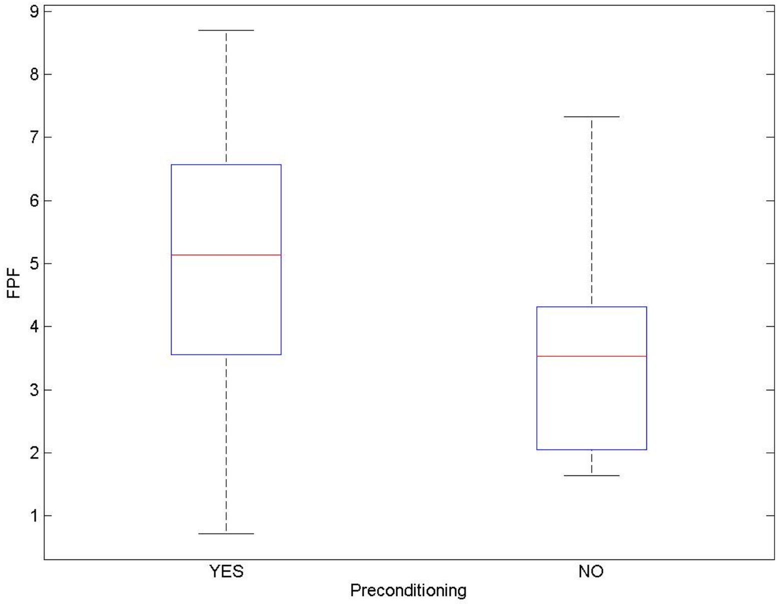

(b) Effect of preconditioning on FPF

Figure 3.44: Effect of preconditioning on vessel functional parameters. Manual frequency calculation (Cont'd).

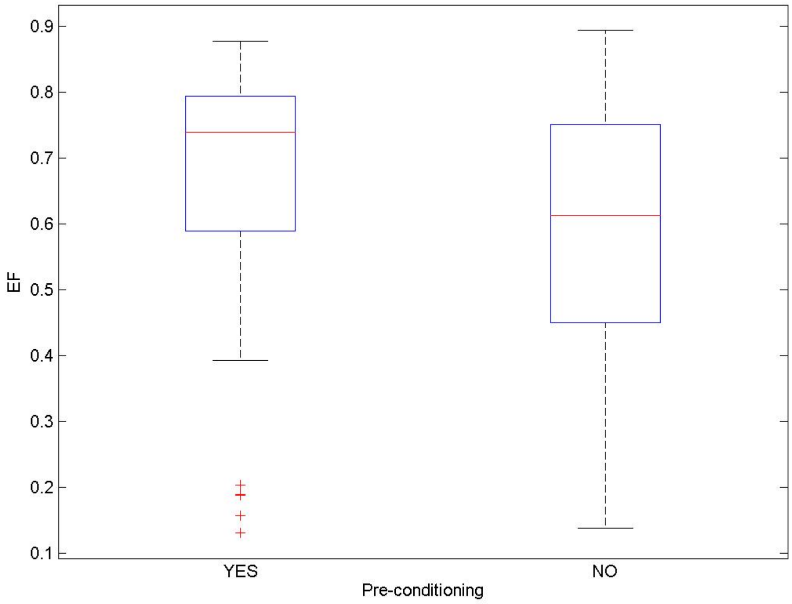

(c) Effect of preconditioning on EF

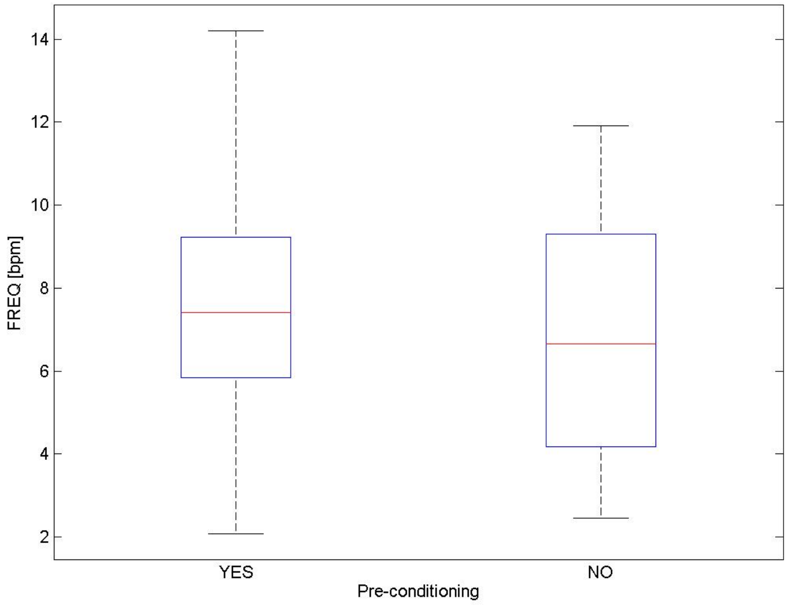

(d) Effect of preconditioning on FREQ

Figure 3.44: Effect of preconditioning on vessel functional parameters. Manual frequency calculation.

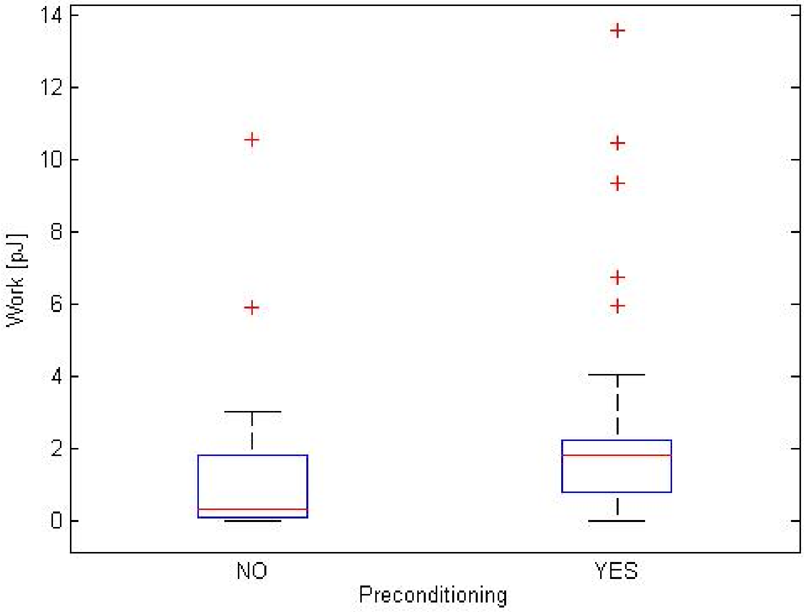

Figure 3.45: Contraction work grouped by preconditioning. The medians of the groups are not equal ($p = 0.0018$).

Chapter 4

Discussion

4.1 LED light source and optical setup

LEDs present a versatile, low cost, safer alternative solution to lasers for micro-fluidic flow measurements. The use of LED micro-PIV systems in physiological flow studies is relatively novel, and their potential has yet to be fully realised. The previous study by Willert et al. [156] showed that the driving current can be increased dramatically, without damaging the LEDs. Although the driving electronics limited the maximum current to 36 A, the development of custom electronics that can pulse the LEDs with currents in the range of 200 A, will enable the use of even shorter duration pulses and allow the measurements of even faster flows.

The results presented in the context of this dissertation are restricted to non-fluorescence imaging. However, initial studies in our laboratory have shown that exciting fluorescent emission from micro-particles is feasible with LEDs; however the light pulse duration was significantly higher, or CW illumination was used, restricting the applicability to slower flows than those expected in the lymphatics. Better performance can be obtained by optimizing the optical setup (filter/mirror selection) and with specialized design of lenses and collimating optics at the entry/exit of the fiber optic cable [19]. Furthermore, using blue LEDs and particles dyed or conjugated with a specific fluorochrome matched to the emission spectrum of the LED, may yield better fluorescent signal, as the blue LEDs by the same manufacturer have almost twice the power output than their green counterparts [78] at half the pulse duty cycle. Moreover, using particles that are excited at lower wavelengths increases the spatial resolution of the system [116].

The apparatus and results of the present study are promising, and demonstrate, for the first time, the feasibility of the μ-PIV technique to quantify the two-dimensional flow field within contracting lymphatic vessels. The use of μ-PIV has greatly improved the spatial and temporal resolution with respect to previous work; the latter can be reduced down to 60 μs and at 20x magnification it is possible to measure flow velocities in excess of 100 mm/s [22]. In fact, the temporal resolution achieved is at least on par, if not greater than, the temporal resolution of time-resolved μ-PIV measurements in biofuids reported in the literature by Shinohara et al. [132] (500 μs) Sugii et al. [134] (166.7 μs) and fails short only to high-speed laser based measurements in engineering such as the work by Alharbi and Sick [4] (15-35 μs).[31] Thus, μ-PIV has the potential of becoming a valuable tool for studying the lymphatic system as the method can be readily extended to *in vivo* flow measurements, provided there is optical access to the vessels. More work will be necessary to that end however, as an appropriate route of particle administration needs to be established. Cell trafficking studies are also possible using fluorescently tagged lymphocytes.

The system proved able to reveal flow patterns around valves, although this is a more challenging measurement than flow in straight segments. Flow around and inside valves is of interest, as it has been shown that the endothelial cells produce Nitric Oxide (NO), a substance that affects contractility. It is likely that there is a shear dependent mechanism that influences NO production, which varies locally in lymphatic vessels [13, 157]. In order to quantify the complex flow patterns present around valves, the apparatus may be extended to allow 3D characterisation of the flow field. Several different approaches to 3D μ-PIV exist, such as stereoscopic, holographic and abberation based imaging. For a review of 3D implementations the reader is referred to the review by Cierpka and Kaehler [22].

One drawback of the current setup, in fact of all μ-PIV and apparatus, is the restricted FOV of the available microscope objectives. The magnification of the objective used, is the optimum magnification for flow measurement based on the vessel average diameter of approximately 100 μm. Unfortunately, the resulting FOV at 20x magnification does now allow for simultaneous imaging of adjacent lymphangions, may be contracting with completely different timing than the observed lymphangion. Reducing the magnification will of course increase the FOV but the

---

[31] The light pulse duration used was 50 μs which reduced the minimum temporal resolution to 60 μs. When side scattering is not necessary, e.g. in a micro-channel measurement, or if more electrical current is used to drive the LED, the light pulse duration can be further reduced, thus achieving a temporal resolution comparable to laser based measurements

spatial resolution in the velocity calculation will decrease. In addition, larger diameter particles may be needed which may cause issues depending on their settling velocity. Therefore the phase difference of contraction and the effect on the flow cannot be studied with the current implementation, however recent advancements in Micro-electromechanical (MEMS) optics may offer a solution to this problem [111, 151].

4.2 Analysis of Uncertainty

Quantification of PIV measurement uncertainty is a topic of ongoing research [69, 142]. Uncertainty in PIV has a number of sources; they can be divided into two major categories, uncertainty due to the experimental setup and uncertainty in the PIV algorithm. The former is mainly attributed to optical aberrations and light source timing uncertainty, while the latter is due to the uncertainty in locating the particle displacement from a pair of images.

Another cause of uncertainty is due to particle dynamics. An important assumption in PIV is that the particles faithfully follow the velocity of fluid particles that surround them. This is not always the case, but measurements of compressible flows with high velocity gradients are mostly affected. Hence, this source will be considered to be negligible. Brownian motion and particle settling may become important in low Reynolds number flow; the error due to Brownian motion will be considered here. That of particle settling is negligible during the measurements (section 2.3.3). In the following sections, a discussion of the sources of error is given, with an effort to quantify the uncertainty in velocity and other fluidic and lymphatic parameters.

4.2.1 Errors associated with the experimental setup

The estimation of experimental setup uncertainty follows the analysis by Lazar et al. [69]. The uncertainty on velocity caused by the experimental setup is given by:

$$\epsilon_u = \sqrt{\widetilde{u}^2 \left[(\frac{1}{L} w_l)^2 + (\frac{-l}{L^2} w_{L1})^2 + (\frac{-l}{L^2} w_{L2})^2 + (\frac{l}{\lambda_d L} w_{\lambda_d})^2 \right] + (\frac{-\widetilde{u}}{\Delta t} \frac{l}{L}) \left[w_{t1}^2 + w_{t2}^2 \right]} \quad (4.1)$$

The first term in square brackets under the root represents optical uncertainty and the second represents uncertainty caused in the light pulses and the pulse generator. Optical uncertainty is due to the uncertainty of the calibration scale (first term in round brackets), the uncertainty of the calibration scale length on the sensor, due to calculation of the distance on the image and the aberrations of the image (second and third term, respectively) and the error of the distance of the image plane to the camera sensor. Table 4.1 gives the description of the parameters of equation 4.1, their units, and their values.

Table 4.1: Assumptions on parameters for experimental uncertainty estimation

Parameter	**Symbol**	**Value**	**Unit**	**Note**
Calibration scale length	l	0.5	mm	Physical length of scale
Calibration scale image plane length	L	872.17	px	Measured on the image in Matlab
lens focal length	f	8	mm	Typical value for M20x objective
Distance from calibration scale to camera lens	λ_d	∞	mm	The distance of the calibration to the camera lens is of course finite, however it is much larger than l
Scaling magnification factor	ψ	5.733×10^{-4}	mm/px	Calculated from equation $\psi = l/L$ [69]
Accuracy of scale	w_l	10	μm	From microscope micrometer scale specification
Depth of field	DOF	8.3	μm	Typical value for M20x objective [1, 116]
Uncertainty of λ_d	w_{λ_d}	4.15	μm	Assumed as half the DOF
Uncertainty of L	w_{L1}	1	px	Assumed value
Uncertainty due to image abberations	w_{L2}	4.36	px	Assumed as 0.5% of L
Uncertainty of LED pulse timing	w_{t1}	2	μs	Assumed to be the sum of the LED rise and fall times
Delay generator uncertainty	w_{t2}	10	ns	Taken from TTL specifications
Particle velocity	$\widetilde{u}$	5-10	px/frame	The maximum velocity of particles between was 5-10 px to comply with the PIV quarter rule. Using the calibration scale and known Δt velocity can be converted to mm/s

Using the values of table 4.1 the uncertainty is plotted in figure 4.1a. It is estimated to be in the range of 7 to 120 $\mu m/s$ at high velocities (high ΔP_{axial}), while in low velocities (low ΔP_{axial}) the uncertainty would be in the range of 2.8 to 17 $\mu m/s$. This is a only a fraction of the the velocities observed in the lymphatic μ-PIV experiments (figure 3.28); overall the relative uncertainty due to the experimental setup is in the range of 1 to 2.2%, as shown in figure 4.1b.

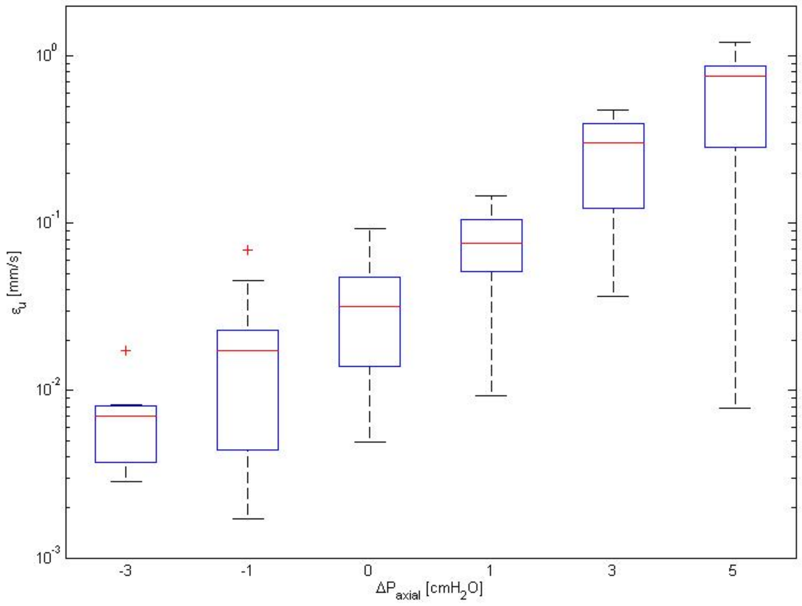

(a) Measurement uncertainty in maximum velocity

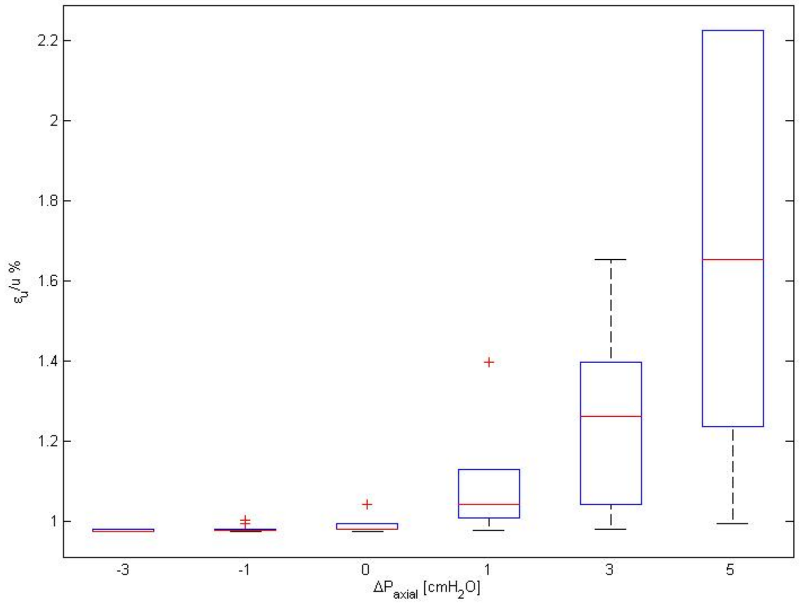

(b) Relative uncertainty in maximum velocity

Figure 4.1: Absolute and relative uncertainty due to the experimental setup

4.2.2 Effects of optical setup on spatial resolution

The optical setup directly affects the attainable spatial resolution of the μ-PIV system [62]. In particular the selected microscope objective and camera pixel size determine the particle diameter on the camera sensor. As a general guideline this diameter must be approximately 2-4 pixels; if the particle image size on the sensor is smaller than 1 pixel, then it will fill an entire pixel but the exact location of its centre within that pixel cannot be determined, thus creating an uncertainty on the displacement calculation between frames. On the other end, a large particle image diameter on the sensor creates another problem. Large particle images may be divided between IWs, reducing the spatial resolution. In this case the reduction in spatial resolution is also a function of IW size; smaller IWs increase the error.[32]

The particle image size on the sensor, for a particle on the focal plane and assuming no aberrations is given by Olsen and Adrian [100], which is in good agreement with experimental results by Rossi et al. [123]

$$d_\tau = \sqrt{(M \cdot d_p)^2 + (2.44 \cdot f_\#(M+1)\lambda)^2} \tag{4.2}$$

where, M is the microscope magnification, $f_\# = 1/(2NA)$ is the f-number, NA the numerical aperture of the objective, λ the wavelegth of the light and d_p the physical particle diameter. For the current setup, $M = 20$, $NA = 0.25$, $\lambda = 620\,nm$, pixel width 17 μm and $d_P = 1\ \mu m$, which yields $d_\tau = 66.9\ \mu m$. The pixel size is $17\mu m$, thus the particle diameter is approximately 4 pixels on the camera sensor. Hence, the particle image diameter is within the empirical estimate for optimum performance; the measurements uncertainty in particle displacement is lowest in this case, approximately 0.02 px to 0.04,[33] determined by Monte Carlo simulations [116]. Bias error due to pixel-locking is also not present in the measurements under such conditions [1].

There are several ways of increasing the spatial resolution.[34] The resolution can be increased by an image pre-processing filter that reduces the particle diameter [62], but in any case the image diameter should not drop below 2-4 pixels. Using ensemble correlation, that is, averaging

---

[32] The random error on particle error location also increases linearly, at least with standard PIV cross-correlation

[33] Recent work by Sciacchitano et al. [129] actually shows that this error is lower in windows deformation PIV algorithms, even below 0.01 px. PIVlab employs such an algorithm

[34] The term spatial resolution here refers to the accuracy in measuring the particle displacement between frames. In PIV there is also a second aspect of spatial resolution, that is, the number of velocity vectors in the FOV. This is influenced by the IW size and IW overlap. In this work approximately 10 vectors along the diameter are achievable at the EDD.

the correlation of several pairs of frames is not applicable when temporal variations of the flow occur during the vessel contraction. Reducing the working distance of the objective can increase the spatial resolution as is the use of high numerical aperture objectives. However, commercially available microscope objectives with high NA, are also of high magnification, which reduces the FOV. Moreover, the side scattering illumination configuration that removes the vessel wall from the background is rendered ineffective; the large angle of light collection that comes with high NA allows the light scattered be the vessel wall to be collected by the objective. This was verified with a M40x, NA 1.3 objective. Alternatively, fluorescent imaging can be used, provided that the light source is improved as recommended in section 6.1.

Finally, using a camera with smaller pixel size and larger sensor will increase the spatial resolution and may also allow the use of smaller particles. The benefit of smaller particles (0.5-0.75 μm) is that settling will be even less and for a given size of IW a larger number of particles will be present, thus improving the cross-correlation procedure. Use of smaller IW may also be possible, yielding a larger number of vectors per vessel diameter.

4.2.3 Numerical uncertainties

In section 4.2.1, equation 4.1 was used to quantify the velocity uncertainty due to the effects of the experimental setup. In PIV the algorithm itself is a source of uncertainty, an uncertainty that is related to the effects of the optical setup on spatial resolution discussed in section 4.2.2. The uncertainty in estimating the particle position in each frame, obviously affects the estimation of velocity through equation:

$$\mathbf{v} = \frac{\Delta \mathbf{X}_p}{\Delta t} \tag{4.3}$$

The velocity in PIV is first order accurate[35] , that is the particle displacement is divided by the time separation of the two successive images. The error in Δt is neglected for simplicity. Hence the error in the velocity measurement is proportional to the error in estimating the particle image displacement between frames.

Errors in PIV measurements can be divided into bias and random errors. Bias error is due to pixel-locking which is not present in the measurements of the present work, as explained in

---

[35] Second order PIV algorithms do exist, but require the acquisition of triple-paired images to measure acceleration

section 4.2.2. The random error has been studied by Westerweel [154] and Sciacchitano et al. [129]. The main sources of random errors are:

1. In plane particle displacement
2. Particle image diameter
3. Particle image density
4. Out of plane motion

The exact value of random errors is not *a priori* known in PIV measurements and they depend on the choice of PIV analysis algorithm. PIVlab uses a algorithm which is more accurate than a simple cross-correlation implementation. However, to the author's knowledge, details on PIVlab performance in terms of random errors have not yet been published by the software developer.[36] It is expected that the rms displacement error in PIVlab will be of the same order of other window deformation implementations [129]. However, due to the lack in information, the velocity error analysis has been performed with rms displacement error values for both standard algorithms [1, 154] and window deformation (WD) ones [129].

The values of the RMS errors for the two different algorithms are shown in table 4.2. The in plane velocity was assumed to be 5 px, the particle image diameter was 4 px and the image density was taken equal to 10 particles per interrogation window. The value of out of plane motion assumed for both the standard and WD algorithms corresponds to 40% out of plane motion with respect to the light sheet thickness; this is perhaps too exaggerated for this case and presents an upper limit value.[37] Owing to the low Reynolds number of the flow the displacement gradient error was assumed to be zero. The total displacement RMS error is assumed to be equal to the square root of the sum of squares of all RMS error components. The velocity uncertainty due to the PIV algorithm is thus given by:

$$\epsilon_d = \frac{\Delta \mathbf{X}_{RMS}}{\Delta t} \cdot \psi \tag{4.4}$$

where ψ is the calibration factor to convert velocity into mm/s.

---

[36] http://pivlab.blogspot.co.uk/p/pivlab-documentation.html, accessed 22/02/2014.

[37] Strictly speaking there is no light sheet in μ-PIV, but the entire volume is illuminated. The light sheet thickness can be thought of been formed by the focal plane of the microscope objective, which has a finite thickness. In μ-PIV, out of plane motion will decrease in the correlation signal peak height [101]

Table 4.2: RMS displacement error

RMS displacement error	Standard Algorithm [1, 154]	Window Deformation [129]	Units
In plane displacement	0.15	0.02	px
Particle image diameter	0.08	0.01	px
Image density	0.05	0.01	px
Out of plane motion	0.1	0.08	px
Total RMS error	**0.2**	**0.08**	px

The results of the velocity error analysis is shown in figures 4.2a and 4.2b, for the Window Deformation (WD) and Standard PIV algorithms, respectively. It is apparent that even standard algorithms have exceptional performance and the error in velocity measurement is small.

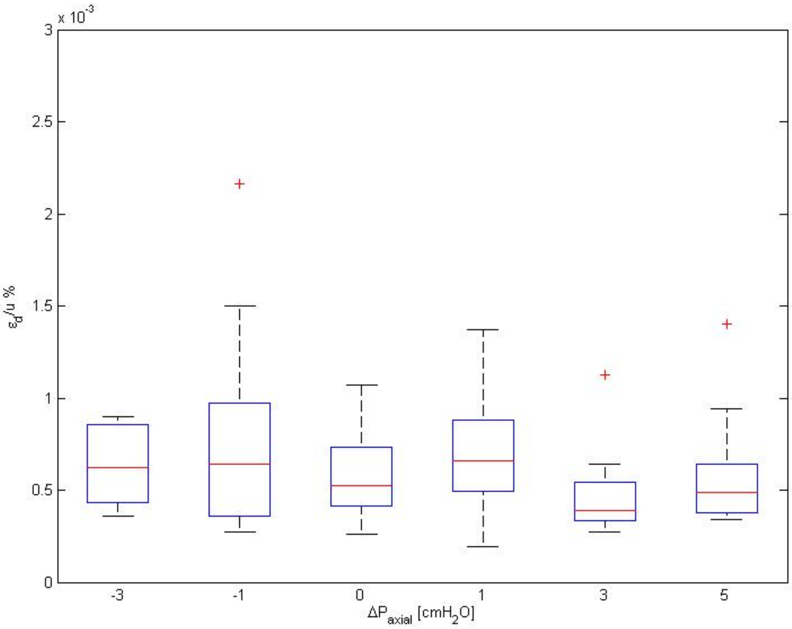

(a) Uncertainty due to particle location estimation, assuming WD PIV algorithm

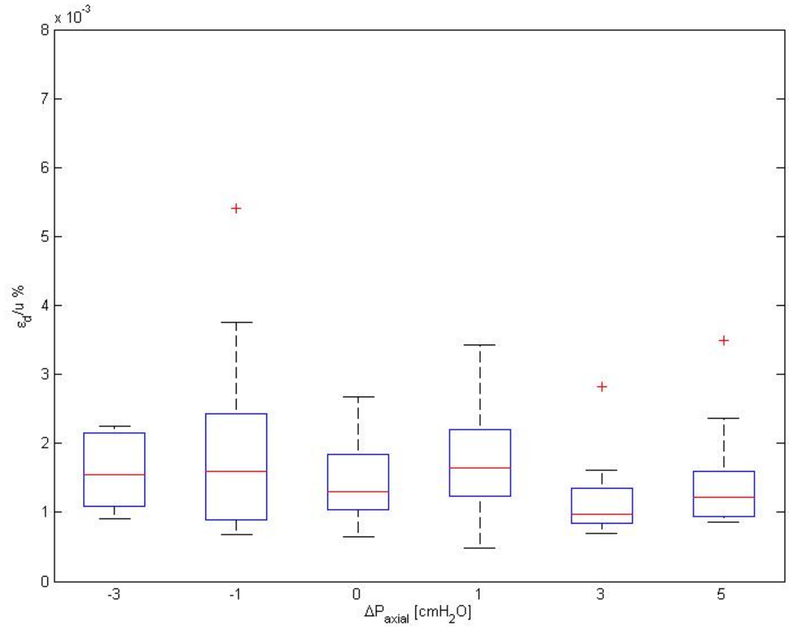

(b) Uncertainty due to particle location estimation, assuming standard PIV algorithm

Figure 4.2: Uncertainty due to particle location estimation

4.2.4 Random errors associated with Brownian motion

The error due to Brownian motion is of interest in micro-flows. Santiago et al. [125] has quantified this error

$$\epsilon_b = \frac{1}{u} \cdot \sqrt{\frac{2D}{\Delta t}}$$

where u is half the maximum velocity [132], D is the Stokes-Einstein diffusion coefficient[38] and Δt is the pulse separation time. Figure 4.3 shows the relative error due to Brownian motion at different axial pressure gradients. This error is negligible and this is not surprising as in general Brownian motion errors become a consideration for particles smaller than 500 nm in diameter and velocities below 1 mm/s [152].

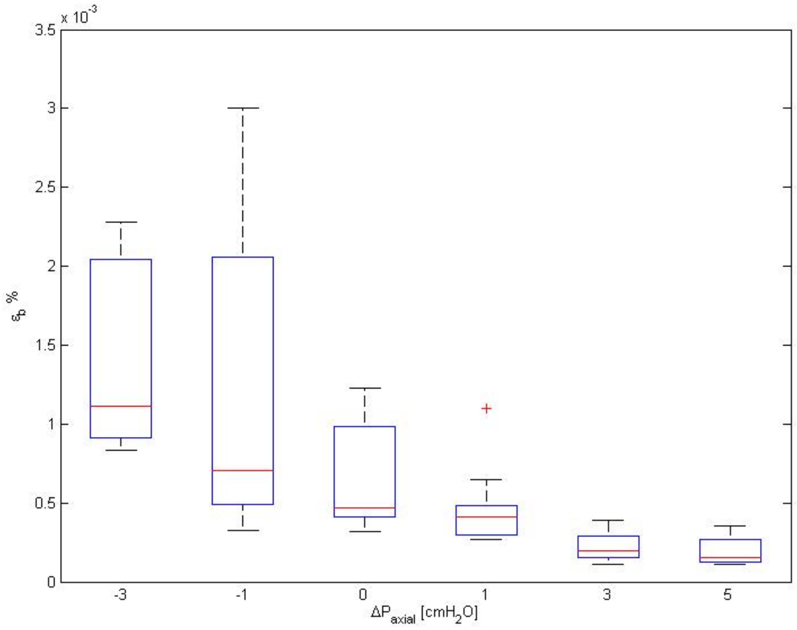

Figure 4.3: Relative error due to Brownian motion with respect to ΔP_{axial}. Calculation based on one half the maximum velocity.

4.2.5 Cumulative error in velocity determination

The total velocity uncertainty can be calculated from the square root of the sum of squares of the uncertainties from all sources, which implies the assumption that all uncertainty sources are independent. Thus the total uncertainty ϵ_t is given by:

---

[38] $D = \frac{k_B T}{3\pi\mu d_p} = 6.7 \cdot 10^{-13}\, m^2/s$

$$\epsilon_t = \sqrt{\epsilon_u^2 + \epsilon_b^2 + \epsilon_d^2} \tag{4.5}$$

Figure 4.4 shows the total uncertainty calculated for the maximum velocity. At negative axial pressure gradient the errors due to brownian motion dominate the relative uncertainty. As the driving force of flow is increased particles are moving at higher velocities and are less affected by Brownian motion; the low Δt in this case increases the uncertainty of velocity measurement. Overall, the total uncertainty is below 6%.

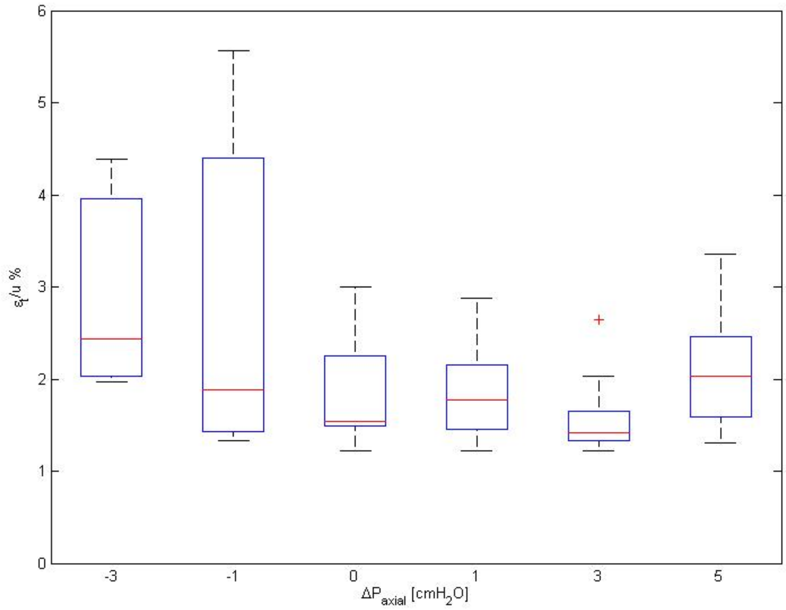

Figure 4.4: Total relative uncertainty

4.2.6 Effects of particles on viscosity

The addition of solid particles increases the viscosity of the APSS solution. The value of viscosity is important in WSS and Reynolds number estimation. For a given volume fraction ϕ of particles in a liquid the relative viscosity is given by Einstein's equation for very low concentrations [33] (cited in Mooney [90]):

$$\mu_r = 1 + 2.5 \cdot \phi \tag{4.6}$$

and by the modified equation by Guth and Simha [52] (cited in Mooney [90]) which takes into account particle interactions:

$$\mu_r = 1 + 2.5 \cdot \phi + 14.1 \cdot \phi^2 \tag{4.7}$$

The volume fraction was $\phi = 0.5\%$ and substituting this value on the equations above yields an increase in viscosity of 1.25% and 1.29%, for the Einstein and Guth/Simha model, respectively. This increase was considered to be negligible and was not taken into account in the results presented in chapter 3.

4.2.7 Fluid mechanical considerations

In general, the fluidic system is not expected to have a significant adverse effect on the accuracy of the measurements. There are, however, two aspects of the system that may have some impact. First of all, the micro-pipettes used in cannulation of the vessels, although carefully selected to have equal resistance, were slightly inclined towards the bottom of the vessel chamber. This angle was approximately 5-8 degrees. However, the entrance length[39] for the Re number for these experiments guarantees the small entrance length (figure 4.5) of the flow and it is expected that the disturbance of the micro-pipette in the flow is negligible at the site of measurement which is at least one lymphangion length[40] downstream of the inflow pipette.

The second cause of concern is the adjustment of the inflow and outflow pressures. This was achieved by manually moving two reservoirs, supported by a string and pulley system. This system was calibrated and a pressure scale was marked on it, but since the adjustment was manual it is a source of operator's error. The axial pressure gradient and average pressure are, then, also random variables and not categorical as treated in the present context.

4.2.8 Errors associated with the uncertainty in diameter estimation

In order to quantify the error of the diameter estimation the same process as the frequency estimation error must be followed, that is, the diameter is traced manually to establish the baseline criterion for error assessment. The result of the automatic estimation is then compared with the baseline. Ideally, this process should be performed for a large number of images for different

---

[39] Entrance length is defined as $L_e = 0.06 \cdot Re \cdot D$ for laminar flow

[40] The length of the rat mesenteric lymphangion is 8 to 10 times its diameter on average, that is, between 0.8 and 1 mm in length

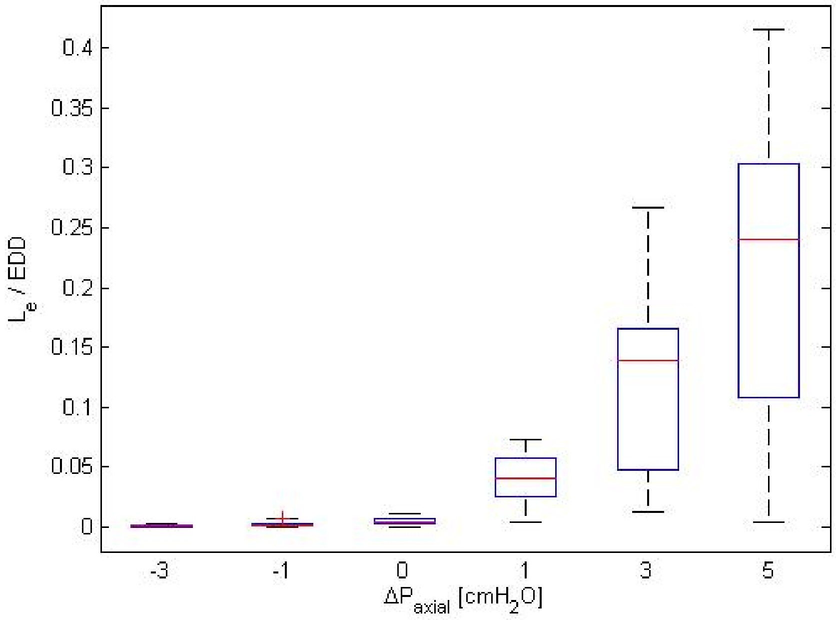

Figure 4.5: Entrance Length L_e normalized with the EDD. The entrance length is less than half the EDD of the vessels, that is approximately 50 μm. Therefore the distance of the measurement plane from the inflow/outflow pipettes is large enough for entrance effect to dissipate.

vessels and at different times during contraction. Given the fact that each PIV measurement consisted of 300 to more than 1000 pairs of frames, this would have been a very laborious task. The algorithm's employed would have made this process even more time-consuming; since it was necessary to mask the vessel wall, the entire internal diameter had to be detected. In contrast, other algorithms [25, 72] track the diameter only at a narrow window selected by the operator.

A rigorous error assessment of diameter measurement uncertainty has not been carried out in the present work. During image analysis the result of the vessel wall detection was overlayed on the PIV image and the algorithm parameters were adjusted to qualitatively obtain a satisfactory result. Examples are shown in figures 2.17c, 2.18c and 2.19c. The Canny edge detector is considered to be one of the most accurate edge detection algorithms [108]. Assuming an error of $\pm 5\ px$[41] in diameter estimation and given the range of minimum and maximum lymphatic diameters (figure 3.36) is approximately between 40-170 μm (70-300 px) the relative error in flow rate is (equation B.3) between 14% to 3% for 70 and 300 px diameter on the image plane, respectively.

EF and CAMP are two other quantities affected by the diameter uncertainty. However, the

---

[41] Probably this is a very exaggerated value of error in diameter estimation

analysis of EF and CAMP uncertainty is not straightforward, due to the fact that the uncertainties of EDD and ESD are not independent [55]. The error in diameter depends on the selection of parameters for the edge detector algorithm, which in the case of Canny edge detection constitutes of the standard deviation of the Gaussian filter and two threshold values. The Gaussian filter blurs the image and the threshold values determine whether a pixel is classified as edge or background. The edges detected lie always on the same side of the true edge for a given set of parameters for both the EDD and ESD.

4.2.9 Wall shear stress estimation

Wall shear stresses are a very difficult quantity to measure. Particle concentration is lower close to the wall and the seeding becomes inhomogeneous. Reflections from the wall are also present and cause noise in the PIV image. In the particular application the wall motion complicates the WSS estimation even further. Techniques such as the single-pixel ensemble correlation cannot be used; perhaps they can be of use only during the end diastolic phase of the contraction cycle, when the vessel is at its EDD. However, even when and EDD plateau is present the diameter may increase slightly towards the start of contraction (See figures in section 3.2).

The difference in theoretical to experimental WSS depicted in figure 3.33 can be attributed to a number of sources. First of all, the accuracy of WSS estimation depends on the accuracy of the vessel wall detection. A thorough quantitative study of the accuracy of the algorithms has not been conducted. Such a study has the same problem faced in the study of the accuracy of the automatic frequency estimation, that is, there is no other method available, other than manually locating the wall and comparing the manual observation (in itself not lacking of errors) with an automated one. During, automatic masking, PIVlab was modified to show the result of the wall detection on screen and through manual observation the algorithms appeared to have a good degree of accuracy, at least qualitatively.

In addition, WSS estimation accuracy is affected by the choice of PIV correlation method [63]. In fact, as shown by Kaehler et al. [63], window deformation based correlation methods, as is the one employed, exhibit a bias error proportional to one-quarter of the IW size at the wall and reduces to zero at a distance of half the IW size from the wall. This bias is systematic and perhaps can be removed, but this has not been performed here.

Finally, the theoretical WSS value assumes a parabolic velocity profile with a ratio of maximum to average velocity of 2. The PIV measured velocity profile maximum to average ratio may deviate from this value, as shown in figure 3.29, and the reasons for this are most likely the non-straight vessel wall, as well as experimental errors in velocity estimation near the wall.

4.2.10 Pressure estimation

The pressure estimation algorithm employed in the analysis of the lymphatic PIV data has been characterized by the authors of the algorithm.[42] The algorithm was characterised in terms of global errors, boundary conditions/interfaces and spatial/temporal convergence and was shown to behave quite well, with errors in the benchmark test cases of less than 10%. Higher errors may occur in PIV measurements with very noisy velocity data, high gradients of velocity near boundaries or out of plane motion; the data collected in lymphatics do not seem to be affected by the aforementioned issues.

4.3 Vessel motions

Vessel motions along, about or orthogonal to its longitudinal axis may interfere with the μ-PIV measurements. Vessels may exhibit axial motion along or rotation about their longitudinal axis during contraction. It is also possible that the vessel moves orthogonal to the camera FOV. Orthogonal motion of the vessel was observed in combination with rotational motion during contraction. Rotational motion caused the most severe interference with the flow measurement, due to the fact that the vessel wall came into focus and obscures particle visibility. When such rotational motion was observed, the vessel was uncannulated and re-cannulated on one end in order to relieve some of the residual stress in the smooth muscle fibres that may be introduced during tightening of the sutures used in the cannulation. When it was not possible to reduce the rotational motion to a degree that particle visibility was not obscured, these measurement were discarded.

The code used to estimate the lymphatic and fluidic parameters did not account for vessel motions; this is left for future work. Therefore it is expected that there will be an error associated with vessel motions in those measurements were such motion is significant. Vessel motion may be taken into account by employing advanced vessel wall detection algorithms that will be able to detect vessel motion and not just the vessel inner wall boundary, as was done in this thesis.

---

[42] For further details see the work by Dabiri et al. [24] and the associated supplementary data.

An alternative approach that may reduce the error in flow rate determination due to vessel motion is to perform a Control Volume (CV) analysis over the FOV [59]. The CV approach is defined by equation 4.8, which simply states that the mass balance entering and exiting the CV from the Control Surface (CS) (left hand side) equals the rate of change of mass within the CV (right hand side):

$$\int_{CS} \rho(\mathbf{V} \cdot \mathbf{n}) dA = -\frac{d}{dt} \int_{CV} \rho d\bar{V} \tag{4.8}$$

The approach used in this work (Section 2.4.4), that is, integrate the velocity profile at a cross section in the middle of the FOV is simple in its implementation, but suffers from vessel motion. Both approaches assume that the vessel has a circular cross section.

4.4 Main findings of μ-PIV in lymphatic vessels

From the time series of fluidic parameters and lymphatic diameter presented in section 3 several observations can be made. At positive ΔP_{axial} the flow rate follows the diameter curve, that is, contraction inhibits flow and distension allows fluid to pass through. Contraction does not contribute to the net flow, a finding that is in-line with the observation of Dixon et al. [30].

The flow rate curve appears to follow the diameter tracing faithfully during distension or contraction, as figures in section 3.2.1 demonstrate. In most figures in this section there is no discernible time difference however between the diameter tracing and flow rate curves, however figures 3.6a and 3.8a clearly shows a time lag between d and Q.

The method employed is also able to show the out of phase contraction of adjacent lymphangions, albeit indirectly. By having an excellent temporal resolution, out of phase contractions can be identified by a sudden drop in flow rate during the EDD phase of contraction. The time lag between the Q and d curves during contraction may also be attributed to out-of-phase contraction of adjacent lymphangion.

At zero pressure gradient there is no flow at the relaxed lymphangion state. Positive flow occurs during distension and contraction. As figure in section 3.2.2 show the largest amount of volume is pumped during distension and not during contraction. However, this is not a general case, as there may be significant volume of fluid been pumped during contraction, as well (figures 3.9 and 3.11a).

The shape of the contraction shows different patterns. During contraction at positive and zero axial pressure gradient distension and contraction constitute a small amount of the overall contraction period; the vessel remains at its EDD most of the time (plateau of diameter curve, see figure in sections 3.2.1 and 3.2.3). In contrast, at negative ΔP_{axial}, the plateau may disappear and the diameter curve attains a shark-tooth shape (figures 3.13 and 3.16). However, this is not a general case and contraction with a plateau at the EDD is still possible at negative axial pressure gradient (figure 3.14).

The necessary temporal resolution as a function of ΔP_{axial} is shown in figure 4.6. As expected, the higher the flow driving force, the lower the temporal resolution has to be to capture the velocity. It may also be observed that there is quite a large deviation of data from the mean at each value of axial pressure gradient. This is due to variation of vessel diameter and occasionally from lymphangion to lymphangion of the same vessel. It could be also attributed to the uncertainty in inflow and outflow pressure adjustment. Another potential source of this variation is the cannulation micro-pipette resistance, but the experiments on lymphatic vessels were carried out with the same set of resistance-matched micro-pipettes.

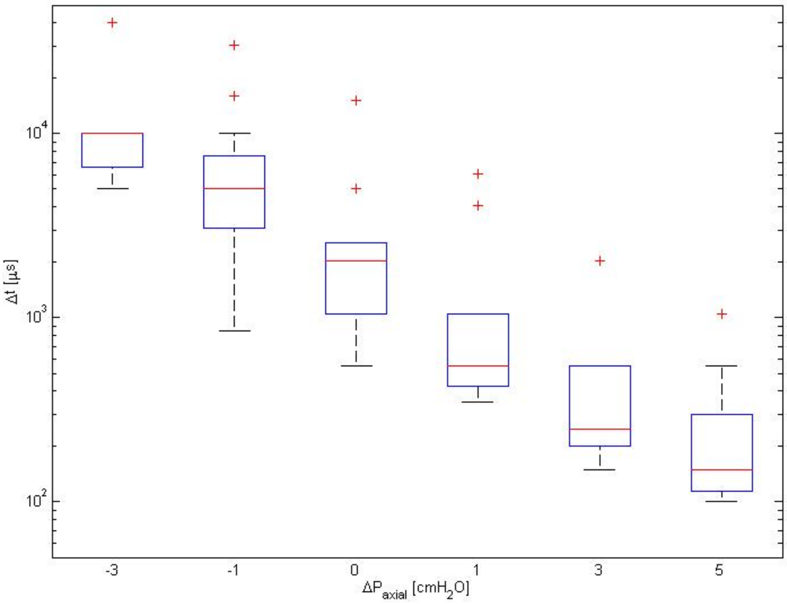

Figure 4.6: Temporal resolution with respect to axial pressure gradient

Figure 4.6 again shows the benefit of employing frame-straddling to measure the instantaneous velocity inside lymphangions The median Δt is 10 ms for $\Delta P_{axial} = -3\ cmH_2O$. Without frame-straddling a camera at working at 100 fps would have been necessary. At this ΔP_{axial} this is not very restrictive, but with frame-straddling the velocity can be measured with much lower fps, resulting into less data to process for a certain measurement duration, or allowing PIV measurements for longer periods of time. On the other extreme, at high positive axial pressure gradients, 10k fps would be necessary without frame-straddling, resulting in a large number of pairs of frames and reducing the measurement duration due to camera memory limitations. Thus, the method by Dixon et al. [30] would be challenged at high positive axial pressure gradients; even at zero gradient a camera with 1000-2000 fps capability is generally required. On the other hand this is not a concern with the current method, as the temporal resolution is mainly limited by camera inter-frame time. Modern PIV cameras can achieve an inter-frame time of the order of nanoseconds.

Finally, in sections 3.3 and 3.6.6 evidence were provided that invalidated the assumption of negligible radial vessel wall velocity with respect to fluid velocity during contraction, at least for a range of hydrodynamic conditions. These conditions, at zero and negative axial pressure gradient are thought to constitute the hydrodynamic conditions at which most lymphatic vessels function in physiological conditions, although positive axial pressure gradient can occur during digestion in the mesentery.

4.5 Correlation of results with lymphatic literature

As already discussed, there are only a few experimental flow measurement in lymphatic vessels, therefore there is a limited amount of data that the results of the present thesis may be compared to. The correlation with the previous studies by Dixon et al. [30] becomes more complicated by the fact that the pressure gradient driving the flow is not known in the *in situ* measurements. Moreover, lymph is a much more viscous fluid than the physiological solution used in the μ-PIV experiments (1.5 cP for dog lymph vs approximately 0.72 cP for water [30, 65]). Therefore, although the results will be compared with the literature in this section, no definitive conclusions can be made.

The average velocity *in situ* was found to be 0.9 mm/s and velocity peaks of 2-9 mm/s were observed. The velocity was also found to be 180^o out-of-phase with contraction. Much higher velocities of up to 40-45 mm/s were recorded in the *in vitro* experiments at $\Delta P_{axial} = 5cmH_2O$, as figure 3.28 indicates. However, the velocity versus time graphs presented in figures in sections 3.2.1 through 3.2.3 do not show the 180^o phase difference reported by Dixon et al. [30]. The average flow rate *in situ* was 14 $\mu L/hr$ considerably lower than the 145 $\mu L/hr$ (52.5 $\mu L/hr$ median value) measured *in vitro* (see figure 3.30).

Dixon et al. [30] found average values of WSS to be in the range of 0.4-0.6 dyn/cm^2 and peaks of 3-10 dyn/cm^2 calculated assuming fully developed laminar flow, *in situ*. Assuming laminar flow, WSS calculated with the present method can reach much higher values, as shown in figures 3.33b and table 3.1b. Calculating the WSS directly from the PIV velocity field gives significantly lower values on average than assuming laminar flow, but still the values obtained are higher (especially peak values) than those reported by Dixon et al. [30]. Of course direct comparison cannot be performed; whereas in this study there was control over input/output and average pressures, there was no control or knowledge of these pressure values in the *in situ* experiments.

4.6 Correlation of experimental results with mathematical models

The experimental μ-PIV data can be used to validate mathematical models of lymphatic system. The first model of a lymphangion and of the human lymphatic system is due to Reddy and co-workers [117, 118, 119]. Direct comparison, however, cannot be made, as the data used were not for rat mesenteric lymphatics, and no lymphatic diameters versus time were reported.

Since the pioneering work by Reddy and co-workers, mathematical modelling of collecting lymphatic vessels, received little attention. Interest in mathematical modelling of the lymphatic system has re-ignited recently, with several attempts of modelling lymphatic initial and collecting vessels, reviewed in Margaris and Black [82].

The model developed by Macdonald et al. [80] shows results qualtitatively similar to what was frequently observed experimentally at negative pressure gradients, that is, positive flow occures during vessel distention and contraction. In fact, the characteristic pattern of the flow curve depicted in section 3.2.2 is qualitative similar to the one obtained from the mathematical model, assuming a very small phase difference in the contraction of adjacent lymphangions [79]. When the phase difference was set to $\phi = \pi$ the flow rate changed, with no flow at all during two successive contraction cycles. A similar behaviour was not observed during the μ-PIV experiments.

Linear models, such as the one by Venugopal et al. [149], may not adequately describe the $Q - \Delta P_{axial}$ over the entire range of ΔP_{axial}, as the relationship appears to be non-linear on inspection of figure 3.30. A more complex model, based on the one previously mentioned, was developed by Quick et al. [114]. The temporal pattern of Q is different from the experimental results, that is, there is absense of flow during distention. This may be due to the simple description of the valves.

Bertram et al. [11] developed a non-linear lumped model with the valve function governed by a sigmoidal function. Qualitatively, the results correlate with the experimental measurements, although only a peak during distention is shown in the published results. However, this may be only a matter of parameter selection in the mathematical model.

4.7 Pressure and P-V loops

Using the developed flow measurement system the temporal changes of pressure and volume were measured and it was thus possible to obtain pressure volume curves during the contraction of lymphangions. Pressure measurement proved to be quite noisy in certain cases; an expected result since experimentally measured velocity gradients are used to estimate pressure. However, despite the noise, very interesting P-V curves were obtained. On inspection of the P-t and P-V curves in section 3.4 in contrast with a typical cardiac cycle shown in figure 4.7, a fundamental difference can be observed. Whereas in the cardiac contraction cycle only one pressure peak is observed in the P-t curve, in most cases in lymphatic vessels, two pressure peaks exist, the first during active contraction and the second during passive relaxation.

Perhaps the difference observed in the P-V loops of lymphangions versus left-ventricular loops lies in the different timings of lymphatic and heart valves. In lymphangions, the one-way valves open/close state is affected by contraction, due to local pressure changes or even perhaps due to tension in the lymphatic wall. An example may be seen in video S5. Despite the fact that the axial pressure gradient is positive, the valve closes during contraction. In contrast, in the heart the aortic valve opens at the non-isovolumic contraction. In addition, the A-V valve has the opposite timing to the aortic one; it is open when the aortic valve is closed, and closed otherwise. In the rat mesenteric lymphatic vessels the evidence show that lymphatic valves have similar timing to cardiac valves only when the afterload is elevated [26]. Moreover, each adjacent lymphangion is likely to have the same mechanical properties as the one upstream; therefore each lymphangion ‘empties‘ in a vessel upstream of similar structural properties. In contrast the ventricle empties in the aorta, a structure with different temporal variations of volume elasticity[43] during the contraction cycle [159].

This difference, which can be attributed to a different physiology between the cardiovascular and lymphatic system, does raise questions on the use of lymphatic functional parameters defined in the same manner as the cardiovascular system. On the other hand, and despite the apparent differences of mechanical properties between the lymphangions and the L-V, cases were the P-V curve in lymphangions resembles that of the L-V have been found as in figure 3.20b.

---

[43] Volume elasticity is synonymous to the bulk modulus in engineering terminology

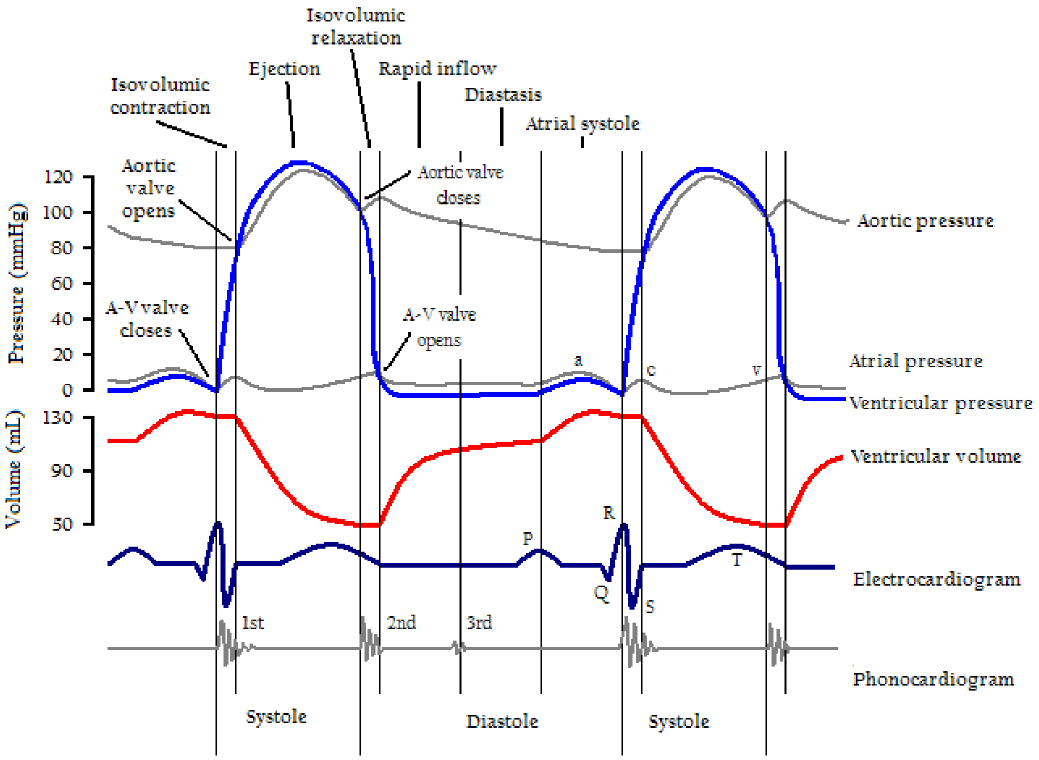

Figure 4.7: Wigger's diagram of cardiac cycles.[44]
a: Atrial contraction, c: Mitral valve bulging, v: Passive atrial filling.
P: Atrial depolarization, QRS: Ventricular depolarization, T: Ventricular repolarization.
1st: Sound from mitral valve closure, 2nd: Sound due to aortic valve closure.

---

[44] Image by DanielChangMD, who revised original work of DestinyQx (CC-BY-SA-2.5, `http://creativecommons.org/licenses/by-sa/2.5`), via Wikimedia Commons. Image is re-used unaltered, `https://commons.wikimedia.org/wiki/File:Wiggers_Diagram.png`, accessed on 03/08/2014.

4.8 Effect of vibrations on lymphatic contractility

One of the most intriguing and also incidental finding from the experiments in lymphatic vessels is the effect of vibrations on the frequency of contraction. Contraction frequency was found to approximately double in the presence of vibrations (figure 3.25b).

This finding only became apparent after the entire set of experiments were conducted. Nevertheless, the results presented in 3.6.1 indicate that statistically the difference in contraction frequency is not random, but due to the air table been activated or not. The exact mechanism remains unclear; presumably the vibrations cause micromotion of fluid inside the vessel which in turn through a shear stress dependent mechanism activates the vessels and increases their contraction frequency. However, this is only a speculation and a totally different mechanism may be responsible for this behaviour.

Establishing the reasons behind the observed increase of frequency with vibrations is not only of potential scientific interest but may also be harnessed for clinical purposes, that is, increase the lymphatic drainage output for oedema resolution. Therefore, this is something that deserves further investigation.

Chapter 5

Conclusions

The results presented in this dissertation, demonstrate the practical application of μ-PIV in measuring the flow field inside contracting lymphatic vessels and valves with high spatial and temporal resolution, that was unattainable by previous studies. In addition, by utilizing LEDs these measurements may be performed at a fraction of the cost of a laser light source, reducing the risk of tissue thermal damage, as well.

In fact, our results indicate that the likelihood of significant damage to the vessel caused by the LED is minimal. In our preparations the vessels attained a physiologic rate of contraction of 6-8 contraction per minute on average. In any case the measurements were performed for no more than 60 seconds at a time, due to camera memory limitations, with short duration light pulses; a considerable amount of light is also lost in the optical system or absorbed from the water bath. It had been possible able to keep the vessels functioning for up to 4 hours.

Accurately measuring the flow field in these vessels will provide insight into their function by way of providing the means of quantifying the fluidic environment and correlating its effect with changes in contractile behaviour. The *in-vitro* setup presented here can be used to study the flow in these vessels, in a controlled hydrodynamic environment using constant inflow and outflow pressures, as performed here, or by automatically adjusting the pressure by means of servomechanisms. Moreover, the effect of other external stimuli can be studied, such as the effect of temperature or chemical agents, under a controlled hydrodynamic environment; this is not easily accomplished in an *in-situ* or *in-vivo* environment.

The μ-PIV experiments carried out revealed an interesting pattern in lymph flow rate. Other studies have shown that as positive axial pressure gradient, contraction inhibits flow rate, but was somewhat unexpected to observe that at zero or negative gradient the largest fraction of volume of fluid pumped by vessels may be during passive distension and not active contraction. Lymphatic pumping has been characterised as been similar to that of the ventricle of the heart, however the experimental evidence presented here does not fully support this theory.

The flow around lymphatic valves has also been visualised (and quantified) with the developed protocol. The detailed visualisation presented here has not previously appeared in the literature. Unfortunately, for reasons related mainly to time and funding restrictions, the number of experiments looking at flow around valves was limited, but the feasibility has been clearly demonstrated. Hence, the present work paves the way for more detailed experiments looking into the flow around valves, its potential mechano-biological effect or simply the estimation of valve resistance, a very important parameter for mathematical models.[45]

With regard to the correlation of the present results with mathematical models of lymph flow, it appears that simple linear models are not adequate to describe the lymphatic pumping behaviour and more complex models are necessary.

The current system does have some limitations in terms of its hardware and software implementation. The hardware implementation limits the FOV and the 2-dimensional nature of the measurement limits the applicability of the measurement in the valve region, however these issues may be somewhat alleviated with appropriate hardware and software. Micro-PIV is a method that has received, and still is, a lot of attention in the scientific community. There are numerous potential improvements of the system described here, both in terms of hardware and software; these have been mentioned in chapter 6. Hence, the work done for this thesis, adds another tool in studying lymphatic biology with a significant potential of improvement and extension.

In conclusion, the key objectives of this work have been met. The developed apparatus and associated software was shown to be able to measure flow inside vessels and in the valve region of lymphatic vessels with great detail. It was also possible to extract important lymphatic functional parameters. It was established that there is great potential in improving the system in terms of hardware and software. Improvements in the latter will allow a second pass analysis of the existing data gathered which may improve the accuracy of WSS and pressure, by using more advanced algorithms. The experiments carried out, involved only the adjustment of the hydrody-

---

[45] Prof. J. Moore, personal communication

namic environment, while other stimuli effects on lymphatic vessels were not investigated. This was due to time and funding limitations. However, the data and results derived can serve as a baseline for comparison with future experiments. Even so, the incidental finding of the effect of vibrations on contraction frequency, which merits a more thorough investigation demonstrates that the methodology employed can offer insight in lymphatic function. The method was not applied *in-situ* or *in-vivo*, though, again due to restriction in terms of time and funding, but the work reported in this thesis can serve as the starting point for such goals.

The research undertaken in the context of this PhD thesis has resulted into findings that have not been reported previously in the literature or that are contradicting published results. The author considers that this is the significant contribution of the present work.

In summary:

1. This is the first report of 2-D experimentally resolved flow fields within lymphatic vessels
2. Eddies around lymphatic valve leaflets have been resolved for the first time since the first report by Florey [36] more than 80 years ago
3. Pressure-Volume relationships and work during active contraction are reported here for the first time.[46] The P-V relationships did not resemble the L-V ones, showing double pressure peaks. Although, the physiological significance of this result is not certain at present, the methodology established herein may be used to further investigate the pressure in lymphatic vessels
4. The results on the ratio of wall radial velocity to the fluid velocity showed that the former is not negligible with respect to the latter, especially when the lymphatic vessels face an adverse pressure gradient, which is thought to be the more frequently occurring hydrodynamic environment *in-vivo*

The incidental, and intriguing finding, that is, the effect of external vibrations on the contraction frequency, is added to the above findings and merits further investigation, which may prove to be of clinical significance.

---

[46] Pressure in bovine and ovine lymphatic vessels has been reported previously by McGeown et al. [85] and McHale and Roddie [87]. The pressure reported was inflow and outflow pressure of lymphatic vessels with several valves, measured by means of pressure transducer. In contrast the pressure estimated in this context is the local pressure within a single lymphangion. Moreover, the results of McGeown et al. [85] and McHale and Roddie [87] were not presented in P-V loop format, nor was the work performed estimated

However, this work did not only produce contributions in the knowledge of lymphatic biology and function under different hydrodynamic environments, but adds a methodology that has extended capabilities over previous studies, has achieved its intended purpose at relatively low cost, while at the same time is based at an established experimental method, namely, μ-PIV. This is perhaps a significant contribution, that balances with those in the biological aspect of this work, as μ-PIV is a method that is under continuous development and is been constantly improved and extended both in terms of hardware and algorithms employed.

Chapter 6

Recommendations for future work

6.1 Improvement of the optical system

There are a number of improvements that can be made to the optical system. The microscope used for the lymphatic vessels experiments had a red dichroic mirror in from of the camera. This mirror directed the red wavelengths towards the camera and the rest of the visible spectrum towards the eyepiece. Therefore, a considerable amount of light power was not directed towards the camera. In addition, imaging only red wavelengths reduces the spatial resolution due to the higher wavelength. In μ-PIV systems it is common to use green fluorescent particles with a green laser. These particles emit in the red spectrum therefore the current system suffers from the same degradation of spatial resolution than any other μ-PIV system.

Still there will be more benefits gained, besides spatial resolution, by directing the entire spectrum to the camera. Blue LEDs may be used; the blue LEDs from the same manufacturer are almost four times more powerful than the other monochromatic LEDs. The white LEDs are essentially blue diodes with a layer of phosphorus that is excited by the blue light and emits light in a broader spectrum; the combined emission makes the LED light white to the observer.

During the development of the LED light source and the experiments in the lymphatic vessels, several different microscopes and cameras were used in three different locations, Glasgow, College station (Texas) and Temple (Texas). It was necessary for the light source to be flexible and be able to couple with all the different systems. To accomplish this the light was delivered via a fibre-optic cable and this results into considerable losses at the cable itself and the LED-cable interface. These losses may be reduced if the LED (with a heat-sink for cooling) is attached directly at the epi-fluorescent module of the microscope, with and appropriate lens to collimate the light beam and direct it towards the microscope objective. This lens may be selected from commercially available components, but a custom lens can also be manufactured. Information can be found in the literature for designing a lens to take advantage of total internal reflection and increase the amount of light collected from the LED [19, 91, 146, 158].

Finally, the driving current of the LED can be increased in the range of 200 A, with custom electronics, without causing damage provided that the light pulse duration remains short. This has been demonstrated by Willert et al. [156] and will allow the reduction of the light pulse duration to measure faster flows and/or allow measurements of fast using fluorescent particles, which has been unattainable with the current system.

6.2 Pressure adjustment system

One source of uncertainty in the measurements that should be removed in future experiments, is the regulation of inflow and outflow pressure. In the present setup this was done by manually adjusting the height of the inflow and outflow reservoirs. The reservoirs were supported by a system of rope and pulleys. The pressure adjustment system had been calibrated previously. Obviously, this method of pressure adjustment is susceptible to parallax error from the operator. Hence, the value of ΔP_{axial} in all the results presented here is not actually a categorical variable, but it is a random variable with a mean and a variance. To alleviate this problem, an electromechanical pressure adjustment system can be constructed. With appropriate design and calibration the uncertainty in pressure setting can be minimized.

6.3 WSS estimation

WSS are an important physiological parameter, and the degree of accuracy of the estimation is affected by both the experimental method/setup and the image analysis algorithm. By using more elaborate techniques WSS estimation will certainly be improved. In respect with the choice of experimental method it appears that, based on recent evidence [1], PTV methods can be superior to PIV in the WSS estimation, for the same experimental setup (optical system, sensor, magnification).

The setup used in the present work can be improved by using a camera with smaller pixel size while at the same time reducing the particle diameter, and increasing the magnification. However, increasing the magnification to 40x will not allow the imaging of scattered light due to the high NA of commercial microscope objectives, hence the vessel wall will introduce noise to the images which in turn will have to be dealt with with appropriate methods [57]. The FOV will also be reduced and it may not be possible to view the entire width of the vessel.

The images collected already may still contain information that has not been extracted yet as a consequence of the software used. PIVlab analysis algorithm does not have means of dealing with the curved boundary of the vessel wall. Taking into account the reduction of spatial resolution close to the wall that is present in any particle tracing flow visualization method, it becomes apparent that the accuracy of WSS estimation will suffer close to the wall. This problem may be alleviated with the use of advanced PIV analysis methods that are specifically designed to handle flows close to curved boundaries, such as the interfacial PIV method. In interfacial PIV the images are transformed via a conformal transformation, such as that the curved boundaries become straight. A one dimensional correlation is then performed on each pixel line in the transformed images. Details of the method are found in Nguyen et al. [95, 96].

6.4 Lymphatic wall stress

In addition to the hydrodynamic stresses exerted on the wall, the tensile stress inside the lymphatic vessel wall itself may be estimated from pressure by using the well known Laplace Law for wall stresses in circular cylinders:

$$\sigma_w = \frac{P \cdot r_i}{d_w} \tag{6.1}$$

where σ_w, P, r_i and d_w are the wall stress, internal pressure, internal radius and wall thickness respectively. This calculation can easily be performed with a simple extension of the rotation algorithm for vessel wall detection. Recall that this algorithm can detect both inside and outside vessel wall edges (figure 2.19a). However, in the current implementation the outer edge was discarded which, in hindsight, was an oversight. By retaining this information the internal diameter and wall thickness at any point along the wall can be calculated and used to estimate the wall stress, potentially extending the developed system beyond flow measurements and into tissue mechanics. Appendix A presents the wall stress per unit wall thickness and for a wall thickness is 16 μm as a first approximation, which will be improved when the wall thickness is measured directly from the PIV data. Wall thickness may depend on the contraction state of the vessels, as does in blood vessels [35], therefore the results presented in the appendix are indicative only. It should be also noted that the validity of the Laplace Law for biological tubular structures has recently been disputed [23].

6.5 Extension to *in situ/in vivo* measurements

The experimental method employed in this dissertation, although applied in *in vitro* experiments, may be extended to *in situ* and *in vivo* measurements. As long as there is optical access to the flow in question, and availability of tracers, μ-PIV may be applied with minimal modification. The need for optical access may be alleviated by using ultra-violet or infra-red emission, but the signal attenuation and loss of spatial resolution have to be considered, respectively. PIV has been extended to echo-PIV using ultrasound. X-Ray and MRI implementations of PIV have also been developed [38]. Tracers may be artificial, but immune cells can also be utilised, with or without fluorescent tagging, and serve as flow tracers. Immune cells may not be the perfect tracers due to their large diameter, however cell trafficking studies are important to study the response of the lymphatic system to physiological and non-physiological stimuli and methods such as PIV can be adapted to that purpose, thus extending the applicability of PIV to physiological measurements.

The work performed herein was restricted to collecting lymphatic vessels, however there is no physical restriction to the size of the vessels. With appropriate adaptation of the method in terms of microscope objective magnification power and tracer size, this method can be applied to initial lymphatic vessels and even perhaps to the more challenging problem of flow within lymph nodes.

6.6 System compliance

In the current experimental arrangement, the vessel was immersed in a bath physiological solution with the surface of this bath open to the atmosphere. Hence, it was not possible to control the system compliance. Such control may be implemented with the construction of a specialized vessel chamber were the top bath surface may be sealed from the environment. A hydraulic circuit may then be constructed that will allow for the regulation of the system compliance.

6.7 Contraction work

The work done by the external forces on the fluid, that is, the contraction work may also be computed by a CV approach. Such an approach is expected to be computationally less expensive than the pressure estimation via numerical integration. The CV work estimation takes the form:

$$\sum F = \frac{d}{dt}\int_{CV} \mathbf{V}\rho d\bar{V} + \int_{CS} \mathbf{V}\rho(\mathbf{V}\cdot\mathbf{n})dA \tag{6.2}$$

where $\sum F$ is the resultant of all external forces. The product of the external force resultant with the volume variation during contraction would yield the contraction work.

6.8 Valve resistance

The experimental results obtained can be used to develop/validate mathematical models. One particular parameter is the valve resistance to flow, for which experimental results are not available. Determining valve resistance is a very challenging measurement especially if one desires to measure the resistance during the opening and closing of valves. That would require an accurate and fast system for inflow/outflow pressure regulation that will work in synchrony with the μ-PIV system. Such a system should be able to measure back flow inside a valve during the fraction of time that the valve remains open when facing a negative pressure gradient. Although this time is short, the author believes that this is within the capabilities of modern hardware and with the appropriate resources available such a measurement is feasible.

Appendix A

Lymphatic wall stress

As discussed in section 6.4 it would have been possible to calculate the wall stress σ_w of the lymphatic vessel wall, using the law of Laplace, equation 6.1. The vessel wall thickness was not calculated from the PIV images, therefore it is not possible to calculate the wall stress, figure A.1 shows the maximum σ_w per unit wall thickness, as a function of the axial pressure gradient. The figure also gives the value of stress, assuming a nominal wall thickness of 16 μm. The average transmural pressure also contributes to the wall stress value, approximately by 1839 (3 cmH_2O) and 3065 (5 cmH_2O) Pa.

Figure A.2 shows the wall stress dependence on P_{avg}. Statistically it was found that the two groups with different transmural pressure have equal medians. Moreover it was found that other parameters, such us the air table activation did not affect the wall stress.

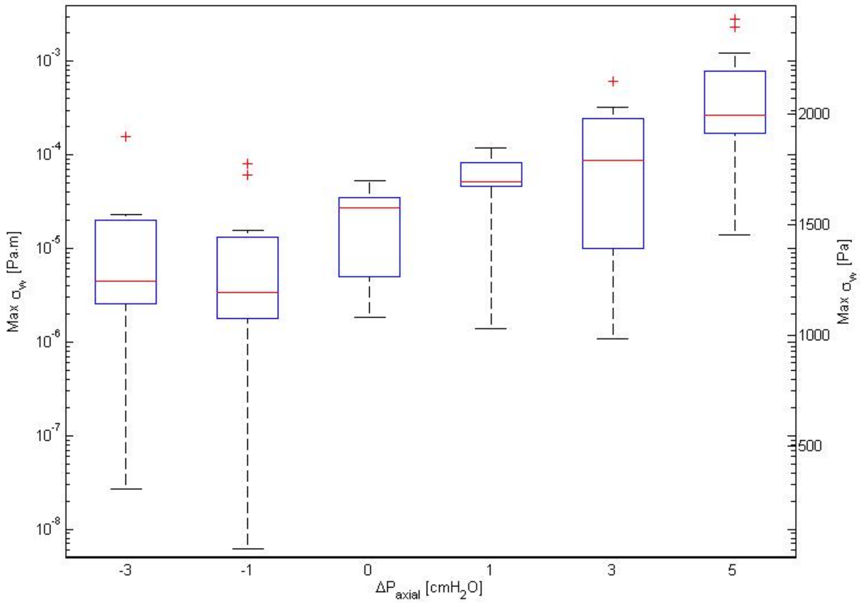

Figure A.1: Lymphatic wall tensile test vs ΔP_{axial} as calculated using the Laplace law. On the left the scale of stress is given as Pa per unit width of wall. On the right the stress in Pa is given for a nominal lymphatic wall width of 16 μm. Scales are logarithmic.

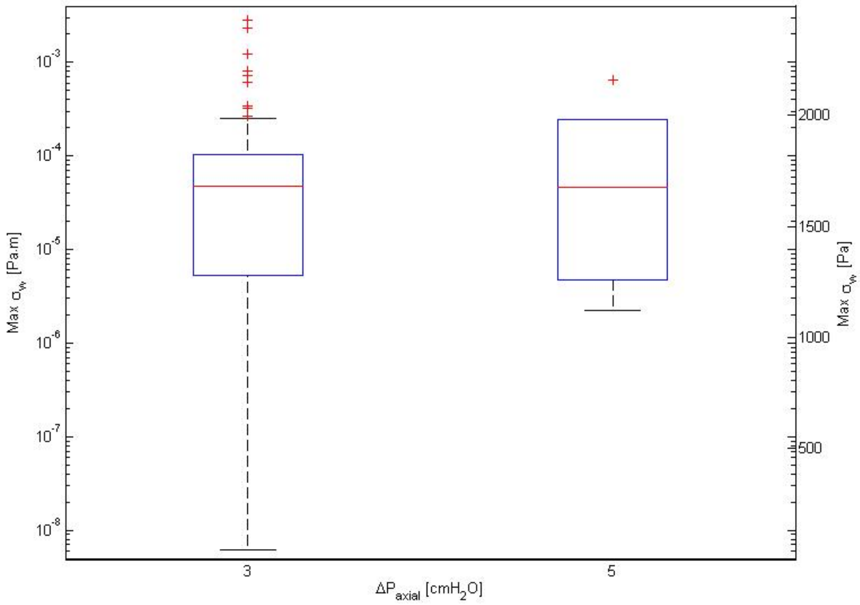

Figure A.2: Lymphatic wall tensile test vs P_{avg} as calculated using the Laplace law. Scales are logarithmic.

Appendix B

Flow rate error

Flow rate is a derived quantity hence contains errors from other directly measured quantities. Flow rate is a function of the diameter $Q = f(d)$ and the error due to diameter uncertainty is given by [139]:

$$\delta Q = \frac{\partial f}{\partial d} \cdot \delta d \tag{B.1}$$

For laminar flow, volumetric flow rate is given in terms of diameter d and average velocity v_{avg}

$$Q = \frac{\pi \cdot v_{avg}}{4} \cdot d^2 \tag{B.2}$$

Differentiating equations B.2 with respect to the diameter and substituting in equation B.1, yields the relationship of the relative error δQ in terms of the absolute value of Q, diameter d and diameter uncertainty δd

$$\frac{\delta Q}{Q} = 2 \cdot \frac{\delta d}{d} \tag{B.3}$$

Equation B.3 simply states that the relative error in diameter produces twice as much relative error in flow rate estimation.

Appendix C

Particle Tracing mode

Using Particle Tracing Mode (PTM) illumination, also referred to as Particle Streak Velocimetry [133], the flow in the valve region was interrogated. Images of fluorescent emmision of particles ($3 \mu m$ diameter) with long exposure times and CW illumination are shown in figure C.1. Due to the long exposure time, particle images appear as streaks. The average velocity of the particles as they travel through the valve region may be computed manually by measuring the particle streak in the image using ImageJ.[47]

Measuring the differences in particle streak lengths it is seen that the velocity of particles approximately doubles inside the valve, owing to their nozzle-like shape, but quickly reduces as the particles exit the valve an enter the much wider sinus region downstream.

Only a few measurements of this type were performed; without an automatic method of computing the velocity the task is too laborious and time consuming to be of practical use.

---

[47] http://rsb.info.nih.gov/ij/

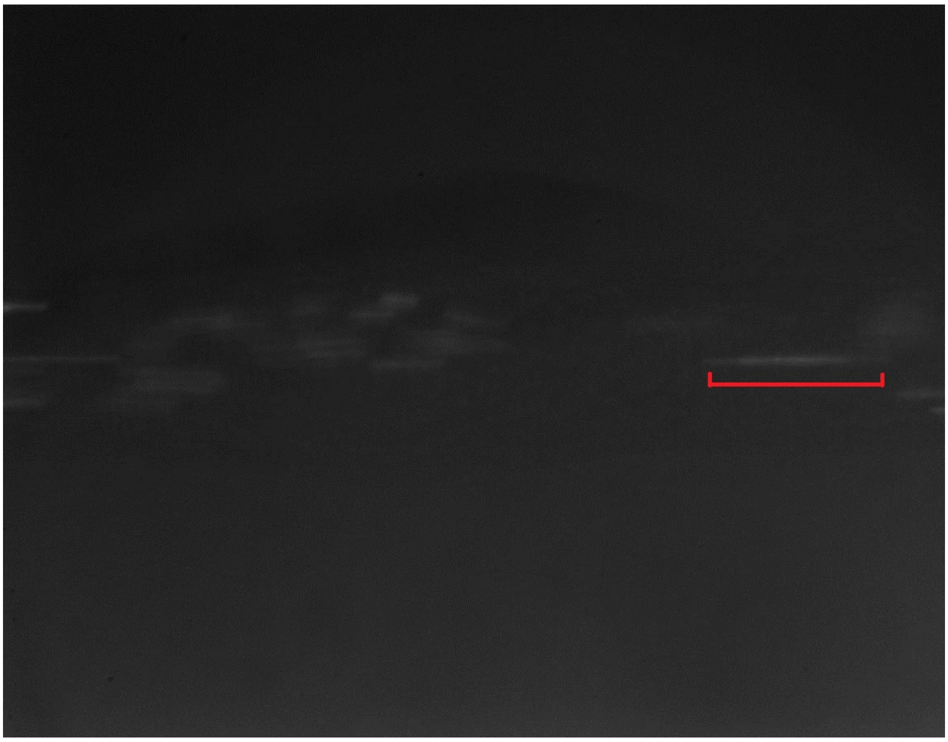

(a) Frame 1

(b) Frame 2

(c) Frame 3

(d) Frame 4

Figure C.1: Result of particle tracing mode. The particle streak is initially located at the centre and right of frame 1 and is denoted by a red line (a). As the particle enters the valve (b) the streak increases in length indicating that velocity increases. At the valve exit the particle slows down due to the expansion in diameter at the sinus region (c). The particle continues with rougly the same velocity (d).

Appendix D

Valve anatomy

Lymphatic valve anatomy differs from heart valve anatomy. Figure D.1 shows examples of rat lymphatic valves. Figure D.1a is a 3-d valve image that was reconstructed from confocal images by Davis et al. [26]. When a valve is viewed under a microscope in brighfield imaging from direction A (Figure D.1a) it appears as in Figure D.1b, which shows a rat mesenteric valve in the open and closed state. However, when a valve is viewed from direction B (Figure D.1a) it appears as in Figure D.1c; the valve leaflets have a semi-lunar shape from this viewing angle. The semi-lunar edge of the valve leaflet is highlighted in Figure D.1d for better clarity. Figure D.1d also points the reader to the location of the buttress structure that connects the valve leaflets to the vessel wall; there is one buttress structure at each side along direction A, but only one is shown in Figure D.1d.

Due to the presence of the buttress structure the valve leaflets are rigidly attached to the vessel wall. As a result the ratio of the valve open area to the vessel EDD is small, approximately 1:7. Lymphatic valves open/close with the leaflets stretching/collapsing along direction B.

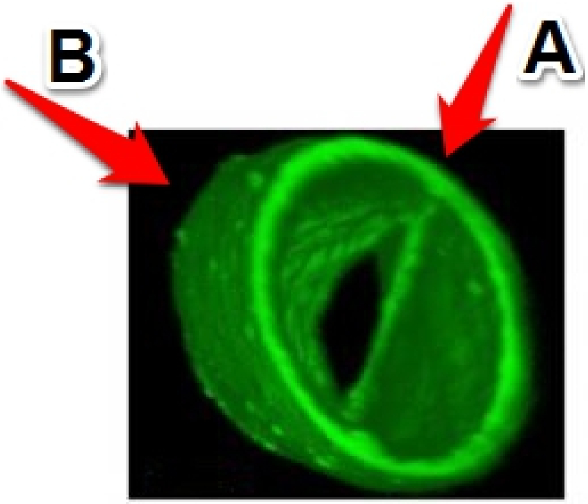

(a) 3-dimensional reconstruction of rat mesenteric lymphatic valve from confocal microscopy.

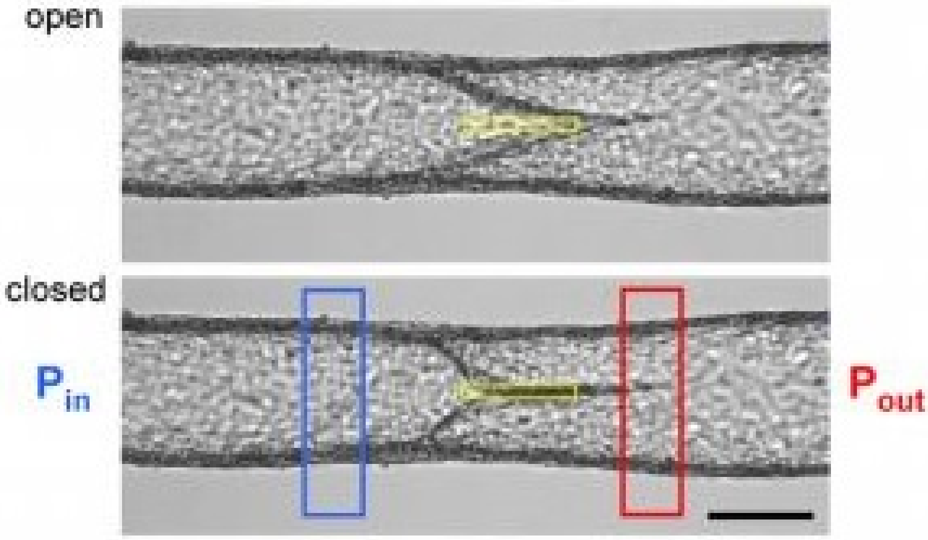

(b) Open and close state of valve when viewed from direction A. Forward flow direction is from left to right. Images taken at 10x magnification.

Figure D.1: Anatomy of rat lymphatic valves (Cont'd).

(c) Valve from rat thoracic duct as viewed from direction B at 10x magnification (See also supplementary video S2)

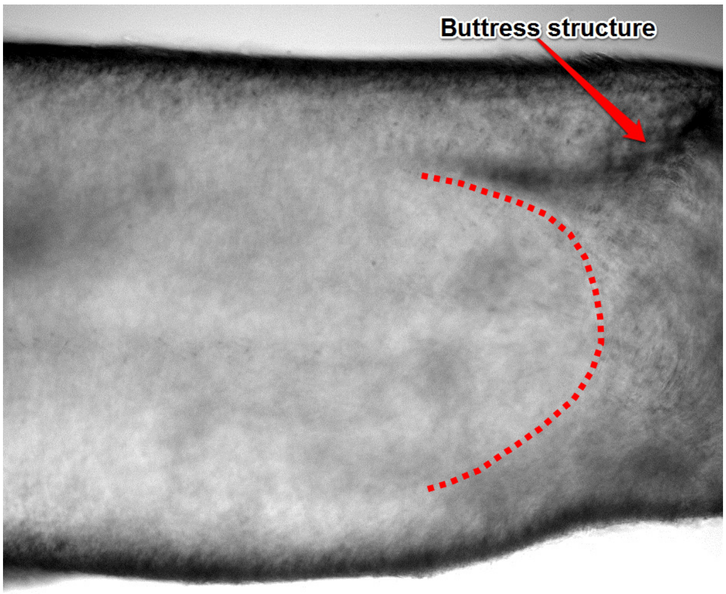

(d) Same as Figure D.1c, with the semi-lunar valve edge highlighted with a red line.

Figure D.1: Anatomy of rat lymphatic valves. Subfigures (a) and (b) reprinted from Davis et al. [26] with permission.

Appendix E

Research Output

E.1 Journal Publications

Margaris, K. N. and Black, R. A. (2012). Modelling the lymphatic system: challenges and opportunities. *Journal of the Royal Society Interface*, 9(69):601–612

E.2 Conference Contributions

Sep 2013	Bionegineering13, 6th annual symposium of the UK Bioengineering Society, Glasgow, UK. “A Micro-PIV approach to flow measurements in lymphatic vessels”
Aug 2013	19th Congress of the European Society of Biomechanics Conference, Patras, Greece. “Development of a time resolved micro-PIV system for flow velocity measurements”
Feb 2013	Universities of Glasgow and Strathclyde, Centre for Mathematics Applied to the Life Sciences. Research Student and RA Meeting on Mathematical Modelling in the Life Sciences. “Modelling the hydrodynamics/biomechanics of the lymphatic system”

Appendix F

About the author

Konstantinos Margaris,
born on Wednesday, March 14, 1979
in Thessaloniki, Greece

Since Oct 2013	BPP-Technical Services Limited, London, UK
Oct 2010 - Sep 2013	University of Strathclyde, Glasgow, UK, Department of Biomedical Engineering, PhD thesis: “Micro-Particle Image Velocimetry for Lymphatic Flow”
Sep 2009 - Sep 2010	University of Strathclyde, Glasgow, UK, Department of Biomedical Engineering, MSc in Bioengineering, Thesis title: “Development of a plastic alignment device for incorporation in a trans-tibial prosthesis for use in developing countries”
Oct 2007 - Oct 2008	Compite Nt SA, Lakkoma, Greece
Feb 2006 - Sep 2007	Flow Dynamics Hellas SA, Thessaloniki, Greece
Sep 2004 - Sep 2005	National Service
Sep 1997 - Jul 2003	Aristotle University of Thessaloniki, Greece, Department of Mechanical Engineering, MEng in Mechanical Engineering, Degree project: “Dynamic analysis of automobile internal combustion engine crankshaft”

References

[1] Adrian, R. J. and Westerweel, J. (2011). *Particle Image Velocimetry*. Cambridge University Press.

[2] Akl, T. J., Nagai, T., Cote, G. L., and Gashev, A. A. (2011a). Mesenteric lymph flow in adult and aged rats. *American journal of physiology. Heart and circulatory physiology*, 301(5):H1828–40.

[3] Akl, T. J., Nepiyushchikh, Z. V., Gashev, A. A., Zawieja, D. C., and Cote, G. L. (2011b). Measuring contraction propagation and localizing pacemaker cells using high speed video microscopy. *Journal of Biomedical Optics*, 16(2):9.

[4] Alharbi, A. Y. and Sick, V. (2010). Investigation of boundary layers in internal combustion engines using a hybrid algorithm of high speed micro-PIV and PTV. *Experiments in Fluids*, 49(4):949–959.

[5] Aukland, K. (2005). Arnold heller and the lymph pump. *Acta Physiologica Scandinavica*, 185(3):171–180.

[6] Aukland, K. and Reed, R. K. (1993). Interstitial-lymphatic mechanisms in the control of extracellular fluid volume. *Physiological Reviews*, 73(1):1–78.

[7] Azooz, A. A. and Owaid, A. Y. (2012). Experimental Investigation of Low Pressure Audio Frequency Discharge in Argon. *Chinise Physics Letters*, 29(10).

[8] Benoit, J. N., Zawieja, D. C., Goodman, A. H., and Granger, H. J. (1989). Characterization of intact mesenteric lymphatic pump and its responsiveness to acute edemagenic stress. *American Journal of Physiology*, 257(6):H2059–H2069.

[9] Beresford-Smith, B., Nesbitt, K. V., and Vanhelden, D. F. (1993). Edge-detection at multiple

locations using a radar tracking algorithm as exemplified in isolated guinea-pig lymphatic vessels. *Journal of Neuroscience Methods*, 49(1-2):69–79.

[10] Berk, D., Swartz, M., Leu, A., and Jain, R. (1996). Transport in lymphatic capillaries .2. Microscopic velocity measurement with fluorescence photobleaching. *American Journal of Physiology-Heart and Circulatory Physiology*, 270(1):H330–H337.

[11] Bertram, C. D., Macaskill, C., and Moore, J. E. (2011). Simulation of a chain of collapsible contracting lymphangions with progressive valve closure. *Journal of Biomechanical Engineering-Transactions of the ASME*, 133(1):10.

[12] Boggon, R. P. and Palfrey, A. J. (1973). Microscopic anatomy of human lymphatic trunks. *Journal of Anatomy*, 114(APR):389–405.

[13] Bohlen, H. G., Gasheva, O. Y., and Zawieja, D. C. (2011). Nitric oxide formation by lymphatic bulb and valves is a major regulatory component of lymphatic pumping. *American Journal of Physiology-Heart and Circulatory Physiology*, 301(5):H1897–H1906.

[14] Bridenbaugh, E. A., Gashev, A. A., and Zawieja, D. C. (2003). Lymphatic muscle: a review of contractile function. *Lymphatic research and biology*, 1(2):147–58.

[15] Browse, N. L., Doig, R. L., and Sizeland, D. (1984). The resistance of a lymph-node to lymph-flow. *British Journal of Surgery*, 71(3):192–196.

[16] Cabral, B. and Leedom, L. C. (1993). Imaging vector fields using line integral convolution. In *Proceedings of the 20th Annual Conference on Computer Graphics and Interactive Techniques*, SIGGRAPH ’93, pages 263–270, New York, NY, USA. ACM.

[17] Charman, W. N. and Stella, V. J. (1992). *Lymphatic transport of drugs*. CRC Press.

[18] Charonko, J. J., King, C. V., Smith, B. L., and Vlachos, P. P. (2010). Assessment of pressure field calculations from particle image velocimetry measurements. *Measurement Science & Technology*, 21(10).

[19] Chen, J.-J., Wang, T.-Y., Huang, K.-L., Liu, T.-S., Tsai, M.-D., and Lin, C.-T. (2012). Freeform lens design for LED collimating illumination. *Optics Express*, 20(10):10984–10995.

[20] Cheng, S., Clarke, E. C., and Bilston, L. E. (2009). The effects of preconditioning strain on measured tissue properties. *Journal Of Biomechanics*, 42(9):1360–1362.

[21] Chetelat, O. and Kim, K. (2002). Miniature particle image velocimetry system with LED in-line illumination. *Measurement Science & Technology*, 13(7):1006–1013.

[22] Cierpka, C. and Kaehler, C. J. (2012). Particle imaging techniques for volumetric three-component (3D3C) velocity measurements in microfluidics. *Journal of Visualization*, 15(1):1–31.

[23] Costanzo, F. and Brasseur, J. G. (2013). The invalidity of the laplace law for biological vessels and of estimating elastic modulus from total stress vs. strain: a new practical method. *Mathematical Medicine and Biology*.

[24] Dabiri, J. O., Bose, S., Gemmell, B. J., Colin, S. P., and Costello, J. H. (2014). An algorithm to estimate unsteady and quasi-steady pressure fields from velocity field measurements. *Journal of Experimental Biology*, 217(3):331–336.

[25] Davis, M. J. (2005). An improved, computer-based method to automatically track internal and external diameter of isolated microvessels. *Microcirculation*, 12(4):361–372.

[26] Davis, M. J., Rahbar, E., Gashev, A. A., Zawieja, D. C., and Moore, J. E. (2011). Determinants of valve gating in collecting lymphatic vessels from rat mesentery. *American Journal of Physiology-Heart and Circulatory Physiology*, 301(1):H48–H60.

[27] Deen, N. G., Willems, P., Annaland, M. v. S., Kuipers, J. A. M., Lammertink, R. G. H., Kemperman, A. J. B., Wessling, M., and van der Meer, W. G. J. (2010). On image preprocessing for PIV of single- and two-phase flows over reflecting objects. *Experiments in fluids*, 49(2):525–530.

[28] Dielenberg, R., Halasz, P., Hosaka, K., and van Helden, D. (2006). Vessel motion measurement in real-time using movement detection at multiple regions of interest. *Journal of Neuroscience Methods*, 152(1-2):40–47.

[29] Dietrich, T., Bock, F., Yuen, D., Hos, D., Bachmann, B. O., Zahn, G., Wiegand, S., Chen, L., and Cursiefen, C. (2010). Cutting edge: Lymphatic vessels, not blood vessels, primarily mediate immune rejections after transplantation. *Journal of Immunology*, 184(2):535–539.

[30] Dixon, J. B., Gashev, A. A., Zawieja, D. C., Moore, J. E., and Cote, G. L. (2007). Image correlation algorithm for measuring lymphocyte velocity and diameter changes in contracting microlymphatics. *Annals of Biomedical Engineering*, 35(3):387–396.

[31] Dixon, J. B., Greiner, S. T., Gashev, A. A., Cote, G. L., Moore, J. E., and Zawieja, D. C. (2006). Lymph flow, shear stress, and lymphocyte velocity in rat mesenteric prenodal lymphatics. *Microcirculation*, 13(7):597–610.

[32] Dixon, J. B., Zawieja, D. C., Gashev, A. A., and Cote, G. L. (2005). Measuring microlymphatic flow using fast video microscopy. *Journal of Biomedical Optics*, 10(6):7.

[33] Einstein, A. (1906). Eine neue bestimmung der molekuldimensionen. *Annalen der Physik*, 324(2):289–306.

[34] Fedosov, I., Tuchin, V., Galartzha, E., Solov'eva, A., and Stepanova, T. (2002). Recording of lymph flow dynamics in microvessels using correlation properties of scattered coherent radiation. *Quantum Electronics*, 32(11):970–974.

[35] Fischer, J., Mewes, H., Hopp, H., and Schubert, R. (1996). Analysis of pressurized resistance vessel diameter changes with a low cost digital image processing device. *Computer Methods and Programs in Biomedicine*, 50(1):23–30.

[36] Florey, H. (1927). Observations on the contractility of lacteals: Part i. *The Journal of physiology*, 62(3):267–72.

[37] Földi, M., Földi, E., and Kubik, S., editors (2003). *Textbook of Lymphology for Physicians and Lymphedema Therapists*. Urban & Fischer.

[38] Fouras, A., Dusting, J., Sheridan, J., Kawahashi, M., Hirahara, H., and Hourigan, K. (2009). Engineering imaging: Using particle image velocimetry to see physiology in a new light. *Clinical and Experimental Pharmacology and Physiology*, 36(2):238–247.

[39] Fujisawa, N., Nakamura, Y., Matsuura, F., and Sato, Y. (2010). A practical approach to piv uncertainty analysis. *Microfluidics and Nanofluidics*, 2(5):447–453.

[40] Galanzha, E. I., Tuchin, V. V., and Zharov, V. P. (2007). Advances in small animal mesentery models for in vivo flow cytometry, dynamic microscopy, and drug screening. *World Journal of Gastroenterology*, 13(2):192–218.

[41] Garcia, D. (2011). A fast all-in-one method for automated post-processing of PIV data. *Experiments in Fluids*, 50(5):1247–1259.

[42] Gashev, A. A. (1991). The mechanism of the formation of a reverse fluid filling in the lymphangions. *Fiziologicheskii Zhurnal SSSR Imeni I M Sechenova*, 77:63–69. in Russian.

[43] Gashev, A. A. (2008). *Lymphatic vessels: Pressure- and flow-dependent regulatory reactions*, volume 1131 of *Annals of the New York Academy of Sciences*, pages 100–109. Blackwell Publishing, Oxford.

[44] Gashev, A. A., Davis, M. J., and Zawieja, D. C. (2002). Inhibition of the active lymph pump by flow in rat mesenteric lymphatics and thoracic duct. *Journal of Physiology-London*, 540(3):1023–1037.

[45] Gashev, A. A. and Zawieja, D. C. (2001). Physiology of human lymphatic contractility: A historical perspective. *Lymphology*, 34(3):124–134.

[46] Gashev, A. A. and Zawieja, D. C. (2010). Hydrodynamic regulation of lymphatic transport and the impact of aging. *Pathophysiology*, 17(4):277–87.

[47] Goss, L. P., Estevadeordal, J., and Crafton, J. W. (2007). Velocity measurements near walls, cavities, and model surfaces using Particle Shadow Velocimetry (PSV). In *2007 22nd International Congress on Instrumentation in Aerospace Simulation Facilities*, pages 7–14.

[48] Gresho, P. and Sani, R. (1987). On pressure boundary-conditions for the incompressible navier-stokes equations. *International Journal for Numerical Methods in Fluids*, 7(10):1111–1145.

[49] Gretz, J. E., Anderson, A. O., and Shaw, S. (1997). Cords, channels, corridors and conduits: Critical architectural elements facilitating cell interactions in the lymph node cortex. *Immunological Reviews*, 156:11–24.

[50] Gui, L., Wereley, S., and Lee, S. (2002). Digital filters for reducing background noise in micro-piv. In *11th Intl. Symposium on Appl. of Laser Techniques to Fluid Mechanics*.

[51] Gurka, R., Liberzon, A., Hefetz, D., Rubinstein, D., and Shavit, U. (1999). Computation of pressure distribution using piv velocity data. In *3rd Int. Workshop on PIV. Santa Barbara, CA*, pages 101–106.

[52] Guth, E. and Simha, R. (1936). Untersuchungen uber die viskositat von suspensionen und losungen. 3. uber die viskositat von kugelsuspensionen. *Kolloid-Zeitschrift*, 74(3):266–275.

[53] Hagsater, S. M., Westergaard, C. H., Bruus, H., and Kutter, J. P. (2008). Investigations on led illumination for micro-piv including a novel front-lit configuration. *Experiments in Fluids*, 44(2):211–219.

[54] Hain, R., Kahler, C. J., and Tropea, C. (2007). Comparison of ccd, cmos and intensified cameras. *Experiments in Fluids*, 42(3):403–411.

[55] Hannig, J., Wang, C., and Iyer, H. (2003). Uncertainty calculation for the ratio of dependent measurements. *Metrologia*, 40(4):177–183.

[56] Hargens, A. R. and Zweifach, B. W. (1977). Contractile stimuli in collecting lymph vessels. *American Journal of Physiology*, 233(1):H57–H65.

[57] Honkanen, M. and Nobach, H. (2005). Background extraction from double-frame PIV images. *Experiments in Fluids*, 38(3):348–362.

[58] Hughes, G. A. and Allen, J. M. (1993). Neural modulation of bovine mesenteric lymph-node contraction. *Experimental Physiology*, 78(5):663–674.

[59] Hughes, W. F. and Brighton, J. A. (1999). *Schaum's Outline of: Theory and Problems of Fluid Mechanics*. McGraw-Hill, 3rd edition.

[60] Jianwen, L., Jing, B., and Jinhua, S. (2006). Application of the wavelet transforms on axial strain calculation in ultrasound elastography. *Progress in Natural Science*, 16(9):942–947.

[61] Jones, D. and Min, W. (2011). An overview of lymphatic vessels and their emerging role in cardiovascular disease. *Journal of cardiovascular disease research*, 2(3).

[62] Kaehler, C. J., Scharnowski, S., and Cierpka, C. (2012a). On the resolution limit of digital particle image velocimetry. *Experiments in Fluids*, 52(6):1629–1639.

[63] Kaehler, C. J., Scharnowski, S., and Cierpka, C. (2012b). On the uncertainty of digital PIV and PTV near walls. *Experiments in Fluids*, 52(6):1641–1656.

[64] Keane, R. D. and Adrian, R. J. (1992). Theory of cross-correlation analysis of piv images. *Applied Scientific Research*, 49(3):191–215.

[65] Kestin, J., Sokolov, M., and Wakeham, W. (1978). Viscosity of liquid water in range $-8\,^{\circ}\mathrm{C}$ to $150\,^{\circ}\mathrm{C}$. *Journal of physical and chemical reference data*, 7(3):941–948.

[66] Kim, H. B., Hertzberg, J. R., Lanning, C., and Shandas, R. (2003). In vitro study of wall shear stress measurement using a non invasive echo piv technique. In *Proceedings of the ASME Summer Bioengineering Conference*, pages 71–72.

[67] Kowala, M. C. and Schoefl, G. I. (1986). The popliteal lymph-node of the mouse - internal architecture, vascular distribution and lymphatic supply. *Journal of Anatomy*, 148:25–46.

[68] Kwon, S. and Sevick-Muraca, E. M. (2007). Noninvasive quantitative imaging of lymph function in mice. *Lymphatic Research and Biology*, 5(4):219–231.

[69] Lazar, E., Glumac, N., Dutton, C., and Elliot, G. (2010). A practical approach to piv uncertainty analysis. In *27th AIAA Aerodynamic Measurement Technology and Ground Testing Conference*.

[70] Leak, L. V. and Burke, J. F. (1968). Ultrastructural studies on the lymphatic anchoring filaments. *J Cell Biol*, 36(1):129–49.

[71] Lee, E. C., Lee, H. C., and Park, K. R. (2009a). Finger Vein Recognition Using Minutia-Based Alignment and Local Binary Pattern-Based Feature Extraction. *International Journal of Imaging Systems and Technology*, 19(3):179–186.

[72] Lee, J., Jirapatnakul, A. C., Reeves, A. P., Crowe, W. E., and Sarelius, I. H. (2009b). Vessel Diameter Measurement from Intravital Microscopy. *Annals of Biomedical Engineering*, 37(5):913–926.

[73] Lee, S. H., Wen, H. J., and Shen, C. L. (1993). Ultrastucture of the monkey thoracic-duct and the cisterna chyli. *Journal of Anatomy*, 182:205–212.

[74] Lee, Y.-S., Koo, H.-S., and Jeong, C.-S. (2006). A straight line detection using principal component analysis. *Pattern Recognition Letters*, 27(14):1744–1754.

[75] Lindken, R., Rossi, M., Grosse, S., and Westerweel, J. (2009). Micro-particle image velocimetry (mu piv): Recent developments, applications, and guidelines. *Lab on a Chip*, 9(17):2551–2567.

[76] Liu, X. and Katz, J. (2006). Instantaneous pressure and material acceleration measurements using a four-exposure PIV system. *Experiments in Fluids*, 41(2):227–240. 6th International Symposium on Particle Image Velocimetry (PIV), Pasadena, CA, SEP 21-23, 2005.

[77] Lucarelli, R. T., Ogawa, M., Kosaka, N., Turkbey, B., Kobayashi, H., and Choyke, P. L. (2009). New approaches to lymphatic imaging. *Lymphatic research and biology*, 7(4):205–14.

[78] Luminus Devices Inc (2010). *Phlatlight PT120 Projection Chipset, Summary datasheet.*

[79] Macdonald, A. J. (2008). *The Computational Modelling of Collecting Lymphatic Vessels*. PhD thesis, University of Exeter.

[80] Macdonald, A. J., Arkill, K. P., Tabor, G. R., McHale, N. G., and Winlove, C. P. (2008). Modeling flow in collecting lymphatic vessels: one-dimensional flow through a series of contractile elements. *American Journal of Physiology-Heart and Circulatory Physiology*, 295(1):H305–H313.

[81] Maragos, P. (1987). Tutorial on advances in morphological image-processing and analysis. *Optical Engineering*, 26(7):623–632.

[82] Margaris, K. N. and Black, R. A. (2012). Modelling the lymphatic system: challenges and opportunities. *Journal of the Royal Society Interface*, 9(69):601–612.

[83] Mazzoni, M. C., Skalak, T. C., and Schmidschonbein, G. W. (1987). Structure of lymphatic valves in the spinotrapezius muscle of the rat. *Blood Vessels*, 24(6):304–312.

[84] McGeown, J. G. and Gallagher, M. J. P. (1990). The effects of field stimulation on bovine mesenteric lymph-node contractility. *Pflugers Archiv-European Journal of Physiology*, 416(6):667–672.

[85] McGeown, J. G., McHale, N. G., Roddie, I. C., and Thornbury, K. (1987). Peripheral lymphatic responses to outflow pressure in anesthetized sheep. *Journal Of Physiology-London*, 383:527–536.

[86] McHale, N. G. and Meharg, M. K. (1992). Coordination of pumping in isolated bovine lymphatic vessels. *Journal of Physiology-London*, 450:503–512.

[87] McHale, N. G. and Roddie, I. C. (1976). Effect of transmural pressure on pumping activity in isolated bovine lymphatic vessels. *Journal of Physiology-London*, 261(2):255–269.

[88] Mei, R. (1996). Velocity fidelity of flow tracer particles. *Experiments in Fluids*, 22(1):1–13.

[89] Meinhart, C. D., Wereley, S. T., and Gray, M. H. B. (2000). Volume illumination for two-dimensional particle image velocimetry. *Measurement Science & Technology*, 11(6):809–814.

[90] Mooney, M. (1951). The Viscosity of a Concentrated suspension of Spherical Particles. *Journal of Colloid Science*, 6(2):162–170.

[91] Munoz, F., Benitez, P., Dross, O., Minano, J., and Parkyn, B. (2004). Simultaneous multiple surface design of compact air-gap collimators for light-emitting diodes. *Optical Engineering*, 43(7):1522–1530.

[92] Muthuchamy, M. and Zawieja, D. (2008). *Molecular regulation of lymphatic contractility*, volume 1131 of *Annals of the New York Academy of Sciences*, pages 89–99. Blackwell Publishing, Oxford.

[93] Naito, T., Ozawa, Y., Tomoyasu, M., Inagaki, M., Fukue, M., Sakai, M., Yamamoto, T., Ishikawa, S., and Onizuka, M. (2006). New method for evaluation of lung lymph flow rate with intact lymphatics in anaesthetized sheep. *Acta Physiologica*, 188(2):139–149.

[94] Negrini, D., Ballard, S. T., and Benoit, J. N. (1994). Contribution of lymphatic myogenic activity and respiratory movements to pleural lymph-flow. *Journal of Applied Physiology*, 76(6):2267–2274.

[95] Nguyen, C. V., Nguyen, T. D., Wells, J. C., and Nakayama, A. (2010a). Interfacial PIV to resolve flows in the vicinity of curved surfaces. *Experiments in Fluids*, 48(4):577–587.

[96] Nguyen, T. D., Wells, J. C., and Nguyen, C. V. (2010b). Wall shear stress measurement of near-wall flow over inclined and curved boundaries by stereo interfacial particle image velocimetry. *International Journal of Heat and Fluid Flow*, 31(3, SI):442–449.

[97] Nisimaru, Y. (1982). Summary of our studies concerning the structure and function of lymphatic-system. *Hiroshima Journal of Medical Sciences*, 31(3):145–160.

[98] Ohhashi, T., Azuma, T., and Sakaguchi, M. (1980). Active and passive mechanical characteristics of bovine mesenteric lymphatics. *American Journal of Physiology*, 239(1):H88–H95.

[99] Ohtani, O. and Ohtani, Y. (2008). Structure and function of rat lymph nodes. *Archives of Histology and Cytology*, 71(2):69–76.

[100] Olsen, M. and Adrian, R. (2000). Out-of-focus effects on particle image visibility and correlation in microscopic particle image velocimetry. *Experiments in Fluids*, 29(S):S166–S174. 3rd International Workshop on Particle Image Velocimetry, Santa Barbara, California, SEP 16-18, 1999.

[101] Olsen, M. and Bourdon, C. (2003). Out-of-plane motion effects in microscopic particle image velocimetry. *Journal of Fluids Engineering-Transactions of the ASME*, 125(5):895–901.

[102] Olszewski, W. L. (2002). *Contractility patterns of normal and pathologically changed human lymphatics*, volume 979 of *Annals of the New York Academy of Sciences*, pages 52–63. New York Acad Sciences, New York.

[103] Olszewski, W. L. and Engeset, A. (1980). Intrinsic contractility of pre-nodal lymph vessels and lymph-flow in human leg. *American Journal of Physiology*, 239(6):H775–H783.

[104] Onizuka, M., Flatebo, T., and Nicolaysen, G. (1997). Lymph flow pattern in the intact thoracic duct in sheep. *Journal of Physiology-London*, 503(1):223–234.

[105] Pan, W. R., le Roux, C. M., and Levy, S. M. (2011). Alternative lymphatic drainage routes from the lateral heel to the inguinal lymph nodes: anatomic study and clinical implications. *Anz Journal of Surgery*, 81(6):431–435.

[106] Pan, W. R., Le Roux, C. M., Levy, S. M., and Briggs, C. A. (2010). The morphology of the human lymphatic vessels in the head and neck. *Clinical Anatomy*, 23(6):654–661.

[107] Papp, M., Makara, G. B., and Hajtman, B. (1971). Resistance of in-situ perfused lymph trunks and lymph nodes to flow. *Experientia*, 27(4):391–392.

[108] Pellegrino, F., Vanzella, W., and Torre, V. (2004). Edge detection revisited. *IEEE Transactions on Systems Man and Cybernetics Part B-Cybernetics*, 34(3):1500–1518.

[109] Poelma, C., Van der Heiden, K., Hierck, B. P., Poelmann, R. E., and Westerweel, J. (2010). Measurements of the wall shear stress distribution in the outflow tract of an embryonic chicken heart. *Journal of the Royal Society Interface*, 7(42):91–103.

[Polysciences] Polysciences. Microspheres & particles handling guide.

[111] Potsaid, B. and Wen, J. T.-Y. (2008). Adaptive scanning optical microscope: large field of view and high-resolution imaging using a MEMS deformable mirror. *Journal of Micro-Nanolithography MEMS and MOEMS*, 7(2):021009:1–10.

[112] Prasad, A. K. (2000). Particle image velocimetry. *Current Science*, 79(1):51–60.

[113] Quere, I. (2010). Lymphatic system: Anatomy, histology and physiology. *Presse Medicale*, 39(12):1269–1278.

[114] Quick, C. M., Venugopal, A. M., Dongaonkar, R. M., Laine, G. A., and Stewart, R. H. (2008). First-order approximation for the pressure-flow relationship of spontaneously contracting lymphangions. *American Journal of Physiology-Heart and Circulatory Physiology*, 294(5):H2144–H2149.

[115] Quick, C. M., Venugopal, A. M., Gashev, A. A., Zawieja, D. C., and Stewart, R. H. (2007). Intrinsic pump-conduit behavior of lymphangions. *American Journal of Physiology-Regulatory Integrative and Comparative Physiology*, 292(4):R1510–R1518.

[116] Raffel, M. (2007). *Particle image velocimetry : a practical guide*. Springer Verlag.

[117] Reddy, N. P. and Kesavan, S. K. (1989). Low reynolds-number liquid propulsion in contracting tubular segments connected through valves. *Mathematical and Computer Modelling*, 12(7):839–844.

[118] Reddy, N. P., Krouskop, T. A., and Newell, P. H. (1977). Computer-model of lymphatic-system. *Computers in Biology and Medicine*, 7(3):181–197.

[119] Reddy, N. P. and Patel, K. (1995). A mathematical-model of flow-through the terminal lymphatics. *Medical Engineering & Physics*, 17(2):134–140.

[120] Reneman, R. S., Arts, T., and Hoeks, A. P. G. (2006). Wall shear stress - an important determinant of endothelial cell function and structure - in the arterial system in vivo. *Journal of Vascular Research*, 43(3):251–269.

[121] Rockson, S. G. (2010). Current concepts and future directions in the diagnosis and management of lymphatic vascular disease. *Vascular Medicine*, 15(3):223–231.

[122] Roozendaal, R., Mebius, R. E., and Kraal, G. (2008). The conduit system of the lymph node. *International Immunology*, 20(12):1483–1487.

[123] Rossi, M., Segura, R., Cierpka, C., and Kaehler, C. J. (2012). On the effect of particle image intensity and image preprocessing on the depth of correlation in micro-PIV. *Experiments in Fluids*, 52(4):1063–1075.

[124] Sacchi, G., Weber, E., Agliano, M., Raffaelli, N., and Comparini, L. (1997). The structure of superficial lymphatics in the human thigh: Precollectors. *Anatomical Record*, 247(1):53–62.

[125] Santiago, J. G., Wereley, S. T., Meinhart, C. D., Beebe, D. J., and Adrian, R. J. (1998). A particle image velocimetry system for microfluidics. *Experiments in Fluids*, 25(4):316–319.

[126] Schafer, R. W. (2011). What Is a Savitzky-Golay Filter? *IEEE Signal Processing Magazine*, 28(4):111–117.

[127] Schmid-Schonbein, G. W. (1990a). Mechanisms causing initial lymphatics to expand and compress to promote lymph flow. *Archives of Histology and Cytology*, 53(Suppl):107–114.

[128] Schmid-Schonbein, G. W. (1990b). Microlymphatics and lymph flow. *Physiological Reviews*, 70(4):987–1028.

[129] Sciacchitano, A., Wieneke, B., and Scarano, F. (2013). PIV uncertainty quantification by image matching. *Measurement Science & Technology*, 24(4).

[130] Sharma, R., Wang, W., Rasmussen, J. C., Joshi, A., Houston, J. P., Adams, K. E., Cameron, A., Ke, S., Kwon, S., Mawad, M. E., and Sevick-Muraca, E. M. (2007). Quantitative imaging of lymph function. *American Journal of Physiology-Heart and Circulatory Physiology*, 292(6):H3109–H3118.

[131] Sheng, Y. M. and Xiu, R. J. (2012). Automated method for tracking vasomotion of intravital microvascular and microlymphatic vessels. *Clinical Hemorheology and Microcirculation*, 52(1):37–48.

[132] Shinohara, K., Sugii, Y., Aota, A., Hibara, A., Tokeshi, M., Kitamori, T., and Okamoto, K. (2004). High-speed micro-piv measurements of transient flow in microfluidic devices. *Measurement Science & Technology*, 15(10):1965–1970.

[133] Sinton, D. (2004). Microscale flow visualization. *Microfluidics and Nanofluidics*, 1(1):2–21.

[134] Sugii, Y., Okuda, R., Okamoto, K., and Madarame, H. (2005). Velocity measurement of both red blood cells and plasma of in vitro blood flow using high-speed micro piv technique. *Measurement Science & Technology*, 16(5):1126–1130.

[135] Swartz, M., Berk, D., and Jain, R. (1996). Transport in lymphatic capillaries .1. Macroscopic measurements using residence time distribution theory. *American Journal of Physiology-Heart and Circulatory Physiology*, 270(1):H324–H329.

[136] Swartz, M. A. (2001). The physiology of the lymphatic system. *Advanced Drug Delivery Reviews*, 50(1-2):3–20.

[137] Swartz, M. A., Hubbell, J. A., and Reddy, S. T. (2008). Lymphatic drainage function and its immunological implications: From dendritic cell homing to vaccine design. *Seminars in Immunology*, 20:147–156.

[138] Swartz, M. A. and Skobe, M. (2001). Lymphatic function, lymphangiogenesis, and cancer metastasis. *Microscopy Research and Technique*, 55(2):92–99.

[139] Taylor, R. J. (1997). *An Introduction to Error Analysis: The study of uncertainties in physical measurements*. University Science Books.

[140] Telinius, N., Drewsen, N., Pilegaard, H., Kold-Petersen, H., de Leval, M., Aalkjaer, C., Hjortdal, V., and Boedtkjer, D. B. (2010). Human thoracic duct in vitro: diameter-tension properties, spontaneous and evoked contractile activity. *American Journal of Physiology-Heart and Circulatory Physiology*, 299(3):H811–H818.

[141] Thornbury, K. D., McHale, N. G., Allen, J. M., and Hughes, G. (1990). Nerve-mediated contractions of sheep mesenteric lymph-node capsules. *Journal of Physiology-London*, 422:513–522.

[142] Timmins, B. H., Wilson, B. W., Smith, B. L., and Vlachos, P. P. (2012). A method for automatic estimation of instantaneous local uncertainty in particle image velocimetry measurements. *Experiments in Fluids*, 53(4):1133–1147.

[143] Tretbar, L. L., Morgan, L. C., Lee, B. B., Simonian, J. S., and Bloneau, B. (1992). *Lymphedema: Diagnosis and Treatment*. Springer.

[144] Trzewik, J., Mallipattu, S. K., Artmann, G. M., Delano, F. A., and Schmid-Schonbein, G. W. (2001). Evidence for a second valve system in lymphatics: endothelial microvalves. *Faseb Journal*, 15(10):1711–1717.

[145] Tumer, A., Ozturkdemir, N., Basareroglu, C., and Noyan, A. (1983). Spontaneous contractions and stretch-evoked responses of isolated lymph-nodes. *Journal of Muscle Research and Cell Motility*, 4(1):103–113.

[146] Van Giel, B., Meuret, Y., and Thienpont, H. (2006). Design of axisymmetrical tailored concentrators for led light source applications - art. no. 619603. In *Conference on Photonics in Multimedia*, volume 6196, pages 19603–19603. Spie-Int Soc Optical Engineering.

[147] van Oudheusden, B. W. (2013). PIV-based pressure measurement. *Measurement Science & Technology*, 24(3).

[148] Vennemann, P., Lindken, R., and Westerweel, J. (2007). In vivo whole-field blood velocity measurement techniques. *Experiments in Fluids*, 42(4):495–511.

[149] Venugopal, A. M., Stewart, R. H., Laine, G. A., Dongaonkar, R. M., and Quick, C. M. (2007). Lymphangion coordination minimally affects mean flow in lymphatic vessels. *American Journal of Physiology-Heart and Circulatory Physiology*, 293(2):H1183–H1189.

[150] Von Der Weid, P. Y. (2001). Review article: lymphatic vessel pumping and inflammation - the role of spontaneous constrictions and underlying electrical pacemaker potentials. *Alimentary Pharmacology & Therapeutics*, 15(8):1115–1129.

[151] Webb, R. and Rogomentich, F. (1999). Confocal microscope with large field and working distance. *Applied Optics*, 38(22):4870–4875.

[152] Wereley, S. T. and Meinhart, C. D. (2010). Recent advances in micro-particle image velocimetry. *Annual Review of Fluid Mechanics*, 42:557–576.

[153] Westerdale, J., Belohlavek, M., McMahon, E. M., Jiamsripong, P., Heys, J. J., and Milano, M. (2011). Flow velocity vector fields by ultrasound particle imaging velocimetry. *Journal of Ultrasound Medicine*, 30(2):187–195.

[154] Westerweel, J. (2000). Theoretical analysis of the measurement precision in particle image velocimetry. *Experiments in Fluids*, 29(S):S3–S12. 3rd International Workshop on Particle Image Velocimetry, Santa Barbara, California, SEP 16-18, 1999.

[155] Willard-Mack, C. L. (2006). Normal structure, function, and histology of lymph nodes. *Toxicologic Pathology*, 34(5):409–424.

[156] Willert, C., Stasicki, B., Klinner, J., and Moessner, S. (2010). Pulsed operation of high-power light emitting diodes for imaging flow velocimetry. *Measurement Science & Technology*, 21(7):11.

[157] Wilson, J. T., Wang, W., Hellerstedt, A. H., Zawieja, D. C., and Moore, J. E. (2013). Confocal image-based computational modeling of nitric oxide transport in a rat mesenteric lymphatic vessel. *Journal of Biomechanical Engineering*, 135:051005–1.

[158] Winston, R., Miñano, J., and Benítez, P. (2005). *Non-Imaging Optics*. Elsevier Academic Press.

[159] Wronski, T., Persson, P., Seeliger, E., Harnath, A., and Flemming, B. (2000). Coupling of left ventricular and aortic volume elasticity in the rabbit. *American Journal of Physiology-Regulatory Integrative and Comparative Physiology*, 279(2):R539–R547.

[160] Zawieja, D. C., Davis, K. L., Schuster, R., Hinds, W. M., and Granger, H. J. (1993). Distribution, propagation, and coordination of contractile activity in lymphatics. *American Journal of Physiology*, 264(4):H1283–H1291.

[161] Zhang, F., Niu, G., Lu, G., and Chen, X. (2011). Preclinical Lymphatic Imaging. *Molecular Imaging and Biology*, 13(4):599–612.

[162] Zhang, Z. and Hugo, R. (2006). Stereo particle image velocimetry applied to a vortex pipe flow. *Experiments in Fluids*, 40(3):333–346.